SOMATODENDRITIC OXYTOCIN RELEASE: DYNAMICS AND MOLECULAR MACHINERY

Tesis Doctoral presentada por

Beatriz Aznar Escolano

- 2025 –

Director/a de Tesis: Dra. Sandra Jurado Sánchez

Programa de Doctorado en Neurociencias

Instituto de Neurociencias

Universidad Miguel Hernández de Elche

CSIC UNIVERSITAS Miguel Hernández
INSTITUTO DE NEUROCIENCIAS

EXCELENCIA SEVERO OCHOA
2014 - 2027

La presente Tesis Doctoral, titulada “Somatodendritic oxytocin release: dynamics and molecular machinery”, se presenta bajo la modalidad de **tesis convencional con el siguiente indicio de calidad**:

- Royo, M., Escolano, B. A., Madrigal, M. P., & Jurado, S. (2022). AMPA Receptor Function in Hypothalamic Synapses. Frontiers in Synaptic Neuroscience, 14(January), 1–16. https://doi.org/10.3389/fnsyn.2022.833449

La Dra. Dña. *Sandra Jurado Sánchez*, directora de la tesis doctoral titulada **“Somatodendritic oxytocin release: dynamics and molecular machinery”**

INFORMA:

Que Dña. *Beatriz Aznar Escolano* ha realizado bajo mi supervisión el trabajo titulado “Somatodendritic oxytocin release: dynamics and molecular machinery” conforme a los términos y condiciones definidos en su Plan de Investigación y de acuerdo al Código de Buenas Prácticas de la Universidad Miguel Hernández de Elche, cumpliendo los objetivos previstos de forma satisfactoria para su defensa pública como tesis doctoral.

Lo que firmo para los efectos oportunos, en San Juan de Alicante a 15 de mayo de 2025.

Director/a de la tesis

Dra. Dña. *Sandra Jurado Sánchez*

Sant Joan d'Alacant, 15 de mayo 2025

Dña.Cruz Morenilla Palao, Coordinadora del programa de Doctorado en Neurociencias del Instituto de Neurociencias de Alicante, centro mixto de la Universidad Miguel Hernández (UMH) y de la Agencia Estatal Consejo Superior de Investigaciones Científicas (CSIC),

INFORMA:

Que Dña. Beatriz Aznar Escolano ha realizado bajo la supervisión de nuestro Programa de Doctorado el trabajo titulado

"Somatodendritic oxytocin release: dynamics and molecular machinery" conforme a los términos y condiciones definidos en su Plan de Investigación y de acuerdo al Código de Buenas Prácticas de la Universidad Miguel Hernández de Elche, cumpliendo los objetivos previstos de forma satisfactoria para su defensa pública como tesis doctoral.

Lo que firmo para los efectos oportunos, en San Juan de Alicante a 15 de mayo de 2025

Y para que conste, a los efectos oportunos, firmo el presente certificado.

Dra. Cruz Morenilla Palao

Coordinadora del Programa de Doctorado en Neurociencias

Financiación: FPI PRE2018-083812 asociada al Programa de Excelencia Severo Ochoa SEV2017-0723-18-3 y PROMETEO es CIPROM/2022/08.

ACKOWLEDGEMENTS/AGRADECIMIENTOS

“Voy a terminar la tesis para poder escribir los agradecimientos”. He repetido esta frase muchas veces durante el último año. Y lo he conseguido: tesis terminada y agradecimientos escritos.

Aquí van, de todo corazón:

Quizá sin tod@s vosotr@s también hubiera terminado la tesis, pero estoy segura de que no lo habría hecho de la misma manera. ***Gracias*** a todas aquellas personas dentro Y FUERA del laboratorio que me han ayudado, alegrado, escuchado, animado y aguantado (puede que incluso sin saberlo) durante estos 6 años.

Gracias ***Cristina***, por introducirme en el mundo de la investigación, no darme nunca falsas esperanzas y sí muchas dosis de realidad. Por creer en mi trabajo cuando ni yo misma lo hacía.

Gracias ***Eduardo***, por darme la primera lección de la vida adulta, y porque en tu laboratorio conocí a personas muy válidas y acogedoras, algunas de las cuales son hoy grandes amigos.

Gracias ***Sandra Jurado***, por abrirme las puertas de tu laboratorio sin conocer cómo trabajaba, apostar por mí, hacerme sentir una más, y por transmitir siempre soluciones, ilusión y positividad en el trabajo. Gracias también por tu comprensión en los momentos difíciles, tanto profesionales como personales, que se me presentaron en esta etapa. Gracias por hacer lucir nuestro trabajo, porque vea la luz tanto esfuerzo, y se vean recompensadas tantas horas buscando el marcaje en las células y siguiendo vesículas.

Gracias al laboratorio: ***Pili***, ***Sonia*** y ***Marta*** (<3), ***María Pérez***, ***María Royo*** y ***Adrián***.

Gracias a ***Paola Caro***, ***Nuria Viudes*** y ***Paula Guillamón***, estudiantes de máster que pasaron por el laboratorio, por implicaros en el tema de la oxitocina y ayudar en los experimentos. Paula, la microscopía electrónica no habría salido sin tu ayuda.

Gracias también al laboratorio de Juan Lerma: ***Bea***, ***Sofía***, ***Álvaro***, ***Clara***, ***Mónica***, ***Ana***, ***Isa*** y ***Juan***.

Gracias (mil) a ***Luismi***, ***José*** y ***Yolanda*** (los “hados” de la ciencia), por dejarnos vuestro microscopio, por aconsejarme y ayudarme con los experimentos, por implicaros en ellos casi como si fueran vuestros, y por dejarme estar en vuestro laboratorio como si fuera una más. Luismi, gracias por tu generosidad y tu ilusión. Yolanda, gracias por pasar tantas horas conmigo al inicio de los experimentos ayudándome y enseñándome. José, gracias por tener tanta paciencia, y leer y responder mis numerosos y largos correos con dudas. Es muy fácil y un gusto trabajar contigo.

También quiero dar las gracias a ***Amparo Gil***, por programar un modelo matemático para nuestras vesículas de oxitocina, por recibirme tan bien en su departamento, mostrar tanto interés por el proyecto y ayudarnos a sacarle todo el partido posible a los datos.

Gracias al servicio de microscopía (***Verona***, ***Giovanna*** y ***Almudena***), por echarme una mano con los experimentos de secreción; a ***Marta Blanco*** (animalario) por ser tan amable y

paciente conmigo todas las veces que te he llamado y enviado correos preguntando por los ratones; a ***Ester***, por alegrarme las mañanas con tu sonrisa y buen humor (no sabes lo que me has ayudado algunos días); a ***Trini Gil*** (genotipado), por los viajes en bus y luego en coche, por ser tan amable y buena, y tener siempre unas palabras de aliento; a ***Toñi Ruiz***, por llevar siempre la alegría y una sonrisa, por hacer amenas muchas comidas y por tu amabilidad; a ***Víctor Rodríguez*** (taller electrónico), por sacar un hueco para atender imprevistos siempre con buena disposición; y a los ***ratones***, los cuales son este trabajo, para mí no sois solo una herramienta.

Gracias a todos los grupos de las diferentes ***actividades "extraescolares"*** a las que me he apuntado durante estos años (protectora Baix Vinalopó (Antonio, Ignacio, Flor,…todos los perretes y gatetes; gracias por vuestra ayuda); Mayte y las compis de ballet; David y los compañeros de la academia de baile; Mariví. Me habéis facilitado las semanas y épocas duras, y mejorado las buenas.

Gracias a ***Susi*** y ***Griselda***, por todo lo que me habéis enseñado.

Gracias ***Águeda***, algunas charlas contigo me han ayudado más que cualquier otra cosa.

Gracias ***Andrea***, por tu apoyo, buena intención y ayuda.

Gracias ***Sandra***, ***Laura***, ***Lara***, ***Bea***, ***Silvia*** y ***Yaiza*** por darme ánimos aunque no sepáis bien qué hago, por haber ganado un poquito más de confianza las unas con las otras, y por las charlas profundas compartidas.

Gracias ***Adrián Villamarín***. Vas a ser muy buen doctor, tienes talento y espero que todo te vaya estupedamente. Eres un pozo de sabiduría. Por desahogarnos del trabajo y hablar de emociones. Eres un amigo.

Gracias ***Cris*** y ***Mari***, apoyo incondicional y fans nº 1, por las risas y los llantos compartidos, por las frases célebres, los podcasts, los stickers, los audios y los wasaps quejándonos y dándonos ánimo. Porque aunque estemos lejos, estamos juntas. Todo va a salir bien. Os quiero.

Gracias ***Eli*** y ***Lynette***, de lo mejor que me ha pasado en la vida, por tantas horas de estudio, ordenador y trabajo compartidas a lo largo de los años (no solo durante la tesis). Lynette, me alegras cada día, no sabes lo muchísimo que me ayudas, eres un rayito de luz. Te quiero.

Gracias a mi ***madre*** y mi ***padre***, que no entienden bien lo que hago, pero que "lo hago bien y valgo" según ellos, por el esfuerzo que habéis hecho para que pueda estudiar, y porque lo habéis hecho y hacéis como mejor sabéis y podéis.

Gracias a mi hermana, ***Alejandra***, por los bailoteos, las risas, las frases épicas, el apretón de manos, el cagarse en todo, los abrazos, las verdades, y tu gran sabiduría (aunque seas la pequeña).

Y Gracias ***Momchil***, por la macro para que analizara las imágenes de microscopía electrónica, por quedarte y estar a mi lado (de la mejor forma que sabías y sabes), porque ya sabes que la oxitocina es un neuropéptido, por los bailoteos, tu sinceridad, tu apoyo y cabeza fría, porque no ha sido fácil. Обичам те.

Por darme aire y fuerza para seguir, Gracias. ***Esta tesis también es vuestra***.

Para Alejandra,

INDEX

ABBREVIATIONS

- AN: Accessory nucleus
- AP: Action potential
- AZ: Active zone
- APP: Amiloyd Precursor Protein
- ADPN: Anterodorsal preoptic nucleus
- ARC: Arcuate nucleus
- AVP: Arginine-vasopressin
- ASD: Autism spectrum disorder
- BNST: Bed nucleus of the stria terminalis
- BBB: Blood brain barrier
- BDNF: Brain derived neurotrophic factor
- Calb1: Calbindin
- CAPS: Calcium-activator protein for secretion
- Cnr1: Cannabinoid receptor 1
- CP: Caudate putamen nucleus
- CNS: Central nervous system
- CSF. Cerebrospinal fluid
- CNTNAP2: Contactin Associated Protein-Like 2
- DIV: Day *in vitro*
- DCV: Dense core vesicle
- D: Diffusion coeficient
- DMH: Dorsomedial hypothalamus
- E: Embryonic stage
- ER: Endoplasmic reticulum
- GPCR: G protein coupled receptor
- HFS: High frequency stimulation
- LH: Lateral hypothalamus
- LTP: Long-term potentiation
- LFS: Low frequency stimulation
- MSD: Mean Square Displacement
- MeA: Medial amygdala
- MC4R: Melancortin 4 receptor
- mGluR: Metabotropic glutamate receptor
- NB: Neurobasal
- NPY: Neuropeptide Y
- NMDA: N-methyl-D-aspartate
- NAcc: Nucleus accumbens
- ON: Overnight
- OT: Oxytocin
- OTR: Oxytocin rceptor
- PFA: Paraformaldehyde
- PVN: Paraventricular nucleus
- PeVN: Periventricular nucleus
- PLAP: Placental leucine aminopeptidase

- tPA: Plasminogen activator
- PDL: Poly-D-lysine
- P0: Postnatal day
- PSD: Postsynaptic density
- PFC: Prefrontal cortex
- RRP: Readily Releasable Pool
- ROI: Region of interest
- RP: Reserve pool
- RCH: Retrochiasmatic nucleus
- RT: Room temperature
- SEM: Scanning Electron Microscope
- Reln: Serine protease Reelin
- SNPs: Single Nucleotide Polimorphisms
- SRP: Slow releasable pool
- SDS: Sodium Dodecyl Sulfate
- SNAP: Soluble N-ethylmaleimide-Sensitive Factor Attachment Protein Receptor
- SON: Supraoptic nucleus (SON)
- SCH; SCN: Supraquiasmatic nucleus
- SV: Synaptic vesicle
- Syb: Synaptobrevin
- Syt: Synaptotagmin
- Stx: Syntaxin
- TGN: Trans-Golgi network
- VAMP: Vesicle associated protein
- VMH: Ventromedial hypothalamus
- VMPO: Ventromedial preoptic nucleus
- VGCC: Voltage-gated calcium channel
- PAM: α-amidating monooxygenase
- AMPAR: α-amino-3-hydroxy-5-methyl-4-isoxazolepropionic acid receptor
- α -MSH: α-melanocyte-stimulating hormone

INDEX OF FIGURES AND TABLES

ABSTRACT/RESUMEN

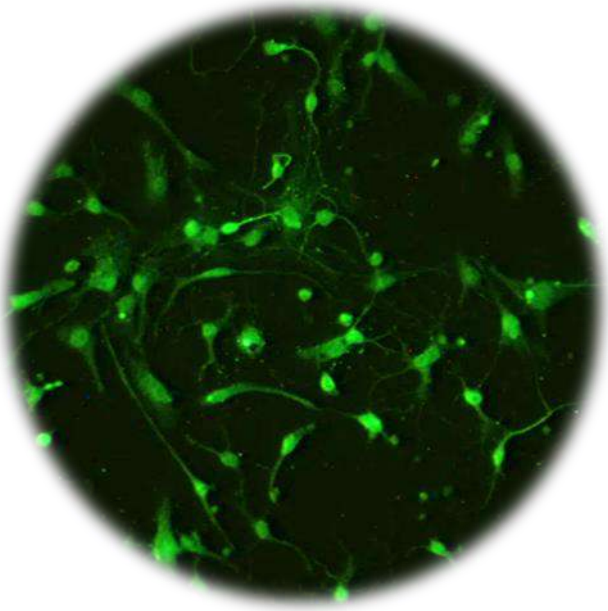

ABSTRACT

Oxytocin (OT) is a neuropeptide hormone that plays a key role in the regulation of social behaviors. Primarily synthesized in the hypothalamus, OT production is centered in the paraventricular (PVN) and supraoptic (SON) nuclei. From there, OT is released into the bloodstream, where it supports functions like childbirth and the milk ejection reflex, and into the brain, where it influences social behaviors, including attachment, maternal care, and aggression. Dysregulation of the oxytocinergic system has been associated with impairments in social behaviors, as seen in autism spectrum disorder (ASD).

OT is stored within Dense Core Vesicles (DCVs), whose release properties remain less understood compared to Synaptic Vesicles (SVs). To address this knowledge gap, the primary aims of this thesis were to characterize the dynamic properties of OT release and to identify the molecular machinery involved.

To achieve these objectives, we used live-cell microscopy and secretion assays in primary hypothalamic cultures to analyze OT-containing compartments' dynamics under both basal and stimulated conditions, with and without extracellular calcium.

A detailed analysis of SNARE protein expression in hypothalamic slices and cultures identified SNAP-47 as a key somatodendritic SNARE protein. This non-canonical SNARE was closely associated with OT-membrane patches, positioning it to play a significant role in OT dynamics and release during both basal and stimulated states. Furthermore, the elimination of SNAP-47 in the PVN reduced sociability in mice, suggesting that alterations in somatodendritic OT dynamics may affect basic aspects of social behavior.

In summary, our findings reveal that OT vesicles represent a heterogeneous population regulated by a unique SNARE complex involving SNAP-47, which contributes to both basal and activity-dependent mobilization of OT in hypothalamic neurons, potentially impacting social behavior.

RESUMEN

La oxitocina (OT) es un neuropéptido que juega un papel importante en la regulación de los comportamientos sociales. Sintetizada principalmente en el hipotálamo, la producción de OT se centra en los núcleos paraventricular (PVN) y supraóptico (SON). Desde aquí, la OT es liberada al torrente sanguíneo, donde desempeña funciones facilitadoras durante el parto y la lactancia, y en el cerebro, donde influencia los comportamientos sociales, incluyendo la formación de vínculos, el cuidado materno, y la agresión. La desregulación del sistema oxitocinérgico se ha asociado con alteraciones en el comportamiento social, como se ha visto en el trastorno del espectro autista (ASD).

La OT se almacena en vesículas de núcleo denso (DCVs), cuyas propiedades de liberación han sido menos estudiadas en comparación con las vesículas ligeras (SVs). Para avanzar en esta línea de conocimiento, los objetivos principales de esta tesis se han centrado en caracterizar las propiedades dinámicas de las vesículas de OT e identificar la maquinaria molecular implicada en su liberación.

Para alcanzar estos objetivos, combinamos técnicas de microscopía en célula viva y ensayos de secreción en cultivos primarios de hipotálamo, para analizar la dinámica de los compartimentos de OT en condiciones basales y en respuesta a protocolos de estimulación, con y sin calcio extracelular.

Un análisis detallado de la expresión de proteínas SNARE en rodajas y cultivos hipotalámicos identificó un papel clave para SNAP-47. Esta proteína SNARE no canónica se encuentra estrechamente asociada con los parches de OT de membrana, indicando una importante función en la dinámica y liberación de OT en condiciones basales y en respuesta a estimulación. La eliminación de SNAP-47 en el PVN redujo la sociabilidad en ratones, sugiriendo que alteraciones en la dinámica de la OT somatodendrítica podrían afectar aspectos fundamentales del comportamiento social.

Nuestros resultados revelan que las vesículas de OT constituyen una población heterogénea regulada por un complejo SNARE que involucra SNAP-47, que contribuye tanto a la movilización de OT en condiciones basales como en respuesta a protocolos de estimulación, potencialmente influyendo en la regulación de aspectos básicos de la conducta social.

INTRODUCTION

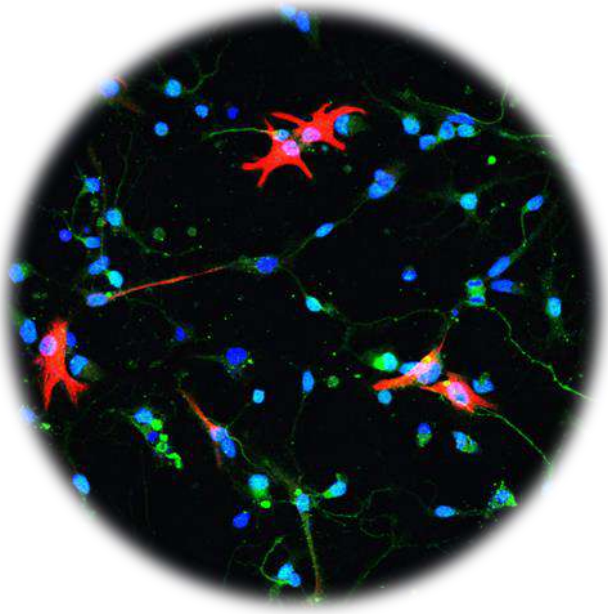

1.- Oxytocin

1.1.- Discovery of oxytocin

Oxytocin (OT) is a neuropeptide that plays a crucial role in various physiological processes, such as social bonding, childbirth, and lactation. The discovery of OT dates back to the early 20th century, and the understanding of its physiological function has evolved over time (Lee et al., 2009; Shen, 2015). OT was first identified and isolated from the posterior pituitary gland by British pharmacologist Sir Henry Dale and his colleague Otto Loewi in 1906 (Dale, 1906; Ott & Scott, 1910). They initially referred to it as "oxytocic principle" due to its ability to stimulate uterine contractions. Subsequent research by Sir Vincent du Vigneaud in the 1950s led to the synthesis and determination of the chemical structure of OT.

Du Vigneaud's work earned him the Nobel Prize in Chemistry in 1955. He identified the exact amino acid sequence of OT, which consists of nine amino acids (Fig. 1). This breakthrough allowed scientists to produce synthetic OT, enabling further research and applications in medicine (Lee et al., 2009).

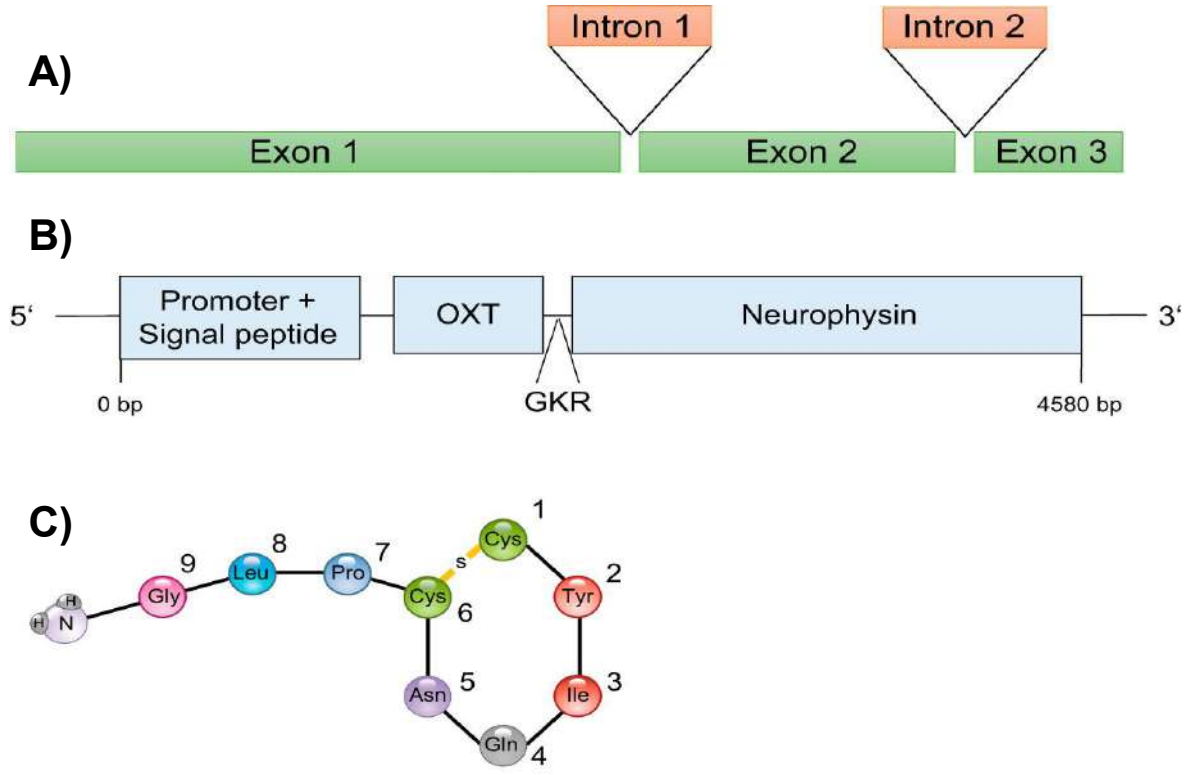

Figure 1.- Structure of the human oxytocin gene and protein. **A)** *OT* gene on human chromosome 20, containing three exons and two introns. Adapted from Jurek & Neumann, 2018. **B)** *OT* gene transcript codes for an initial signal peptide, the nonapeptide OT (OXT in the image), a glycine, lysine, arginine (GKR) processing signal, the variable NH2-terminal region of neurophysin, the core neurophysin, and its COOH-terminal region. Adapted from Jurek & Neumann, 2018. **C)** Schematic representation of the OT structure. OT is a nonapeptide molecule with a tripeptide linear part with an amidated COOH terminus, and a cyclic part that is connected via a disulfide bridge between the two cysteines. Adapted from Jurek & Neumann, 2018.

The fact that OT was first identified in the uterus does not mean that its functions are limited to this organ, although, for the first 50 years after its discovery, research on OT's physiology was limited to it (Camerino, 2023). Indeed, the role of OT in social behavior and emotion regulation has become significant areas of research in modern psychology and neuroscience. It is to the point that OT is often referred to as the "love hormone" or "bonding hormone" due to its association with pro-social and maternal behaviors (Lee et al., 2009).

Today, OT continues to be studied for its potential therapeutic applications, including its use in obstetrics to induce labor and reduce postpartum bleeding, as well as its role in treating certain social and psychological disorders (Benarroch, 2013). However, the understanding of OT's complex functions is an ongoing area of research to which this thesis aims to contribute new pieces of basic knowledge.

1.2.- Oxytocin synthesis

OT is primarily synthesized in the hypothalamus, being the paraventricular (PVN) and the supraoptic (SON) nuclei the best characterized regions (Swanson & Sawchenko, 1983; Gimpl & Fahrenholz, 2001) (Fig. 2A). However, other hypothalamic regions also exhibit OT-containing cells such as the periventricular nucleus (PeVN), the anterodorsal preoptic nucleus (ADPN), the supraquiasmatic nucleus (SCH), and the retrochiasmatic nucleus (RCH) (Hashimoto et al., 2014; Madrigal & Jurado, 2021) (Fig. 2B). Furthermore, OT synthesis has also been reported in extrahypothalamic areas such as the medial amygdala (MeA) and the bed nucleus of the stria terminalis (BNST) (Hashimoto et al., 2014; Madrigal & Jurado, 2021) (Fig. 2B).

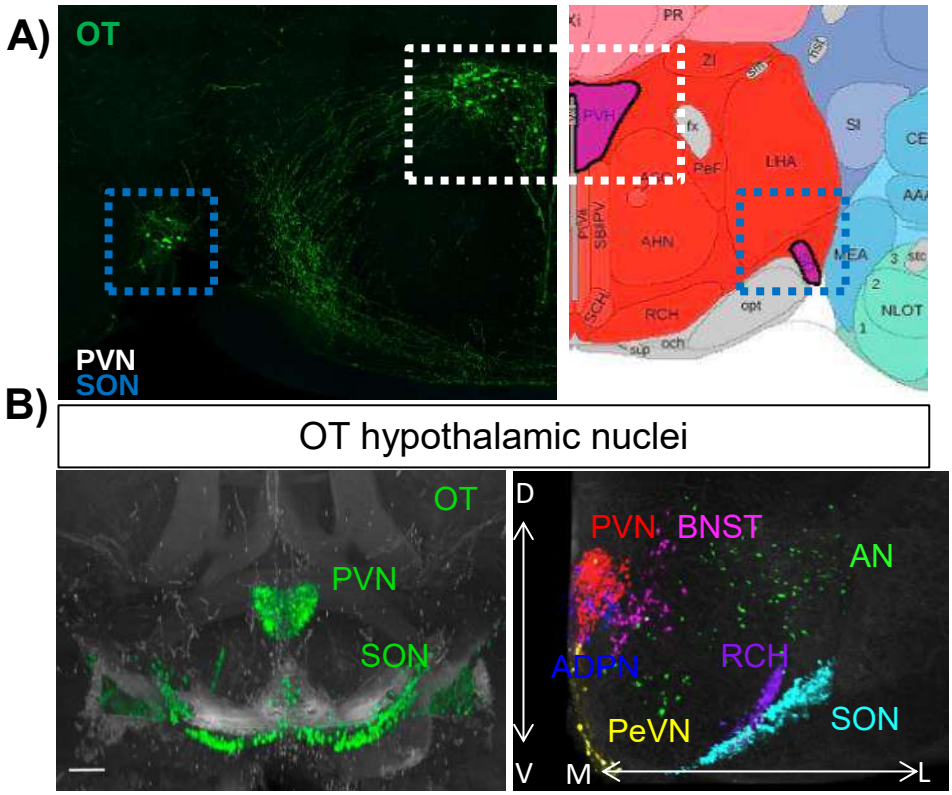

Figure 2.- Mouse brain hypothalamic nuclei. **A)** OT is primarily synthesized in the paraventricular (PVN) and the supraoptic (SON) nuclei. **B)** Representative image of the hypothalamus adult mice brain processed with the iDISCO+ protocol and stained for OT. The image shows the hypothalamic area displaying oxytocinergic neurons pseudocolored in each hypothalamic nucleus and surrounding areas such as the BNST. PeVN: periventricular nucleus; ADPN: anterodorsal preoptic nucleus; BNST: bed nucleus of stria terminalis; SON; supraoptic nucleus, PVN; paraventricular nucleus, RCH; retrochiasmatic area, and AN; accesori nuclei. Scale bars indicate 300 µm. Credit to Pilar Madrigal (lab member).

In a nutshell, the *OT* gene consists of three exons and two introns (Tom & Assinder, 2010) (Fig. 1A) that upon translation results in a pre-pro-peptide that requires extensive processing by peptidases that work across different points of OT's maturation through the secretory pathway and up to vesicle packaging, more often of the dense core vesicle (DCV) type (Kim et al., 2006). OT's mature structure consists of a signal peptide, the nonapeptide OT and the carrier protein neurophysin I, essential for its storage and release (Lee et al., 2009) (Fig. 1B, C, and Fig. 3).

Biosynthesis of oxytocin

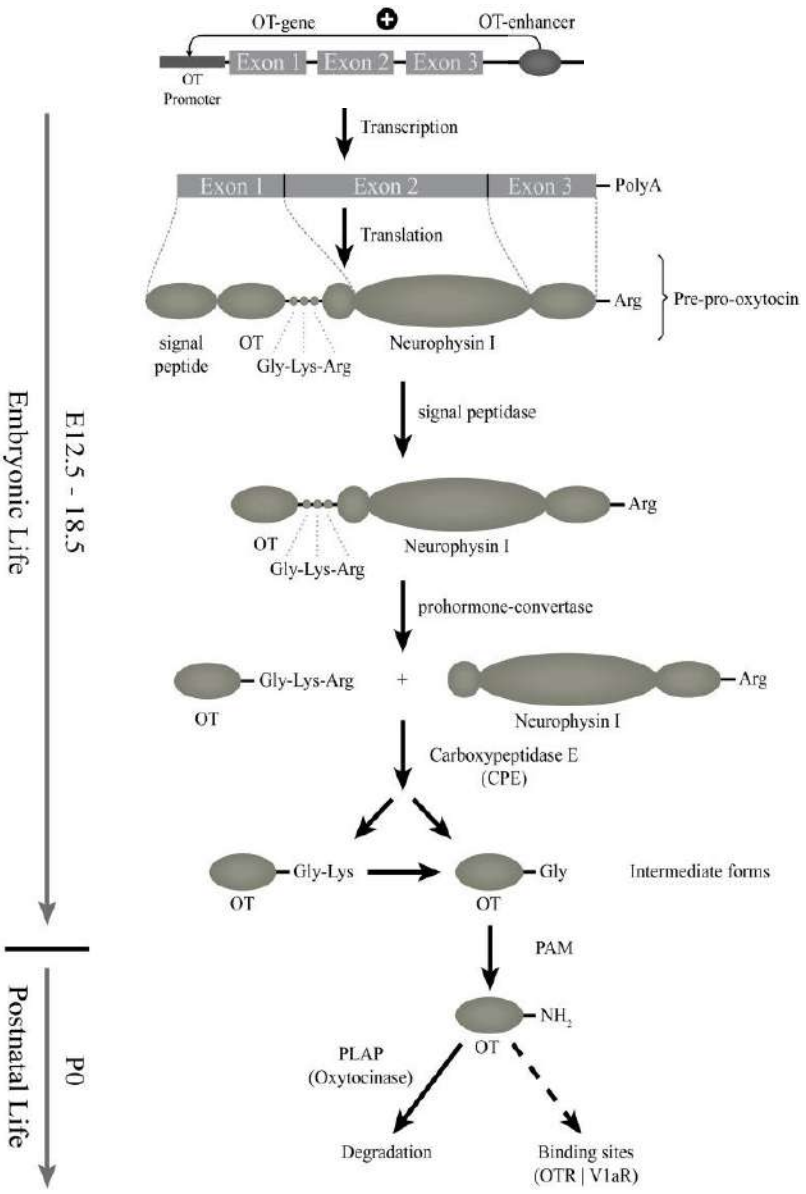

Figure 3.- Biosynthesis of oxytocin through mice development. Genomic structure of the *OT* gene, transcription and translation process. After translation, OT preprohormone is produced. It will be cleaved and matured by successive enzymes, giving rise to intermediate OT forms. Mature OT, detected from birth, is released and degraded or binds to OT receptor (OTR) or V1a receptor (AVP receptor). PAM: α-amidating monooxygenase; PLAP: placental leucine aminopeptidase (oxytocinase). Adapted from Grinevich et al., 2015. During embryonic and early postnatal development, the cleavage of OT by peptidases produces numerous intermediate variants, capable of binding to the oxytocin receptor (OTR), although their functional relevance remains unknown (Grinevich et al., 2015).

1.3.- Types of oxytocin neurons

Oxytocinergic hypothalamic neurons have been typically categorized in two distinct types: magnocellular and parvocellular neurons. Magnocellular neurons present somas of 20-30 µm, are found in the PVN and SON, their axons project to the posterior pituitary and their dendrites into the brain, producing large amounts of neuropeptide (Fig. 4). On the other hand, parvocellular neurons present somas of 10-20 µm, are concentrated in the PVN, their dendrites extend to the brain, as well as their axons which also project to the median eminence, brainstem, and the spinal cord (Van Den Pol, 1982; Eliava et al., 2016; Althammer & Grinevich, 2018) (Fig. 4). Unlike magnocellular neurons, parvocellular axons have been identified in several brain regions such as the olfactory system, prefrontal cortex, entorhinal cortex, central and medial amygdala, BNST, hippocampus, and the lateral septum (Benarroch, 2013). In comparison, parvocellular neurons synthesize less OT than magnocellular neurons.

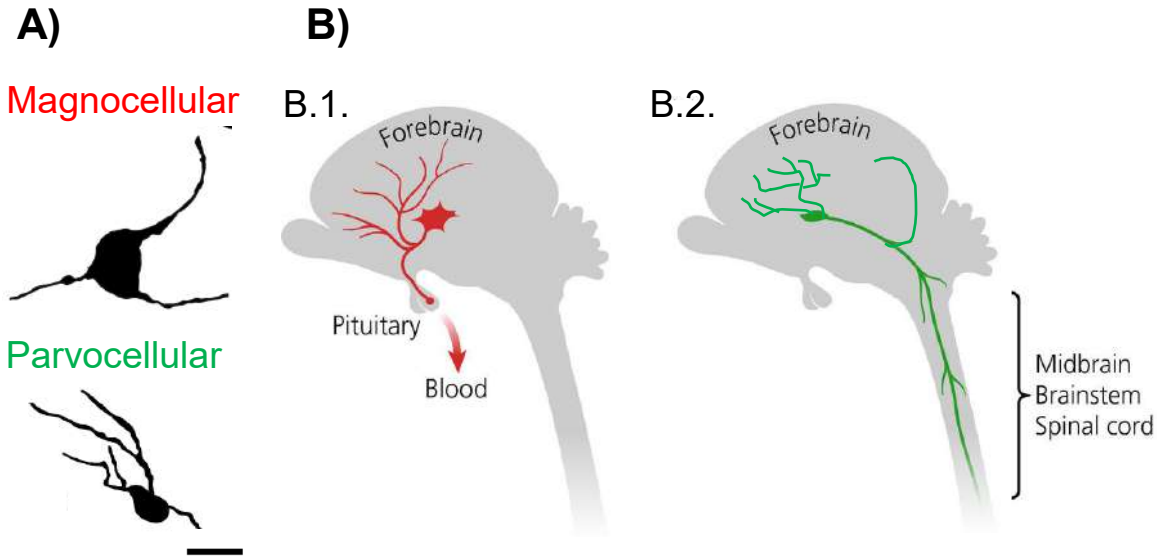

Figure 4.- Oxytocinergic hypothalamic neurons are classified in magnocellular and parvocellular neurons. **A)** Drawing of magnocellular (top) and parvocellular (bottom) OT neurons identified by intravenous FluoroGold labelling. Scale bar indicates 20 µm. Adapted from Lewis et al., 2020. **B)** Schematic representation of projections arising from magnocellular (red) and parvocellular (green) neurons. B.1) Magnocellular neurons of the PVN and SON project their dendrites into the brain, and their axonsto the posterior lobe of the pituitary. B.2) Parvocellular neurons of the PVN send their axons into the brain, and to hindbrain and spinal cord structures, and their dendrites into the brain. Adapted from Althammer & Grinevich, 2018.

Although anatomical considerations for distinguishing these two cell types are prominently used, hypothalamic oxytocinergic neurons can also be classified according to their electrophysiological properties or gene expression. Electrophysiological experiments distinguished type I and II OT neurons. Type I neurons exhibit higher threshold depolarizing potentials and shorter membrane time constant than type II neurons. Interestingly, type I and II neurons loosely correspond to magno- and parvocellular neurons, respectively (Althammer & Grinevich, 2018). Genetically, magnocellular neurons are enriched in the calcium-binding protein Calbindin (Calb1) and a large conductance calcium-activated potassium channel subunit (Kcnmb4), meanwhile parvocellular neurons are enriched in the extracellular matrix

serine protease Reelin (Reln) and the cannabinoid receptor 1 (Cnr1) gene (Lewis et al., 2020).

1.4.- Oxytocin and arginine vasopressin

OT is closely related with arginine-vasopressin (AVP), a nonapeptide that differs from OT in only two amino acids (Stoop, 2012; Benarroch, 2013) (Fig. 5). Likewise OT, AVP is primarily synthesized in the hypothalamus, and requires peptidase processing to reach its mature form (Stoop, 2012). Both OTR and AVP receptors (AVPRs including V1aR, V1bR and V2R) belong to the G protein-coupled receptor superfamily (Stoop, 2012). Although OT and AVP can be found co-expressed in some hypothalamic neurons (Otero-García et al., 2016; Madrigal & Jurado, 2021), their developmental dynamics exhibits significant differences (Madrigal & Jurado, 2021).

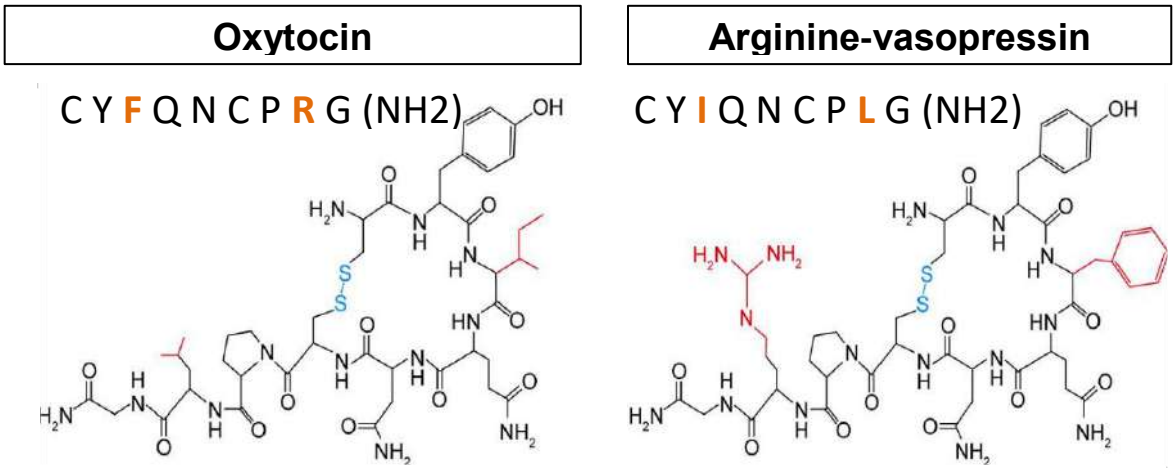

Figure 5.- Peptide sequence and structure of OT and AVP prohormones. Adapted from Otero-García et al., 2016.

Both OT and AVP are released into the bloodstream and into the brain (Fig. 6). Peripherally, OT participates in parturition, milk ejection reflex and sexual behavior; meanwhile AVP primarily participates in circadian rhythms and temperature regulation, water retention and blood pressure (Stoop, 2012). In the brain, both peptides have been postulated to regulate social behavior, usually in opposite ways. Whereas OT has been attributed to anxiolytic, antidepressant, and pro-social properties (Insel & Young, 2001; Benarroch, 2013), AVP has been linked to anxiety, depression, aggression, and enhanced responsiveness to social stressors (Benarroch, 2013; Otero-García et al., 2016). Despite the traditional view that presented OT and AVP as endogenous antagonists, recent evidence revealed a more complementary role (Abramova et al., 2020; Aspesi & Choleris, 2022). Nonetheless, OT can still be considered an “emotionally enhancer”, or prosocial substance depending on the context and the targeted brain region (Duque-Wilckens et al., 2018).

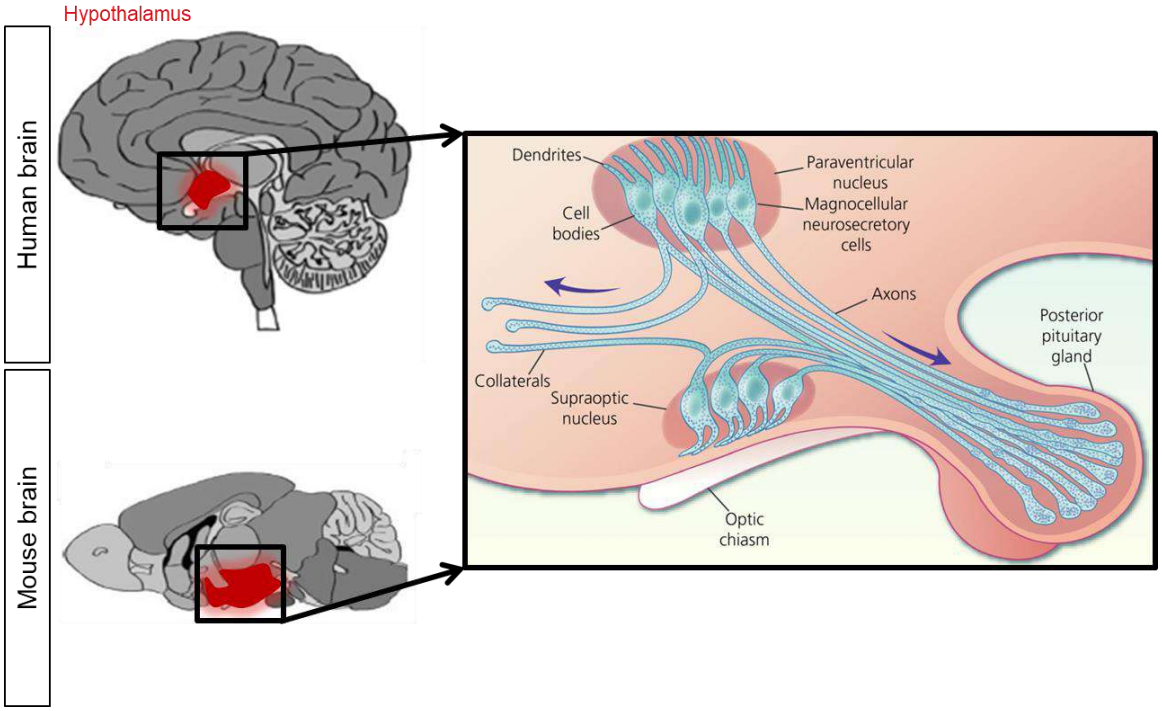

Figure 6.- OT and AVP systems in the human and mouse brain. In the human and mouse hypothalamus, OT and AVP are synthesized in the PVN and SON nuclei, and are processed along the axonal projections to the posterior lobe of the pituitary, where they are stored in secretory vesicles and released into peripheral circulation. In addition to this release from axonal terminals, there is dendritic release of OT and AVP into the extracellular space, resulting not only in local action but also in diffusion through the brain to reach distant targets (dotted arrows). Thus, both peptides have peripheral and central functions. Adapted from Meyer-Lindenberg et al., 2011; Brown et al., 2020; Borie et al., 2021.

1.5.- Oxytocinergic regulation of glutamatergic transmission in the hypothalamus

The α-amino-3-hydroxy-5-methyl-4-isoxazolepropionic acid receptor (AMPAR) is one of the main mediators of fast glutamatergic transmission in the central nervous system (CNS), including brain regions such as the hypothalamus. Activation of AMPARs plays a main role in long-term synaptic plasticity, largely due to the trafficking of AMPAR subunits that adapt the receptor composition in response to various patterns of stimulation (Royo et al., 2022). Interestingly, activity-dependent insertion of AMPAR at the plasma membrane is achieved by the formation of a specific postsynaptic SNARE complex in which SNAP-47 plays a prominent role (Jurado et al., 2013; Arendt et al., 2015).

Glutamatergic transmission influence practically all autonomic and homeostatic responses orchestrated in the hypothalamus including stress, energy and electrolyte balance, circadian rhythms, blood pressure, lactation, and fertility (Royo et al., 2022). OT- and AVP -expressing cells, located in the PVN and SON, receive dense glutamatergic innervation and express both postsynaptic AMPA and N-methyl-D-aspartate (NMDA) receptors, which are believed to influence their firing patterns and ability to release OT and AVP (Royo et al., 2022). In fact, AMPA, kainate, and NMDA receptor mRNA are found in the hypothalamus at similar levels than in the cortex and hippocampus. Interestingly, AMPAR subunits have been postulated to exhibit region- and cell-specific patterns (Fig. 7), which along with subunit composition, give

place to multiple modes of glutamatergic transmission in the hypothalamus, which may underlie and modulate its various central and neuroendocrine functions (Royo et al., 2022).

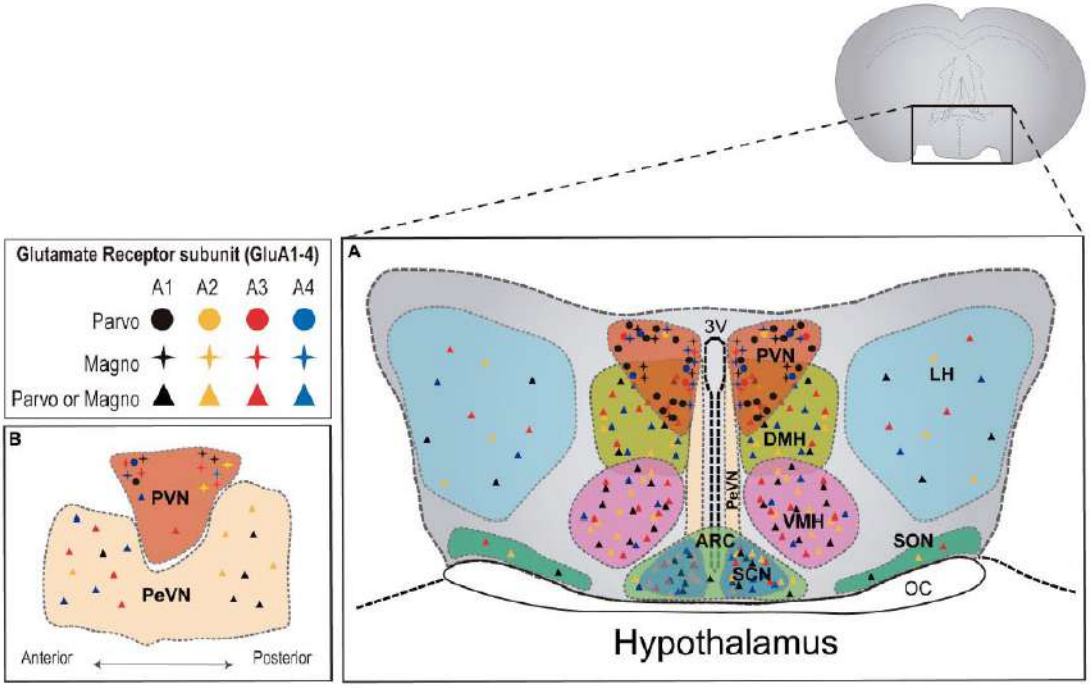

Figure 7.- AMPAR subunit distribution across distinct hypothalamic nuclei in the rat brain. **A)** Coronal plane of the hypothalamus showing the different hypothalamic regions. PVN: paraventricular nucleus; DMH: dorsomedial hypothalamus; VMH: ventromedial hypothalamus; LH: lateral hypothalamus; SON: supraoptic nucleus; PeVN: periventricular nucleus; SCN: suprachiasmatic nucleus; ARC: arcuate nucleus. **B)** Sagital plane of hypothalamic nuclei. AMPAR subunit abundance is represented for each nucleus according to available literature in the rat brain (Van Den Pol, 1994; Eyigor et al., 2001). Detailed information regarding AMPAR subunit abundance in magno- and parvocellular neurons is only available for the PVN (Herman et al., 2000). Adapted from Royo et al., 2022.

Hormonal secretion at neurohypophysial terminals is largely regulated by glutamatergic activity onto both OT and AVP magnocellular neurons. OT release from magnocellular neurons required for lactation is NMDAR and AMPAR-dependent, and NMDARs have been shown to inhibit OT release in the posterior pituitary. On the other hand, a combination of AMPARs and metabotropic glutamate receptors (mGluRs) activation promotes OT somatodendritic release.

A prominent example of homeostatic regulation of glutamatergic transmission in the hypothalamus is osmotic regulation. Water deprivation increases the density of GluN1 in the SON OT and AVP neurons accompanied by a reduction of GluN2B expression. Chronic salt loading stimulation produces an increase in GluA1 protein expression level, potentiating AMPAR-mediated current amplitude in magnocellular hypothalamic neurons (controlling blood pressure, blood volume, and Na balance). Furthermore, PVN and SON magnocellular neurons undergo plastic changes during lactation and milk ejection which involve a two-fold increase in AMPAR-mediated current frequency and decay kinetics, probably due to a switch

in AMPAR subunit composition. However, hypothalamic plasticity differs from the classical molecular mechanisms underlying plasticity in hippocampal synapses (Fig. 8).

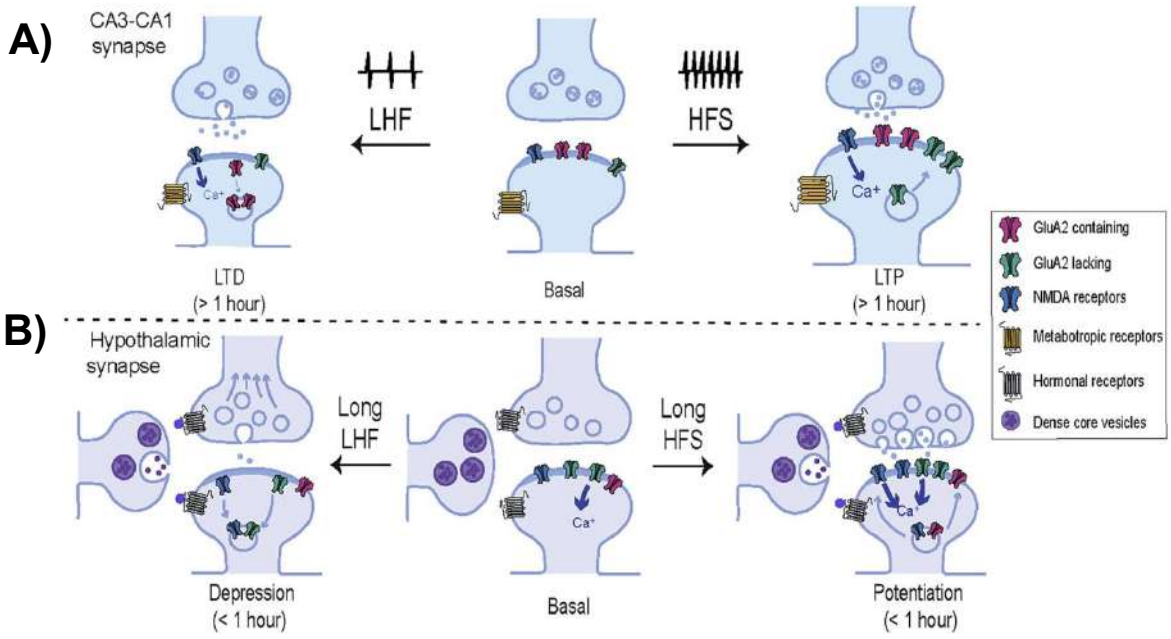

Figure 8.- Comparative representation of the molecular mechanisms underlying plasticity in hippocampal and hypothalamic synapses. **A)** Schematic representation of the model CA3-CA1 synapse. High frequency stimulation (HFS) induces calcium entry trough NMDARs activating intracellular signaling cascades that drive new AMPARs including GluA2-lacking receptors into the synaptic membrane. These changes result in a long-lasting potentiation of the synaptic strength and an increase in spine volume. In contrast, low frequency stimulation (LFS) induces a moderate entry of intracellular calcium which drives AMPARs out from the plasma membrane, weakening synaptic strength and decreasing the spine volume. **B)** Schematic representation of a hypothalamic synapse. In addition to glutamatergic inputs, hypothalamic synapses are heavily influenced by hormonal secretion from neighboring peptidergic neurons. In contrast to classical plasticity protocols in the hippocampus, hypothalamic synapses commonly exhibit short-term adaptions in response to prolong and low frequency patterns of activity. Short-term potentiation of synaptic strength can be achieved by activation of postsynaptic NMDAR and an increase of synaptic AMPARs, enriched in GluA2-lacking subunits. In addition, NMDARs can be rapidly recruited at synaptic localizations in parallel to presynaptic changes. On the other hand, hypothalamic synapses undergo short-term synaptic depression in response to low frequency stimulation by several mechanisms which may involve the activation of peptidergic or NMDA receptors, that drive the removal of synaptic GluA2-lacking AMPARs, NMDARs, and reduce glutamate release probability. Adapted from Royo et al., 2022.

The involvement of AMPAR-mediated transmission in hypothalamic function suggests that dysregulations of AMPAR trafficking, phosphorylation or subunit composition, may be associated with cognitive and behavioral impairments including anxiety, depression, ischemia, intellectual disability, neurodegenerative conditions, drug addiction or social deficits (Royo et al., 2022).

In summary, there are many evidences indicating that hypothalamic neurons undergo plastic events in which AMPAR modifications in terms of subunit composition, post-translational

modifications or subcellular localization are required. Nevertheless, the exact mechanisms involved in these processes in OT and AVP cells are not as well understood as in hippocampal synapses, thus undeniably more research on this topic is needed (Royo et al., 2022).

1.6.- Oxytocin receptor

The oxytocin receptor is a G protein-coupled receptor, which belongs to the rhodopsin-type (class I) G protein coupled receptor (GPCR) family (Lee et al., 2009; Dumais & Veenema, 2016) (Fig. 9A). Recent studies indicate that the canonical OTR transcript, assumed to be the only functional form, is not the only transcript, revealing the existence of up to eight mRNA OTR variants, highlighting a complex transcriptional regulation (Danoff et al., 2023).

OTR is both expressed in peripheral tissues and in the brain. OTR distribution in the brain differs across species, sex, developmental stage and brain region, which may explain the different effects attributed to OT (Viero et al., 2010; Jurek & Neumann, 2018; Sharma et al., 2019).

Intriguingly, OTR also binds AVP, although with less sensitivity than to OT, and undergo desensitization after a persistent agonist stimulation, that ultimately results in the internalization of the receptor (Gimpl & Fahrenholz, 2001).

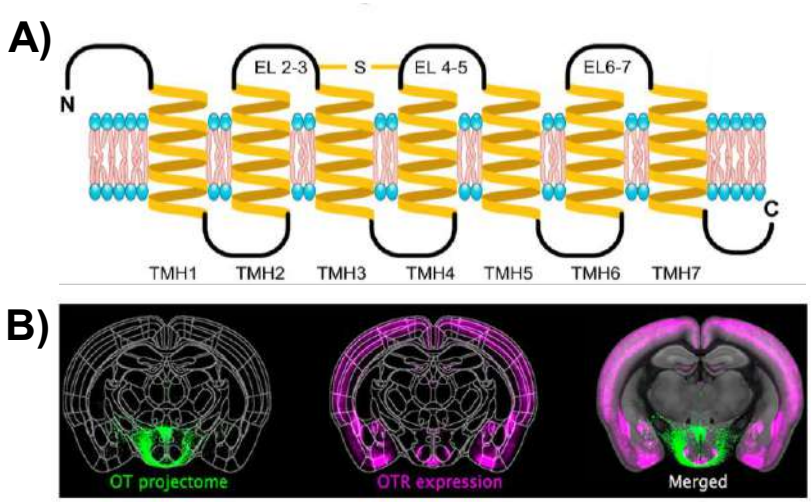

Figure 9.- The oxytocin receptor. **A)** Schematic representation of the OTR structure. The OTR is a seven-transmembrane helix (TMH1–7) receptor with three extracellular loops (2–7) and three intracellular loops (1–6). Adapted from Jurek & Neumann, 2018. **B)** Comparison between OTR expression and projection of hypothalamic oxytocin neurons. Adapted from Son et al., 2022.

Over the years, several strategies have been employed to investigate OTR expression in the brain, although their accuracy has been compromised due to the homology of OTR with other related receptors, such as AVPRs. The most commonly used techniques are receptor autoradiography in fixed tissue (Sharma et al., 2019), commercial antibodies, *in situ* hybridization, qPCR, Western blotting (Jurek & Neumann, 2018), and OTR-reporter mice such as the well-characterized OTR-Venus transgenic line (Sharma et al., 2019).

Interestingly, a recent paper by the Kim lab (Son et al., 2022) revealed a limited correlation between OT and OTR distribution, suggesting an important contribution of volume transmission in OT-dependent signaling (Fig. 9B). In this scenario, OT released at the level of the third ventricle could travel within the cerebrospinal fluid to distant regions, such as the cortex that contain high levels of OTR.

1.7.- Oxytocin and social behavior

OT neurons, primarily of the magnocellular type, project their axons to the neurohypophysis (*a.k.a* the posterior pituitary gland), where they release large amounts of OT into the bloodstream. Systemic OT acts as a hormone with prominent reproductive functions as the aforementioned role in promoting uterine contraction and milk ejection reflex (Tom & Assinder, 2010). OT also participates in kidney functions (urine osmolarity), pancreatic functions (glucagon and insulin secretion), and cardiovascular functions (vasodilation and decreasing myocardial contractility) (Tom & Assinder, 2010).

In addition to peripheral axonal release, OT can also be secreted at the somatodendritic compartment (Ludwig & Leng, 2006), which represents a significant source of OT in the CNS.

The action of OT in the brain has been mostly associated to the regulation of social behavior (Insel and Young, 2001; Ludwig & Leng, 2006; Neumann, 2008; Dölen, 2015b). One of the first evidence that relates OT with social behavior can be found in the classical experiments performed by Young and Wang in 2004. Autoradiography analyses showed that, in contrast to promiscuous voles, monogamous prairie voles exhibited higher densities of OTR in the nucleus accumbens (NAcc) and the caudate putamen (CP) nuclei, two regions involved in reward and behavior reinforcement (Fig. 10A, B). Results from partner-preference behavioral tests also showed that a selective OTR antagonist (OTA) infused bilaterally into the NAcc or the prefrontal cortex (PFC), but not the CP, impairs monogamous partner-preference in female prairie voles (Young & Wang, 2004) (Fig. 10C).

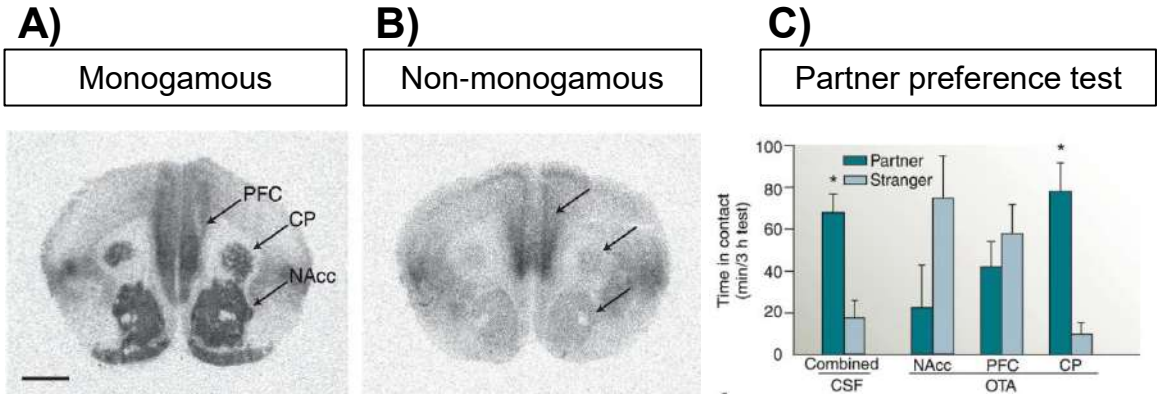

Figure 10.- OTR expression in monogamous and non-monogamous voles. **A, B)** OTR autoradiography experiment in prairie voles' brains. Monogamous prairie voles (A) have higher densities of OTR in the nucleus accumbens (NAcc) and caudate putamen (CP) than do non-monogamous montane voles (B). Both species express OTR in the prefrontal cortex (PFC). Scale bar indicates 1 mm. **C)** A selective OTR antagonist (OTA) infused bilaterally

into the NAcc or PFC, but not the CP, blocks partner-preference formation in female prairie voles. Adapted from Young & Wang, 2004.

One of the most convincing evidence supporting the role of OT in social behavior was obtained exploring KO mice in which either the *OT* or the *OTR* genes were removed or inactivated. Male mice constitutively lacking *OT* ($OT^{-/-}$) fail to recognize females to which they have been previously exposed (identified as reduced olfactory investigation), indicating social memory impairments (Ferguson et al., 2000) (Fig. 11A). Furthermore, postpartum female mice lacking the OTR gene were less efficient retrieving their pups than wild type animals, indicating deficits in this aspect of maternal behavior (Takayanagi et al., 2005) (Fig. 11B). In humans, OT promotes empathy, trusting and cooperation, and reduces social aversion and response to social stress (Benarroch, 2013; Hashimoto et al., 2014), as well as reducing anxiety and fear (Tom & Assinder, 2010). As a consequence of its implication in social behavior, dysregulation of oxytocinergic signaling is believed to lead to autism and obsessive-compulsive disorder (Viero et al., 2010).

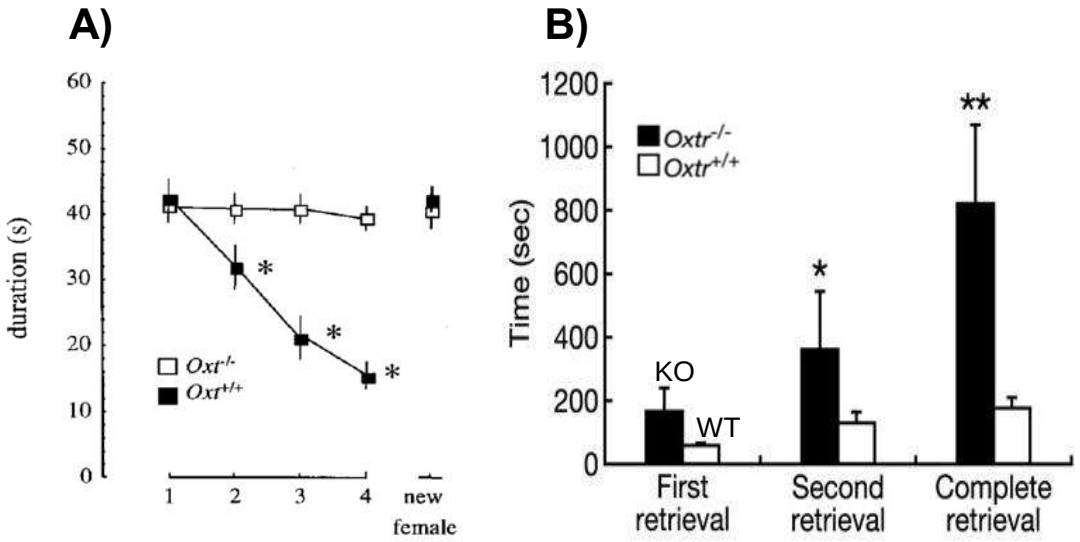

Figure 11.- Oxytocin involvement in social behavior in mice. **A)** Male mice constitutively lacking *OT* (Ot-/-, OXT in the image) present impaired social memory. Social memory by Oxt–/– (open symbols) and Oxt+/+ (filled symbols) male mice was measured as a difference in olfactory investigation. Data depict mean +/–1 s.e.m. for the amount of time (s) allocated to investigation of the same ovariectomized female during each of four successive 1 min trials. Asterisks represent a significant decrease between each trial compared with the first trial for Oxt+/+ males. Adapted from Ferguson et al., 2000. **B)** Pup retrieval and crouching behaviors in Oxtr-/- and Oxtr+/+ postpartum females. Failure to retrieve was assigned as 30 min, the length of the observation period. Adapted from Takayanagi et al., 2005.

Although OT is required as a mediator of maternal and prosocial behaviors, it might not be sufficient. A disruptive article by Berendzen et al., (2023) explored different aspects of maternal behavior in a novel OTR KO mouse line developed by CRISPR-Cas9 technology. These KO animals showed social treats similar to those of the wild type animals. These unexpected data may be explained by the residual activity of the remaining OTR levels (Danoff et al., 2023) or the compensation by AVP-signaling. Moreover, recent research by Dayu Lin's laboratory has uncovered a specific role of OT in modulating social aversion (Osakada et al., 2024), highlighting that a comprehensive understanding of OT's role in brain function is still incomplete.

Brain OT has been implicated in several aspects of social behavior. Classical experiments performed in monogamous prairie voles indicated that OT administration accelerates pair bonding formation (Young & Wang, 2004). Conversely, blocking the OTR impairs pair bonding formation (Insel et al., 1998; Neumann, 2008). Furthermore, OT reduces social fear and anxiety levels (Neumann, 2008; Peñagarikano et al., 2015).

OT and OTR KO mice exhibited reduced social memory and recognition (Neumann, 2008), and developmental dysregulation of the oxytocinergic system leads to several social impairments in humans (Meyer-Lindenberg et al., 2011) as well as in animal models, like Prader-Willi Syndrome, Phelan-McDermid Syndrome, or autism spectrum disorder (ASD) (Rajamani et al., 2018). As an example, a study performed comparing family- and institutionalized-reared children, indicated that social deprivation impairs the development of the oxytocinergic system (Fries et al., 2005).

One of the disorders most commonly associated with OT alterations is ASD. ASD is defined as a neurodevelopmental syndrome characterized by social behavioral deficits as impaired language development, repetitive behavior, and social and communicative deficits (Alarcón et al., 2008; Insel, 2010). ASD is associated with hyperactivity, epilepsy, and sensory processing abnormalities (Peñagarikano et al., 2011). ASD is estimated to be 70 % to 90 % heritable (Alarcón et al., 2008), and has a heterogeneous etiology. 700 genes, most of which are rare variants, have been identified as risk genes (Peñagarikano et al., 2015; Dölen, 2015a; Dölen & Sahin, 2016). As several genes implicated in ASD encode for synaptic proteins, ASD is suggested to be a “synaptopathy” (Dolen and Sahin, 2016; Rajamani et al., 2018).

Alterations in the genes coding for the AVPR1a, the OTR, neurophysin I and II, CD38 (a protein identified to participate in OT release), and OT give rise to social deficits present in autistic patients (Ebstein et al., 2009; Modi & Young, 2012). *FMR1*, *UBE3A*, *DHCR7*, and *MeCP2* genes (Modi & Young, 2012), and the fragile X mental retardation protein (FMRP), UBE3A protein, *T.brain-1* (*TRB1*) gene and *CHD8* (a chromatin remodeling factor) (Dölen & Sahin, 2016), are other genes associated with ASD. Importantly, reduced OT levels are related with ASD (Insel, 2010; Erdozain & Peñagarikano, 2020), determining the severity of the syndrome (Dölen, 2015a).

Different types of animal models have been developed to mimic various characteristics of autistic patients including genotypic, phenotypic and environmental features (Modi & Young, 2012). Contactin Associated Protein-Like 2 (CNTNAP2), a cell adhesion protein of the neurexin family, was discovered to be associated with autism in 2008, in a study performed by Alarcón et al., (2008) that correlated Single Nucleotide Polimorphisms (SNPs) with gene-expression analyses. CNTNAP2 deficits were correlated with language difficulties in autistic patients (Alarcón et al., 2008). CNTNAP2 KO mice present hyperactivity, epileptic seizures, repetitive behaviors (Peñagarikano et al., 2011), and altered synaptic patterns and development (Lazaro et al., 2019). Interestingly, these mice present reduced number of oxytocinergic neurons in the PVN (Peñagarikano et al., 2015). Stimulation of endogenous OT release through activation of the Melancortin 4 receptor (MC4R) in PVN neurons improved social behavior in these mice as well as daily postnatal administration of exogenous OT (Peñagarikano et al., 2015). Intracerebroventricular injection of OT also has been shown to ameliorate social deficits in OT, OTR and CD38 KO mice (Modi & Young, 2012).

These promising data drawn from preclinical studies have inspired OT-based interventions in autism patients, being intranasal application the most common route of administration (Fig. 12A). Intranasal OT treatments may increase emotion recognition, empathic perception, and social memory (Kosfeld et al., 2005; Modi & Young, 2012; Young & Barrett, 2015). However, the high variability across patients and the short duration of the beneficial effects have limited the application of these treatments in the clinic. Furthermore, the ability of exogenous OT to effectively cross the blood brain barrier (BBB) is still under heated debate in the field (Insel, 2010; Dölen, 2015b; Leng & Ludwig, 2016; Erdozain & Peñagarikano, 2020) (Fig. 12B), meanwhile other administration routes like intraperitoneal and intracerebral injections have been less explored in the context of clinical trials (Dölen, 2015b).

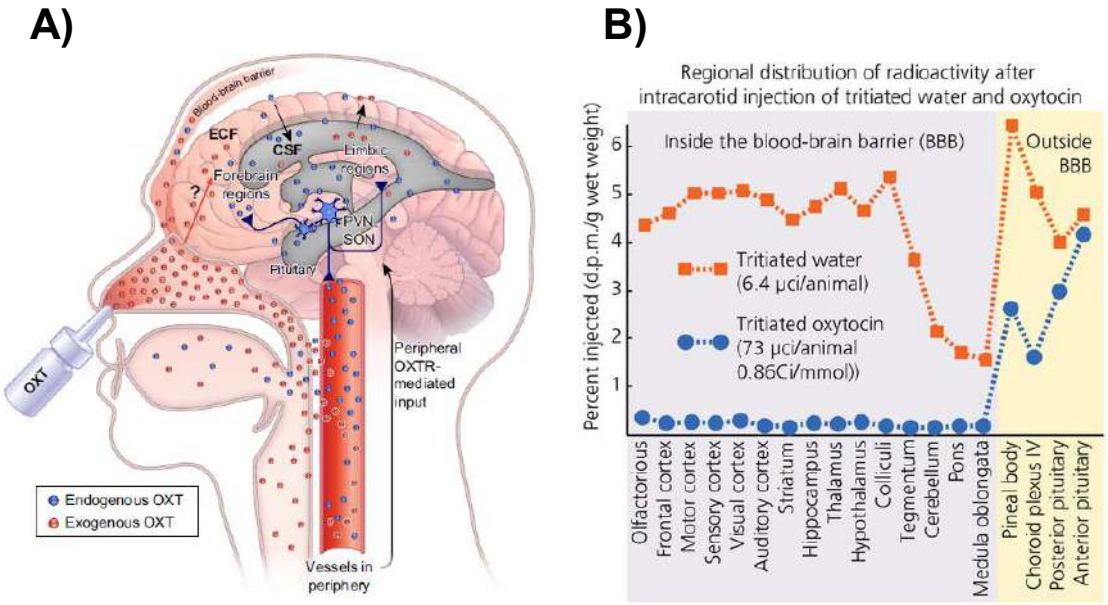

Figure 12.- Intranasal application of OT as a common route of administration for treating social behavior impairments. **A)** The brain OT system: projections, release, neuronal OTR-mediated input from the periphery, and external application. ECF: extracellular fluid; CSF: cerebrospinal fluid; PVN: paraventricular nucleus of the hypothalamus; SON: supraoptic nucleus; AN: accessory nuclei. Adapted from Jurek & Neumann, 2018. **B)** Studies of the central bioavailability of peripherally administered OT have demonstrated that the neuropeptide does not effectively cross the blood–brain barrier (BBB). For example, intracarotid artery injection of tritiated (radiolabelled) water and oxytocin in rats, followed by rapid (15-s post injection) dissection of 19 brain regions, four of which lie outside the BBB (pineal, choroid plexus, poster pituitary, anterior pituitary), and measurement of recovered radioactivity revealed that, even at supraphysiological levels, OT injected peripherally does not appreciably reach the central brain tissue. Adapted from Dölen, 2015b.

Biologically stable OT analogs are an alternative to overcome the poor penetration of OT into the BBB (Modi & Young, 2012; Dölen, 2015b). For example, Pitocin was administered to ASD and Asperger's patients reducing repetitive and stereotypic behaviors (Modi & Young, 2012). Other alternative are non-peptide agonists, which present higher stability, central penetration, and bioavailability than OT. WAY-267464 and the Ferring analog are some viable examples (Modi & Young, 2012). In animal models, activation of receptors at OT neurons has been implemented to promote OT release, like melanocortin, serotonin, or retinoic acid receptors (Modi & Young, 2012).

These results highlight the need to further explore the role of OT in the brain in order to optimize the methodology to detect OT levels and release events to improve correlative and causal studies (Young & Barrett, 2015; Erdozain & Peñagarikano, 2020).

2.- Neurotransmitter exocytosis

Neurotransmitter release is amongst the best understood exocytic processes in eukaryotic cells. Vesicle membrane's fusion with the plasma membrane is essential for neurotransmitter release into the synaptic cleft and subsequent binding and activation of specific receptors, usually located at the postsynaptic cell (Südhof, 2004) (Fig. 13A). Prior to fusion, neurotransmitter-containing vesicles undergo several steps which consist of tethering, docking, and priming (Kasai et al., 2012) (Fig. 13B). These processes are believed to position vesicles to facilitate highly efficient release events upon extracellular calcium influx induced by action potentials (APs) and the formation of the SNARE fusion complex (Gerber & Südhof, 2002; Stojilkovic, 2005; Südhof & Rothman, 2009; Südhof & Rizo, 2011).

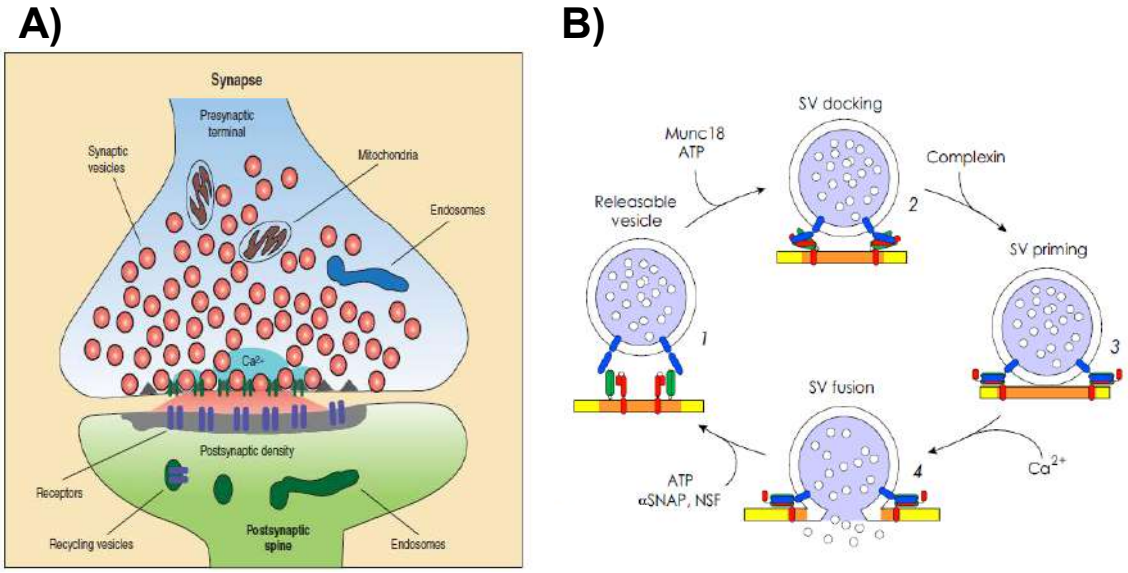

Figure 13.- Exocytosis of synaptic vesicles. **A)** Schematics of synaptic transmission. Chemical neural communication is based in neurotransmitter release. When the vesicle membrane fuses with the cellular membrane, neurotransmitters are released into the synaptic cleft, bind to the postsynaptic receptors and activate them. Adapted from Südhof, 2012. **B)** Synaptic vesicle cycle. Steps in vesicle fusion include vesicle tethering, docking, priming and finally, fusion. These events are driven by high-affinity interactions between SARE proteins, and are regulated by calcium and calcium-binding proteins through their interaction with the SNARE complex. Adapted from Ovsepian & Dolly, 2011.

In general, two main forms of cargo release have been identified: kiss-and-run and full fusion (Stojilkovic, 2005; Vardjan et al., 2007), although exocytosis can also be classified as spontaneous or constitutive, and triggered or stimulated (Kasai et al., 2012).

2.1.- Somatodendritic release

Classically, neuronal exocytosis refers to neurotransmitter release at axon terminals. However, multiple studies suggest that the neuronal somatodendritic compartment is also an active site of release, particularly of neuromodulators from DCVs (Ludwig & Leng, 2006; Kennedy & Ehlers, 2011). Several studies have addressed the postsynaptic release of OT and AVP-containing DCVs in the PVN and SON. The first evidence of OT and AVP somatodendritic secretion was described by Pow and Morris in 1989, employing tannic acid staining in combination with electron microscopy (Fig. 14A).

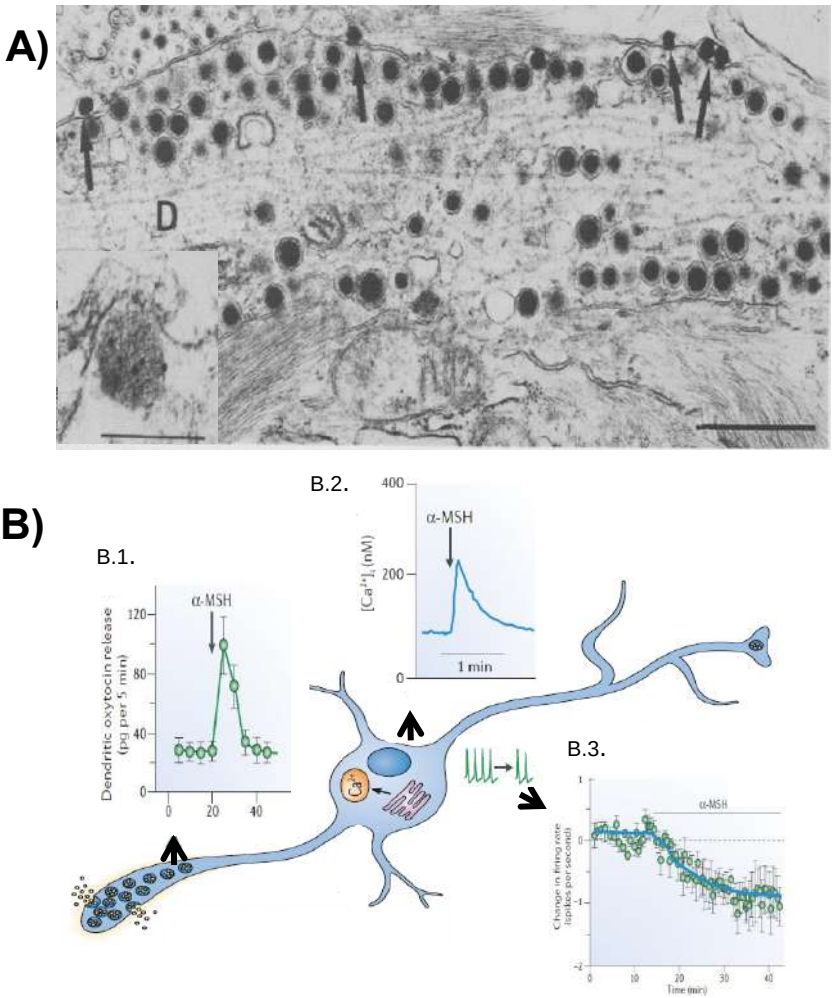

Figure 14.- Somatodendritic release in the hypothalamus. **A)** Longitudinal section of a magnocellular SON dendrite (D) in the ventral glial lamina, from brain slice preparations exposed to 1.2 mM tannic acid in a saline solution containing 56 mM KCl. Numerous DCVs are identified; exocytic figures are indicated by arrows. Scale bar indicates 1 μm. Insert: Immunogold labelled OT-DCV from the cell body of a magnocellular neuron from an animal pre-treated with colchicine. Scale bar indicates 200 nm. Adapted from Pow & Morris, 1989. **B)** Differential regulation of dendritic and axonal oxytocin secretion. Administration of α-melanocyte-stimulating hormone (α-MSH) induces dendritic oxytocin release (B.1.), and a transient increase in the intracellular Ca^{2+} concentration (B.2) while inhibiting the firing rate of OT neurons and reducing secretion from the posterior pituitary (B.3). Adapted from Ludwig & Leng, 2006.

Although somatodendritic release has not been as extensively studied as axonal release, it is believed that this form of neuronal secretion is primarily induced by agents that mobilize intracellular calcium from the endoplasmic reticulum, such as thapsigargin. Other major players in somatodendritic release are:

-Specific SNARE proteins. Data from several brain regions indicate that classical SNARE proteins are not found in the dendrites of secretory neurons, suggesting that variants of these proteins mediate dendritic release (Ludwig & Stern, 2015).

-Actin cytoskeleton. Several studies indicate that actin filaments surround the plasma membrane of the neurons (cortical F-actin). In sites where DCVs have been detected, there is no F-actin filaments. So, it has been proposed that actin cytoskeleton mediates the transport and the organization of the DCVs to the membrane, and that actin depolimerization (G-actin) leads to DCVs' release (Tobin & Ludwig, 2007; Ludwig & Stern, 2015; Ludwig et al., 2017).

-Calcium entry through glutamate NMDARs may mediate dendritic DCVs' release (Ludwig & Stern, 2015).

-Specific voltage-gated calcium channels (VGCCs) may mediate postsynaptic DCVs' exocytosis, specifically N-type channels (Ludwig & Stern, 2015; Ludwig et al., 2017).

-Involvement of specific calcium buffering mechanisms (Ludwig & Stern, 2015; Ludwig et al., 2017).

Somatodendritic release has been shown to be induced either by trains of APs at high frequencies, high potassium or application of neuropeptides (De-Miguel & Trueta, 2005). As such, the activation of the peptide receptors by an intracellular calcium mobilizing agent (in the case of OT, agents such as α-melanocyte-stimulating hormone (MSH), thapsigargin, or cyclopiazonic acid) (Ludwig et al., 2017) has been linked to DCV mobilization and release (Fig. 14B). Importantly, neuropeptide release is self-sustaining, further activating the neuron to amplify subsequent release events. Vesicles from the Readily Releasable Pool (RRP), a set of vesicles ready for fusion, play an important part in this phenomenon as they constitute a "primed" pool able to sustain release in response to future stimulus (electrical or osmotic) (Ludwig et al., 2002; Ludwig & Leng, 2006; Ludwig & Stern, 2015).

To note, somatodendritc release is not restricted to hypothalamic neurons. In peripheral aminergic neurons and the neuropile of the trigeminal nucleus caudalis, DCVs' exocytosis from unspecialized membrane zones has also been reported. Additionally, substance P secreted from the soma of dorsal root ganglion neurons, dopamine from the soma of substantia nigra neurons or from retina amacrine cells, as well as serotonin from Cajal-Retzius neurons are also prominent examples of somatodendritic release (De-Miguel & Trueta, 2005). Other cases of dendritic release occur at the synapse between granule and mitral cells in the olfactory bulb and the release of dynorphin from hippocampal granule cells (Kennedy & Ehlers, 2011).

3.- Dense Core Vesicles vs. Synaptic Vesicles

Neuropeptides, such as OT, as well as other neuromodulators like catecholamines, neurotrophic factors or hormones, are commonly stored in dense core vesicles (Ludwig & Leng, 2006), which exocytosis mechanisms in neurons have not been as extensively studied as the properties of neurotransmitter release (stored in synaptic vesicles). The main differences between DCVs and SVs, and their release properties are summarized in Fig. 15, and tables 1 and 2 (Ludwig and Leng, 2006; Van Den Pol, 2012; Ludwig and Stern, 2015).

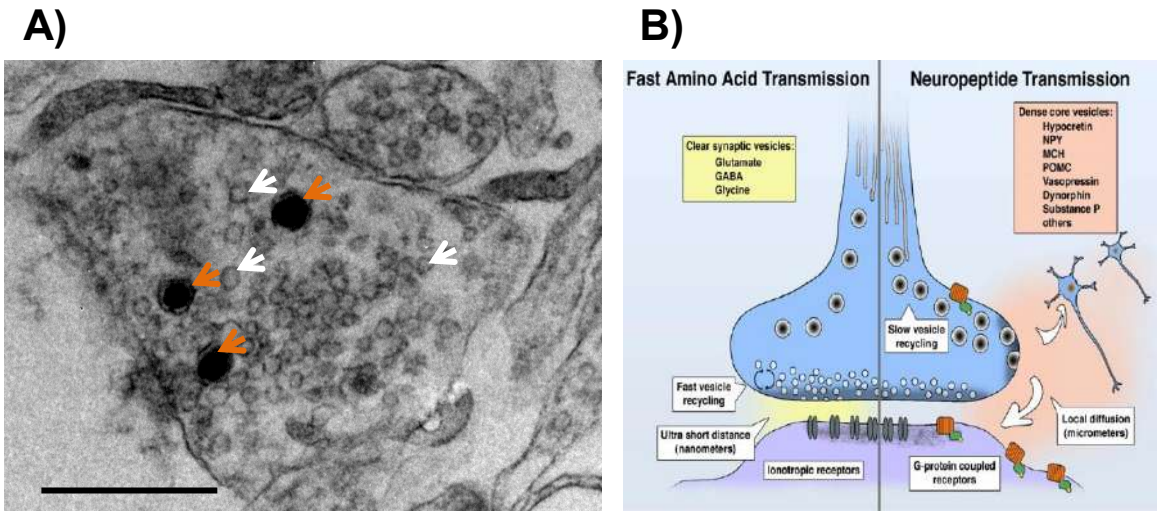

Figure 15.- Dense core vesicles vs. Synaptic vesicles. **A)** Electron micrograph of PVN neuron cell body under basal conditions. SVs are indicated with white arrows; DCVs are indicated with orange arrows. Scale bar indicates 1 µm. **B)** Comparison of fast amino acid synaptic transmission (left) and slower neuropeptide transmission (right). Adapted from Van Den Pol, 2012.

Table 1.- Properties of Synaptic vesicles and Dense core vesicles.

	Synaptic vesicles (SVs)	**Dense core vesicles (DCVs)**
Diameter (nm)	20-50 nm	100-150 nm
Cellular distribution	Presynaptic	Heterogeneously distributed
Site of release	Active Zone (AZ)	Non-specialized region
Release kinetics	Milliseconds	Seconds-Minutes
Cargo	Neurotransmitters	Neuropeptides, catecholamines, hormones, neuromodulators

Table 2.- Differences between classical neurotransmission and peptidergic neuromodulation.

	Neurotransmitters	Neuropeptides
Release stimulus	Action Potential / Calcium influx	Electrical activity / Partially Calcium-dependent
Receptors	Ionotropic / Metabotropic	Mostly Metabotropic
Concentration released	High (micromolar)	Small (nanomolar)
Half-life	ms (5 ms aprox.)	min (e. g. OT: 20 min in brain; 2 min in blood)
After release	Recycled trough specific transporters	Extracellular degradation trough unspecific peptidases, synthesized *de novo*

4.- The SNARE complex

4.1.- The SNARE complex hypothesis

The SNARE complex is a group of proteins that mediate the fusion between vesicles and lipid membranes. SNARE refers to the Soluble N-ethylmaleimide-Sensitive Factor Attachment Protein (SNAP) Receptor. A canonical SNARE complex is constituted by the interaction of three SNARE proteins: synaptobrevin-2 (Syb-2), also known as VAMP-2 (for "vesicle associated membrane protein"), syntaxin-1 (Stx-1), and SNAP-25 (Ramakrishnan et al., 2012) (Fig. 16).

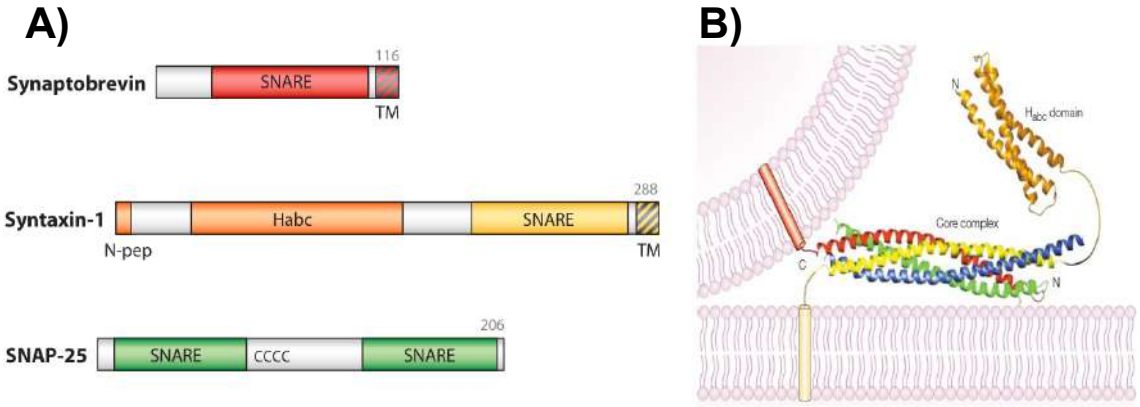

Figure 16.- Canonical SNARE complex for presynaptic neurotransmitter release. **A)** Domain diagrams of the neuronal SNAREs: synaptobrevin, syntaxin-1, and SNAP-25. SNARE motifs are labeled SNARE; the syntaxin-1 N-peptide is labeled N-pep; in SNAP-25, CCCC denotes a cysteine-rich region that is palmitoylated. The numbers at the top right indicate the length of the proteins. Adapted from Rizo & Südhof, 2012. **B)** Model of the neuronal SNAREs assembled into the core complex. The ribbon diagrams represent the crystal structure of the core complex and the structure of the amino-terminal Habc domain of syntaxin-1. The Habc domain is coloured in orange; Syb-2 is colored in red; Stx-1 is colored in yellow; SNAP-25 amino terminus is colored in blue; and SNAP-25 carboxyl terminus is colored in green. The cylinders represent the transmembrane regions of Syb-2 and Stx-1, which are inserted into the synaptic vesicle and plasma membranes, respectively. The curved lines represent short

sequences that connect the SNARE motifs and the transmembrane regions, as well as the linker region between the Habc domain and the SNARE motif of Stx-1. Zero layer is indicated by the dotted line. Adapted from Rizo & Südhof, 2002; Kádková et al., 2019.

The three families of SNARE proteins present a common SNARE motif composed of 60-70 amino acids that contains heptad repeats (Fig. 16A). A fully formed SNARE complex is characterized by a highly stable four-helix bundle resistant to sodium dodecyl sulfate (SDS, detergent that denature proteins) (Rizo & Rosenmund, 2008; Südhof & Rizo, 2011). SNARE proteins can be classified as v-SNAREs, if they are located in the vesicle membrane, as synaptobrevins (Sybs), and t-SNAREs, if they are found in the target plasma membrane, such as syntaxins (Stxs) and some SNAPs (Ovsepian & Dolly, 2011; Ramakrishnan et al., 2012). Synaptobrevins and syntaxins contribute one α-helix to the complex, whereas SNAP proteins like SNAP-25 contribute two α-helices, which leads to the close up of the vesicle and plasma membranes, and the formation of a four-helical coiled coil (Südhof, 2004; Rizo & Rosenmund, 2008; Kádková et al., 2019; Urbina & Gupton, 2020) (Fig. 16B). Specifically, synaptobrevins contribute an arginine residue; meanwhile syntaxins and SNAPs contribute a glutamine residue in the middle of the complex. The nature of these amino acids in the zero layer (Kasai et al., 2012; Kádková et al., 2019) provide the bases for an additional classification of SNARE proteins into Q-SNARE (SNAREs that contribute a glutamine residue) and R-SNARE (SNAREs that contribute an arginine residue) (Ovsepian & Dolly, 2011; Kuster et al., 2015; Kádková et al., 2019; Urbina & Gupton, 2020).

4.2.- Synaptic vesicle fusion

Presynaptic SVs' fusion in excitatory neurons is usually mediated by the canonical SNARE complex, constituted by: Syb-2 or VAMP-2, Stx-1, and SNAP-25 (Südhof, 2004; Kádková et al., 2019), and comprises several steps (Fig. 17). After an action potential, the neuron depolarizes allowing extracellular calcium entering the cell through voltage-gated calcium channels. Synaptic vesicles surrounding the active zone (AZ) get closer to the membrane (tethering) through the zippering action of the SNARE complex formation (Südhof, 2004). Munc18, a cytosolic regulatory protein, binds to Stx-1, which facilitates the interaction between Stx-1 and SNAP-25 and Syb-2. This docking step (Ovsepian & Dolly, 2011) precedes fusion, that is ultimately triggered by the calcium sensor Syt-1 (Südhof, 2004; Ovsepian & Dolly, 2011). When vesicle membrane fuses with the plasma membrane, neurotransmitters are released into the synaptic cleft, where they bind to specific postsynaptic receptors activating the postsynaptic neuron (Stojilkovic, 2005; Ovsepian & Dolly, 2011). After release, the SNARE complex is disassembled by NSF and SNAP proteins (Südhof and Rothman, 2009), and synaptic vesicles are recycled for another round of exocytosis (Südhof, 2004). Meanwhile, the reserve pool replenishes the vesicles that are being recycled, in order to maintain exocytosis in response to subsequent stimulation (Fig. 17).

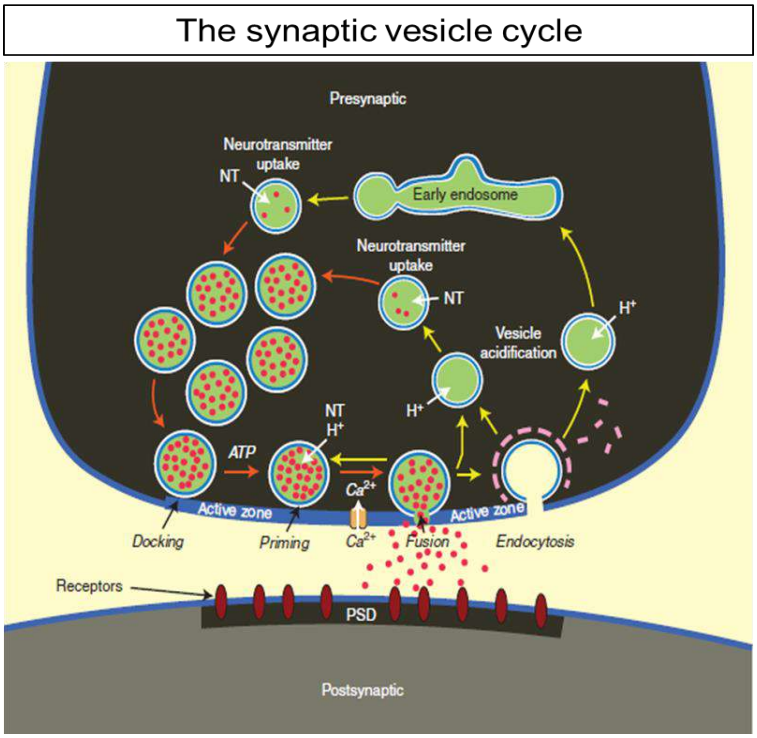

Figure 17.- The synaptic vesicle cycle. Schematics of a presynaptic nerve terminal in contact with a postsynaptic neuron. The synaptic vesicle cycle consists of exocytosis (red arrows) followed by endocytosis and recycling (yellow arrows). SVs (green circles) are filled with neurotransmitters (NT: red dots) by active transport (neurotransmitter uptake) fueled by an electrochemical gradient established by a proton pump that acidifies the vesicle interior (vesicle acidification; green background). In preparation to synaptic exocytosis, SVs are docked at the AZ, and primed by an ATP-dependent process that renders the vesicles competent to respond to a Ca^{2+}-signal. When an action potential depolarizes the presynaptic membrane, Ca^{2+}-channels open, causing a local increase in intracellular Ca^{2+} at the AZ that triggers completion of the fusion reaction. Released neurotransmitters then bind to receptors associated with the postsynaptic density (PSD). Adapted from Südhof & Rizo, 2011.

4.3.- The SNARE proteins

4.3.1.- Synaptobrevin

Sybs or VAMPs are transmembrane proteins constituted by a short amino-terminal sequence, a SNARE motif, and a carboxy-terminal membrane anchor (Südhof & Rizo, 2011). They have 20 kDa of molecular mass approximately, and are the most abundant proteins in SVs. (Gerber & Südhof, 2002; Rizo & Südhof, 2002). Sybs were identified in 1992 by means of specific botulinum toxin subtypes known to block release due to irreversible Syb cleavage (Südhof & Rizo, 2011).

The most prominent Syb isoforms in the brain are Syb-1 and Syb-2. Syb-1 is abundant in the spinal cord and neuromuscular junctions, meanwhile Syb-2 is more commonly found in the forebrain. In addition to the well-described role in mediating presynaptic SVs release, Syb proteins have been also implicated in postsynaptic functions. As such, Syb-1 has been

proposed to participate in NMDARs trafficking. Furthermore, Syb-2 may regulate several processes including the trafficking of AMPAR- and GABAAR-containing endosomes in dendrites (reviewed in Madrigal et al., 2019). Isoforms such as Syb-3, 4 and 7 are found in lower levels in the brain, and Syb-4 and 7 are also expressed in several tissues (Madrigal et al., 2019; Urbina & Gupton, 2020).

4.3.2.- Syntaxin

Stxs are SNARE proteins which structure comprises a transmembrane domain, several hydrophobic regions and the SNARE-domain (Teng et al., 2001; Gerber & Südhof, 2002; Kasai et al., 2012; Rizo & Südhof, 2012).

The Stx family is constituted by 18 isoforms, with some of them also including alternatively spliced isoforms (e.g., Stx-1, 2, 3, 5 and 16) (Teng et al., 2001). Importantly, among the 18 possible isoforms, only Stx1-4 are located in the plasma membrane (Teng et al., 2001).

Stx-1 is the best studied, and presents two isoforms: Stx-1a and Stx-1b, which is the most abundant in the brain (Ramakrishnan et al., 2012; Madrigal et al., 2019). In addition to its well-known role in presynaptic vesicle exocytosis, Stx-1 can also be localized postsynaptically, playing a role in trafficking and exocytosis of excitatory and inhibitory receptors (Madrigal et al., 2019).

Another prominent isoforms found at dendrites are Stx-3 and Stx-4 (Kennedy et al., 2010; Jurado et al., 2013; Arendt et al., 2015). Specifically, Stx-3 has been found in the dendrites of excitatory neurons, where it plays an important role in regulating AMPAR trafficking during long-term potentiation (LTP) (Jurado et al., 2013), whereas Stx-4 may participate in receptor exocytosis during homeostatic plasticity (Arendt et al., 2015).

Other syntaxin isoforms (e.g., Stx-5, Stx-18) are mayor players of the secretory pathway with various roles in vesicle trafficking from the endoplasmic reticulum (ER), the Golgi apparatus, trans-Golgi network (TGN), and the endosome system (Teng et al., 2001).

4.3.3.- SNAPs

The SNAP family is formed by SNAP-25, SNAP-23, SNAP-29, and SNAP-47, receiving its name depending on their molecular weight (Urbina & Gupton, 2020) (Fig. 18). Below, we discussed the main properties of these isoforms, with a special focus on SNAP-47, the main target of the present study.

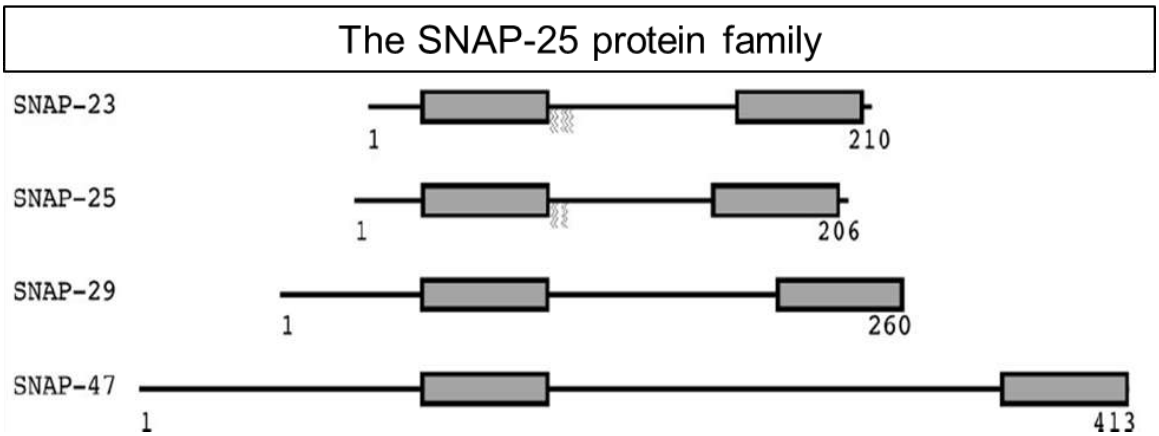

Figure 18.- Schematic view of the domain structure of the members of the SNAP-25 protein family. All SNAP-25 homologues contain tandem SNARE motifs (boxed). Palmitoylation sites in the linker region are indicated on SNAP-23 and SNAP-25. SNAP-47 has an extended N-terminal domain and linker region compared with other SNAPs. Adapted from Holt et al., 2006.

SNAP-25

SNAP-25 was the first identified and best studied SNAP protein (Kádková et al., 2019). SNAP-25 contains a short N-terminus, a SNARE-motif (Qb), a linker region, and a second SNARE-motif (Qc) (Gerber & Südhof, 2002). It is located at the plasma membrane, through the palmitoylation of central cystein residues (Gonzalo & Linder, 1998; Gerber & Südhof, 2002; Rizo & Südhof, 2012).

SNAP-25 is highly abundant in the brain, although it can also be found at high levels in other tissues. The two SNAP-25 exons generate SNAP-25a and SNAP-25b via alternative splicing (Kádková et al., 2019). SNAP-25b dominates in the adult brain, whereas SNAP-25a is expressed in adrenal chromaffin cells and β-cells of the pancreas. SNAP-25a is also expressed in the olfactory bulb, hypothalamus, and the pituitary, as well as brain regions specialized in the release of neuropeptides and hormones (Kádková et al., 2019).

SNAP-25 participates in regulated and spontaneous presynaptic exocytosis (Kádková et al., 2019). In addition, SNAP-25 has been shown to play a postsynaptic role, participating in NMDA-receptor trafficking (Jurado et al., 2013), AMPA-receptor and GABAAR dynamics, and removal of kainate receptors (Kádková et al., 2019). SNAP-25 also participates in spine formation (Fossati et al., 2015). It has also been suggested that SNAP-25 participates in the exocytosis of DCVs in chromaffin cells and in some neurons (Kádková et al., 2019).

SNAP-23

Structurally, SNAP-23 is almost identical to SNAP-25, due to the duplication of the SNAP-25 ancestral gene (Kádková et al., 2019). *In vitro* studies have shown that SNAP-23 can substitute SNAP-25, although with less efficiency (Kádková et al., 2019).

Nonetheless, some differences in expression and function between SNAP-25 and SNAP-23 have been reported. As such, SNAP-23 seems to be less abundant in late endosomes and the trans-Golgi network (Kádková et al., 2019).

SNAP-23 is found in the CNS and in non-neuronal tissue where it can participate in the regulation of exocytosis of platelets and mast cells, pancreatic cells, Schwann cells, juxtaglomerular cells, and alveolar cells. Interestingly, in neurons, SNAP-23 is often found in the soma and dendrites (Kádková et al., 2019) participating in GABAA and NMDA receptor trafficking (Ramakrishnan et al., 2012; Kádková et al., 2019), and in astrocytes (Fukuda & Mikoshiba, 2001).

SNAP-29

SNAP-29 is the less known member of the SNAP family. Unlike SNAP-25 and SNAP-23, SNAP-29 exhibits a long linker and lacks palmitoylation sites for membrane anchoring, suggesting a primarily cytosolic location (Kádková et al., 2019). Nonetheless, SNAP-29 has been reported in synaptic vesicles in neurons, Golgi endosomes, and in close proximity to plasma membrane organelles (Madrigal et al., 2019; Kádková et al., 2019).

SNAP-29 has been reported to interact with Stx-6, Stx-1 and Stx-17 and to partially rescue the effects of SNAP-25 KO in neurons (Arora et al., 2017).

SNAP-47

SNAP-47 was first identified by Holt et al., in 2006 in synaptic vesicles from striata primary neurons from newborn mice (Holt et al., 2006). SNAP-47 has a longer N-terminal tail and a longer linker region than SNAP-29 (Kádková et al., 2019), but similar to SNAP-29, it lacks palmitoylated cysteine residues and is not cleaved by SNAP-specific botulinum neurotoxins A or E (Holt et al., 2006; Kádková et al., 2019).

In epithelial cells, SNAP-47 has been shown to interact with Stx-1 and Stx-5 in the ER and with Stx-1 in the plasma membrane. In addition, SNAP-47 weakly interacts with Syb-2 and Syb-3 and more strongly with Syb-4, 7 and 8, regulating their subcellular localization and exocytosis (Kuster et al., 2015). SNAP-47 is detectable as early as embryonic day 10 (E10) and reaches maximal levels at E18 in brain extracts (Holt et al., 2006) (Fig. 19A). SNAP-47 is expressed mostly in the brain, followed by the liver, kidney, heart, testis, lung, skeletal muscle, and spleen (Holt et al., 2006) (Fig. 19B).

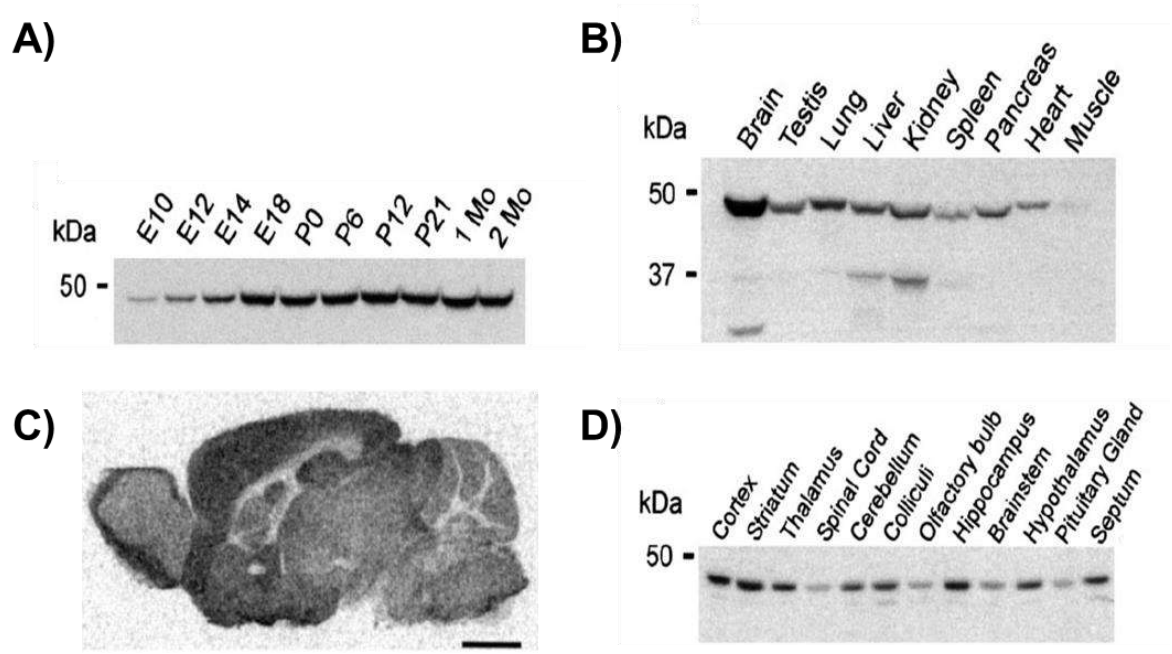

Figure 19.- Developmental profile and tissue distribution of SNAP-47 protein. **A)** SNAP-47 was detected as early in development as embryonic day 10 (E10), with maximal levels of expression reached at embryonic day 18 (E18). These levels were maintained into early adulthood. **B)** SNAP-47 is ubiquitously expressed but is particularly enriched in the brain. In addition, it is abundant in liver, kidney, lung, spleen, and testis. The protein was not detected in skeletal muscle. **C, D)** SNAP-47 is expressed in all brain regions as determined by immunoautoradiography on sagittal mouse brain sections (C) and Western blotting on various brain areas (D). Scale bar indicates 2 mm. Adapted from Holt et al., 2006.

In the brain, SNAP-47 is located in both axons and dendrites (Münster-Wandowski et al., 2017; Madrigal et al., 2019; Kádková et al., 2019) in different brain regions including the cortex, the hippocampus, cerebellar granule cells, the olfactory bulb, the thalamus, the striatum and the brain stem (Holt et al., 2006; Irfan et al., 2019) (Fig. 19C, D). Cumulative evidence suggests that SNAP-47 could be implicated in both pre- and postsynaptic functions. *In vitro*, SNAP-47 forms complexes containing Stx-1 and Syb-2, being capable of promoting membrane fusion at pre- and postsynaptic compartments. As such, axonal brain derived neurotrophic factor (BDNF) secretion requires a SNAP-47-dependent mechanism that is further enhanced by SNAP-25 (Shimojo et al., 2015). Postsynaptically, SNAP-47 associates with Stx-3 and Syb-2 to mediate activity-dependent insertion on AMPARs during LTP (Jurado et al., 2013) and homeostatic plasticity (Arendt et al., 2015), as well as participating in the early secretory pathway of other SNARE proteins (Kuster et al., 2015).

Interestingly, SNAP-47 has been shown to interact with the intracellular domain of Amiloyd Precursor Protein (APP) and huntingtin under physiological conditions (Del Prete et al., 2014; Sap et al., 2021), with reports indicating a decrease of SNAP-47 in Parkinson's disease (Bereczki et al., 2018). These findings suggest that alterations in SNAP-47 may be linked to common neurodegenerative disorders.

Since studies in neuronal tissue are scarce, most information regarding SNAP-47 function has been gathered in cell lines. In these models, SNAP-47 consistently appears to participate in autophagosome formation usually forming stable complexes with Syb-7 and

Stx-16 (Aoyagi et al., 2018; Tang, 2019). Furthermore, SNAP-47 interaction with Stx-17 and Syb-7/Syb-8, mediates autophagosome-lysosome fusion (Jian et al., 2024). In HeLa cells, it was described that a complex constituted by SNAP-47 and Syb-5, and Stx-1 (or Stx-4) regulates exosome release (T. Matsui et al., 2023). More recently, SNAP-47 has also been involved in EV-D68 (enterovirus) replication (Corona et al., 2018).

4.3.4.- Synaptotagmin

The Syt family comprises 16 isoforms in mammals, serving as calcium sensor proteins that activate membrane fusion events by interacting with SNARE proteins (Südhof, 2012; Südhof, 2013).

Structurally, synaptotagmins are vesicle proteins with an N-terminal transmembrane region, a central linear sequence, and two cytoplasmic calcium-binding C2 domains, C2A and C2B. These domains interact with the SNARE complex and phospholipids (Gerber & Südhof, 2002; Südhof, 2013).

Syts work in conjunction with complexin, a small soluble protein binding to the SNARE complex, required to activate and optimize Syt's action (Südhof, 2012; Südhof, 2013).

Among the family members, Syt-1, 2, 9, and 12 are present on both SVs and secretory granules, while Syt-10 is specifically found on secretory vesicles in olfactory mitral neurons. Syt-7 is predominantly located on secretory granules known as "secretory lysosomes" in non-neuronal and non-endocrine cells (Südhof, 2012). Furthermore, Syt-4 is distributed on the trans-Golgi complex, synaptic vesicles, and postsynaptic organelles, possibly widely distributed in neuronal organelles. Syt-3, Syt-6, and Syt-7 are localized on the plasma membrane (Gerber & Südhof, 2002).

In terms of abundance in synaptic vesicles, Syt-1 and Syt-2 are the most prevalent isoforms. Syt-3 and Syt-11 are found in dendrites, Syt-5, 7, 10, and 17 are found in axons, and Syt-4, 6, 9, and 12 are found in both axons and dendrites. These various isoforms play distinct roles in exocytosis and endocytosis, exhibiting different properties and kinetics (Südhof, 2004; Rizo & Rosenmund, 2008; Dean et al., 2012).

4.4.- Pathologies associated to alterations of the SNARE complex: SNAREopathies

Pathologies associated to mutations in the coding genes for the core components of the SNARE complex are known as “SNAREopathies” (Verhage & Sørensen, 2020). These pathologies may present a myriad of symptoms including autistic features, spasms, ataxia, hypotonia, hyperkinesia, or stereotypies (Verhage & Sørensen, 2020). Interestingly, mutations affecting SNARE proteins do not always translate into pathological effects, often requiring the contribution of specific environmental factors to trigger a disorder (Verhage & Sørensen, 2020). When manifested, symptoms usually start in the first year of life, as the affected genes participate in the release of important molecules for brain development (Verhage & Sørensen, 2020).

Research on this topic has been primarily focused on the members of the canonical SNARE complex (Syb-2, Stx-1, SNAP-25, and Syt-1) (Ramakrishnan et al., 2012; Praschberger et al., 2021; Uzay & Kavalali, 2023). Moreover, mutations and dysregulations in other isoforms of the SNAP and Syt families have been described. Mammary and prostate adenocarcinomas and ovarian cancer present increased levels of SNAP-23 (Kádková et al., 2019); biallelic loss-of-function in Stx-3 gene is linked to severe retinal dystrophy (Perez-Hurtado et al., 2023) ; and Stx-18 deficiency impairs vesicular transport of collagen II, leading to osteochondrodysplasia (Guillemyn et al., 2023).

At the moment, there are no effective treatments for SNAREopathies (Verhage & Sørensen, 2020),despite employment of aminopyridines has been proposed to rescue exocytosis, as it increases presynaptic calcium in non-epileptic patients (Uzay & Kavalali, 2023).

4.5.- SNARE complex involved in oxytocin release

As aforementioned, the formation of the SNARE complex is crucial for neurotransmitter release and its dysregulation or mutation of one of its core components leads to devastating disorders. Although the kinetic properties and molecular mechanisms involved in SNARE-dependent presynaptic neurotransmitter exocytosis have been extensively studied, much less is known regarding neuropeptide release, usually involving DCVs.

As such, whereas axonal OT release into the bloodstream is mediated by classical SNARE proteins (Miyata et al., 2001; Tobin et al., 2012), the proteins mediating OT somatodendritic release into the brain are not well characterized.

Evidence indicates some classic neurotoxins cleave postsynaptic OT release (De Kock et al., 2003; Bergquist & Ludwig, 2008), indicating the involvement of a SNARE complex constituted by some canonical SNARE proteins. As such, Stx-1 was found in the cytoplasm of soma and dendrites of hypothalamic neurons, partially colocalizing with OT (Tobin et al., 2012), and Stx-1a KO mice exhibit social behavior impairments likely due to the dysregulation of oxytocinergic and dopaminergic systems. Importantly, administration of OT partially restores social deficits in these animals (Fujiwara et al., 2016; Fujiwara et al., 2021), suggesting a role of Sxt-1a in OT release.

However, the components of the SNARE complex and Syt proteins involved in OT release during basal and stimulated conditions remain to be identified. Immunohistochemistry experiments in SON hypothalamic slices showed no expression of SNAP-25, Syb-1,2,3, Syt-1 and Syt-7 in the soma and dendrites of these neurons (Tobin et al., 2012). Given the unique properties and kinetics of DCVs exocytosis, it is likely that the SNARE complex involved in their release includes distinct SNARE proteins (Van Den Pol, 2012).

OBJECTIVES

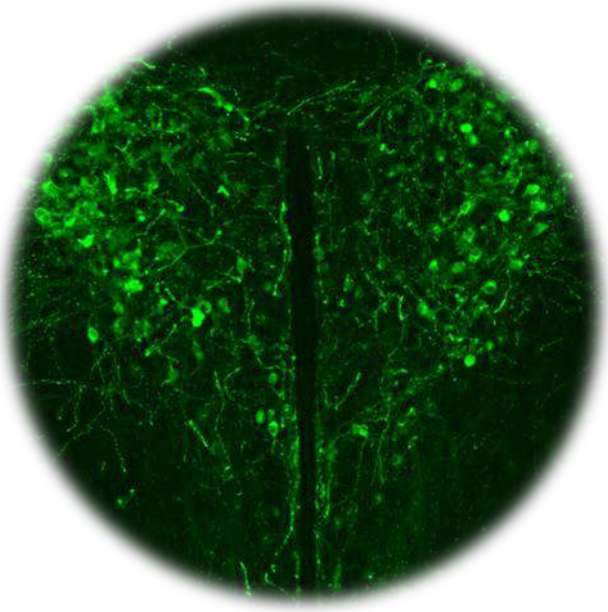

To deepen our understanding of the properties and underlying mechanisms of OT regulation in the soma of hypothalamic neurons, we set out to achieve the following specific objectives:

1. **To describe the morphological properties of hypothalamic OT-containing Dense Core Vesicles (DCVs) under basal and stimulated conditions.**

2. **To analyze the dynamics and trafficking of somatic OT-containing compartments under basal conditions and in response to neuronal stimulation.**

3. **To examine the recruitment and release of somatic OT-containing compartments to the membrane under basal and stimulated conditions.**

4. **To characterize SNARE and synaptotagmin proteins expression in the somatic compartment of OT-producing hypothalamic neurons.**

5. **To analyze the interaction between somatic OT- and SNAP-47-containing compartments under basal and stimulated conditions.**

6. **To examine the role of SNAP-47 in OT trafficking to the membrane and its implications for social behavior in mice.**

Our results shed light on the dynamic properties of OT vesicles, contributing to our understanding of OT regulation in the brain and its potential impact on social behavior.

MATERIALS AND METHODS

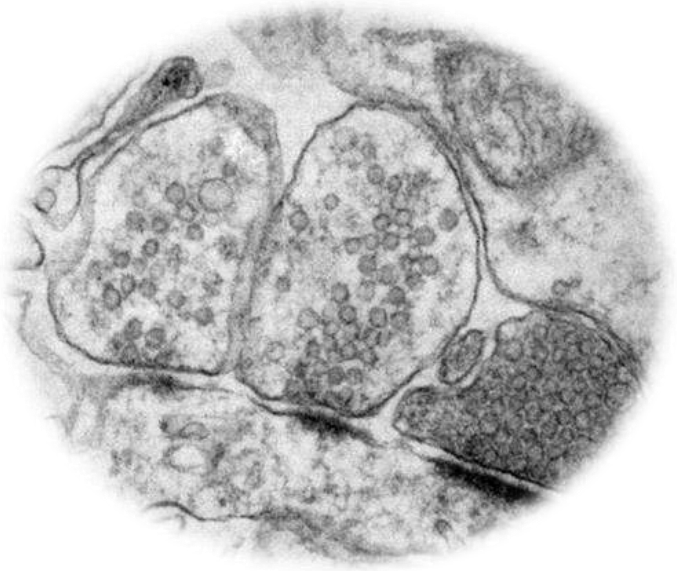

1.- Animals

The mouse has been the experimental animal model employed in the present study. Three mouse strains were employed depending on the purpose of the experiment (Table 3).

Table 3.- Mice strains employed in the experimental procedures of this thesis.

Genotype	Experiment	Age	Sex
BL6/C57 (Wild Type-WT)	○ Primary culture for immunocytochemistry ○ Immunohistochemistry	○ Postnatal day 0 (P0) ○ Adult (3-4 months)	Male and female
OT^{tdTom}	○ Electron microscopy ○ Immunohistochemistry ○ Social behavior ○ Primary culture for chasing, dynamics, and cytotoxicity assay	○ Adult (3-4 months) ○ Adult (3-4 months) ○ Adult (2 months aprox.) ○ P0	Male and female
OT^{EYFP}	○ Primary culture for chasing and immunocytochemistry	○ P0	Male and female

To unambiguously identify OT-expressing neurons, we employed the mouse transgenic line OT-Ires-Cre:Rosa26iDTR/+OT-Cre (OT^{Cre} thereafter) (Jackson Laboratories, strain ID: 024234) originally generated by Wu et al., 2012, which express Cre recombinase under the control of endogenous OT promoter (Fig. 20A). These animals were bred with reporter mice, expressing either tdTomato (Ai9, Jackson Laboratories, strain ID: 007909) or EYFP (R26-stop-EYFP, Jackson Laboratories, strain ID: 006148) (Fig. 20B). The resulting animals are referred to as OT^{tdTom} and OT^{EYFP}, in which oxytocinergic cells are identified by either the expression of tdTomato or EYFP, respectively (Fig. 20C).

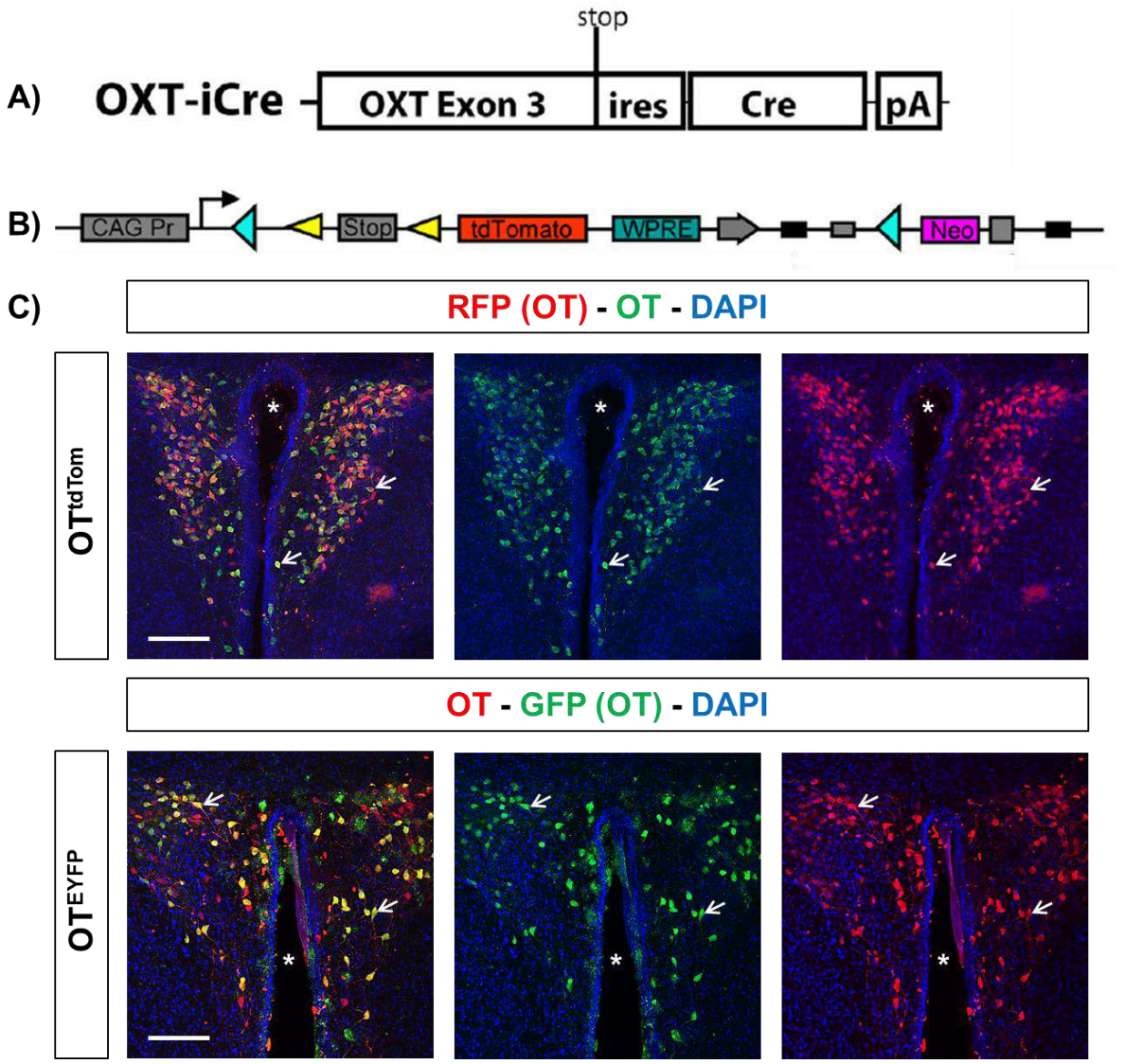

Figure 20.- Characterization of the transgenic mouse lines employed in this study. **A)** Schematics of the design to generate the transgenic mouse line OT^{Cre}. Cre recombinase was targeted just after the stop codon of the OT gene using an internal ribosomal entry site (Ires). Adapted from Wu et al., 2012. **B)** Schematics of the Cre-reporter construct inserted into the Rosa26 locus. Adapted from Madisen et al., 2009. **C)** Pictures of the PVN of OT^{tdTom} and OT^{EYFP} adult mice. Endogenous signal from OT^{tdTom} neurons was amplified with anti-RFP antibody (red); OT neurons were also stained with and anti-OT antibody (green). Endogenous signal from OT^{EYFP} neurons was amplified with anti-GFP (green) antibody; OT neurons were also stained with an anti-OT antibody (red). Arrows indicate OT neurons stained with anti-RFP/anti-GFP and anti-OT antibodies; asterisk indicates the third ventricle. Credit to Pilar Madrigal (lab member). Scale bar indicates 150 µm.

All experiments were performed according to Spanish and European Union regulations regarding animal research (2010/63/EU). Experimental procedures were approved by the Bioethical Committee at the Institute of Neuroscience (CSIC-UMH) and the Consejo Superior de Investigaciones Científicas. Animals were born and maintained in the Animal Facility of the Institute of Neuroscience (CSIC-UMH), and were housed in ventilated cages in a standard pathogen-free facility, on a 12 h light/dark cycle, with free access to food and water, controlled temperature (23-25 °C) and humidity (40-60 %). The experimental design was optimized to minimize the number of animals.

For genotyping, PCR analysis for the Cre allele was performed using the following primers and PCR program (Fig. 21):

Primers:

ACACCGGCCTTATTCCAAG (R)

TTTGCAGCTCAGAACACTGAC (F)

AGCCTGCTGGACTGTTTTTG (WT- R)

Denature: 95 ºC, 3 min

Amplification: 94 ºC, 15 s

62 ºC, 20 s

72 ºC, 30 s

Elongation: 72 ºC, 10 min

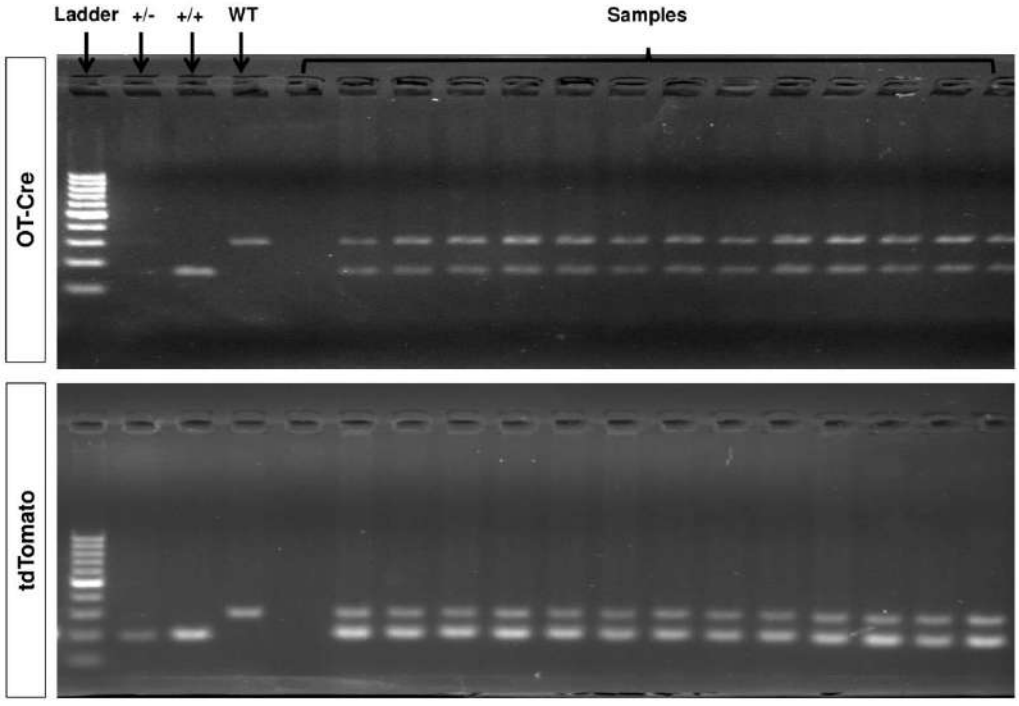

Figure 21.- PCR gel from OT^{tdTom} mice. OT-Cre and tdTomato alleles.

2.- Electron microscopy

2.1.- Acute hypothalamic slices and treatment

Acute hypothalamic brain slices from OT^{tdTom} male mice (3-4 months old) were obtained by Paula Guillamón (TFM alumni).

Animals were anesthetized injecting Dolethal (Vetoquinol Especialidades Veterinarias S.A., Dolethal 200 mg/mL) intraperitoneally, and were perfused with cold sucrose cutting solution (composition in mM: 185 sucrose; 25 $NaHCO_3$; 25 glucose; 2.5 KCl; 1.2 NaH_2PO_4 H_2O; 10 $MgSO_4$; 0.5 $CaCl_2$; < 4 ºC). Then, animals were decapitated and their brains were dissected in cold sucrose cutting solution. Hypothalamic brain slices (250-300 µm thick) were processed in a vibratome (Leica VT1000 S). The vibratome chamber contained ice-cold sucrose cutting solution bubbled with carbogen (95 % oxygen/5 % carbon dioxide) to preserve slices' health. Hypothalamic slices were incubated in Tyrode's solution (composition in mM: 125 NaCl; 2 KCl; 30 glucose; 25 HEPES; 2 $CaCl_2$; 2 $MgCl_2$; pH 7.4) 30 min at 32-34 ºC, and then 30 min at room temperature (RT) for recovery.

Hypothalamic slices were individually transferred to a multi-well plate (Falcon, Ref: 353043) and incubated either in Tyrode's solution or 100 mM KCl Tyrode's solution (composition in mM: 27 NaCl; 100 KCl; 30 glucose; 25 HEPES; 2 $CaCl_2$; 2 $MgCl_2$; pH 7.4) 1 min at 37 ºC.

2.2.- Hypothalamic slices processing for transmission electron microscopy

Once hypothalamic brain slices were obtained and treated, they were processed for electron microscopy. Only brain slices that contained clearly identifiable PVN regions were selected to be incubated in fixation buffer during 4 h at 4 ºC. Fixation buffer was composed of sodic cacodylate buffer 0.1 M, pH 7.3 (ANAME, Ref.12300, 100 g), PFA 2 % (ANAME, Ref: 15710, 10x10 mL), and glutaraldehyde 2.5 % (ANAME, Ref. 16220, 10x10 mL). Then, the PVN region was dissected and transferred to fixation buffer for 2-3 hrs at 4 ºC. Fixation buffer was replaced by sodic cacodylate buffer 0.1 M + sucrose 8 %. Samples were stored at 4 ºC until they were processed at the electron microscopy service of the University of Murcia, where image acquisition through transmission electron microscopy was conducted.

2.3.- Image acquisition

Electron microscopy images were obtained at the Servicios de Apoyo a la Investigación of the University of Murcia employing a JEOL JEM-1011 microscope, a Gatan BioScam 792 digital camera and the Digital Micrograph 3.11.0 software (Gatan, Inc., Pleasanton., CA, USA). Images of hypothalamic terminals were acquired at 10000X.

The Scanning Electron Microscope (SEM) uses as lighting source a beam of electrons generated by the thermionic effect of a tungsten filament. Electrons are accelerated and

directed towards the sample, collide with it, are selectively scattered, and all of them are driven by electromagnetic lenses in high vacuum conditions to form the image (UPV Electronic microscopy service, 2020).

Image acquisition was carried out operating the SEM at 80-90 kV and image capture was made using a digital camera Gatan Bioscam Model 792 through the Digital Micrograph 3.11.0 software. Resulting images were visualized in gray scale. Dense samples present higher degree of electron dispersion, resulting in dark images (as happens with DCVs); meanwhile electrons pass through thinner structures, resulting in clearer images (as is the case of SVs) (Ubero, 2008).

2.4.- Electron microscopy image analysis

Images were analyzed using the open image analysis software Fiji (ImageJ 1.53t, National Institutes of Health, USA) employing a homemade plugin ("SynVesMeasuring", https://github.com/mdimitrovg/SynVesMeasuring) (Fig. 22). "SynVesMeasuring" was custom-developed by Momchil D. Georgevski employing Cellpose 2.0, a general-purpose algorithm for cellular segmentation (Stringer et al., 2021), and leveraging deep learning image segmentation models. These models were trained using our own electron microscopy images to generate regions of interest (ROIs) for vesicles within the cells. The cellular membrane and AZ were delineated manually, and subsequent measurements were conducted by the plugin from the vesicle's centroid to the nearest point on these structures, thereby yielding high resolution measurements.

The parameters analyzed were: area and diameter of DCVs, DCVs' density within the terminal, distance from DCVs to the membrane, and distance from the DCVs to the AZ. Data were statistically analyzed with the data analysis software GraphPad Prism 8 (GraphPad Prism version 8.0.01 for Windows, GraphPad Software, Boston, Massachusetts USA, www.graphpad.com). Results are shown as mean ± SEM.

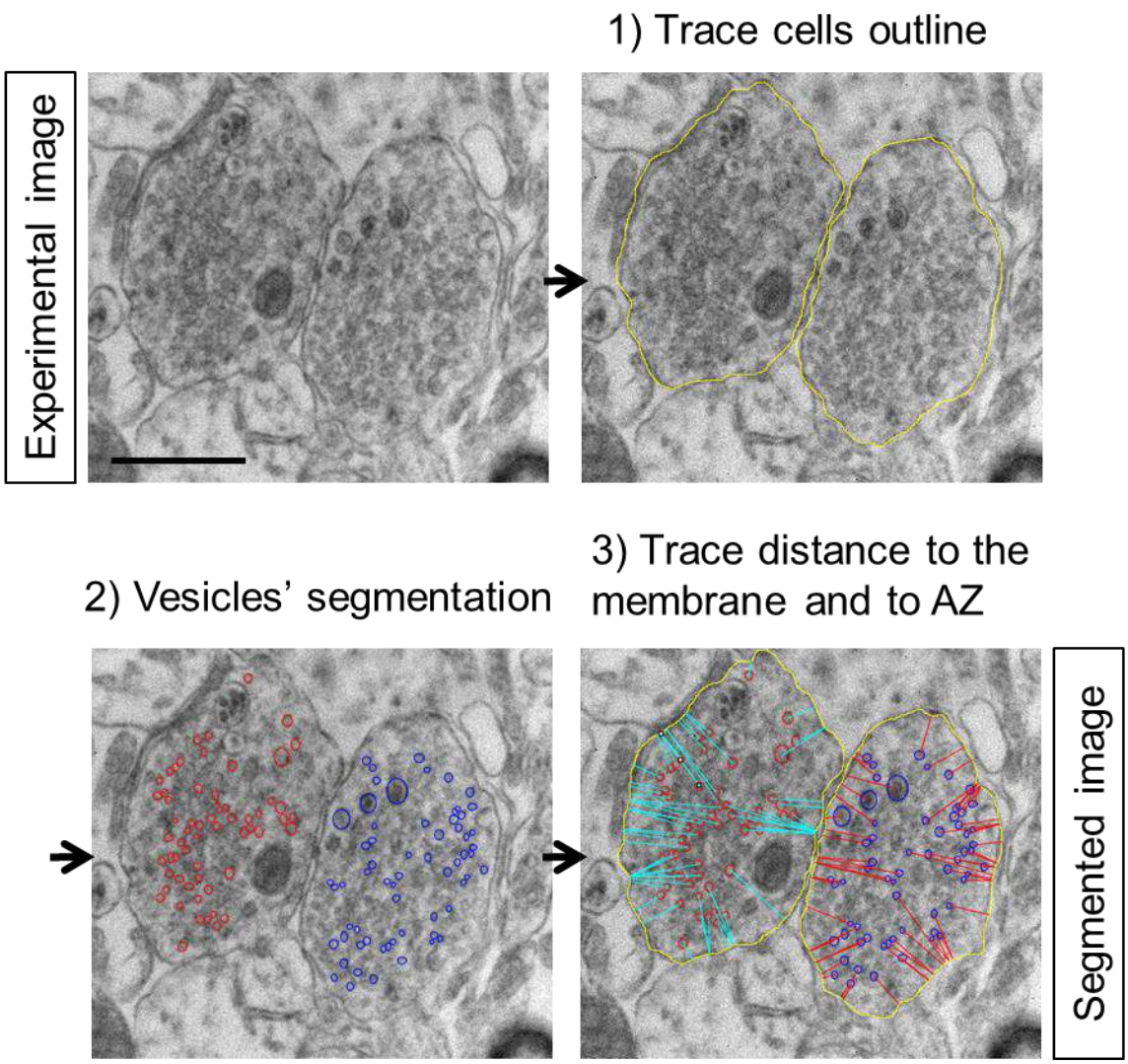

Figure 22.- Segmentation process for electron microscopy images. 1) Outline tracing: from the experimental images, first step is tracing the cells outline. 2) Vesicles' segmentation: the macro segments the vesicles within the cells. 3) Distance measurement: the macro measures the vesicles' distance to the membrane and to the AZ (when present). Measured parameters are displayed in an excel sheet. Scale bar indicates 1 μm.

3.- Primary culture of hypothalamic neurons

3.1.- Treatment of cell culture coverslips

24 mm or 12 mm diameter coverslips (VWR, Ref: 631-0153; Ref: MENZCB00120RAC20, respectively) were employed depending on experiment requirements (Table 4). Pretreatment with poly-D-lysine (PDL, Sigma Aldrich, Ref: P7886) was performed following standard procedures. Briefly, we washed the coverslips with 100 % ethanol (Ethanol absolute,

Vidrafoc, Ref: 141086.1211), let them dry and placed them in a cell culture multiwell plate (P6 or P12 multiwell plate, Falcon, Ref: 353046; Ref: 353043, respectively). PDL was added to the coverslips, and plates were placed in a cell incubator (Thermo Scientific™ Heracell™ 150i) during 2 h at 37 ºC. Then, PDL was removed and coverslips were washed x3 with autoclaved distilled water and dried. Culture plates were wrapped with parafilm (American National Can., Menasha, WI 54952) and stored until use. All procedures were performed in sterile conditions.

3.2.- Hypothalamic dissection for primary culture

P0 male and female mice were decapitated (mice genotype depended on the experiment, see Table 3), brains were carefully removed and hypothalami were dissected in cold HBSS 1X (< 4 ºC, Fisher, Ref: 14175-053) as described in Fig. 23.

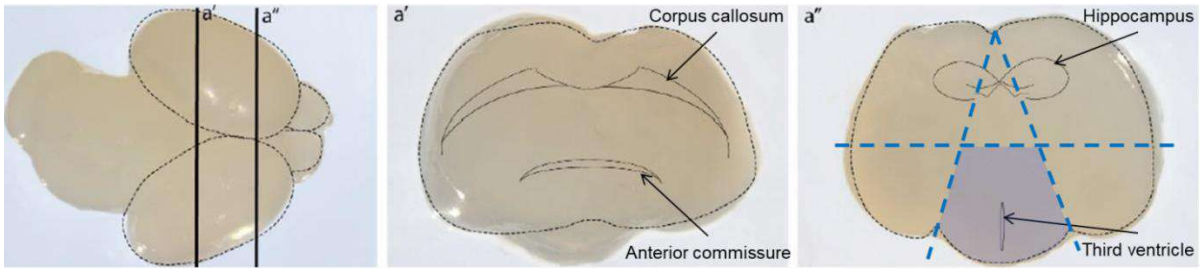

Figure 23.- Hypothalamic dissection from P0 mouse brain. Solid black lines represent the anatomical reference to separate the brain and obtain the hypothalamus. Dotted black lines serve as references to visualize the anatomical structures to dissect the hypothalamus. **a')** Caudal view of the brain regions exposed after the first incision to locate the end of the hypothalamus. **a'')** Coronal view of the regions visible upon the second incision. Dotted blue lines indicate the cutting zones to isolate the hypothalamus. Blue shaded area represents the dissected hypothalamus. Adapted from Viudes, 2021 (TFM alumni).

Dissected hypothalami were transferred to a falcon tube (15 or 50 mL), and were incubated in digestion solution during 18 min at 37 ºC, to break cell unions and disintegrate the tissue. Digestion solution contained Recombinant DNase I (10 U/uL, Sigma Aldrich, Ref: 04716728001), $MgCl_2$ 20 nM (Sigma Aldrich, Ref: M2670), $CaCl_2$ 20 nM (Merk, Ref: 102378), papain (Sigma Aldrich, Ref: P3125), and EBSS 1X (Gibco, Ref: 14155-063). After incubation, hypothalami were disaggregated mechanically pipetting through a P1000 pipette. Then, tissue was centrifuged (Eppendorf Centrifuge 5810) 5 min, 200 rpm. Supernatant was discarded and the pellet was resuspended in a solution containing EBSS 1X, trypsin inhibitor type III Ovomucoid (Sigma Aldrich, Ref: T2011) and DNAse I. Cells were then transferred to a density gradient made of trypsin inhibitor type III Ovomucoid, carefully placed with a P1000 pipette. Cells were centrifuged 5 min at 1000 rpm. Supernatant was discarded and cells were resuspended in culture medium. Culture medium was composed of Neurobasal culture medium 1X (NB, Fisher, Ref: 21103-049) supplemented with B27 1X (Thermo Fisher, Ref: 17504-044, Stock 50X), Penicilin/Streptomycin (10.000 U/mL, Thermo Fisher, Ref: 15140122), L-Glutamine (2X, Thermo Fisher, Ref: 11500626, Stock 200 mM), and D-(+)-Glucose solution (45 % in H_2O, Sigma Aldrich, Ref: G8769). Then, 10 uL of cells were mixed

with 10 uL of trypan blue solution (Sigma Aldrich, Ref: T8154) to estimate the cell number in a Neubauer chamber. Cells were plated and placed in a cell incubator at 37 ºC, 5 % CO_2. After 1 h, culture medium was added to each well. Half of the culture medium was refreshed each 2/3 days.

Cell density (nº cells/well) plated depended on the purpose of the experiment (Table 4).

Table 4.- Density of cultured neurons for each experiment.

Experiment	Number of cells per well	Coverslip diameter (mm)
Immunocytochemistry	$15x10^4$	12
Cytotoxicity assay	$12.5x10^4$	24
Vesicle dynamics	$12.5x10^4$	24
Chasing	$15x10^4$	24
Viral infection + Chasing	$20x10^4$	24

3.3.- Endogenous OT expression in hypothalamic primary cultured neurons

As in the case of hypothalamic slices (Fig. 20C), we amplified endogenous signal of oxytocinergic neurons from OT^{tdTom} and OT^{EYFP} mice with anti-RFP and anti-GFP antibodies, respectively (Fig. 24A, B, and Table 5). In cell culture, the RFP fluorescent signal was not as bright as the GFP signal. However, we identified a similar number of oxytocinergic neurons in both OT^{tdTom} and OT^{EYFP} mice (Fig. 24C). Furthermore, RFP and GFP antibodies stained an equivalent number of oxytocinergic cells as identified by a specific anti-OT antibody (Fig. 24D). Number of OT cells was normalized with respect the total cell number in the culture plate. Data were statistically analyzed with GraphPad Prism 8. Results are shown as mean ± SEM.

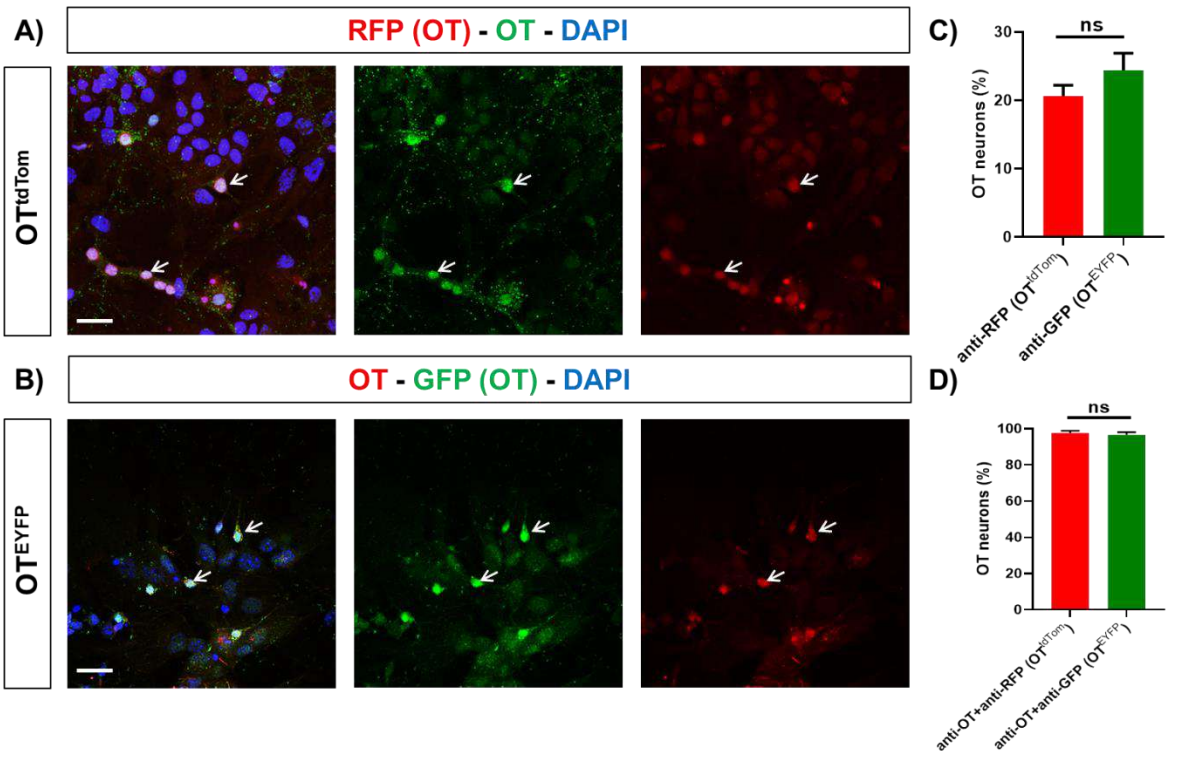

Figure 24.- Identification of oxytocinergic cultured neurons employing OT^{tdTom} and OT^{EYFP} transgenic mice. **A)** Expression of endogenous signal from OT^{tdTom} was amplified with anti-RFP (red); OT neurons were also stained with and anti-OT antibody (green). **B)** Expression of endogenous signal from OT^{EYFP} was amplified with anti-GFP (green); OT neurons were also stained with and anti-OT antibody (red). Arrows indicate OT neurons stained with anti-RFP/anti-GFP and anti-OT antibodies. Scale bar indicates 50 µm. **C)** The number of identified OT neurons was similar between OT^{tdTom} and OT^{EYFP} mice strains (anti-RFP (OT^{tdTom}): 20.6 %; anti-GFP (OT^{EYFP}): 24.39 %). **D)** Oxytocinergic neurons identified either with anti-RFP or anti-GFP antibodies coexpressed with OT neurons identified with an anti-OT antibody (anti-OT+anti-RFP (OT^{tdTom}): 97.7 %; anti-OT+anti-GFP (OT^{EYFP}): 96.6 %). Adapted from Caro, 2020 (TFM alumni). Statistical analysis: Mann-Whitney non-parametric test; p-value> 0.05 (ns), ≤ 0.05 (*), ≤ 0.01 (**), ≤ 0.001 (***), ≤ 0.0001 (****). Appendix, tables 1 and 2.

4.- Primary culture viral infection

Hypothalamic primary cultures from OT^{tdTom} P0 mice were infected at 7 day *in vitro* (DIV) with an adeno-associated virus (AAV) AAV-OT-SNAP-47-KD-GFP (SNAP-47-KD from now on, Fig. 25A).

A specific shRNAs designed to target the untranslated (UTR) region of mouse SNAP-47 (shRNAs: SNAP-47: ATAGCAATAGAATCAGCAGAGC) was subcloned into an AAV2 viral backbone containing GFP as a reporter employing an EcoRI restriction site. The effectiveness of the shRNA was determined using RT-PCR standard procedures described

in Jurado et al., (2013). Viral particles were generated at the Viral Core Facilities at the University of Barcelona. Briefly, HEK293 cells were transfected using the calcium phosphate method. Culture media was collected 40-44 h after transfection and filtered with 0.45 µm PVDF filter (Millipore) to remove cellular debris followed by centrifugation at 50,000 x g to concentrate the viral particles ($4.6x10^{12}$ viral genomes per mL (vg/mL). Concentrated virus was dissolved in a small volume of medium, aliquoted and stored frozen at -80 °C.

Before infecting the cells, half of the culture medium was replaced for fresh medium. Virus (0.5 µL/well from stock) was added to 2 mL of culture medium (virus final concentration was $1.15x10^{9}$). Infected neurons were identified 4 days post-infection by green fluorescence signal (Fig. 25B). Chasing experiments were performed 4 days post-infection, as described in the "*Chasing experiments*" section. As control for chasing experiments, we employed uninfected wells.

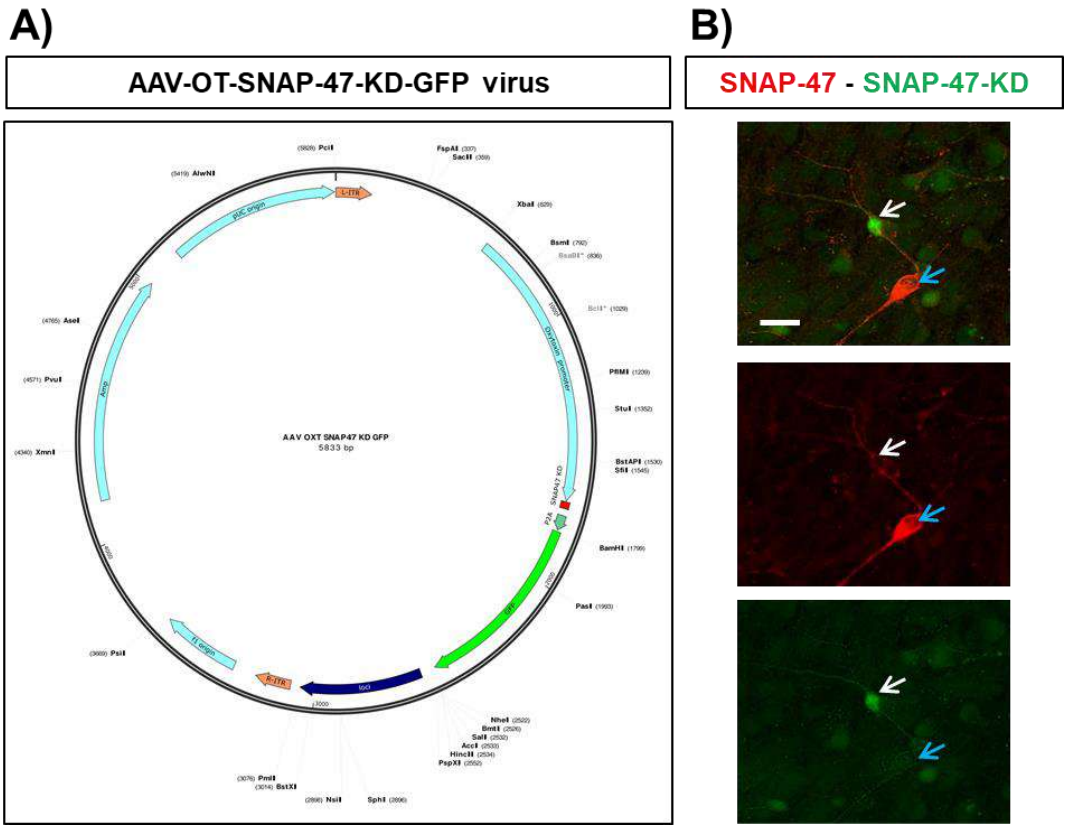

Figure 25.- AAV-OT-SNAP-47-KD-GFP virus. **A)** Map of the AAV-OT-SNAP-47-KD-GFP virus employed in this thesis. **B)** Hypothalamic primary culture 4 days post-infection with SNAP-47-KD virus. Infected neurons present green fluorescence (as virus construct includes GFP as reporter gene for infection), and no SNAP-47 signal (white arrows). Not infected neurons present SNAP-47 signal (blue arrows, anti-SNAP-47 staining, Table 5). Adapted from Caro, 2020 (TFM alumni). Scale bar indicates 30 µm.

5.- Immunochemistry

5.1.- Hypothalamic slices for immunohistochemistry

Immunochemistry was performed in either hypothalamic primary cultured neurons or hypothalamic brain slices (mouse strain, sex and age depended on the experiment, see Table 3).

For immunohistochemistry, animals were anesthetized with isofluorane (Isoflutek 1000 mg/g, Laboratorios Karizoo S.A.) and were transcardially perfused with paraformaldehyde (PFA) 4 % (Sigma Aldrich, Ref. 441244). Brains were dissected and maintained in PFA 4 % overnight (ON) at 4 ºC. Then, brains were washed x3 with PBS 1X, embedded in agarose 4 % (Lonza, Ref: 50100), and sliced in a vibratome at 50 µm thickness.

5.2.- Immunohisto- and -cytochemistry

Samples were fixed or perfused with PFA 4 % (primary cultures were fixed and hypothalamic slices were obtained from perfused mice), rinsed in PBS 1X during 10 min x3, and incubated in blocking solution during 1 h 30 min at RT. Cell blocking solution was composed by PBS azide 0.5 % (Sodium Azide 99.5 %, Sigma Aldrich, Ref: S2002), 0.1 % Triton X-100 (Sigma Aldrich, Ref: X-100), and 2 % Normal Goat Serum (Sigma Aldrich, Ref: G9023); tissue blocking solution was composed by PBS azide 0.5 %, 0.3 % Triton X-100, and 2 % Normal Goat Serum. After that, samples were incubated ON at 4 ºC with primary antibodies prepared in blocking solution. Samples were incubated with antibodies against OT, SNARE and synaptotagmin proteins: SNAP-25, SNAP-23, SNAP-47, Synaptotagmin-4 (Syt-4), Synaptotagmin-1 (Syt-1), Synaptotagmin-7 (Syt-7), Synaptobrevin-1, 2, 3, Syntaxin-1 (Stx-1), Stx-3 and Stx-4 (Table 5). RFP and GFP antibodies were used to amplify endogenous signal of oxytocinergic neurons from OT^{tdTom} and OT^{EYFP} mice, respectively (Table 5). Golgin-GM-130 antibody was used to detect Golgi apparatus, and α-tubulin antibody for axonal detection (Table 5).

Samples were rinsed with PBS 1X during 10 min x3, and incubated with Alexa secondary antibodies (Table 6) prepared in blocking solution during 2 h at RT.

Samples were rinsed with PBS 1X during 10 min x3 and incubated with DAPI (Sigma Aldrich, Ref: D9542) during 5 min (cells) or 10 min (brain slices). Finally, samples were mounted in coverslips employing Mowiol-Dabco-Glycerol (Mowiol: Merk, Ref: 475904; Dabco: Sigma Aldrich, Ref: 10981; Glycerol: Sigma Aldrich, Ref: G5516).

Table 5.- Primary antibodies used in this thesis.

Primary antibody	Host	Supplier	Dilution cells; tissue	Reference	Observations
SNAP-25	mouse	Synaptic Systems	1.500; 1:100	111-011	
SNAP-23	rabbit	Synaptic Systems	1:100; 1:100	111-202	
SNAP-47	rabbit	Synaptic Systems	1:100; 1:100	111-403	
Synaptotagmin-4 (Syt-4)	rabbit	Synaptic Systems	1:100; 1:200	105-143	
Synaptotagmin-1 (Syt-1)	mouse	Synaptic Systems	1:100; 1:100	105-011	
Synaptobrevin-1,2,3 (Syb-1,2,3)	mouse	Synaptic Systems	1:500; 1:50	104-011	
Syntaxin-1 (Stx-1)	mouse	Synaptic Systems	1:100; 1:100	110-011	
Oxytocin (OT)	rabbit	Millipore	1:800; 1:800	Ab911	
Oxytocin (OT)	mouse	NIH (Dr. Gainer)	1:300; 1:800		Does not work in culture
GFP	chicken	Aves Lab	1:1000; 1:1000	GFP-1020	
RFP	rat	Chromotek	-;1:1000	5f8-100	Does not work in culture
Golgin-GM-130	mouse	BD-Biosciences	1:1000; no used	610822	
α-Tubulin	mouse	Abcam	1:5000;1:5000	Ab7291	

Table 6.- Alexa secondary antibodies used in this thesis.

Secondary antibody	Host	Supplier	Dilution cells; tissue	Reference
Anti-mouse Alexa 488	goat	Invitrogen	1:500	A32723
Anti-mouse Alexa 594	goat	Invitrogen	1:500	A11032
Anti-rabbit Alexa 488	goat	Invitrogen	1:500	A11034
Anti-rabbit Alexa 594	goat	Invitrogen	1:500	A11072
Anti-rabbit Alexa 647	donkey	Jackson ImmunoResearch	1:500	711-605-152
Anti-chicken Alexa 488	goat	Invitrogen	1:500	A11039
Anti-rat Alexa 594	donkey	Jackson ImmunoResearch	1:500	712-585-153

5.3.- Image acquisition

Images were acquired with a Leica SPEII confocal microscope (Leica Microsystems), LAS X software, 405 nm, 488 nm, 561 nm, and 635 nm diode lasers, using oil immersion objectives 20X (0.6 ACS APO IMM CORR), 40X (1.15 ACS APO CS), and 63X (1.40 HCX PL APO CS).

5.4.- Golgin GM-130 immunocytochemistry: image acquisition and analysis

Anti-OT and anti-Golgin GM-130 antibodies (Table 5) were employed to stain OT and the Golgi apparatus, respectively, in hypothalamic primary cultured neurons from BL6/C57 P0 mice at 14 DIV. Identification of individual OT vesicles was challenging due to the inherent limitations of confocal microscopy. Given these limitations, as much as possible we have avoided the term OT vesicles and used OT-containing compartments, OT-membrane patches or OT-containing vesicles instead to refer to these subcellular structures.

Images were acquired with a confocal laser system Olympus Fluoview FV300 (Olympus Corp., Tokio, Japan), mounted in an inverted IX71 microscope, with a 100X oil immersion objective (A.N = 1.45), and the FluoView 5.0 software. Each image was composed of several z stacks in order to acquire the entire structure of Golgi apparatus. For image analysis we employed the free image analysis software Fiji (ImageJ 1.48v, National Institutes of Health, USA) and, specifically the "UCSD Control" (Kelly and Karten, 2000) and JACoP plugins (Bolte & Cordelières, 2006). Data were statistically analyzed with GraphPad Prism 8. Results are shown as mean ± SEM; colocalization parameters are shown as percentage.

<u>Image analysis protocol for Golgi images:</u>

1.- Images were opened with the "UCSD Control" plugin in Fiji software. An image was separated into the different planes that composed it. Each z stack was checked for the Golgi channel. Stacks in which the Golgi apparatus was present were selected for the analysis.

2.- A 3D projection of the image was made with the selected stacks. OT-containing compartments from the 3D projection were drawn and saved in the ROI manager.

3.- OT-containing compartments (green channel) in each stack from the 3D projection were analyzed for colocalization with Golgi (red channel) employing the JACoP plugin, and threshold was set automatically. Colocalization parameters were obtained for individual OT-compartments from each z stack.

<u>Colocalization analysis between OT-compartments and Golgi</u>

Colocalization analysis renders two parameters: Manders' coefficient and Pearson's coefficient.

Manders' coefficient refers to the overlapping degree of pixels from two channels. In our case, that means the overlapping between an OT-containing compartment staining and Golgi staining. Manders' overlapping coefficient values range from 0 (no overlapping) to +1 (total overlapping) (Fig. 26B). Two Manders' coefficients are obtained: Manders_A refers to

channel 1 (red) overlapping with channel 2 (green); and Manders_B refers to channel 2 (green) overlapping with channel 1 (red). In our case, since the Golgi apparatus was bigger than OT-containing compartments (Fig. 26D), we just reported Manders_B values (Manders' overlapping coefficient from now on), since Manders_A always indicated an artificial 100 % overlap. That is, the overlapping of the OT-containing compartment (channel 2, green, the smaller structure) with the Golgi channel (channel 1, red, the bigger structure).

Pearson's coefficient refers to the correlation degree of pixels from two channels. In our case, that means the correlation between an OT-containing compartment staining and Golgi staining. Pearson's correlation coefficient values range from -1 (perfect inverse correlation: objects do not touch), 0 (no correlation: objects are close but they are not in contact), and +1 (perfect correlation: both objects are entirely in contact) (Bolte & Cordelières, 2006; Labrador, 2014) (Fig. 26C).

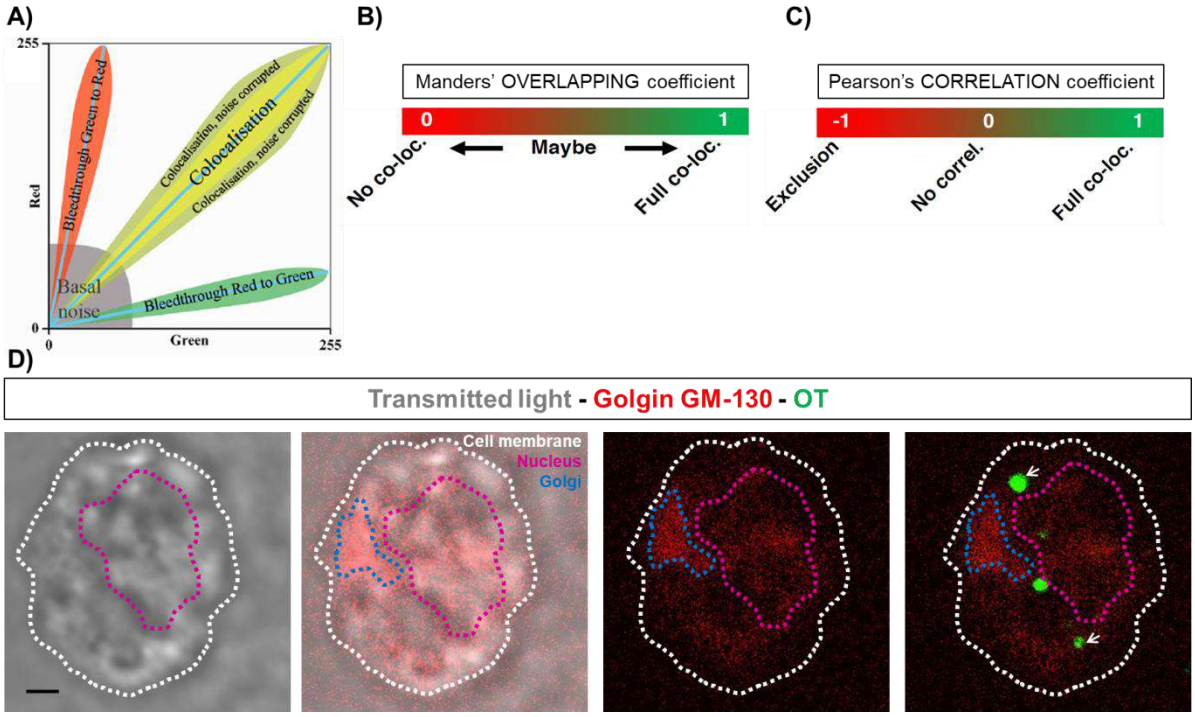

Figure 26.- Colocalization analysis between OT-containing compartments and the Golgi apparatus. **A)** Colocalization scatter plot of channel 1 (red) and channel 2 (green). Red shaded area indicates that green channel predominates over red channel; yellow shaded area indicates that both channels present the same intensity, which means colocalization; and green shaded area indicates that red channel predominates over green channel. Adapted from Meas-Yedid, 2017. **B)** Manders' overlapping coefficient indicates overlapping between two channels, and values range from 0 to +1. Adapted from Mascalchi & Cordelières, 2019. **C)** Pearson's correlation coefficient indicates correlation between two channels, and values range from -1 to +1. Adapted from Mascalchi & Cordelie, 2019. **D)** Hypothalamic cultured neuron stained with anti-OT and anti-Golgin GM-130 antibodies. OT-containing compartments are identified by green fluorescence (white arrows). Golgi is identified by red fluorescence (dotted blue line). Dotted white line indicates cell membrane, and dotted pink line indicates cell nucleus. Scale bar indicates 3 µm.

It is important to consider that despite both parameters inform about colocalization between pixels of two channels, Manders' and Pearson's coefficients present notable differences. Manders' overlapping coefficient compares the area of pixels between two channels, does not depend on the objects size, and it is independent of channels intensity; meanwhile Pearson's correlation coefficient compares channels pixel by pixel, and it requires that both objects present the same size. In our case, colocalization analysis was performed between OT-containing compartments and Golgi or OT-containing compartments and SNAP-47-containing compartments (colocalization analysis described in "*Colocalization analysis between OT- and SNAP-4-membrane patches*" section). Golgi and SNAP-47-containing compartments were commonly bigger than OT-containing compartments. So, we presented Manders' and Pearson's coefficients taking this into account. Considering the size differences, Manders' overlapping coefficient was considerable more reliable than Pearson's coefficient. Thus, we mostly rely on Manders_B referring to the overlap of OT-containing compartments with Golgi or SNAP-47 patches.

We generated a random data set as an additional control for the colocalization analysis. To generate the random data set we employed the "UCSD Control" and JACoP plugins in Fiji (ImageJ 1.48v, National Institutes of Health, USA). The random data set was generated from the experimental stack that presented the highest Manders' overlapping value for each OT-containing compartment. The Golgi channel was maintained and random OT-containing compartments were generated manually over it. Random OT-containing compartments were generated choosing an experimental compartment closest to the mean compartments' size, and placing it at random x, y positions in the cell soma (excluding the nucleus and extracellular locations). We placed as many random OT-containing compartments as experimental OT-containing compartments were observed in each cell. The final random image (control) was generated overlapping the image containing the randomly generated OT-containing compartments with the experimental Golgi image (Fig. 27). Colocalization analysis was performed in these images in the same manner as in the case of experimental data.

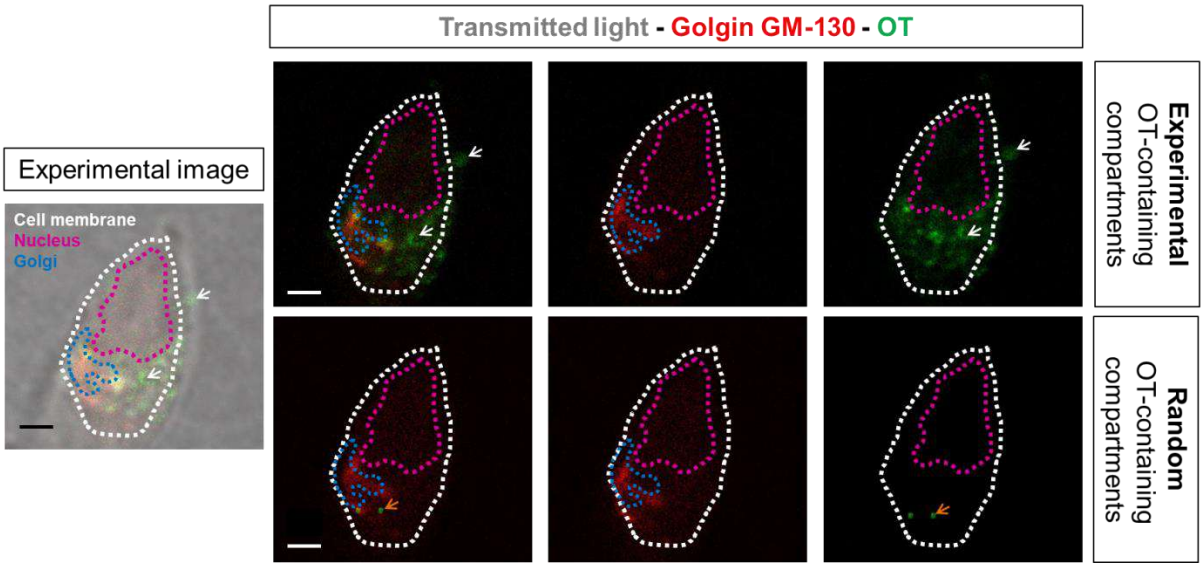

Figure 27.- Experimental (top) and random (bottom) images employed for colocalization analysis between OT-containing compartments and Golgi apparatus. To generate random images, OT-containing compartments were generated manually over the experimental Golgi

channel. OT-containing compartments are identified by green fluorescence; Golgi is identified by red fluorescence (dotted blue line). Experimental OT-compartments are indicated by white arrows, and random OT-compartments are indicated by orange arrows. Dotted white line indicates cell membrane, and dotted pink line indicates cell nucleus. Scale bar indicates 3 µm.

As we worked with fluorescent images, presented data is an approximation in pixels, due to the light scattering intrinsic to fluorescence techniques. To note, the resolution limit of our microscope was estimated around 100 nm, making impossible to resolve images beyond that limit.

6.- Cytotoxicity

6.1.- Cytotoxicity experiment

Citotoxicity experiments were performed in 12 DIV hypothalamic primary cultured neurons obtained from OT^{tdTom} P0 mice. The objective was to test the potential toxicity of the stimulation protocols elicited by high KCl (50 or 100 mM KCl Tyrode's solution). To do so, we implemented the "LIVE/DEAD® Cell Imaging Kit" (Thermo Fisher, Ref: R37601). "LIVE/DEAD® Cell Imaging Kit" contains a non-fluorescent green cell-permeant molecule (calcein AM) that becomes fluorescent when it is enzymatically processed by esterases, and a red cell-impermeable molecule only visible in dying or death cells, whose nucleus integrity is compromised.

Cells were incubated during 1 or 10 min, 37 ºC in Tyrode's basal solution, EtOH 70 %, 50 mM KCl Tyrode's solution (composition in mM: 77 NaCl; 50 KCl; 30 glucose; 25 HEPES; 2 $CaCl_2$; 2 $MgCl_2$; pH 7.4) or 100 mM KCl Tyrode's solution. "LIVE/DEAD® Cell Imaging Kit" 2X was added to each well and cells were incubated during 15 min at 20-25 ºC. After that, cells were fixed with PFA 4 % during 10 min, were rinsed with PBS 1X during 10 min x3, incubated with DAPI during 6 min, rinsed with PBS 1X during 10 min x3, and mounted in coverslips with Mowiol-Dabco-Glycerol.

6.2.- Image acquisition and analysis

We acquired 5 images/condition from at least two different primary cultures with a Leica SPEII confocal microscope, LAS X software, 405 nm, 488 nm, 561 nm, and 635 nm diode lasers, using oil immersion objective 20X (0.6 ACS APO IMM CORR).

Image analysis consisted of the quantification of live (green) and death (red) cells employing the open image analysis software Fiji (version 1.52t, National Institute of Health, USA) and normalizing them based on the DAPI staining. Data were statistically analyzed with GraphPad Prism 8. Results are shown as mean ± SEM.

6.3.- Neuronal stimulation with high KCl does not affect cell viability

Results indicated that across conditions, except for the EtOH 70 % treatment, cell viability was not significantly affected by KCl solution (Fig. 28). From these experiments, we concluded that the application of either 50 mM or 100 mM KCl does not significantly affect cell health, thus, providing a viable stimulation protocol for our experimental setup majorly based on cultured neurons.

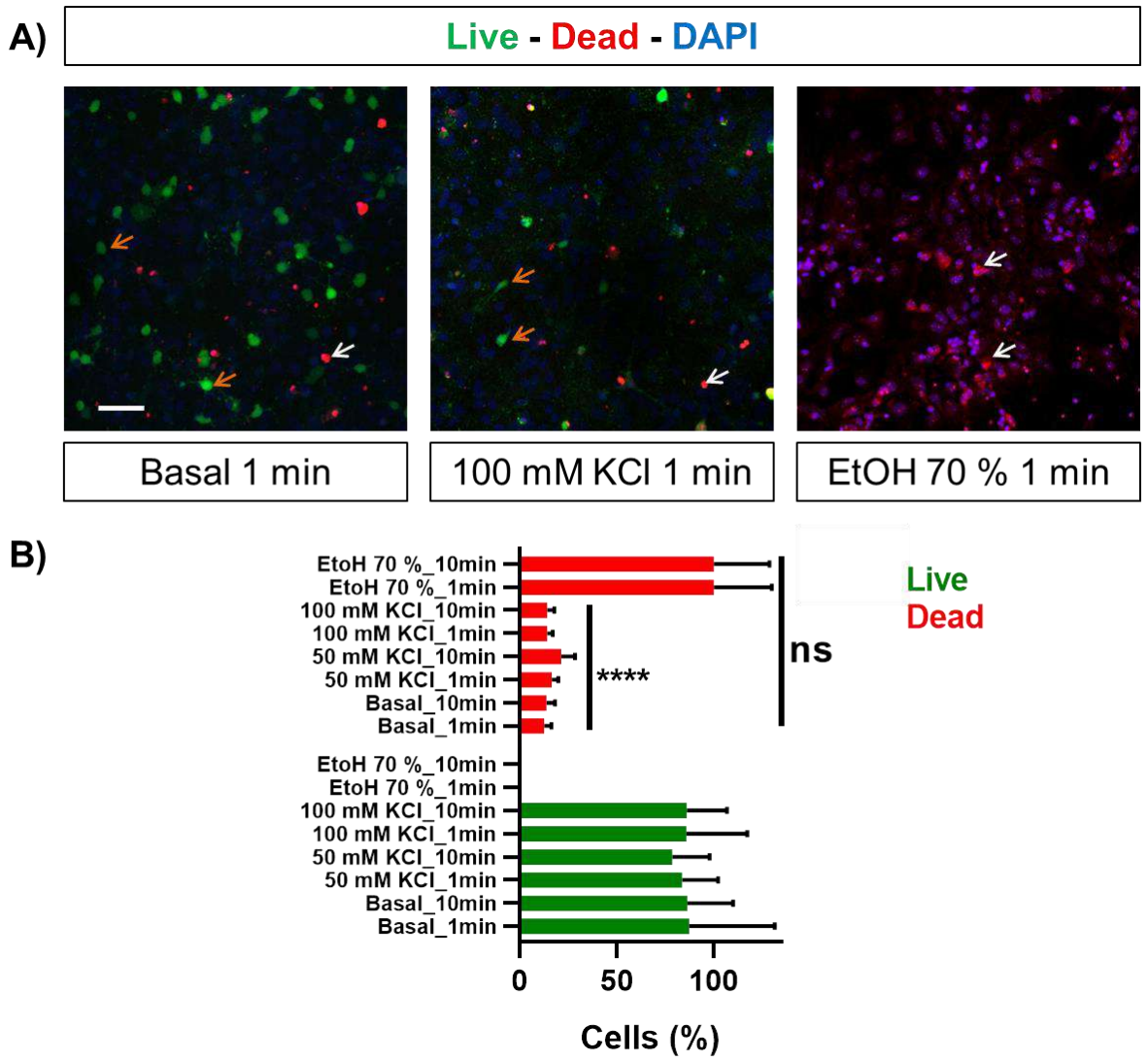

Figure 28.- Cytotoxicity assay in hypothalamic primary cultured neurons**. A)** Example pictures of hypothalamic primary cultured neurons incubated with basal, 100 mM KCl, and EtOH 70 % solutions during 1 min. After treatment with different media and incubation with "LIVE/DEAD® Cell Imaging Kit", live cells were stained in green (orange arrows), and dead cells were stained in red (white arrows). Scale bar indicates 50 µm. **B)** Quantification of live and dead cells from hypothalamic primary cultures after different treatment conditions and incubation times indicated that the number of dead cells was significantly lower in all assayed conditions, except for EtOH 70 % medium. Statistical analysis: Mann-Whitney non-parametric test was employed for comparisons between same incubation conditions; Kruskal-Wallis non-parametric test was employed for multiple comparisons between different

incubation times; p-value> 0.05 (ns), ≤ 0.05 (*), ≤ 0.01 (**), ≤ 0.001 (***), ≤ 0.0001 (****). Appendix, tables 3-6.

Our results are consistent with previous work that used stimulation solutions based on high KCl as an effective and safe stimulus to induce DCVs' exocytosis in *in vitro* models (Vardjan et al., 2007). Furthermore, DCVs in neurons, including OT-containing DCVs (Pow & Morris, 1989), have been shown to require robust and sustained stimulation protocols, conditions that are efficiently achieved with high KCl concentrations (Castel et al., 1996; Xia et al., 2009; Persoon et al., 2018).

7.- OT vesicle dynamics

7.1.- Image acquisition

We employed 7-14 DIV hypothalamic primary cultured neurons from OT^{tdTom} P0 mice obtained as described in the "*Primary culture of hypothalamic neurons"* section. Image experiments were performed with a confocal laser system Olympus Fluoview FV300, mounted in an inverted IX71 microscope, with a 100X oil immersion objective (A.N = 1.45). FluoView 5.0 software was used to monitor the experiments. A perfusion system was coupled to the microscope to apply different media to the cells. The experimental routine consisted of the identification of an oxytocinergic cell (recognized by the endogenous red fluorescent signal, Fig. 29) and focusing on the soma. Data was collected during the perfusion with Tyrode's basal medium during 10 s, followed by stimulation with 100 mM KCl (Stimulation) during 60 s, and a final application of Tyrode's basal solution during 10 s. Solutions were tempered at 37 ºC before application. Imaging recordings consisted of a continuous time lapse of each individual cell acquired at 1 Hz during 80 s. Although endogenous OT fluorescence signal from OT^{tdTom} neurons was clearly visible, identification of individual OT-containing compartments was challenging due to the inherent limitations of confocal microscopy.

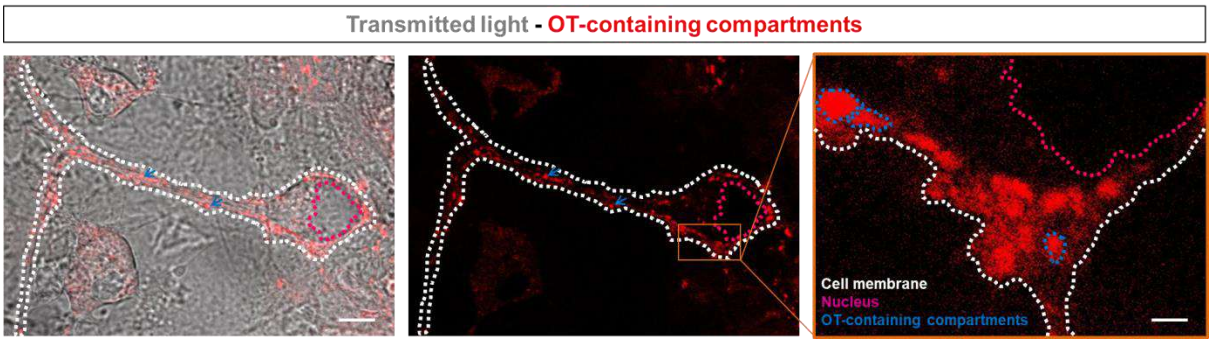

Figure 29.- Oxytocinergic primary cultured neuron from OT^{tdTom} mouse. OT-containing compartments are identified by endogenous fluorescence from reporter tdTomato (red). Dotted blue line delineates a few OT-containing compartments (also indicated by blue arrows), dotted white line indicates cell membrane, and dotted pink line indicates cell nucleus. Scale bars indicate 7.9 µm (left and middle images) and 3 µm (right image).

7.2.- Image analysis

Time lapse experiments were analyzed semiautomatically employing the image analysis software Imaris (Imaris x64 9.3.1, Oxford instruments). Images were filtered employing Gaussian and background subtraction filters to enhance OT-containing compartments' detection by the software. We focused our analysis in the somatic OT-compartments, which were segmented with the "Spots" tool. Then, we tracked OT-compartments' movement selecting "Brownian movement" algorithm (used for randomly moving objects) as we did not know a priori the type of movement expected for OT-compartments in the soma (Fig. 30).

Figure 30.- OT-containing compartments were semiautomatically tracked with Imaris.

Analyzed parameters were: number of OT-containing compartments, OT-compartments' displacement length (μm), speed (μm/s), and Mean Square Displacement (MSD, μm^2). Displacement length refers to the displacement of a spot (in our case, an OT-compartment) from its origin over time. MSD refers to the area explored by a spot (in our case, an OT-compartment) over time, which is related to its migration efficiency.

MSD analysis of each OT-containing compartment was obtained by performing a linear regression analysis. The particle fits to the linear equation if its R^2 is above 0.6 (a perfect fit is considered $R^2 > 0.9$). The slope of the diffusion equation indicates whether the particle follows a diffusive movement (slope value greater than two decimal places: 0.00X, indicates significant diffusive movement) or not (slope value greater than three decimal places: 0.000X, indicates not significant diffusion). The diffusion coefficient (D) was calculated following the linear equation (y= slope*x), in which the slope is proportional to the diffusion, as follows:

$y = slope * x$

$d^2 = 4D * t$

$d^2 = value * t$

$4D = value$

$D = value/4$.

These parameters were statistically analyzed with GraphPad Prism 8. Results are shown as mean ± SEM.

7.3.- Mathematical model

In order to further characterize the OT-containing compartments' dynamics, we implemented a mathematical model based on a prototypical hypothalamic neuron containing OT vesicles distributed throughout the cell. The model was designed in collaboration with Prof. Amparo Gil, from the Department of Applied Mathematics and Computer Science, at the University of Cantabria.

Our working model assumes almost spherical cells, in which a regular cone can be inferred as a model domain (Fig. 31A). In this model, a cone that reaches the center of the soma can be considered as a representative portion of the entire cell, in turn formed by a set of cones. This segmentation is performed to improve computational efficiency, as analyzing the entire cell would be highly resource-intensive.

From measurements performed in hypothalamic cells in culture, we estimated a mean cell radius of 4 µm and a mean nucleus radius of 2.3 µm. For the base of the model cone, we used a radius of 1 µm. Fig. 31A depicts the conical domain used to perform the simulations in a prototypical hypothalamic neuron.

An orthogonal 3D regular grid maps the conical domain with a distance between grid points of Δl= 0.1 µm. Each point of the grid is associated with a cubic compartment of volume $(\Delta l)^3$. With the chosen cone height of 4 µm and excluding the nucleus region, which we have assigned 2.3 µm, this corresponds to a discretization of 17 slices along the height of the cone. These estimations are represented in Fig. 31B.

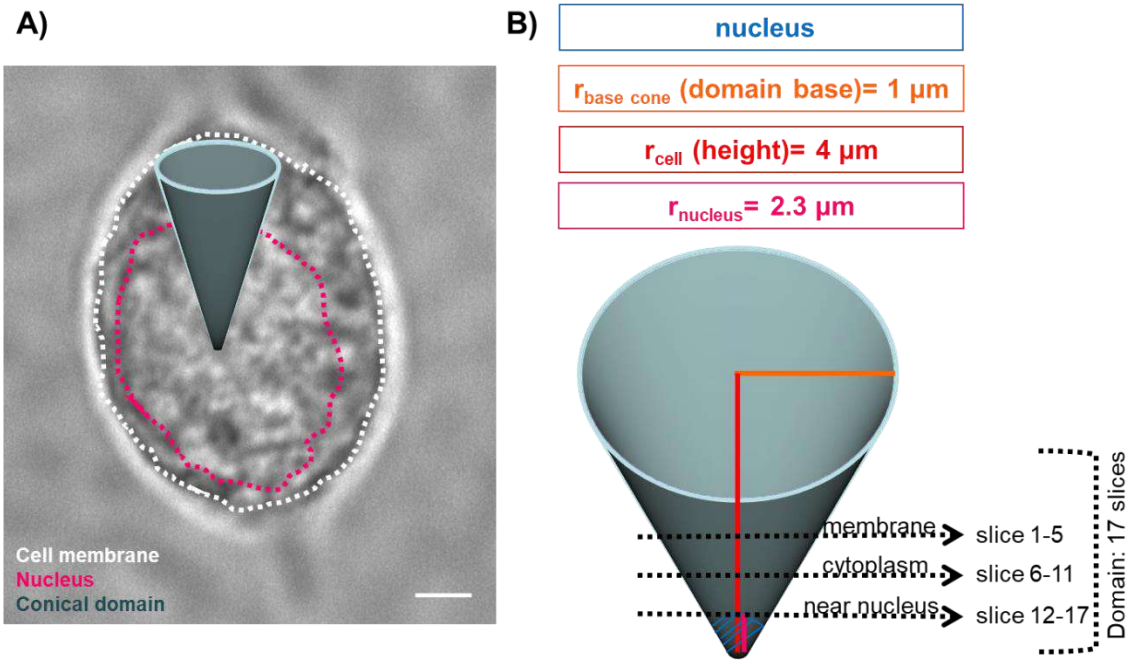

Figure 31.- Geometrical model. **A)** Prototypical hypothalamic neuron and conical domain superimposed representing a portion of the cell. Dotted white line indicates cell membrane, and dotted pink line indicates cell nucleus. Scale bar indicates 3 µm. **B)** Conical domain representing a portion of the cell. The cone is divided in 17 slices; 5/6 slices represent a portion of the cell.

In our model, vesicles move from one compartment to another compartment of the grid due to diffusion, which is modeled as a random displacement process. The time scale for the random displacement is given by the spatial resolution (0.1 μm) and the diffusion coefficient. The relation between those scales is given by: $\Delta t = (\Delta l)^2/(4D)$, being Δl the spatial resolution and D the diffusion coefficient. The time resolution Δt is the time step of the simulation: dots (vesicles) will be moved every time step Δt using a random walk algorithm in which each vesicle will have a 50 % chance to remain in its initial position and a 25% chance to move either in the positive or negative direction for each spatial dimension.

The conical domain (17 slices) was divided in three portions composed of 5/6 slices: membrane (slices from 1 to 5), cytoplasm (slices from 6 to 11), and near the nucleus (slices from 12 to 17) (Fig. 31B). In the simulations, OT vesicles were randomly distributed in each portion as starting point, and freely diffused through the cell during the simulation time, being the nucleus a forbidden zone. That is, OT vesicles could arrive near but not inside the nucleus.

Simulations consisted of 1 min of basal followed by 1 min of KCl for diffusive and non-diffusive compartments, indicated with the experimentally obtained diffusion coefficient, starting either near the nucleus, from the cytoplasm, or from the cell membrane. The number of diffusive and non-diffusive OT-compartments was selected according to the experimental data obtained (n= 11 diffusive compartments; n= 93 non-diffusive compartments). The model was configured to simulate compartments' movement throughout the cell, and not to or from the extracellular space.

As it was not possible to perform a simulation employing two different diffusion coefficients, we performed basal and stimulus simulations separately. Because of this, the starting position of compartments in basal and stimulus conditions are the same, despite under experimental conditions, compartments' dynamics were acquired through a time lapse. Thus, for statistical analysis, we considered t1_KCl as t0_KCl, to simulate the already exposed to basal conditions OT-compartments, which could be already mobilized from their starting point.

Statistical analysis was performed with GraphPad Prism 8. XY plots and scatter plots are the average of three simulations, and results are shown as mean ± SEM; dynamic plots are the representation of a model compartment, and were represented with MATLAB (R2017b, The MathWorks, Inc.).

8.- Chasing experiments

8.1.- Chasing experiment

We employed hypothalamic primary cultured neurons between 10-13 DIV obtained from either P0 OT^{tdTom} or OT^{EYFP} mice. Primary cultures were performed according to the "*Primary culture of hypothalamic neurons*" section.

To perform chasing experiments, cells were rinsed twice with tempered Tyrode's basal solution during 3 min in a shaker. Then, cells were incubated with Tyrode's basal solution, 100 mM KCl Tyrode's solution, chelated extracellular calcium Tyrode's basal solution or chelated extracellular calcium 100 mM KCl Tyrode's solution during 1 min or 10 min, 37 ºC. 0.5 mM EGTA was added to Tyrode's basal medium or 100 mM KCl Tyrode's medium to chelate extracellular calcium. Solutions were tempered at 37 ºC before its application to the cells.

After incubation, and in order to avoid endocytosis, multiwells were placed on ice and cells were rinsed once with 4 ºC calcium-free Tyrode's solution during 3 min in a shaker. Then, cells were incubated with primary antibodies prepared in 4 ºC calcium-free Tyrode's solution (Table 5. Primary antibodies: anti-OT rabbit, anti-SNAP-47 rabbit, and anti-GFP chicken). Multiwells were transferred to a humid chamber, and placed on ice inside a cold camera for incubation during 2 h in a shaker.

After primary antibody incubation, cells were rinsed twice with calcium-free Tyrode's solution at 4 ºC during 3 min in a shaker and were fixed with 4 ºC PFA 4 % during 10 min. Next, cells were incubated with Triton X-100 0.1 % (Sigma Aldrich, Ref. X-100) in 3.6 % formaldehyde 37 % (Sigma Aldrich, Ref. F1635) in PBS 1X during 10 min, with PBS 1X during 10 min, and with PBS 1X 1 % BSA (Sigma Aldrich, Ref. A7906) during 10 min at RT in a shaker. During these steps, multiwell plates were maintained in a humid chamber on ice.

Then, cells were incubated with Alexa secondary antibodies prepared in PBS 1X (Table 6. Secondary antibodies: anti-Rabbit Alexa 488, anti-Rabbit Alexa 594, and anti-chicken Alexa 488, depending on the experiment) during 2 h at RT in a shaker. Multiwell plates were placed into a humid chamber and protected from light during secondary antibody incubation. Finally, cells were rinsed x4 with PBS 1X during 10 min at RT in a shaker.

8.2.- Image acquisition

Images were acquired with a confocal laser system Olympus Fluoview FV300, mounted in an inverted IX71 microscope, with a 100X oil immersion objective (A.N = 1.45). FluoView 5.0 software was used to monitor the experiments. Image acquisition was made in the z plane, where the cell nucleus was clearly visible, corresponding approximately to the middle portion of the cell. As a consequence, acquired images presented a single z stack.

8.3.- Image analysis

Images were analyzed using the open image analysis software Fiji (versions 1.48v and 1.52t, National Institute of Health, USA), employing a custom made macro by the Instituto de Neurociencias imaging facility, and the image analysis software Imaris. We analyzed the number and area of OT- and SNAP-47-containing membrane patches, the distance between OT- and SNAP-47-membrane patches (from centroid to centroid), and the colocalization between them. Data were statistically analyzed with GraphPad Prism 8. Results are shown as mean ± SEM; colocalization parameters are shown as percentage.

8.4.- Colocalization analysis between OT- and SNAP-47-membrane patches

Colocalization analysis between OT- and SNAP-47-membrane patches was performed with the image analysis software Imaris. OT- and SNAP-47-membrane patches were found to show a high degree of colocalization (Fig. 32, top). Clearly separated patches were not considered for analysis (Fig. 32, bottom). To calculate the number of OT-patches colocalizing with SNAP-47, we considered the total OT-membrane patches in each cell as the 100 %.

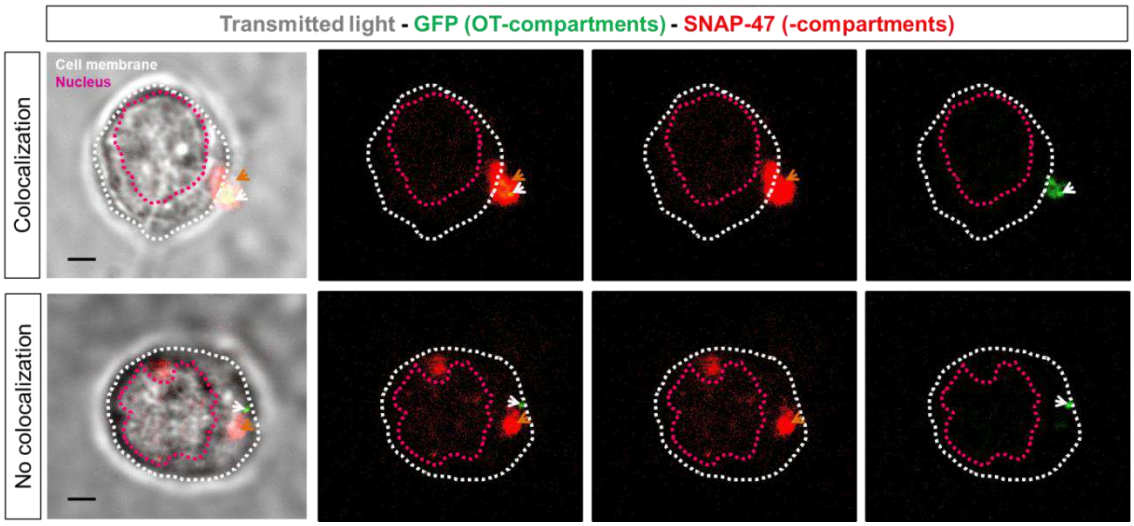

Figure 32.- Hypothalamic cultured neurons in which OT- and SNAP-47-compartments colocalize (top) and not colocalize (bottom). Clearly separated patches were not considered for analysis. OT-compartments were stained in green (white arrows), and SNAP-47-compartments were stained in red (orange arrows). Dotted white line indicates cell membrane, and dotted pink line indicates cell nucleus. Scale bar indicates 3 µm.

Green (OT-membrane patches) and red (SNAP-47-membrane patches) channels were segmented with Imaris “Surface” tool (Fig. 33: “Segmented channels”). Then, a mask was generated over each channel, to isolate the staining and to represent virtually the stained structure (Fig. 33: “Masked channels”). Colocalization analysis was performed onto the generated masks, selecting and establishing a threshold for each one, and generating a colocalization channel from which we obtained the colocalization results (Fig. 33: “Colocalization channel”).

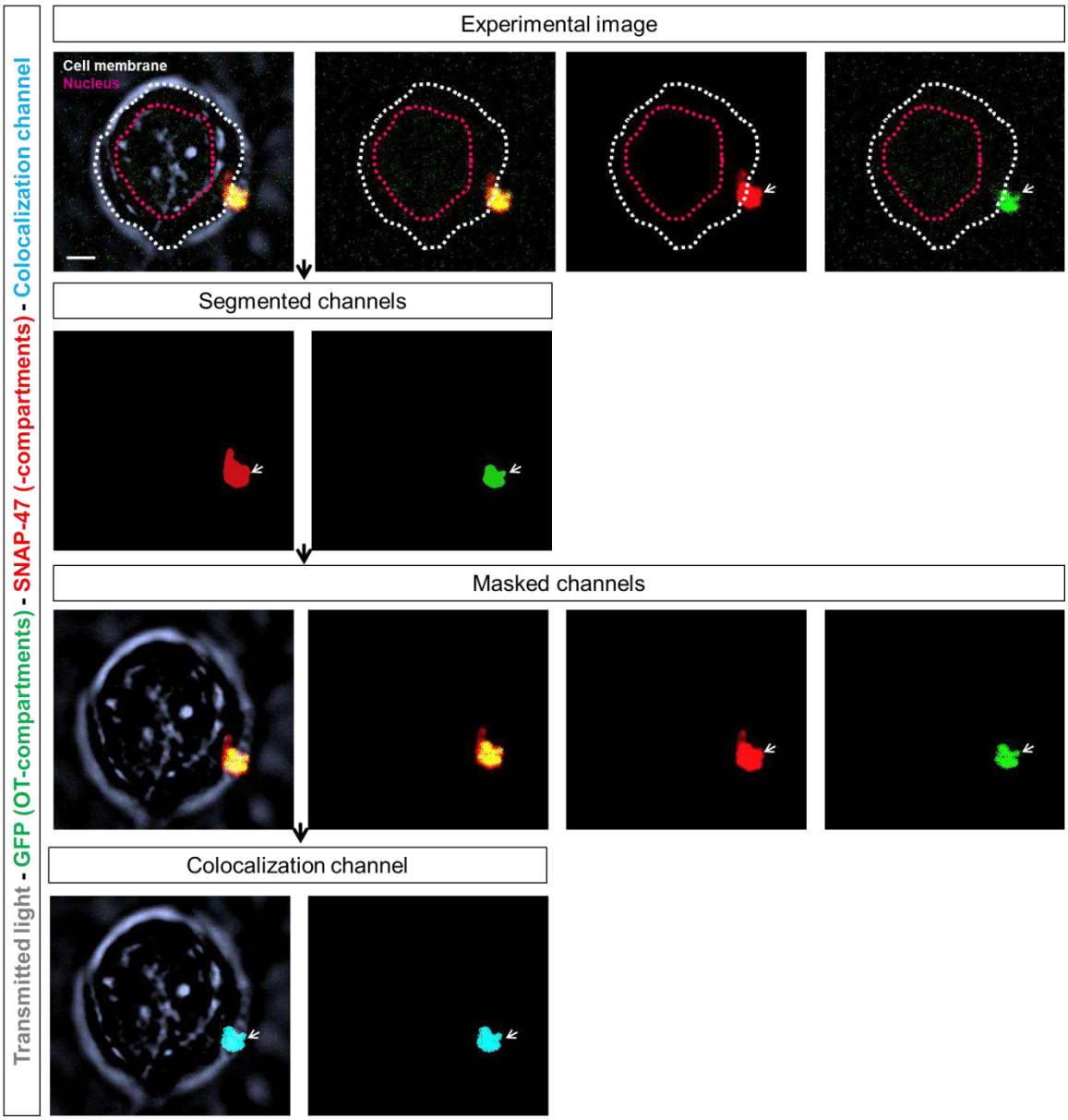

Figure 33.- Colocalization analysis between OT-membrane patches (green fluorescence) and SNAP-47-membrane patches (red fluorescence). Colocalization analysis was performed in Imaris. Green and red channels were segmented with Imaris "Surface" tool. Then, a mask was generated over each segmented channel, and colocalization analysis was performed onto the generated mask. A colocalization channel was generated, from which we obtained colocalization parameters. Experimental, segmented, masked and colocalization channels are indicated with white arrows. Dotted white line indicates cell membrane, and dotted pink line indicates cell nucleus. Scale bar indicates 4 μm.

Colocalization parameters (Manders' overlapping and Pearson's correlation coefficients) were obtained. In this case, Manders' coefficient indicates the overlapping between an OT-membrane patch and a SNAP-47-membrane patch; and Pearson's coefficient indicates the correlation between an OT-membrane patch and a SNAP-47-membrane patch. Similar to the colocalization analysis between OT-membrane patches and the Golgi apparatus, OT-membrane patches and SNAP-47-membrane patches differed in size, as SNAP-47-

membrane patches were bigger than OT-containing ones (Fig. 34B). So, we only reported the Manders' value corresponding to the overlapping of an OT-membrane patch (channel 2, green, smaller) with a SNAP-47-membrane patch (channel 1, red, bigger).

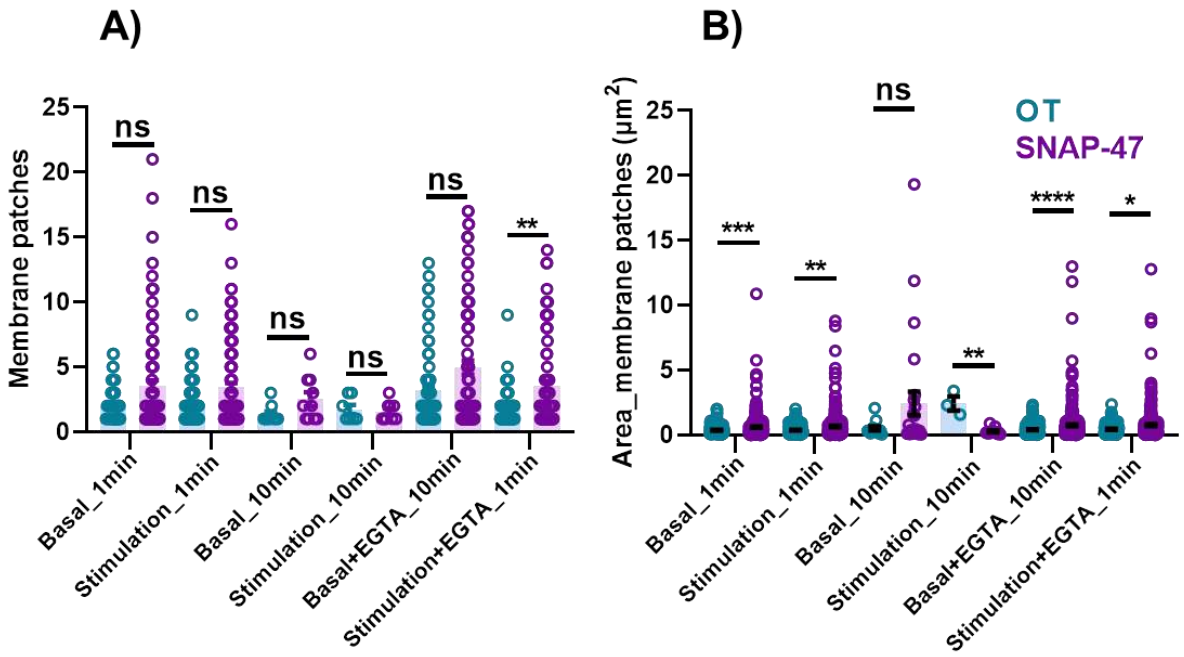

Figure 34.- Number and area of OT- and SNAP-47-membrane patches. **A)** Number of OT- and SNAP-47-membrane patches was similar across all analyzed conditions (Number of patches. Basal_1 min, OT: 1.96 ± 0.16 vs. SNAP-47: 3.56 ± 0.41, p-value= 0.1001; Stimulation_1 min, OT: 2.15 ± 0.18 vs. SNAP-47: 3.44 ± 0.33, p-value= 0.0558; Basal_10 min, OT: 1.33 ± 0.24 vs. SNAP-47: 2.50 ± 0.54, p-value= 0.0859; Stimulation_10 min, OT: 1.71 ± 0.36 vs. SNAP-47: 1.56 ± 0.24, p-value= 0.7944; Basal+EGTA_1 min, OT: 3.21 ± 0.36 vs. SNAP-47: 4.96 ± 0.56, p-value= 0.1426; Stimulation+EGTA_1 min, OT: 1.76 ± 0.16 vs. SNAP-47: 3.51 ± 0.40, p-value= 0.0032). **B)** SNAP-47-membrane patches were bigger than OT-membrane patches (Area in μm^2. Basal_1 min, OT: 0.35 ± 0.03 vs. SNAP-47: 0.59 ± 0.05, p-value= 0.0004; Stimulation_1 min, OT: 0.37 ± 0.03 vs. SNAP-47: 0.66 ± 0.06, p-value= 0.0024; Basal_10 min, OT: 0.50 ± 0.16 vs. SNAP-47: 2.43 ± 0.92, p-value= 0.6255; Stimulation_10 min, OT: 2.43 ± 0.53 vs. SNAP-47: 0.28 ± 0.07, p-value= 0044; Basal+EGTA_1 min, OT: 0.39 ± 0.02 vs. SNAP-47: 0.75 ± 0.06, p-value< 0.0001; Stimulation+EGTA_10 min, OT: 0.42 ± 0.04 vs. SNAP-47: 0.76 ± 0.08, p-value= 0.0163). Statistical analysis: Mann-Whitney non-parametric test; p-value> 0.05 (ns), ≤ 0.05 (*), ≤ 0.01 (**), ≤ 0.001 (***), ≤ 0.0001 (****). Appendix, tables 7-10.

It is also important to indicate that 48 data points were not considered for the statistical analysis because they presented negative Pearson values.

As control for colocalization analysis, we generated a random data set. Random data set was generated as in the "*Colocalization analysis between OT-compartments and Golgi*" section. In this case, SNAP-47 channel was maintained and random OT-membrane patches were generated manually over it. All SNAP-47 images were selected for generating the random data set, as each image was composed by a single stack. First, we measured the distance between OT- and SNAP-47-membrane patches from random images. As random distance values were extremely elevated in comparison with experimental distance values, it

was clear that length values obtained from the experimental data set were not random. Therefore, colocalization analysis was not performed for the random data set.

8.5.- Chasing experiments with OT^{tdTom} and OT^{EYFP} mice: identification of OT-membrane patches

As shown in Fig. 24 ("*Endogenous OT expression in hypothalamic primary cultured neurons*" section), the anti-RFP rat antibody did not work properly in culture. So, in chasing experiments, we employed an anti-OT rabbit antibody to identify OT-containing compartments in cultures from OT^{tdTom} mice. Since we were also interested in identifying SNAP-47-containing compartments, we employed OT^{EYFP} mice for dual quantifications, staining SNAP-47 with an anti-SNAP-47 rabbit antibody, and amplifying the signal from OT-containing compartments with an anti-GFP chicken antibody. In summary, we performed chasing experiments in hypothalamic primary cultures from OT^{tdTom} and OT^{EYFP} mice strains, identifying OT-containing molecules with anti-OT or anti-GFP antibodies (Table 5). We performed control chasing experiments to check whether we were capable of identifying the same number of OT-containing compartments in both mouse strains, since the antibodies were different (anti-OT in the case of OT^{tdTom}, and anti-GFP in the case of OT^{EYFP} mice). Data were statistically analyzed with GraphPad Prism 8. Results are shown as mean ± SEM; colocalization parameters are shown as percentage.

As shown in Fig. 35A and B, we did not find significant differences between the two approaches, since the number of OT-membrane patches obtained in both mouse strains was equivalent under basal and stimulus conditions (Fig. 35A. Number of OT-patches. OT^{tdTom}_Basal: 1.71 ± 0.15 vs. OT^{EYFP}_Basal: 2.4 ± 0.33, p-value= 0.1218; OT^{tdTom}_Stimulation: 2.76 ± 0.24 vs. OT^{EYFP}_Stimulation: 3.06 ± 0.32, p-value=0.7098).

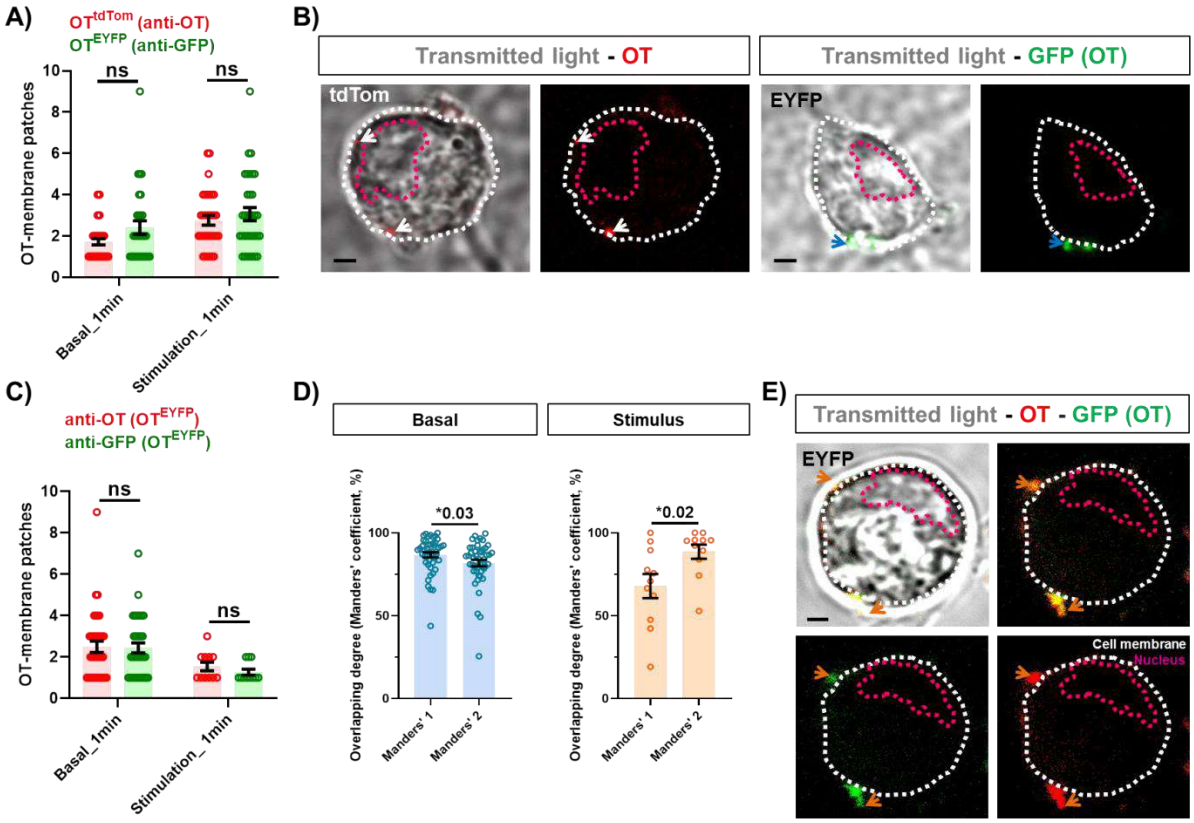

Figure 35.- Chasing experiments performed in cultured neurons from OT^{tdTom} and OT^{EYFP} mice. **A)** The number of OT-containing compartments identified with an anti-OT antibody in OT^{tdTom} mouse, and identified with an anti-GFP antibody in OT^{EYFP} mouse, under basal and stimulus conditions was similar (Number of OT-patches. OT^{tdTom}_Basal: 1.71 ± 0.15 vs. OT^{EYFP}_Basal: 2.4 ± 0.33, p-value= 0.1218; OT^{tdTom}_Stimulation: 2.76 ± 0.24 vs. OT^{EYFP}_Stimulation: 3.06 ± 0.32, p-value=0.7098). **B)** Hypothalamic primary cultured neurons from OT^{tdTom} and OT^{EYFP} mice. OT-containing compartments were identified with an anti-OT antibody in OT^{tdTom} mouse (red patches, white arrows); OT-containing compartments were identified with an anti-GFP antibody in OT^{EYFP} mouse (green patches, blue arrows). Dotted white line indicates cell membrane, and dotted pink line indicates cell nucleus. Scale bar indicates 3 µm. **C)** The number of OT-containing compartments identified with an anti-OT and an anti-GFP antibodies in OT^{EYFP} mice, under basal and stimulus conditions, was similar (Number of OT-patches. anti-OT_Basal: 2.5 ± 0.27 vs. anti-GFP_Basal: 2.44 ± 0.24, p-value= 0.9936; anti-OT_Stimulation: 1.54 ± 0.21 vs. anti-GFP_Stimulation: 1.27 ± 0.14, p-value= 0.4807). **D)** Colocalization analysis between OT-containing compartments identified with an anti-OT antibody or with an anti-GFP antibody indicated high level of overlapping between the two antibodies, either under basal or stimulus conditions (Basal, Manders' 1: 0.87 ± 0.02 vs. Manders' 2: 0.82 ± 0.02, p-value= 0.0270; Stimulation, Manders' 1: 0.68 ± 0.07 vs. Manders' 2: 0.89 ± 0.04, p-value= 0.0232). **E)** Hypothalamic primary cultured neuron from OT^{EYFP} mouse. OT-containing compartments were identified with an anti-OT (red patches, orange arrows), and anti-GFP (green patches, orange arrows) antibodies. Dotted white line indicates cell membrane, and dotted pink line indicates cell nucleus. Scale bar indicates 3 µm. Statistical analysis: Mann-Whitney non-parametric test; p-value> 0.05 (ns), ≤ 0.05 (*), ≤0.01 (**), ≤ 0.001 (***), ≤ 0.0001 (****). Appendix, tables 11-16.

Additionally, OT-membrane patches signal revealed by different antibodies (anti-OT and anti-GFP) in the same mouse strain (OT^{EYFP} mice) showed more than 80 % of overlapping under basal and stimulus conditions (Fig. 35C. Number of OT-patches. anti-OT_Basal: 2.5 ± 0.27 vs. anti-GFP_Basal: 2.44 ± 0.24, p-value= 0.9936; anti-OT_Stimulation: 1.54 ± 0.21 vs. anti-GFP_Stimulation: 1.27 ± 0.14, p-value= 0.4807. Fig. 35D. Manders' 1_Basal: 0.87 ± 0.02 vs. Manders' 2_Basal: 0.82 ± 0.02, p-value= 0.0270; Manders' 1_Stimulation: 0.68 ± 0.07 vs. Manders' 2_Stimulation: 0.89 ± 0.04, p-value= 0.0232).

We concluded that both mouse strains, combined with the use of these antibodies, could be employed to adapt the experimental conditions to our needs without compromising reliability.

9.- Stereotaxic injections

In vivo stereotaxic injections were performed in male and female OT^{tdTom} mice 1.5 months-old. AAV-OT-SNAP-47-KD-GFP virus (SNAP-47-KD, see "*Primary culture viral infection*" section) was injected bilaterally in the PVN with the objective of reducing endogenous SNAP-47 protein expression in this area. As control, we injected animals with an AAV-GFP virus.

9.1.- Injector preparation

Glass pipettes (3.5"" Drummond #3-000-203-G/X, Drummond Scientific Company, USA) were made in a puller (P-2000, Sutter Instrument Co., USA) with the following parameters: Heat-84, Fil-5, Vel-40, Del-115, and Pul-65 to obtain a fine and long tip to reach the PVN in the most effective and painless way for the animals. Glass pipettes were filled with mineral oil and inserted into the injector (Nanoliter 2010, World Precision Instruments). Next, we filled the glass pipette with either the SNAP-47-KD or the AAV-GFP virus (control).

9.2.- Preparing animals for the surgery

Animals were anesthetized with 4-5 % isoflurane (Isoflutek 1000 mg/g, Laboratorios Karizoo S.A). The isoflurane machine was connected to an isoflurane filter (gas filter canister, RWD) and to an oxygen concentrator at level 2 % (525 Oxygen concentrator, DeVilbiss Healthcare). When the animal was asleep, it was placed on an electric blanket (Temperature Control Unit HB 101/2, Panlab, Harvard apparatus) at 22-23 ºC in the stereotaxic table (Just for Mouse Stereotaxic Instrument, Ref: 51730, Stoelting). We applied ophthalmic gel in the mouse eyes to avoid possible wounds and ulcers because of the cold light (Leica KL 1500 LCD) used to visualize the skull. Then, we fixed the head of the animal in the stereotaxic frame to avoid movements and damage to the animal during the surgery. Next, we employed fine surgery grade scissors to cut the head skin and visualize Bregma and Lambda as reference sutures, and cleaned the uncovered area with physiological serum (FisioVet,

Braun). We employed a magnifying glass 1.6X (Carl Zeiss Meditec aG, Ref: 000000-1403-542, OPMI 1-FC, Zeiss) to identify Bregma and Lambda sutures and to perform the required alignments to locate the PVN (injection site). PVN coordinates from Bregma were: AP: -0.94; DV: 4.75; and ML: 0.25.

9.3.- Stereotaxic injection

Once the injection site was located, we drilled the head bone (Omni Drill 35, World Precision Instruments), cleaned the area with physiological serum and introduced the glass pipette into the brain at the PVN coordinates. We waited 5-10 min before injecting 150 nL of virus in 36.8 nL serial pulses. We waited additional 10-15 min before removing the pipette in order not to drag the virus from the tissue.

After the injection, the zone was cleaned with physiological serum and the wound was closed with cicastick (Chemical iberica). Then, betadine (10 % gel) and blastostimulin (Almirall, 1%) were applied, and 0.2 uL of buprex (Bupaq multidosis, Ritcher pharma, 0.3 mg/mL; 3 µL/g dose) was injected intraperitoneally.

The animal was placed in a recovery chamber (Vetario Intensive Care Unit) at 25 ºC until waking up. When the animal moved freely around the chamber it was returned to its home cage. Behavioral experiments and processing of the tissue were performed 3-4 weeks after injection. Animals were checked regularly to make sure the wound had healed and that their behavior was normal.

9.4.- Processing of injected hypothalamic brain slices

3-4 weeks post injection, brains were extracted from mice and hypothalamic brain slices (290 µm) were obtained and fixed in PFA 4 % ON. Then, immunohistochemistry was performed following the protocol explained in the "*Immunohisto- and cytochemistry*" section. We employed primary antibody anti-GFP chicken to stain infected neurons, anti-RFP rat to stain OT neurons, and anti-SNAP-47 rabbit to stain SNAP-47-containing neurons (Table 5).

Images of the PVN region were acquired with a Leica SPEII confocal microscope, LAS X software, 405 nm, 488 nm, 561 nm and 635 nm diode lasers, using objective 10X (0.3 ACS APO CS dry) and 63X (HCX PL APO CS). SNAP-47 fluorescence channel was deconvoluted with the image analysis software Huygens (Huygens Professional) to obtain better spatial resolution and to reduce out of focus. Then, images were processed with the image analysis software Imaris. The analyzed parameters were: number of OT neurons in the PVN, number of infected and uninfected OT neurons in the PVN, number of OT infected neurons with SNAP-47 staining, and florescence intensity of the SNAP-47 channel in the PVN from SNAP-47-KD virus injected and non-injected mice. Data were statistically analyzed with GraphPad Prism 8. Results are shown as mean ± SEM.

10.- Social behavior: three chamber test

Three-chamber test was performed by Adrián Portalés (lab member) in male and female mice 3-4 weeks after injection.

Three-chamber test (Fig. 36) consisted in testing mice sociability in a cage (60 × 40 × 22 cm) following standard procedures (Nadler et al., 2004). Dividing walls were made from clear Plexiglas, with openings allowing access into each chamber. The test mouse was first placed in the middle chamber and allowed to explore for 10 min. After the habituation period, an unfamiliar subject of the same sex (mouse 1, M1) was placed in one of the side chambers. The unfamiliar mouse was enclosed in a small, round wire cage, which allowed nose contact between the bars. In this first session (sociability), the test mouse had a choice of spending time in either the empty chamber (E) or the chamber occupied by M1. At the end of the sociability session, each mouse was tested in a second 10 min session to evaluate social preference for a new subject. A second, unfamiliar mouse (mouse 2, M2) of the same sex was placed in the chamber that had been empty during the first session. This second unfamiliar mouse was enclosed in an identical wire cage than M1. The test mouse had a choice between the first, already-investigated mouse (M1) and the novel unfamiliar mouse (M2), which indicates social preference or social novelty (Nadler et al., 2004). Continuous video recordings were collected and analyzed offline using BORIS and SMART video-tracking software (PanLab S.L.). Measures of time spent sniffing from E, M1, and M2 mice were quantified for each session. Social index and social novelty index (which indicate how many time spent the test mouse exploring both cages) were calculated dividing sniffing time from M1 and E, and M2 and M1, respectively. Data were statistically analyzed with GraphPad Prism 8. Results are shown as mean ± SEM.

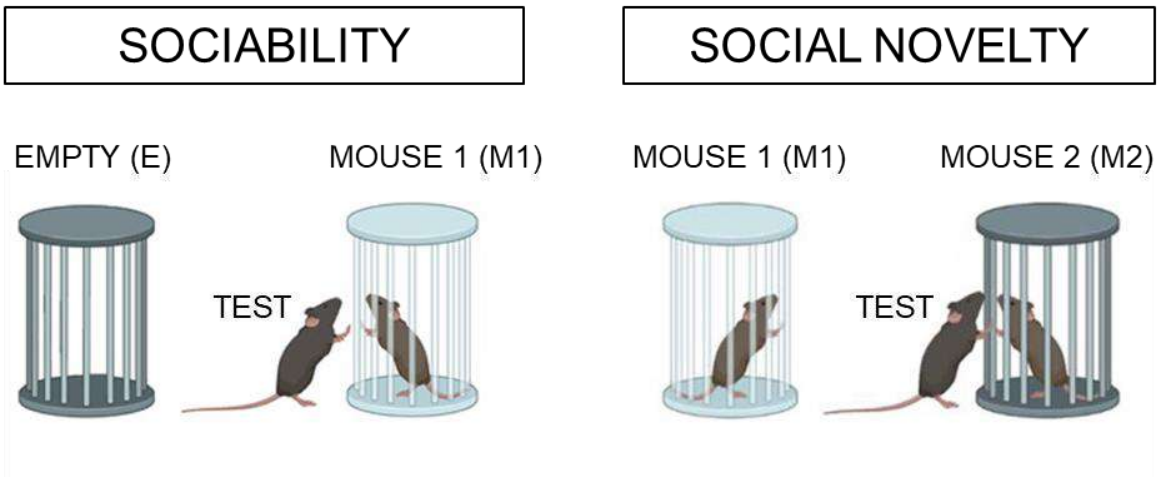

Figure 36.- Schematics of the three-chamber test used in this study to test sociability and social novelty. In the sociability phase, the sniffing time of E and M1 is compared. Social novelty is estimated by quantifying the sniffing time of exploring M1 vs. M2. Adapted from Portalés et al., 2023.

11.- Statistical analysis

Statistical analyses were performed with the data analysis software GraphPad Prism 8. Non-parametric, unpaired t-test (Mann-Whitney test); non-parametric, unpaired, multiple comparisons ANOVA test (Kruskal-Wallis test); or non-parametric, paired, multiple comparisons ANOVA test (Friedman test) were performed depending on data type (Table 7). Linear regression and frequency distribution were also performed with some data. Results are shown as mean ± standard error of the mean (SEM), and/or percentage, and/or number of values (n). P-value: > 0.05 (ns), ≤ 0.05 (*), ≤ 0.01 (**), ≤ 0.001 (***), ≤ 0.0001 (****). All statistical analyses were performed with raw data; some data has been normalized for graphing, with the purpose of a clearer representation of the results.

Table 7.- Statistical analysis employed in each experiment.

Statistical test	Experiment
Mann-Whitney	○ Electron microscopy ○ Chasing OT ○ Vesicle dynamics ○ Mathematical model ○ Immunocytochemistry Golgin ○ Chasing SNAP-47 ○ Immunohistochemistry injected mice ○ Social behavior
Kruskal-Wallis	○ Electron microscopy ○ Vesicle dynamics ○ Immunohistochemistry injected mice
Friedman	○ Vesicle dynamics
Linear regression	○ Vesicle dynamics (MSD data)
Frequency distribution (raw data and %)	○ Electron microscopy ○ Immunocytochemistry Golgin ○ Chasing SNAP-47

RESULTS

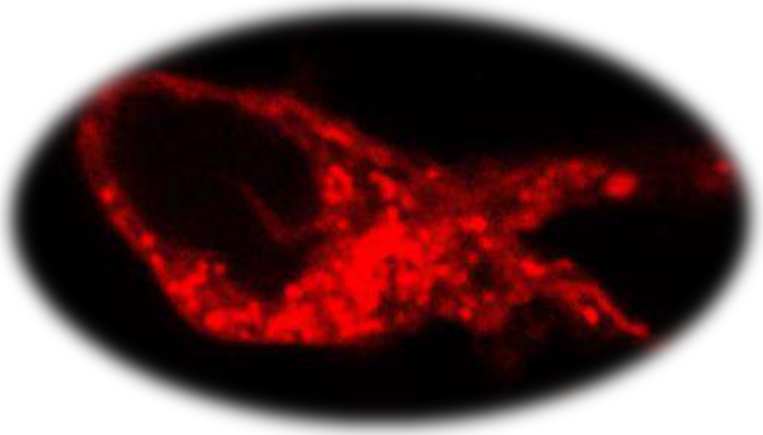

1.- Electron microscopy: properties and localization of hypothalamic DCVs under basal and stimulated conditions

In order to better understand the properties of hypothalamic DCVs, particularly those containing OT in the PVN, we conducted a morphological characterization employing electron microscopy techniques in fixed tissue. To this aim, hypothalamic brain slices were obtained from OT^{tdTom} male mice (3-4 months old) and incubated in either Tyrodes' solution (Basal) or 100 mM KCl Tyrodes' solution (Stimulation) during 1 min. This stimulation solution has been previously reported to mobilize DCVs (Castel et al., 1996; Xia et al., 2009), including OT-containing DCVs (Pow & Morris, 1989). Hypothalamic slices were prepared for transmission electron microscopy as described in the "*Electron microscopy*" section from materials and methods, and were imaged in the Electron Microscopy Facility at the University of Murcia. From these high resolution images, we characterized morphologically DCVs under both basal and stimulus conditions employing a homemade plugin in Fiji (see "*Electron microscopy image analysis*" section from materials and methods).

Hypothalamic DCVs were clearly identified as electron-dense subcellular compartments, as these kind of vesicles present high degree of electron dispersion, in contrast to SVs, that were visualized as clearer compartments (Fig. 37). We analyzed the following parameters to characterize DCVs' properties: area and diameter, vesicles density within the terminal, vesicle distance to the plasma membrane, and vesicle distance to the AZ.

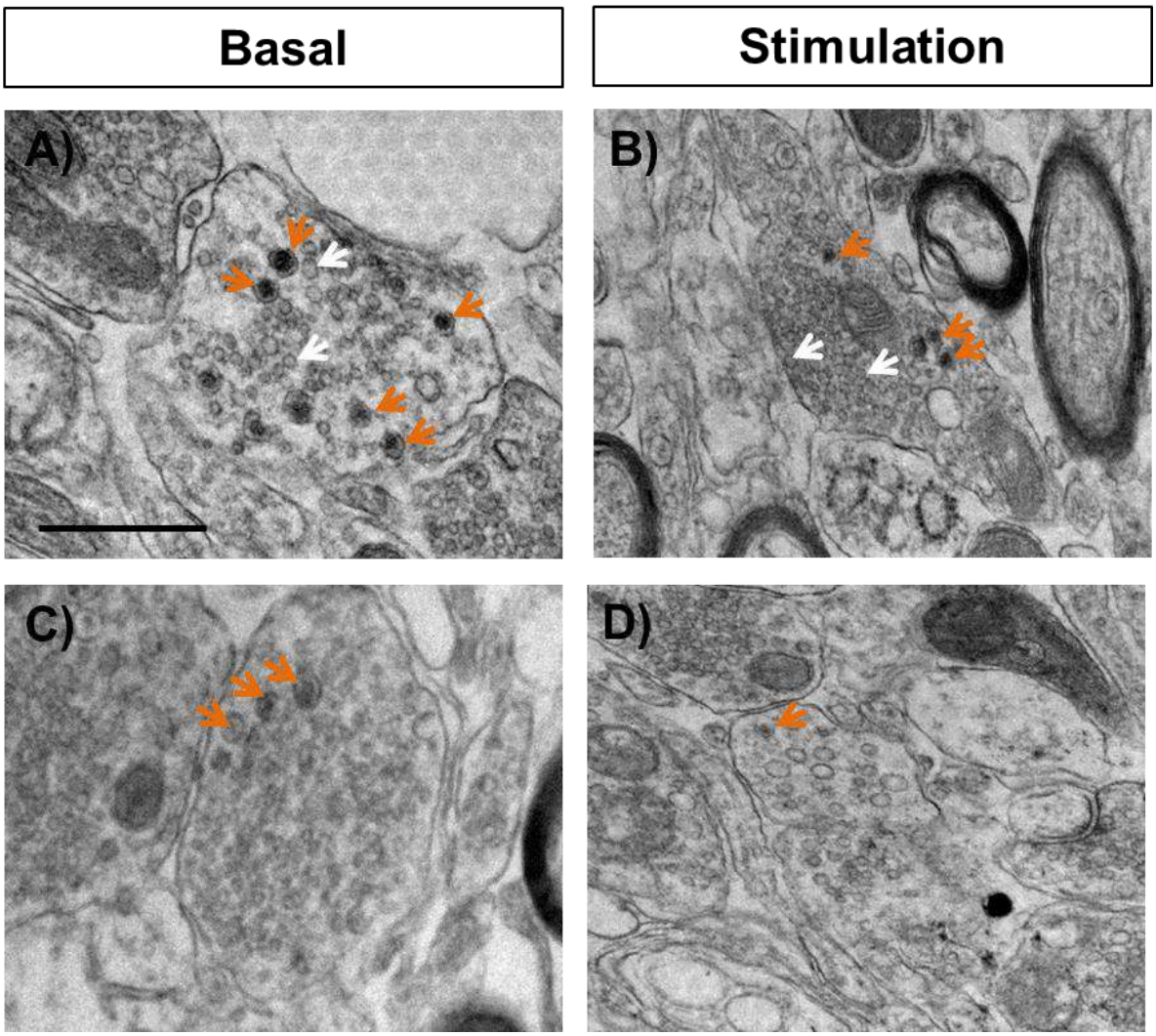

Figure 37.- Hypothalamic brain slices visualized by transmission electron microscopy under basal and stimulus (100 mM KCl) conditions. Compared with basal conditions **(A, C)**, DCVs' number was reduced **(B)** and presented smaller size **(D)** in response to 100 mM KCl stimulation. DCVs are indicated with orange arrows; SVs are indicated with white arrows. Scale bar indicates 1 µm.

1.1.- Neuronal stimulation decreases hypothalamic DCVs' area

In general, under basal conditions DCVs could be classified in two main populations according to their area: a pool with a maximum area of 220 nm^2 (that constituted 26 % of DCVs), and a second population with a maximum area of 280 nm^2 (74 % of DCVs) (Fig. 38A. Area in nm^2. Pob1_Basal: 202.6 ± 4.1 vs. Pob2_Basal: 293.7 ± 5.1, p-value< 0.0001).

Our data indicated a significant decrease in DCVs' mean area in response to stimulation compared to basal conditions (Fig. 38B. Area in nm^2. Basal: 270.1 ± 5.8 vs. Stimulation: 233.9 ± 7.3, p-value= 0.0002). This result is clearly visualized in the histogram shown in Fig. 38C, with the majority of DCVs (70.21 %) presenting an area ranging from 180 to 260 nm^2 after stimulation.

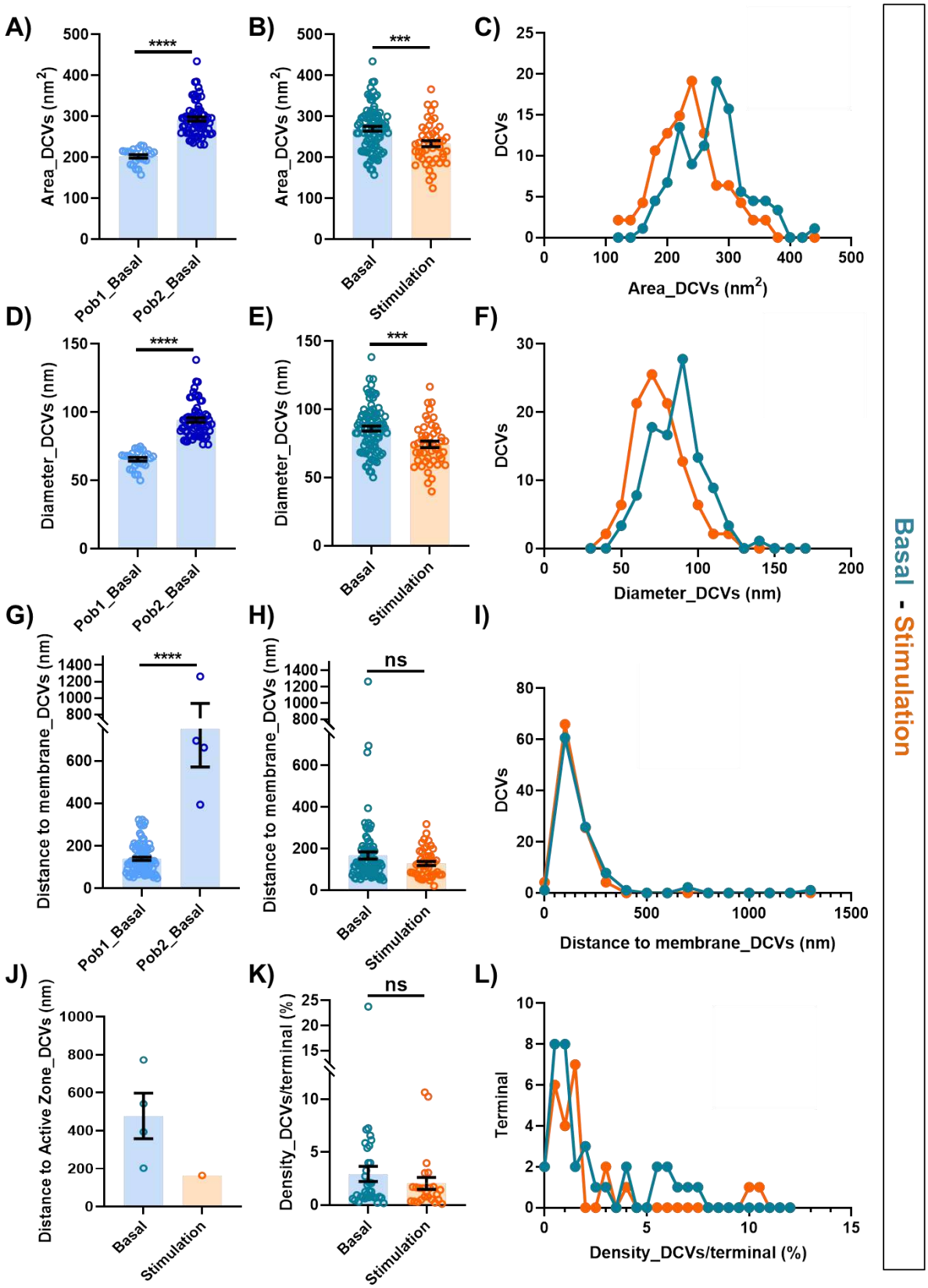

Figure 38.- Morphological analysis of DCVs in hypothalamic brain slices under basal and stimulus conditions. **A)** According to their area, two populations of DCVs could be distinguished under basal conditions (Area in nm^2. Pob1_Basal: 202.6 ± 4.1 vs. Pob2_Basal: 293.7 ± 5.1, p-value< 0.0001). **B)** DCVs' mean area was reduced under stimulus conditions compared with DCVs' mean area under basal conditions (Area in nm^2. Basal: 270.1 ± 5.8 vs.

Stimulation: 233.9 ± 7.3, p-value= 0.0002). **C)** Histogram of DCVs' area under basal and stimulus conditions. DCVs' area was smaller under stimulus conditions compared with basal conditions (Frequency distribution, Appendix, table 19). **D)** According to the diameter of DCVs, two populations could be distinguished under basal conditions (Diameter in nm. Pob1_Basal: 65.60 ± 1.30 vs. Pob2_Basal: 94.31 ± 1.60, p-value< 0.0001). **E)** DCVs' diameter was reduced under stimulus conditions compared with basal conditions (Diameter in nm. Basal: 86.01 ± 1.80 vs. Stimulation: 74.4 ± 2.3, p-value= 0.0002). **F)** Histogram of DCVs' diameter under basal and stimulus conditions. DCVs' diameter was smaller under stimulus conditions compared with basal conditions (Frequency distribution, Appendix, table 22). **G)** Considering distances larger or shorter than 400 nm from the DCVs to the plasma membrane under basal conditions, two populations could be distinguished (Distance in nm. Pob1_Basal: 139.2 ± 7.7 vs. Pob2_Basal: 753.3 ± 182.5, p-value< 0.0001). **H)** DCVs' distance to the membrane did not differ under basal and stimulus conditions (Distance to the plasma membrane in nm. Basal: 166.8 ± 17.0 vs. Stimulation: 127.9 ± 9.8, p-value= 0.2222). **I)** Histogram of DCVs' distance to the membrane under basal and stimulus conditions. The majority of DCVs, either under basal or stimulated conditions, were found ≤ 100 nm away from the plasma membrane (Frequency distribution, Appendix, table 25). **J)** DCVs' distance to the AZ under basal and stimulus conditions suggested a decrease in the distance to the AZ in response to stimulation, despite not statistically analyzed (Distance to the AZ in nm. Basal: 478.0 ± 120.3, Stimulation: 164.2 ± 0.0, Appendix, table 26). **K)** DCVs' density did not differ between basal and stimulus conditions (Density as percentage. Basal: 3.0 ± 0.7 vs. Stimulation: 2.0 ± 0.6, p-value= 0.3614). **L)** Histogram of DCVs' density indicated variability under both basal and stimulus conditions (Frequency distribution, Appendix, table 29). Statistical analysis: Mann-Whitney non-parametric test; p-value> 0.05 (ns), ≤ 0.05 (*), ≤ 0.01 (**), ≤ 0.001 (***), ≤ 0.0001 (****). Appendix, tables 17-29.

1.2.- Neuronal stimulation decreases hypothalamic DCVs' diameter

In parallel to the area, DCVs in basal conditions could be divided in two populations depending on their diameter: one population (29 % of DCVs), in which the majority of vesicles (61.5 %) presented a diameter of 70 nm, and a more prevalent population (71 % of DCVs), in which the majority of vesicles (39. 1 %) presented a diameter of 90 nm (Fig. 38D. Diameter in nm. Pob1_Basal: 65.60 ± 1.30 vs. Pob2_Basal: 94.31 ± 1.60, p-value< 0.0001). The estimation of DCVs' diameter correlated with the results of the area, revealing a smaller diameter in response to stimulation (Fig. 38E, F. Diameter in nm. Basal: 86.01 ± 1.80 vs. Stimulation: 74.4 ± 2.3, p-value= 0.0002).

1.3.- Analysis of DCVs' proximity to the plasma membrane

The distance of DCVs to the plasma membrane was also analyzed. We found not significant differences between basal and stimulus conditions (Fig. 38H. Distance to the plasma membrane in nm. Basal: 166.8 ± 17.0 vs. Stimulation: 127.9 ± 9.8, p-value= 0.2222), despite a trend towards shorter distances was noted in response to stimulation. The majority of DCVs either in basal or stimulated conditions were found ≤ 100 nm away from the plasma

membrane (Fig. 38I. Percentage of DCVs at ≤ 100 nm from the plasma membrane. Basal: 61.8, Stimulation: 70.21). Nonetheless, it is noteworthy that in response to stimulation, no DCVs were found further than 400 nm from the membrane, whereas about 4 % of DCVs under basal conditions can be found further than 400 nm (Fig. 38I). An additional classification considering distances larger or shorter than 400 nm from the plasma membrane under basal conditions rendered two subpopulations: a major pool (95.5 % of DCVs), within the 400 nm range, and a minor one (4.5 % of DCVs) that was located at distances ≥ 400 nm from the plasma membrane (Fig. 38G. Distance to the plasma membrane in nm. Pob1_Basal: 139.2 ± 7.7 vs. Pob2_Basal: 753.3 ± 182.5, p-value< 0.0001).

1.4.- Analysis of DCVs' distance to the AZ

Furthermore, the distance of DCVs to the AZ was analyzed. Our data suggested a decrease in the distance to the AZ in response to stimulation (Fig. 38J. Distance to the AZ in nm. Basal: 478.0 ± 120.3, Stimulation: 164.2 ± 0.0), despite the fact that the minimum value in baseline (203.3 nm) was two times higher than the mean distance under stimulated conditions (164.2 nm) (Fig. 38J). Unfortunately, no statistical analysis could be performed due to the low number of DCVs found in terminals with clearly identifiable AZs.

1.5.- Analysis of DCVs' density at synaptic terminals

Finally, DCVs density (number of vesicles per terminal) was calculated. Results indicated not significant differences in DCVs density between basal and stimulation conditions (Fig. 38K. Basal: 0.03 ± 0.01 vs. Stimulation: 0.02 ± 0.01, p-value= 0.3614). Nevertheless, similar to the estimations of distance from the plasma membrane shown in Fig. 38H, the stimulated conditions showed a trend toward lower DCVs' density (Fig. 38K). However, it is important to note that DCVs' density in basal conditions is quite variable, ranging from 0.2 % to 7.5 % (Fig. 38L), with 47 % of the terminals presenting a low DCVs mean density between 0.5 - 1.0 %. On the other hand, the majority of terminals in stimulation conditions (92 %) exhibited a vesicle density ranging between 0.1 - 4.0 %, with 8 % of the terminals showing a higher density of 10 - 10.5 % (Fig. 38L).

2.- Chasing of OT-containing compartments: OT recruitment to the somatic plasma membrane

The electron microscopy analyses suggested that neuronal stimulation induced changes in the morphology and organization of hypothalamic DCVs. Due to difficulties for using our validated OT antibody in pre-embedding protocols to label OT vesicles, we analyzed the specific properties of OT-containing compartments using fluorescence labelling techniques in cultured hypothalamic cells.

Hypothalamic primary cultured neurons were obtained from OT^{tdTom} and OT^{EGFP} P0 mice. 10-13 DIV cultures were incubated with either Tyrode's solution (Basal), 100 mM KCl Tyrode's solution (Stimulation), chelated extracellular calcium Tyrode's basal solution (0.5 mM EGTA) or chelated extracellular calcium 100 mM KCl Tyrode's solution during 1 or 10 min, to perform vesicle chasing procedures (see details in the "*Chasing experiment*" section from materials and methods). After treatment, cells were incubated with specific anti-OT antibody (Table 5. Primary antibody: anti-OT rabbit) to identify OT-containing microdomains at the plasma membrane (Fig. 39). As this technique involves the halting of the endocytic processes, fluorescence signals post-fixation were interpreted as OT-containing compartments prepared to undergo exocytosis or already fused to the plasma membrane, due to difficulty to resolve individual OT vesicles (referred to as OT-containing compartments, OT-membrane patches or OT-containing vesicles from now on).

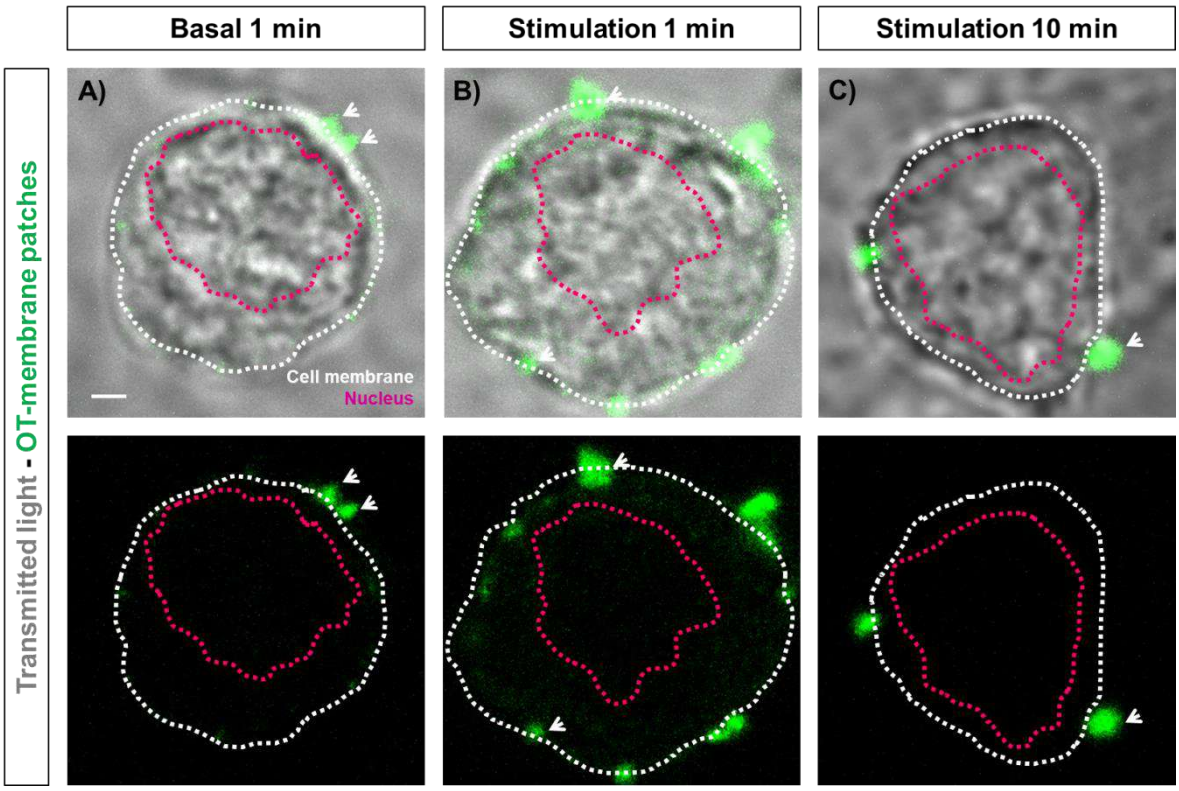

Figure 39.- OT-membrane patches in hypothalamic primary cultured neurons under different conditions. OT neurons incubated with Tyrode's basal solution during 1 min **(A),** 100 mM KCl Tyrode's solution (Stimulation) during 1 min **(B)** or 10 min **(C).** OT-membrane patches were identified with an anti-OT antibody and visualized as green dots (white arrows). Dotted white line indicates cell membrane, and dotted pink line indicates cell nucleus. Scale bar indicates 3 µm.

2.1.- Properties of OT-membrane patches

2.1.1.- Neuronal stimulation increases the number of OT-membrane patches

Neuronal stimulation during 1 min significantly increased OT-membrane patches in hypothalamic primary cultured neurons (Fig. 40A. Number of OT-patches. Basal_1 min: 1.9 ± 0.1 vs. Stimulation_1 min: 2.8 ± 0.17, p-value< 0.0001). In contrast, neurons incubated during 10 min exhibited the opposite trend (Fig. 40A. Number of OT-patches. Basal_10 min: 2.3 ± 0.2 vs. Stimulation_10 min: 1.6 ± 0.1, p-value= 0.0002). This finding suggested that with longer stimulation times, most OT-containing vesicles may have already been released. Consequently, prolonged stimulation does not allow recovery for subsequent exocytic events. As a consequence, after 1 min of high potassium stimulation, the number of OT-membrane patches was higher than after 10 min of stimulation (Fig. 40A. Number of OT-patches. Stimulation_1 min: 2.85 ± 0.17 vs. Stimulation_10 min: 1.61 ± 0.13, p-value< 0.0001). Unexpectedly, spontaneous OT secretion probability showed a not significant trend toward higher values in response to longer incubation times (10 min) with basal solution (Fig. 40A. Number of OT-patches. Basal_1 min: 1.9 ± 0.1 vs. Basal_10 min: 2.3 ± 0.2, p-value= 0.1023).

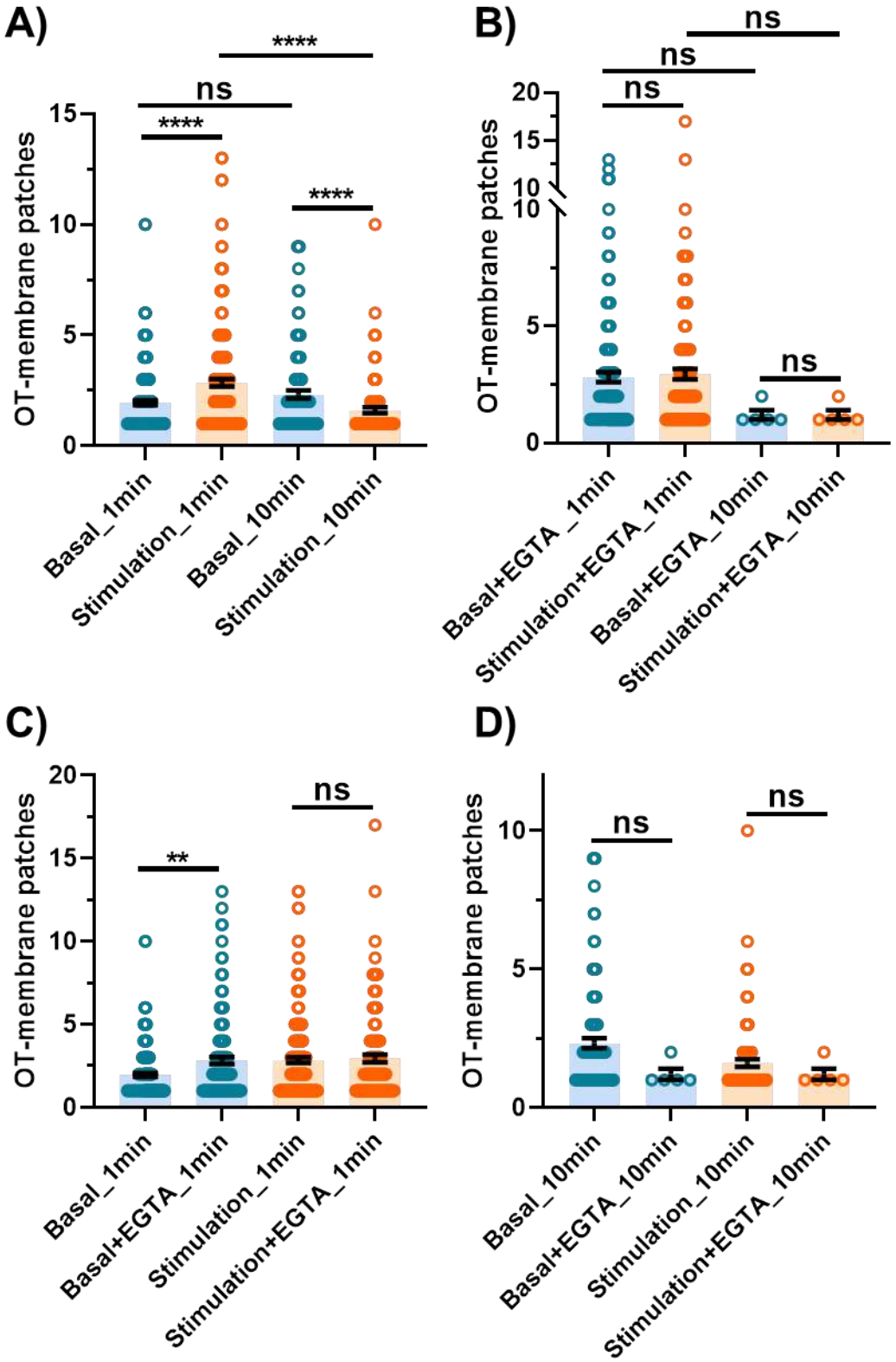

Figure 40.- Number of OT-membrane patches in hypothalamic primary cultured neurons. **A)** 1 min stimulation increased OT-membrane patches (Number of OT-patches. Basal_1 min: 1.9 ± 0.1 vs. Stimulation_1 min: 2.8 ± 0.17, p-value< 0.0001); 10 min stimulation reduced OT-membrane patches (Number of OT-patches. Basal_10 min: 2.3 ± 0.2 vs. Stimulation_10 min: 1.6 ± 0.1, p-value= 0.0002). Longer incubation times under basal conditions did not increase

OT-membrane patches (Number of OT patches. Basal_1 min: 1.9 ± 0.1 vs. Basal_10 min: 2.3 ± 0.2, p-value = 0.1023); and under stimulation, the number of OT-membrane patches was higher after 1 min of stimulation compared with 10 min incubation (Number of OT-patches. Stimulation_1 min: 2.85 ± 0.17 vs. Stimulation_10 min: 1.61 ± 0.13, p-value< 0.0001). **B)** The number of OT-membrane patches was similar between cells incubated either with basal or stimulus conditions during 1 or 10 min in the presence of extracellular calcium chelator EGTA (Number of OT-patches. Basal+EGTA_1 min: 2.8 ± 0.2 vs. Stimulation+EGTA_1 min: 2.9 ± 0.2, p-value= 0.5976; Basal+EGTA_10 min: 1.2 ± 0.2 vs. Stimulation+EGTA_10 min: 1.2 ± 0.2, p-value> 0.99999; Stimulation+EGTA_1 min: 2.9 ± 0.2, Stimulation+EGTA_10 min: 1.2 ± 0.2, p-value= 0.0619; Basal+EGTA_1 min: 2.82 ± 0.21 vs. Basal+EGTA_10 min: 1.20 ± 0.20, p-value= 0.0833). **C)** The number of OT-membrane patches was increased in extracellular calcium-free basal medium compared with basal medium incubation during 1 min (Number of OT-patches. Basal_1 min: 1.95 ± 0.12 vs. Basal+EGTA_1 min: 2.82 ± 0.21, p-value= 0.0011). The number of OT-membrane patches was the same under stimulus conditions with or without extracellular calcium (Number of OT-patches. Stimulation_1 min: 2.84 ± 0.17 vs. Stimulation+EGTA_1 min: 2.94 ± 0.23, p-value= 0.8934). **D)** The number of OT-membrane patches was similar between cells incubated during 10 min under basal or stimulation conditions with and without extracellular calcium (Number of OT-patches. Basal_10 min: 2.3 ± 0.2 vs. Basal+EGTA_10 min: 1.2 ± 0.2, p-value= 0.15; Stimulation_10 min: 1.6 ± 0.1 vs. Stimulation+EGTA_10 min: 1.2 ± 0.2, p-value= 0.6824). Statistical analysis: Mann-Whitney non-parametric test; p-value> 0.05 (ns), ≤ 0.05 (*), ≤ 0.01 (**), ≤ 0.001 (***), ≤ 0.0001 (****). Appendix, tables 30 and 31.

2.1.2.- Membrane recruitment of OT under stimulus conditions depends on extracellular calcium

A key factor to trigger vesicle exocytosis is calcium influx, thus we ought to investigate the role of extracellular calcium in the recruitment of OT-containing compartments in response to neuronal stimulation. The role of extracellular calcium is particularly controversial for OT vesicles, as their release has been previously reported to primarily depend on intracellular calcium stores (Van Den Pol, 2012). Thus, in the following experiments we explored OT dynamics in free-extracellular calcium solutions.

Our results indicated a not significant increase in OT-membrane patches in response to an extracellular calcium-free stimulation solution, either during 1 or 10 min incubation (Fig. 40B. Number of OT-patches. Basal+EGTA_1 min: 2.8 ± 0.2 vs. Stimulation+EGTA_1 min: 2.9 ± 0.2, p-value= 0.5976; Basal+EGTA_10 min: 1.2 ± 0.2 vs. Stimulation+EGTA_10 min: 1.2 ± 0.2, p-value> 0.99999), which could indicate that OT recruitment to the plasma membrane, at least partly, depends on extracellular calcium influx.

Interestingly, despite a not significant trend, the number of OT-membrane patches detected under 1 min stimulation without extracellular calcium was higher than the number detected under 10 min stimulation without extracellular calcium (Fig. 40B. Number of OT-patches. Stimulation+EGTA_1 min: 2.9 ± 0.2 vs. Stimulation+EGTA_10 min: 1.2 ± 0.2, p-value= 0.0619), suggesting longer stimulation times reduce the number of OT-membrane patches. Despite not significant, the same tendency was observed under basal conditions (Fig. 40B.

Number of OT-patches. Basal+EGTA_1 min: 2.82 ± 0.21 vs. Basal+EGTA_10 min: 1.20 ± 0.20, p-value= 0.0833).

2.1.3.- Membrane recruitment of OT under basal conditions is negatively regulated by extracellular calcium

However, the removal of extracellular calcium increased the number of OT-membrane patches under basal conditions (Fig. 40C. Number of OT-patches. Basal_1 min: 1.95 ± 0.12 vs. Basal+EGTA_1 min: 2.82 ± 0.21, p-value= 0.0011). This result suggested that extracellular calcium influx may inhibit the spontaneous recruitment of OT to the plasma membrane. In this scenario, stimulation with high KCl may not further increase the number of OT-containing compartments, which are similar under stimulation and calcium-free stimulation medium (Fig. 40C. Number of OT-patches. Stimulation_1 min: 2.84 ± 0.17 vs. Stimulation+EGTA_1 min: 2.94 ± 0.23, p-value= 0.8934).

Not significant differences were identified in response to calcium-free solutions (basal and stimulation) after 10 minutes, despite the number of OT-membrane patches was higher in the presence of extracellular calcium (Fig. 40D. Number of OT-patches. Basal_10 min: 2.3 ± 0.2 vs. Basal+EGTA_10 min: 1.2 ± 0.2, p-value= 0.15; Stimulation_10 min: 1.6 ± 0.1 vs. Stimulation+EGTA_10 min: 1.2 ± 0.2, p-value= 0.6824). These results could indicate that extracellular calcium is necessary for maintenance of exocytosis in hypothalamic neurons during prolonged incubation times.

2.2.- Area of OT-membrane patches

2.2.1.- OT-membrane patches' area depends on the stimulus duration

Our data indicated no changes in the area of OT-membrane patches in response to 1 min stimulation compared with 1 min incubation under basal conditions (Fig. 41A. Area in μm^2. Basal_1 min: 0.36 ± 0.03 vs. Stimulation_1 min: 0.34 ± 0.02, p-value= 0.4634), indicating that stimulation did not affect the area of OT-membrane patches. In response to 10 min incubation time, OT-membrane patches were bigger under stimulus conditions compared with basal conditions (Fig. 41A. Area in μm^2. Basal_10 min: 0.24 ± 0.02 vs. Stimulation_10 min: 0.40 ± 0.04, p-value< 0.0001).

Furthermore, the area of OT-membrane patches seemed larger in basal conditions during 1 min than in basal conditions during 10 min (Fig. 41A. Area in μm^2. Basal_1 min: 0.36 ± 0.03 vs. Basal_10 min: 0.24 ± 0.02, p-value< 0.0001), which could be linked to the depletion of OT-compartments in response to longer incubation times.

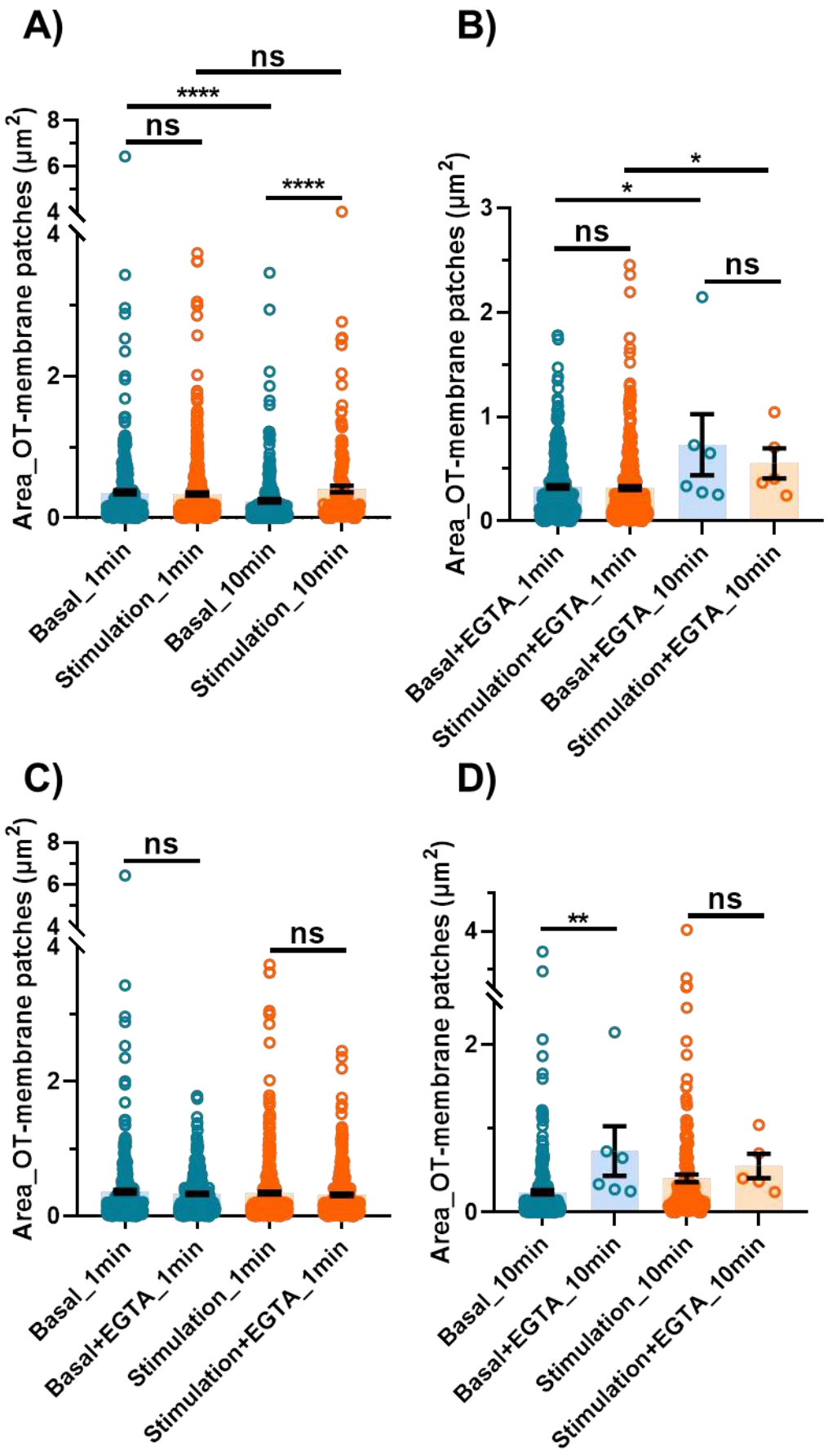
A)
B)
C)
D)
Area_OT-membrane patches (µm²)
ns
****
*
**
Basal_1min
Stimulation_1min
Basal_10min
Stimulation_10min
Basal+EGTA_1min
Stimulation+EGTA_1min
Basal+EGTA_10min
Stimulation+EGTA_10min

Figure 41.- Area of OT-membrane patches in hypothalamic primary cultured neurons**. A)** The area of OT-membrane patches was similar under basal and stimulated conditions during 1 min (Area in μm^2. Basal_1 min: 0.36 ± 0.03 vs. Stimulation_1 min: 0.34 ± 0.02, p-value= 0.4634). Under 10 min incubation, OT-membrane patches were bigger under stimulus conditions compared with basal conditions (Area in μm^2. Basal_10 min: 0.24 ± 0.02 vs. Stimulation_10 min: 0.40 ± 0.04, p-value< 0.0001). The area of OT-membrane patches seemed larger in basal conditions during 1 min than in basal conditions during 10 min (Area in μm^2. Basal_1 min: 0.36 ± 0.03 vs. Basal_10 min: 0.24 ± 0.02, p-value< 0.0001), and no differences were found under stimulus conditions (Area in μm^2. Stimulation_1 min= 0.34 ± 0.02 vs. Stimulation_10 min= 0.41 ± 0.04, p-value= 0.6985). **B)** In the presence of EGTA, the size of OT-membrane patches was bigger when incubating the cells during 10 min in comparison with 1 min incubation, either in basal or stimulus conditions (Area in μm^2. Basal+EGTA_1 min= 0.33 ± 0.02 vs. Basal+EGTA_10 min= 0.73 ± 0.29, p-value= 0.0308; Stimulation+EGTA_1 min= 0.31 ± 0.02 vs. Stimulation+EGTA_10 min= 0.55 ± 0.14, p-value= 0.0271). OT-membrane patches' size was similar under same incubation times (Area in μm^2. Basal+EGTA_1 min= 0.33 ± 0.02 vs. Stimulation+EGTA_1 min= 0.31 ± 0.02, p-value= 0.1217; Basal+EGTA_10 min= 0.73 ± 0.29 vs. Stimulation +EGTA_10 min= 0.55 ± 0.14, p-value> 0.9999). **C)** Incubating the cells during 1 min with a medium with or without extracellular calcium, either in basal or stimulus conditions, did not modify the size of OT-membrane patches (Area in μm^2. Basal_1 min: 0.36 ± 0.03 vs. Basal+EGTA_1 min: 0.33 ± 0.02, p-value= 0.1592; Stimulation_1 min: 0.34 ± 0.02 vs. Stimulation+EGTA_1 min: 0.31 ± 0.02, p-value= 0.3376). **D)** Incubating the cells during 10 min with free-extracellular calcium led to bigger OT-membrane patches than when incubated with extracellular calcium either in basal or stimulus conditions (Area in μm^2. Basal_10 min: 0.24 ± 0.02 vs. Basal+EGTA_10 min: 0.73 ± 0.30, p-value= 0.0014; Stimulation_10 min: 0.41 ± 0.04 vs. Stimulation+EGTA_10 min: 0.55 ± 0.14, p-value= 0.0598). Statistical analysis: Mann-Whitney non-parametric test; p-value> 0.05 (ns), ≤ 0.05 (*), ≤ 0.01 (**), ≤ 0.001 (***), ≤ 0.0001 (****) Appendix, tables 32 and 33.

Interestingly, this trend was reversed in the absence of extracellular calcium (Fig. 41B. Area in μm^2. Basal+EGTA_1 min: 0.33 ± 0.02 vs. Basal+EGTA_10 min: 0.73 ± 0.30, p-value= 0.0308), suggesting that, despite inducing a reduction in the number of OT-containing compartments upon longer treatments (Fig. 40B. Number of OT-patches. Basal+EGTA_1 min: 2.82 ± 0.21 vs. Basal+EGTA_10 min: 1.20 ± 0.20, p-value= 0.0833; Stimulation+EGTA_1 min: 2.9 ± 0.2, Stimulation+EGTA_10 min: 1.2 ± 0.2, p-value= 0.0619), the area is increased maybe as a result of impaired calcium-dependent recycling pathways.

Extracellular calcium-free solutions, either basal or stimulation solutions, did not affect the area of OT-membrane patches compared with their respective mediums containing calcium during 1 min incubation (Fig. 41C. Area in μm^2. Basal_1 min: 0.36 ± 0.03 vs. Basal+EGTA_1 min: 0.33 ± 0.02, p-value= 0.1592; Stimulation_1 min: 0.34 ± 0.02 vs. Stimulation+EGTA_1 min: 0.31 ± 0.02, p-value= 0.3376).

Furthermore, we observed that the area of OT-membrane patches from cells incubated during 10 min with basal medium without extracellular calcium was larger than the area of OT-membrane patches from cells incubated during 10 min with basal medium containing extracellular calcium (Fig. 41D. Area in μm^2. Basal_10 min: 0.24 ± 0.02 vs. Basal+EGTA_10 min: 0.73 ± 0.30, p-value= 0.0014), suggesting that despite a reduction in the number of OT-patches, they could be larger (Fig. 40D. Number of OT-patches. Basal_10 min: 2.3 ± 0.2 vs.

Basal+EGTA_10 min: 1.2 ± 0.2, p-value= 0.15). Although not statistically significant, the size of OT-membrane patches incubated during 10 min under stimulated conditions without extracellular calcium was also larger than the size of the patches incubated in the presence of extracellular calcium (Fig. 41D. Area in μm^2. Stimulation_10 min: 0.41 ± 0.04 vs. Stimulation+EGTA_10 min: 0.55 ± 0.14, p-value= 0.0598).

3.- Dynamic properties of OT-containing compartments in response to neuronal stimulation

Although vesicular chasing experiments provided crucial information about the properties of OT-containing compartments, they did not offer insight into their dynamics and kinetics. To delve deeper into this aspect, we took advantage of the properties of the transgenic OT^{tdTom} mouse, which allowed us to analyze subcellular compartments in OT cells (Fig. 29). To this aim, 7-14 DIV hypothalamic primary cultures were treated with basal and stimulation Tyrode´s solutions as described in "*OT vesicle dynamics. Image acquisition*" section from materials and methods.

Fluorescence dispersion and the resolution limitations of confocal microscopy did not allow resolving single vesicles. So these signals were considered as clusters of OT-containing compartments, similarly to the vesicle chasing experiments aforementioned. Our analysis focused primarily on the somatic OT-containing compartments, which were tracked semiautomatically employing the image analysis software Imaris (see "*OT vesicle dynamics. Image analysis*" section from materials and methods).

3.1.- Mobility of OT-containing compartments

Employing this experimental strategy, we first explored the mobility of OT-containing compartments in response to 1 min stimulation protocol. Our results indicated a reduction of OT-containing compartments of 20 %, suggesting that neuronal stimulation could induce the release of these compartments (Fig. 42). Importantly, the application of Tyrode's basal medium indicated low probability of spontaneous release of OT-containing compartments, that was promoted in response to stimulation with high KCl (Fig. 42B. t50. Basal: 2.42 ± 0.08 vs. Stimulation: 2.56 ± 0.1, p-value= 0.0240; t60. Basal: 2.4 ± 0.08 vs. Stimulation: 2.48 ± 0.1, p-value= 0.0109; t80. Basal: 2.32 ± 0.08 vs. Stimulation: 2.43 ± 0.09, p-value= 0.0281).

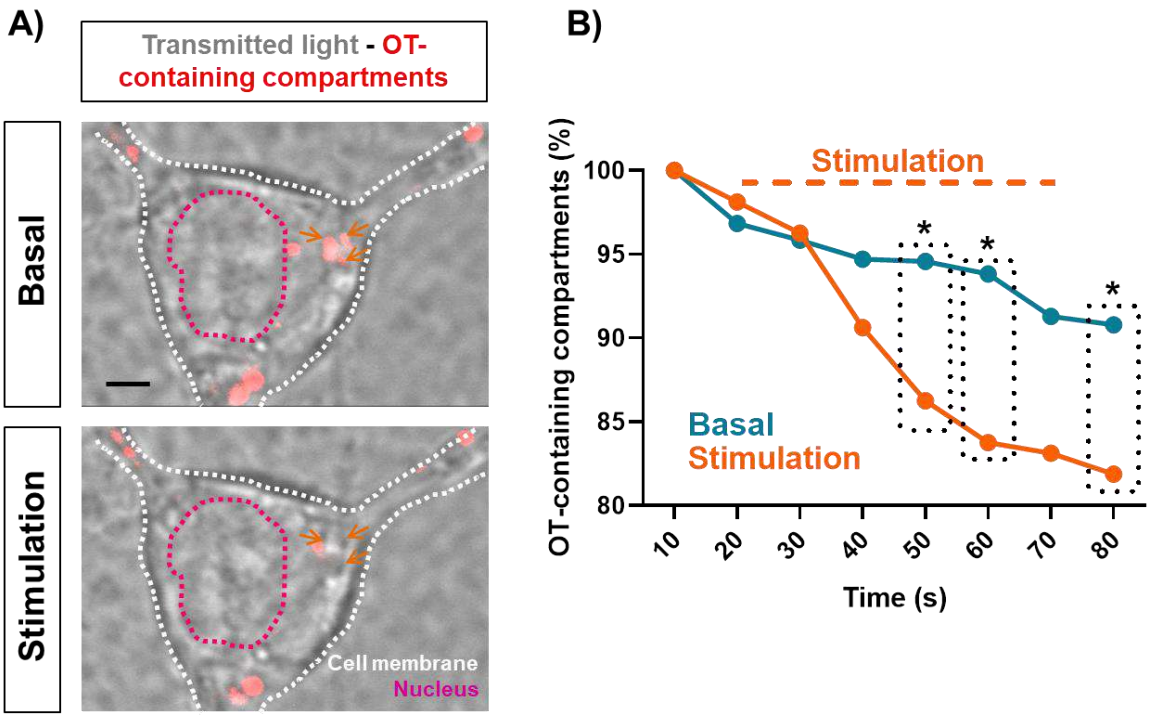

Figure 42.- Dynamics of OT-containing compartments under basal and stimulus conditions. **A)** Cell body of an OT^{tdTom} hypothalamic cultured neuron before and after stimulation. OT-containing compartments (identified by red fluorescence, orange arrows) disappeared from the plane of acquisition, probably due to exocytosis. Dotted white line indicates cell membrane, and dotted pink line indicates cell nucleus. Scale bar indicates 3 µm. **B)** OT-containing compartments decreased 20 % under 100 mM KCl stimulation (t50. Basal: 2.42 ± 0.08 vs. Stimulation: 2.56 ± 0.1, p-value= 0.0240; t60. Basal: 2.4 ± 0.08 vs. Stimulation: 2.48 ± 0.1, p-value= 0.0109; t80s. Basal: 2.32 ± 0.08 vs. Stimulation: 2.43 ± 0.09, p-value= 0.0281). Statistical analysis: Mann-Whitney non-parametric test; p-value> 0.05 (ns), ≤ 0.05 (*), ≤ 0.01 (**), ≤ 0.001 (***), ≤ 0.0001 (****). Appendix, tables 34-38.

We then studied the kinetics of OT-containing compartments during basal and stimulated conditions, identifying distinct populations according to different parameters analyzed.

3.2.- Displacement of OT-containing compartments

Displacement length refers to the distance of a spot (in our case, an OT-compartment) travelled from its point of origin over the course of the experiment. We classified OT-containing compartments according to the first time point that resulted in a significant difference in the displacement length compared to the baseline.

Our analysis revealed that OT-containing compartments were highly heterogeneous regarding their mobility in response to neuronal stimulation (Fig. 43A-H). According to the displacement criterion, OT-containing compartments were classified in four main subgroups: dynamic, delayed, uncoupled and stable (Fig. 43I, J).

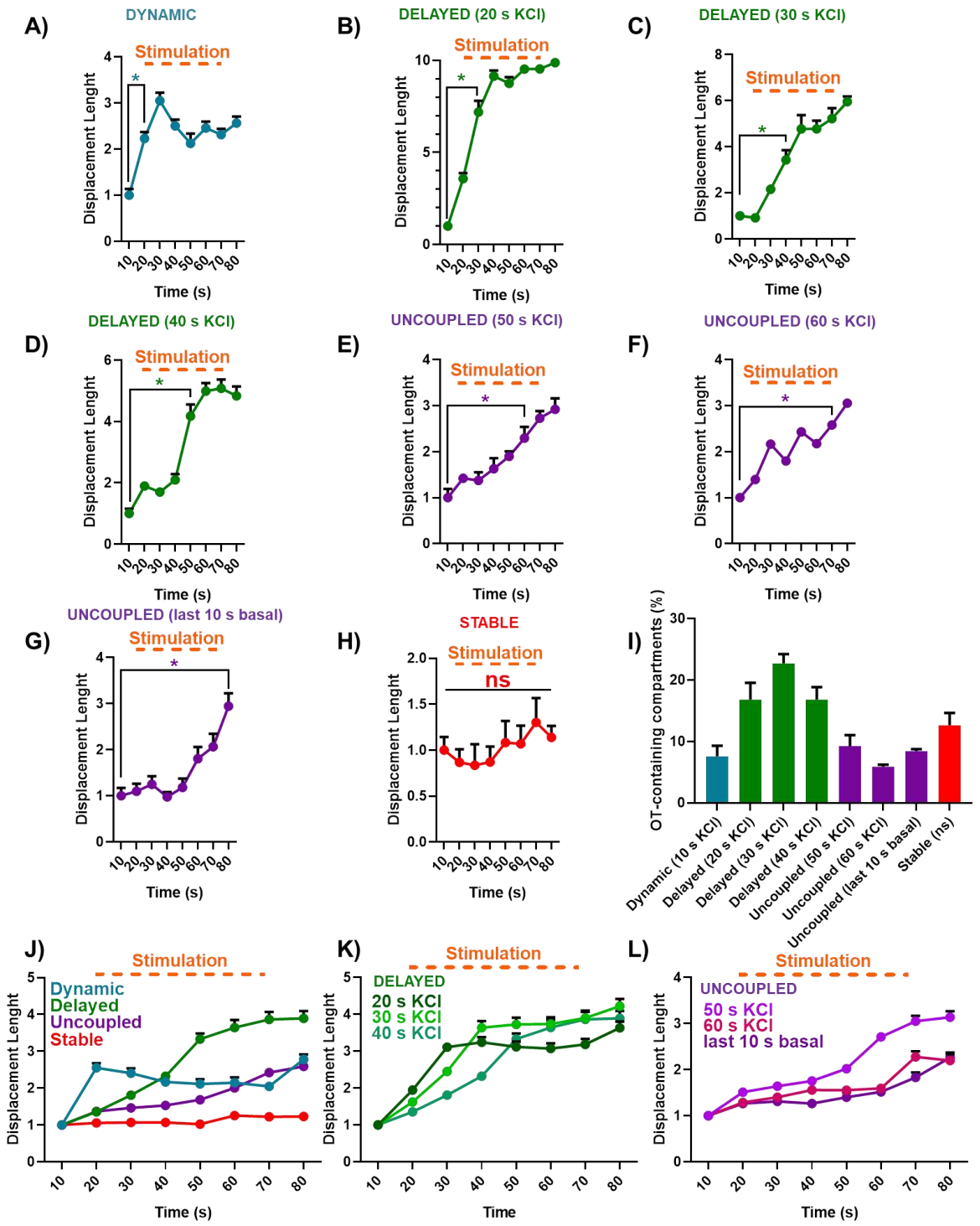

Figure 43.- OT-containing compartments classification depending on their displacement in response to neuronal stimulation. **A-H)** OT-containing compartments could be classified according to the time point in which their displacement showed a significant difference compared to their baseline. Each graph corresponds to an individual example of the different types of OT-containing compartments identified. **I)** Classification of OT-containing compartments depending on their displacement length in response to stimulation. **J)** OT-containing compartments could be classified in four groups depending on their displacement length in response to stimulation: dynamic, delayed, uncoupled, and stable. **K-L)** Delayed (K) and uncoupled (L) subgroups could be subclassified depending on the time point they

modified their displacement length in response to high KCl stimulation. Presented data are normalized. Statistical analysis: Friedman non-parametric; p-value> 0.05 (ns), ≤ 0.05 (*), ≤ 0.01 (**), ≤ 0.001 (***), ≤ 0.0001 (****). Asterisks in graphs represent the first time point in which the OT-compartment changed its displacement length compared to the baseline. Appendix, tables 39-55. The dynamic pool modified their displacement during the first 10 s of stimulation and comprised the 7.3 % of the total OT-containing compartments (Fig. 43A, I, and J).

The majority of compartments belonged to the delayed group (57.7 %), which modified their displacement length 20, 30 or 40 s after stimulation (Fig. 43B-D, I, J, and K). The population that responded to the stimulus after 50-60 s of KCl application or during the last seconds of basal medium application was classified as uncoupled (22.8 %) (Fig. 43E-G, I, J, and L). Finally, OT-containing compartments which did not respond to KCl were classified as stable (12.2 %) (Fig. 43H, I, and J).

Interestingly, uncoupled and stable OT-containing compartments presented more displacement than dynamic and delayed ones under basal conditions (Table 8). Under stimulus application, dynamic, delayed, and uncoupled OT-containing compartments increased their displacement, and all of them presented similar mean displacement values (Table 8). Top displacement values corresponded to mean displacement values in basal conditions, when uncoupled and stable OT-containing compartments presented their higher displacement (Table 8). Nevertheless, top displacement values between the different OT-containing compartments groups were different under stimulus conditions, the opposite that happened with mean values (Table 8).

Table 8.- Mean and top displacement length of OT-containing compartments.

	Mean displacement length (Mean ± SEM), µm		**Top displacement length (Mean ± SEM), µm**	
OT-containing vesicles	Basal	100 mM KCl	Basal	100 mM KCl
Dynamic	0.09 ± 0.01	0.18 ± 0.005	0.34 ± 0.01	0.80 ± 0.005
Delayed	0.08 ± 0.002	0.20 ± 0.002	0.43 ± 0.002	0.95 ± 0.002
Uncoupled	0.11 ± 0.005	0.18 ± 0.003	0.45 ±0.005	0.75 ± 0.003
Stable	0.12 ± 0.01	0.12 ± 0.003	0.54 ± 0.01	0.64 ± 0.003

3.3.- Speed of OT-containing compartments

We also analyzed the speed of OT-containing compartments, which allowed us to perform an additional classification. In this case, the criterion followed was the speed changes (or not) in comparison to the baseline. According to their speed, OT-containing compartments could be classified in: responding (as an alternative: mobile, Fig. 44A, B) and non-responding (alternative: immobile, Fig. 44C). These results were in agreement with the displacement data, that indicated that most OT-compartments belonged to the delayed pool.

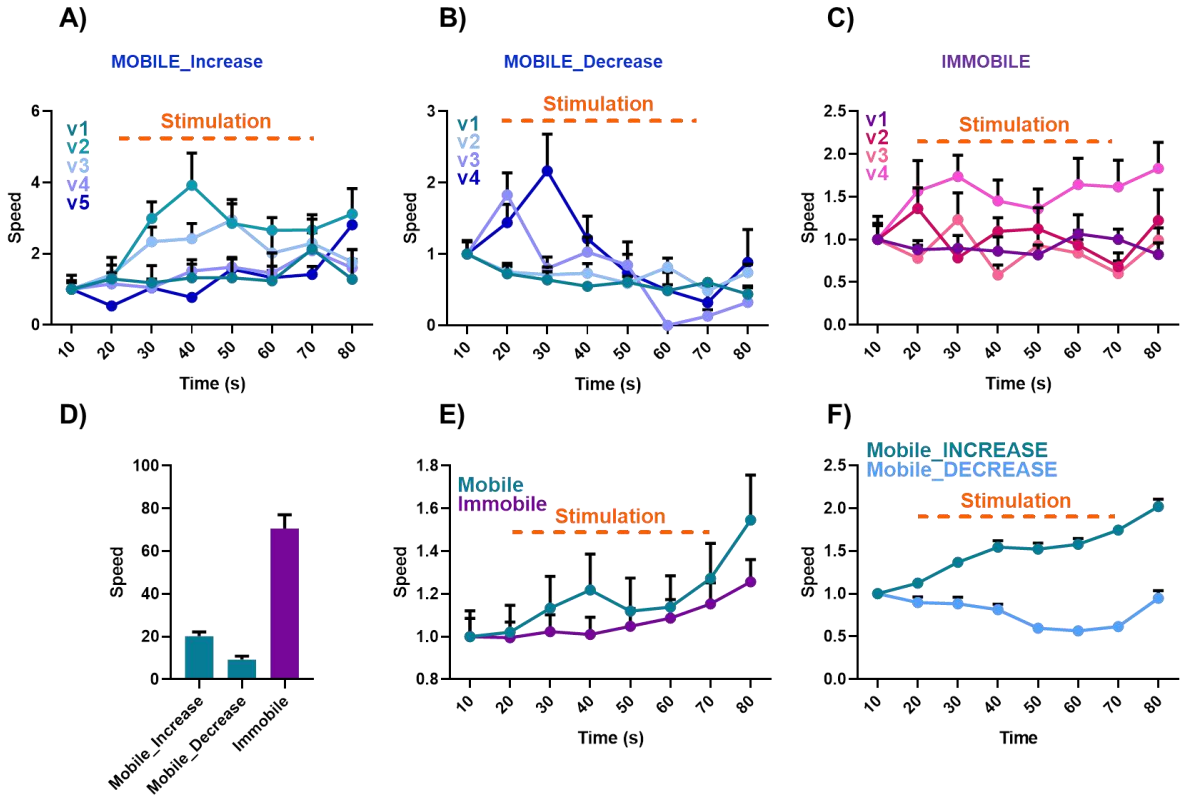

Figure 44.- OT-containing compartments classification depending on their speed in response to neuronal stimulation. **A-B)** OT-containing compartments modified their speed at different time points, either increasing or decreasing it. Each graph represents several individual OT-containing compartments increasing (A) or decreasing (B) their speed at specific time points (mobile). **C)** Individual examples of OT-containing compartments that did not modify their speed in response to stimulation (immobile). **D)** Classification of OT-containing compartments depending on their speed in response to stimulation. **E)** OT-containing compartments could be classified in two groups depending on their speed changes in response to stimulation: responding or mobile, and non-responding or immobile. **F)** Mobile OT-containing compartments could increase or decrease their speed. Presented data are normalized. Statistical analysis: Friedman non-parametric; p-value> 0.05 (ns), ≤ 0.05 (*), ≤ 0.01 (**), ≤ 0.001 (***), ≤ 0.0001 (****). Asterisks in graphs represent the first time point in which the OT-compartment changed its speed compared to the baseline. Appendix, tables 56-82.

The vast majority of OT-containing compartments (70.6 %) belonged to the immobile group (Fig. 44C, D, and E). The remaining 30 % (29.4 %), which could be classified as mobile, showed two subcategories: a subgroup that increased their speed (68.6 % of OT-compartments from the mobile group) and a subgroup that decreased their speed (31.4 % of OT-compartments from the mobile group) (Fig. 44A, B, D, E, and F).

Under basal conditions, OT-containing compartments presented mean speed values ranging from 0.04 to 0.06 µm/s, depending on the group, with top mean speeds ranging from 0.15 to 0.32 µm/s (Table 9). Under stimulus conditions, the three OT-containing compartments subgroups presented similar mean speed values (Table 9).

Table 9.- Mean and top speed of OT-containing compartments.

	Mean speed (± SEM), µm/s		**Top speed (± SEM), µm/s**	
OT-containing compartments	Basal	100 mM KCl	Basal	100 mM KCl
Mobile_Increase	0.04 ± 0.15	0.07 ± 0.12	0.15 ± 0.15	0.34 ± 0.12
Mobile_Decrease	0.06 ± 0.27	0.05 ± 0.10	0.27 ± 0.27	0.28 ± 0.10
Immobile	0.05 ± 0.09	0.05 ± 0.03	0.32 ± 0.09	0.34 ± 0.03

3.4.- Mean Square Displacement of OT-containing compartments

As an additional parameter for characterization, we analyzed the Mean Square Displacement (MSD) of OT-containing compartments. MSD is defined as the surface area covered by a spot (in our case, an OT-compartment) over the time course of the experiment, and it is related to migration efficiency.

First, we conducted a linear fitting to obtain the value of the diffusion coefficient (D) from the MSD parameter for each OT-containing compartment. This analysis yielded two populations: a predominant population (91.1 %) with low slope values, indicating non-diffusive dynamics (Table 10), and a minority pool (8.9 %) with higher slope values, suggesting diffusive movement (Table 10). These populations were named as “Non-diffusive” population and “Diffusive” population, respectively (Table 10, and Fig. 45A-C).

Table 10.- Linear regression analysis of the two populations of OT-containing compartments identified by MSD.

Condition	**R^2**	**Linear regression equation** (slope)	**Diffusion coefficient (D), $\mu m^2/s$**
Diffusive_10 s of basal	0.8846	Y = 0.001414*X + 0.002306	3.53*10-4
Non-diffusive_10 s of basal	0.6735	Y = 0.001608*X + 0.007355	4.02*10-4
Diffusive_10 s of stimulation	0.0303	Y = -0.0001803*X + 0.02199	-4.5*10-5
Non-diffusive_10 s of stimulation	0.0862	Y = 0.0003032*X + 0.02447	7.58*10-5
Diffusive_20 s of stimulation	0.8062	Y = 0.01030*X – 0.2007	0.002.57*10-3
Non-diffusive_20 s of stimulation	0.0862	Y = 0.0003032*X + 0.02447	7.58*10-5
Diffusive_60 s of stimulation	0.9150	Y = 0.004969*X – 0.05056	$1.24*10^{-3}$
Non-diffusive_60 s of stimulation	0.8258	Y = 0.0005905*X + 0.02207	$1.48*10^{-4}$

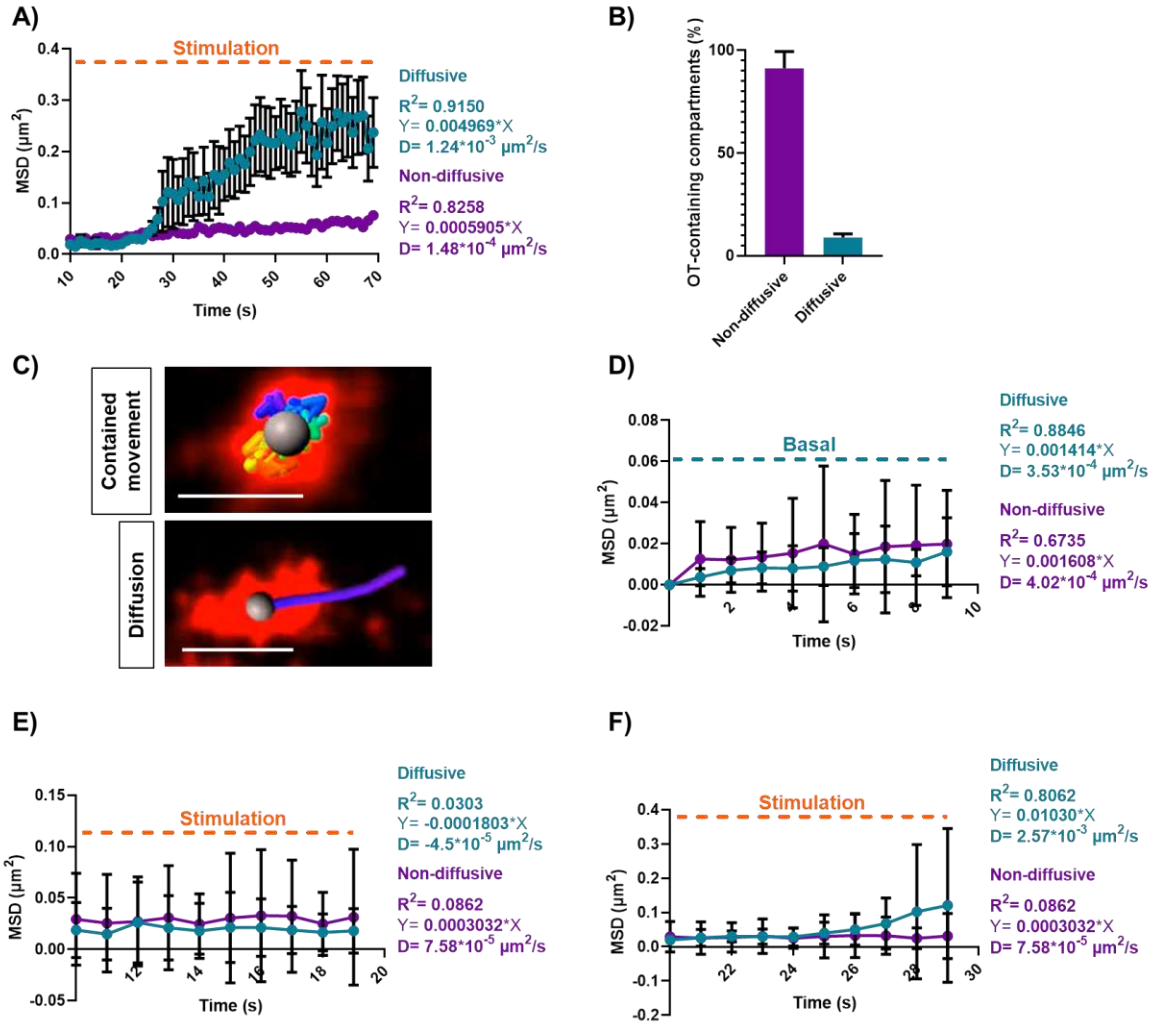

Figure 45.- OT-containing compartments classification depending on their MSD in response to neuronal stimulation. **A)** OT-containing compartments could be classified in two groups depending on their MSD: diffusive and non-diffusive. **B)** The vast majority of the OT-containing compartments analyzed (91.1 %) exhibited non-diffusive movement, meanwhile a small percentage (8.9 %) could be classified as diffusive. **C)** Non-diffusive (top) and diffusive (bottom) OT-containing compartments trajectories. Scale bars indicate 0.4 µm (contained movement) and 0.7 µm (diffusive movement). **D)** MSD of the two identified populations of OT-containing compartments in the first ten seconds of basal application. **E)** MSD of the two identified populations of OT-containing compartments in the first ten seconds of KCl application. **F)** MSD of the two identified populations of OT-containing compartments after ten seconds of KCl application. Appendix, table 83.

Both populations (non-diffusive and diffusive) exhibited significant linearity during the first 10 s of basal application, indicating that in the initial phase of the experiment, OT-containing compartments exhibited diffusive dynamics (Table 10, and Fig. 45D). To note, the “Diffusive” population showed a better fit overall.

During the first ten seconds of stimulation neither population exhibited significant changes in MSD (Table 10, and Fig. 45E). Diffusive movement appeared 10 s after KCl application (20 s after the beginning of the experiment) (Table 10, and Fig. 45F) just in a few compartments (8.9 % of OT-compartments analyzed), indicating an overall delayed mobilization.

These findings were again consistent with the displacement length analysis in which the majority of OT-containing compartments could be classified as “Delayed” (displacement changed after 20-40 s of stimulation). Despite the vast majority of OT-containing compartments did not significantly diffuse over large areas, most exhibited some type of contained movement (as seen in the displacement length results), which could be related to passive vibration of compartments anchored to the cytoskeleton or to the plasma membrane.

4.- Subcellular localization of OT-containing compartments

Our analyses revealed that the majority of the OT-containing compartments were immobile or presented slow kinetics within the second time-scale. Thus, we investigated whether this limited mobility could be due to the presence of OT-containing compartments near the Golgi apparatus. To explore this possibility, we performed immunocytochemistry experiments to analyze the colocalization between OT and the Golgi matrix protein of 130 KDa (Golgin-GM130) in 14 DIV hypothalamic primary cultures from WT P0 mice (Table 5. Primary antibodies: anti-OT rabbit, and anti-Golgin mouse).

The Golgi apparatus was clearly identified with the Golgin-GM130 staining as a well-defined organelle near the cell nucleus (Fig. 46). OT-containing compartments were distributed throughout the soma, some of them in close proximity to the plasma membrane, and others overlapping with Golgin-GM130 (Fig. 46).

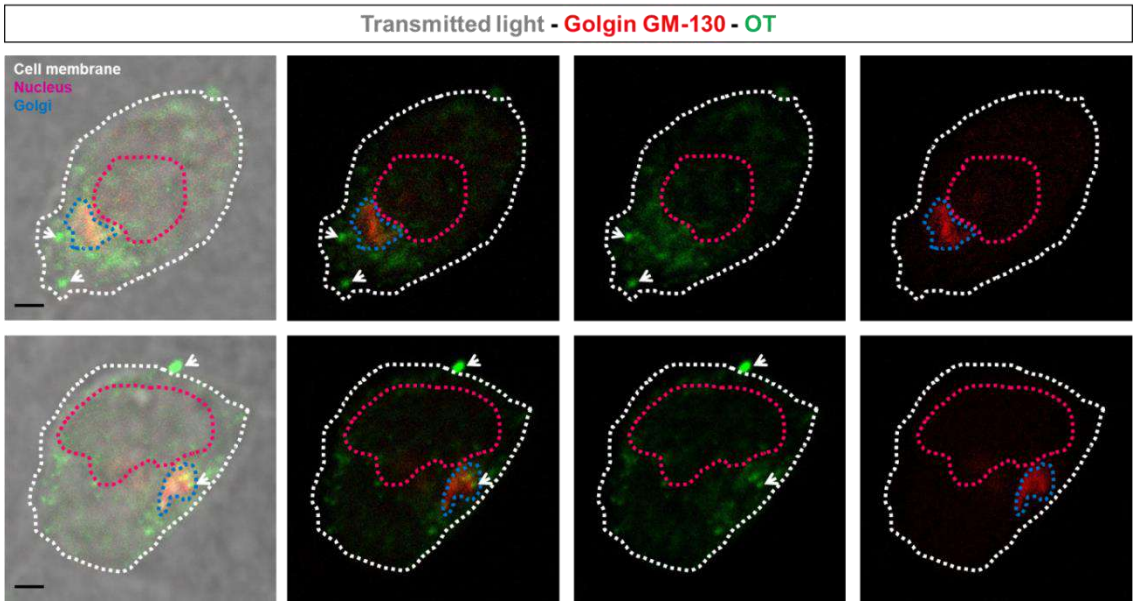

Figure 46.- OT-containing compartments and Golgin-GM-130 in primary hypothalamic cultured neurons. Golgi apparatus (red fluorescence, dotted blue line) was located adjacent to the cell nucleus. OT-containing compartments (green fluorescence, white arrows) were found either in close proximity to the Golgi apparatus, distributed throughout the cytoplasm, or close to the plasma membrane. Dotted white line indicates cell membrane, and dotted pink line indicates cell nucleus. Scale bar indicates 3 μm.

First, we analyzed how many OT-containing compartments were close to the Golgi apparatus with respect to the total number of OT-compartments in the cell. Quantification analysis indicated that around 22 % of the OT-containing compartments were in close contact with Golgi (Fig. 47).

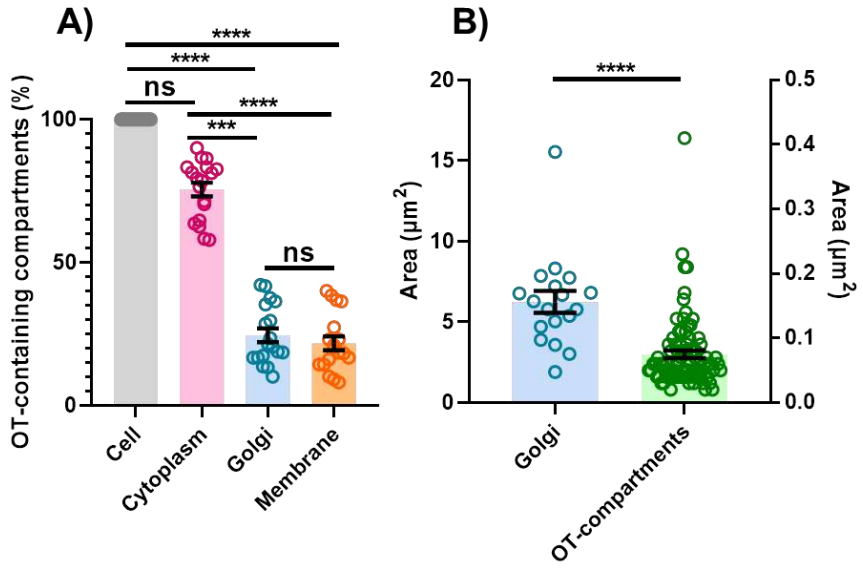

Figure 47.- OT-containing compartments were distributed throughout the cell cytoplasm, and a small percentage was located near Golgi apparatus. **A)** OT-containing compartments distribution throughout the cell indicated that around 22 % of the compartments were in close contact with Golgi (Number of OT-compartments. Cell= 21.39 ± 2.55 vs. Cytoplasm= 16.72 ± 2.35, p-value> 0.9999; Cell= 21.39 ± 2.55 vs. Golgi= 4.68 ± 0.45, p-value< 0.0001; Cell= 21.39 ± 2.55 vs. Membrane= 3.39 ± 0.47, p-value< 0.0001; Cytoplasm= 16.72 ± 2.35 vs. Golgi= 4.68 ± 0.45, p-value= 0.0004; Cytoplasm= 16.72 ± 2.35 vs. Membrane= 3.39 ± 0.47, p-value< 0.0001; Golgi= 4.68 ± 0.45 vs. Membrane= 3.39 ± 0.47, p-value> 0.9999). Statistical analysis: Kruskal-Wallis non-parametric test. **B)** Golgi apparatus presented bigger area than OT-containing compartments (Area in μm^2. OT-compartments= 0.07 ± 0.01 vs. Golgi= 6.23 ± 0.69, p-value< 0.0001). Statistical analysis: Mann-Whitney non-parametric test; p-value> 0.05 (ns), ≤ 0.05 (*), ≤ 0.01 (**), ≤ 0.001 (***), ≤ 0.0001 (****). Appendix, tables 84-87.

Then, we analyzed the degree of colocalization between the OT-containing compartments in close proximity to the Golgi apparatus (22 %) and Golgin-GM130. The colocalization analysis was performed in Fiji using the "UCSD Control" and JACoP plugins (see "*Golgin GM-130 immunocytochemistry: image acquisition and analysis*" section from materials and methods). Colocalization analysis rendered two coefficients: Manders' overlapping coefficient and Pearson's correlation coefficient.

Manders' coefficient refers to the overlapping degree of pixels from two channels. In our case, Manders' coefficient indicates the overlapping between an OT-containing compartment staining and Golgi staining. Pearson's coefficient refers to the correlation degree of pixels from two channels. In our case, Pearson's coefficient corresponds to the correlation between an OT-containing compartment and the Golgi staining.

The percentage of overlapping (Manders' coefficient) between OT-containing compartments and Golgi ranged between 20 and 90 % (Fig. 48A, blue), with a mean overlapping value of 55 ± 1. % (Fig. 48B, blue). Approximately, half of the OT-containing vesicles (54 %) presented Golgi overlapping values between 50 and 60 % (Fig. 48A, blue).

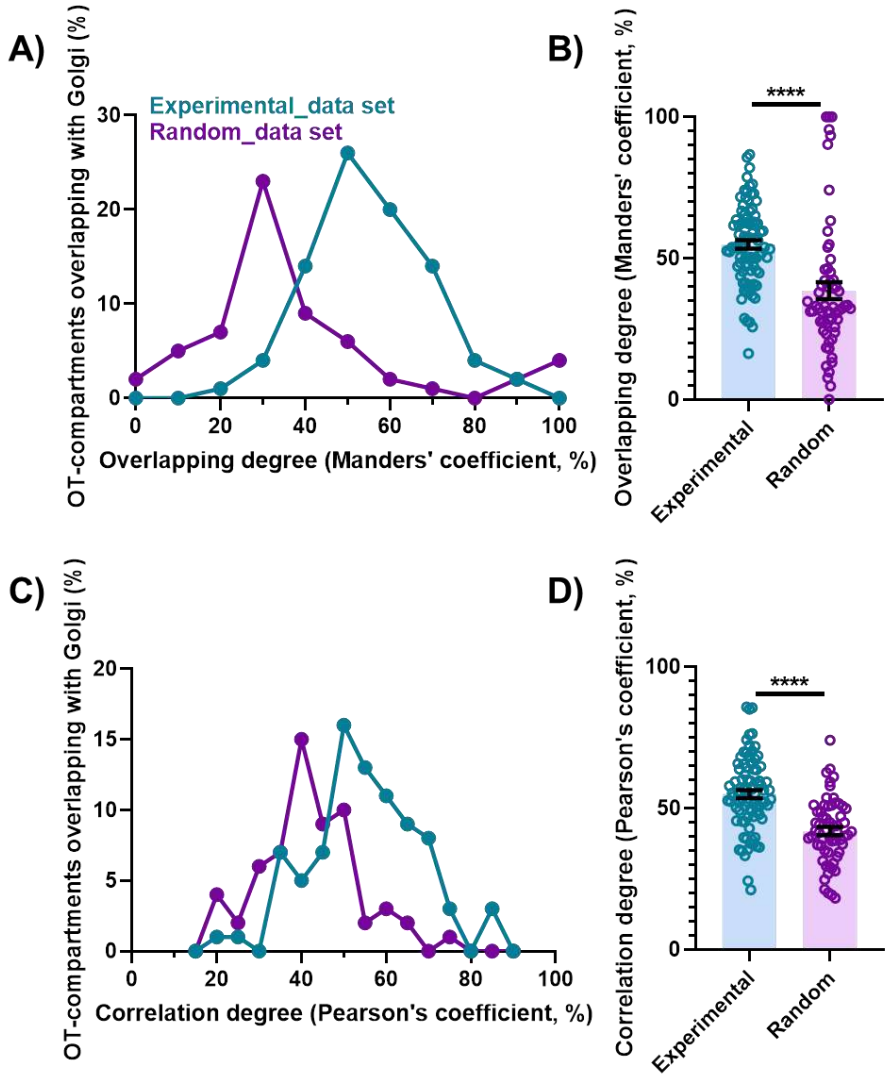

Figure 48.- Colocalization analysis between OT-containing compartments and Golgi apparatus. **A-B)** Manders' overlapping coefficient. OT-containing compartments overlapping coefficient ranged between 20 and 90 % (A, blue. Frequency distribution, Appendix, table 89); the mean overlapping coefficient was 55 % (B, blue. Manders_Experimental= 0.55 ± 0.01 vs. Manders_Random = 0.38 ± 0.03, p-value< 0.0001). **C-D)** Pearson's correlation coefficient. OT-containing compartments correlation coefficient ranged between 20 and 85 % (C, blue. Frequency distribution, Appendix, table 90); the mean correlation coefficient was 55 % (D, blue. Pearson_Experimental = 0.55 ± 0.01 vs. Pearson_Random = 0.42 ± 0.01, p-value< 0.0001). Statistical analysis: Mann-Whitney non-parametric test; p-value> 0.05 (ns), ≤ 0.05 (*), ≤ 0.01 (**), ≤ 0.001 (***), ≤ 0.0001 (****). Appendix, tables 88-91.

Mean Pearsons' coefficient values indicated correlation values ranging between 20 and 85 % (Fig. 48C, blue), with a mean correlation of 55 ± 1 % (Fig. 48D, blue), suggesting that half of the pixels corresponding to the OT-containing compartments overlapped with the Golgin-

GM130 staining. Interestingly, one of the OT-containing compartments presented a Pearson´s coefficient of -4.8 %, indicating an inverse correlation between these two compartments. This value was excluded from the statistical analysis.

We generated a random data set as control to identify the degree of arbitrariness in our experimental conditions. Generation of the random data set is explained in detail in "*Golgin GM-130 immunocytochemistry: image acquisition and analysis. Colocalization analysis between OT-compartmentes and Golgi*" section from materials and methods.

The randomly-generated OT-containing compartments presented a mean value of Manders' overlapping coefficient of 38 ± 3 % (Fig. 48A, B, purple), suggesting that the values obtained with the experimental data set were not due to chance (Fig. 48B, purple. Manders' coefficient_Experimental: 0.55 ± 0.01 vs. Manders' coefficient_Random: 0.38 ± 0.03, p-value< 0.0001). Similar scenario was found in the case of Pearson's correlation coefficient, presenting mean values of the randomly-generated OT-containing compartments of 42 ± 1 %, whereas the mean value of the experimental OT-containing compartments was 55 ± 1 % (Fig. 48C, D, purple. Pearson's_coefficient_Experimental: 0.55 ± 0.01 vs. Pearson's coefficient_Random: 0.42 ± 0.01, p-value <0.0001).

5.- Modeling OT-compartments' dynamics

Following the dynamics experiments, we conducted simulations to analyze the movement of OT-compartments in greater detail. A mathematical model of oxytocinergic neurons was developed in collaboration with Prof. Amparo Gil (University of Cantabria), as described in "*OT vesicle dynamics. Mathematical model*" section from materials and methods.

Using the geometrical model (conical domain: 17 slices), we simulated the dynamic behavior of diffusive and non-diffusive OT-containing compartments over 1 min of basal incubation, followed by 1 min of stimulus incubation. The simulations started from three distinct cellular zones: near the nucleus (slices from 12 to 17), in the cytoplasm (slices from 6 to 11), and at the membrane (slices from 1 to 5).

These simulations were generated by modifying the script to specify the diffusion coefficient and the initial position of the OT-compartments. The number of diffusive (n= 11) and non-diffusive (n= 93) OT-compartments was selected based on experimental data, with "n" indicating the actual difference in the number of diffusive and non-diffusive compartments.

Results indicated that, during 1 min of stimulation, OT-containing compartments, either diffusive or non-diffusive, remained within their initial region (near the nucleus, at the cytoplasm or at the membrane), and did not move to a different region (Fig. 49A, B, and C).

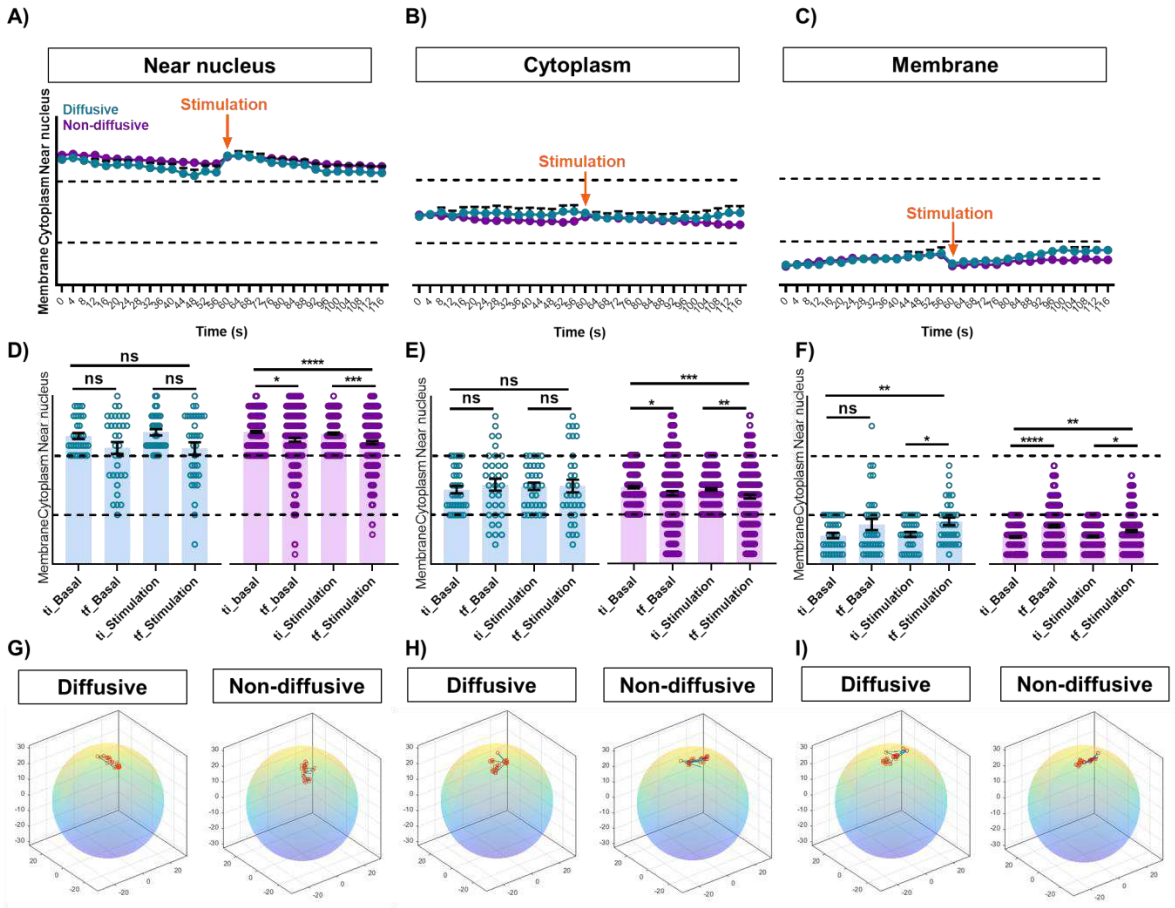

Figure 49.- Modeling of OT-compartments' dynamics. **A-C)** Simulations of diffusive and non-diffusive OT-compartments over time were conducted under basal and stimulation conditions, starting near the nucleus (A), within the cytoplasm (B), and at the membrane (C). **D-F)** Statistical analysis of the positions of diffusive OT-compartments between the initial and final time points under basal and stimulation conditions was performed for compartments near the nucleus (D, blue. ti_Basal: 12.97 ± 0.31 vs. tf_Basal: 11.76 ± 0.61, p-value= 0.3015; ti_Stimulation: 13.36 ± 0.40 vs. tf_Stimulation: 11.70 ± 0.63, p-value= 0.0827; ti_Basal: 12.97 ± 0.31 vs. tf_Stimulation: 11.70 ± 0.63, p-value= 0.2577), in the cytoplasm (E, blue. ti_Basal: 7.58 ± 0.37 vs. tf_Basal: 8.06 ± 0.60, p-value= 0.5833; ti_Basal: 7.58 ± 0.37 vs. tf_Stimulation: 7.94 ± 0.64, p-value= 0.9310; ti_Stimulation: 7.58 ± 0.43 vs. tf_Stimulation: 7.94 ± 0.64, p-value= 0.9821), and at the membrane (F, blue. ti_Basal: 2.91 ± 0.27 vs. tf_Basal: 4.03 ± 0.57, p-value= 0.3087; ti_Stimulation: 3.24 ± 0.21 vs. tf_Stimulation: 4.33 ± 0.38, p-value= 0.0591; ti_Basal: 2.91 ± 0.27 vs. tf_Stimulation: 4.33 ± 0.39, p-value= 0.0079). Similarly, statistical analysis of non-diffusive OT-compartments' positions was conducted between initial and final time points under basal and stimulus conditions for compartments starting near the nucleus (D, purple. ti_Basal: 13.39 ± 0.11 vs. tf_Basal: 12.58 ± 0.19, p-value= 0.0435; ti_Stimulation: 13.34 ± 0.12 vs. tf_Stimulation: 11.98 ± 0.17, p-value< 0.0001; ti_Basal: 13.39 ± 0.11 vs. tf_Stimulation: 12.31 ± 0.17, p-value< 0.0001), in the cytoplasm (E, purple. ti_Basal: 7.74 ± 0.11 vs. tf_Basal: 7.13 ± 0.22, p-value = 0.0270; ti_Stimulation: 7.54 ± 0.12 vs. tf_Stimulation: 6.80 ± 0.20, p-value= 0.0022; ti_Basal: 7.74 ± 0.11 vs. tf_Stimulation: 6.80 ± 0.20, p-value< 0.0001), and at the membrane (F, purple.ti_Basal: 2.76 ± 0.08 vs. tf_Basal: 3.88 ± 0.14, p-value< 0.0001; ti_Stimulation: 2.91 ± 0.09 vs. tf_Stimulation: 3.39 ± 0.12, p-value= 0.0404; ti_Basal: 2.76 ± 0.08 vs. tf_Stimulation: 3.39 ±

0.12, p-value= 0.0037). **G-I)** Schematic representation of a model vesicle is provided for those starting near the nucleus (G), in the cytoplasm (H), and at the membrane (I). Vesicles' positions are indicated by the number slice: membrane (slices from 1 to 5), cytoplasm (slices from 6 to 11), and near the nucleus (slices from 12 to 17). Statistical analysis: Mann-Whitney non-parametric test; p-value> 0.05 (ns), ≤ 0.05 (*), ≤ 0.01 (**), ≤ 0.001 (***), ≤ 0.0001 (****). Appendix, tables 92-97.

5.1.- Modeling OT compartments' dynamics near the nucleus

When OT compartments started near the nucleus, diffusive compartments appeared to migrate toward the cytoplasm under basal conditions (Fig. 49D, blue. Diffusive, ti_Basal: 12.97 ± 0.31 vs. tf_Basal: 11.76 ± 0.61, p-value= 0.3015). A similar trend was observed for non-diffusive vesicles, which were capable of reaching the membrane (Fig. 49D, purple. Non-diffusive, ti_Basal: 13.39 ± 0.11 vs. tf_Basal: 12.58 ± 0.19, p-value= 0.0435).

In the final seconds of stimulation, both diffusive and non-diffusive OT-compartments migrated toward the cytoplasm and even reached the membrane (Fig. 49D. Diffusive, ti_Stimulation: 13.36 ± 0.40 vs. tf_Stimulation: 11.70 ± 0.63, p-value= 0.0827; Non-diffusive, ti_Stimulation: 13.34 ± 0.12 vs. tf_Stimulation: 11.98 ± 0.17, p-value< 0.0001).

Comparing the initial (basal) and final (stimulation) points, we observed that KCl mobilized OT-compartments from the nucleus to the cytoplasm, and even to the membrane (Fig. 49D. Diffusive, ti_Basal: 12.97 ± 0.31 vs. tf_Stimulation: 11.70 ± 0.63, p-value= 0.2577; Non-diffusive, ti_Basal: 13.39 ± 0.11 vs. tf_Stimulation: 12.31 ± 0.17, p-value< 0.0001), reinforcing the mobilizing effect of our stimulation protocol observed in chasing experiments (Fig. 40A). Consequently, extending the simulation time might result in an even greater number of OT-compartments reaching the cytoplasm and membrane.

5.2.- Modeling OT-compartments' dynamics in the cytoplasm

The modeling results for OT-compartments originating in the cytoplasm closely mirrored those observed for compartments starting near the nucleus.

In the final seconds of basal simulation, diffusive compartments that started in the cytoplasm were found near the nucleus, within the cytoplasm, and at the membrane, although the changes were not significant (Fig. 49E, blue. Diffusive, ti_Basal: 7.58 ± 0.37 vs. tf_Basal: 8.06 ± 0.60, p-value = 0.5833). This result suggested that cytoplasmic OT-compartments move throughout the entire cell. Similarly, non-diffusive compartments were distributed throughout the cell after 1 min of basal simulation (Fig. 49E, purple. Non-diffusive, ti_Basal: 7.74 ± 0.11 vs. tf_Basal: 7.13 ± 0.22, p-value = 0.0270).

During the stimulation, both diffusive and non-diffusive compartments were distributed throughout the cell at the starting point. By the end of the stimulation, OT-compartments became even more heterogeneously distributed (Fig. 49E. Diffusive, ti_Stimulation: 7.58 ± 0.43 vs. tf_Stimulation: 7.94 ± 0.64, p-value= 0.9821; Non-Diffusive, ti_Stimulation: 7.54 ± 0.12 vs. tf_Stimulation: 6.80 ± 0.20, p-value= 0.0022). The increased mobility of these

compartments under stimulation may suggest that molecular anchors could have been disrupted to facilitate mobility.

Finally, stimulation induced redistribution of OT-compartments from the cytoplasm to other parts of the cell (Fig. 49E. Diffusive, ti_Basal: 7.58 ± 0.37 vs. tf_Stimulation: 7.94 ± 0.64, p-value= 0.9310; Non-diffusive, ti_Basal: 7.74 ± 0.11 vs. tf_Stimulation: 6.80 ± 0.20, p-value= 0.0001), indicating active trafficking of these compartments, and further supporting the mobilizing effect of KCl observed in our experiments (Fig. 40A).

5.3.- Modeling OT-compartments' dynamics in the membrane

Both diffusive and non-diffusive OT-compartments exhibited similar results starting from the membrane.

Several diffusive and non-diffusive compartments moved to the cytoplasm, and even approached the nucleus, after 1 min under basal conditions (Fig. 49F. Diffusive, ti_Basal: 2.91 ± 0.27 vs. tf_Basal: 4.03 ± 0.57, p-value= 0.3087; Non-diffusive, ti_Basal: 2.76 ± 0.08 vs. tf_Basal: 3.88 ± 0.14, p-value< 0.0001). It is important to note that the mathematical model was configured to simulate compartments' movement throughout the cell, not to or from the extracellular space. Therefore, the model could not identify release events expected to occur under physiological conditions.

Under stimulus conditions, both diffusive and non-diffusive compartments were found mostly at the membrane (Fig. 49F. Diffusive, ti_Stimulation: 3.24 ± 0.21 vs. tf_Stimulation: 4.33 ± 0.38, p-value= 0.0591; Non-diffusive, ti_Stimulation: 2.91 ± 0.09 vs. tf_Stimulation: 3.39 ± 0.12, p-value= 0.0404), indicating that, when compartments are positioned in the membrane, the stimulation strengthen the interaction. These findings support the chasing experiments' results, which showed a significant increase in the number of OT-containing compartments following KCl stimulation (Fig. 40A).

Comparison between the initial (basal) and final (stimulation) points of the simulation revealed that under KCl incubation, OT-compartments originating from the membrane were predominantly found in the membrane but also in the cytoplasm (Fig. 49F. Diffusive, ti_Basal: 2.91 ± 0.27 vs. tf_Stimulation: 4.33 ± 0.39, p-value= 0.0079; Non-diffusive, ti_Basal: 2.76 ± 0.08 vs. tf_Stimulation: 3.39 ± 0.12, p-value= 0.0037).

From these simulations, we can conclude that both diffusive and non-diffusive OT-compartments could be able to reach different subcellular regions, despite their distinct movement patterns.

6.- SNARE proteins' expression in hypothalamic oxytocinergic neurons

Results from the dynamics' analysis of OT-containing compartments indicated distinct properties of release and recruitment to the plasma membrane upon neuronal stimulation. We thus hypothesized that such properties could be underlined by a specific SNARE fusion machinery acting at the somatodendritic compartment of oxytocinergic neurons. We then ought to analyze the expression of common presynaptic SNARE proteins, as well as unconventional isoforms previously described to play a role in dendritic trafficking (Jurado et al., 2013; Arendt et al., 2015; Jurado, 2014). To this aim, we performed a detailed immunochemistry characterization in hypothalamic slices at postnatal and adult developmental stages from WT mice as well as in hypothalamic primary cultures from OT^{EYFP} P0 mice.

6.1.- Expression of SNAP isoforms in the adult PVN and SON

Immunohistochemistry experiments showed that non-canonical SNAREs could be found at the somatodendritic compartment of oxytocinergic neurons in both the PVN and SON (Fig. 50). As such, SNAP-25, a prototypical presynaptic SNARE protein highly expressed in the brain (Kádková et al., 2019), was not found in the soma and dendrites of hypothalamic neurons, but identified in their fibers and axonal projections. In contrast, two less common isoforms, SNAP-23 and SNAP-47, were found in the cell bodies of oxytocinergic neurons in the PVN and SON (Fig. 50).

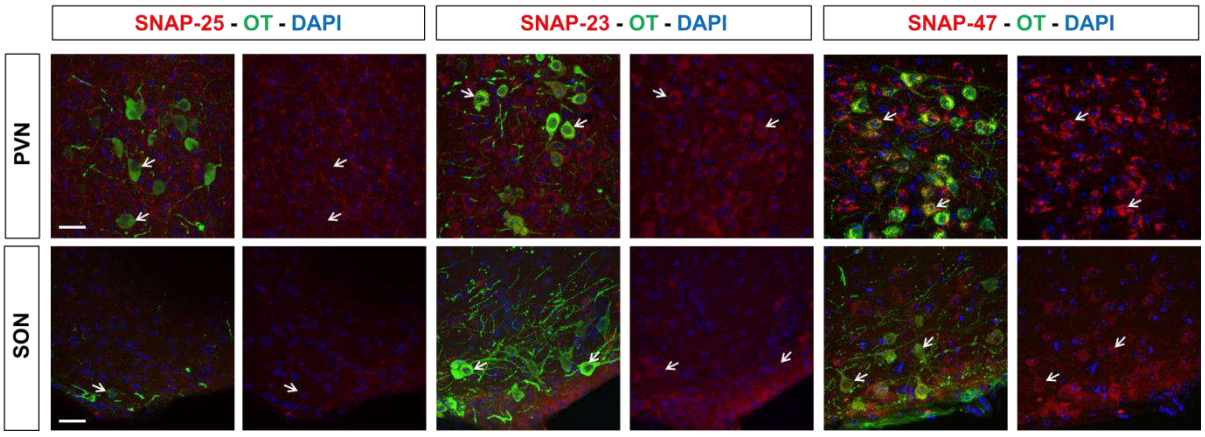

Figure 50.- Expression of SNAP proteins in OT hypothalamic neurons in the adult brain. In the adult brain, canonical presynaptic SNAP-25 was concentrated in the fibers of hypothalamic neurons within the PVN and SON, but not in the somas of OT neurons. The SNAP isoforms SNAP-23 and SNAP-47 were found expressed in PVN and SON OT hypothalamic neurons. OT is stained in green; SNAPs are stained in red; white arrows point oxytocinergic neurons coexpressed or not with SNAP proteins. Scale bar indicates 30 µm.

6.2.- Expression of syntaxin proteins in the adult PVN and SON

We expanded our characterization by analyzing the expression of syntaxin proteins, another essential member of the SNARE fusion complex. Immunohistochemistry experiments indicated that Stx-1, a canonical presynaptic syntaxin isoform, was confined to fibers in the PVN, but it did not colocalize with oxytocinergic neurons. In contrast, Stx-1 expression was found in some oxytocinergic cells in the SON, suggesting a region–specific expression pattern. Furthermore, either Stx-3 or Stx-4 did not colocalize with OT neurons, although Stx-4 was found in non-OT neurons in the SON (Fig. 51).

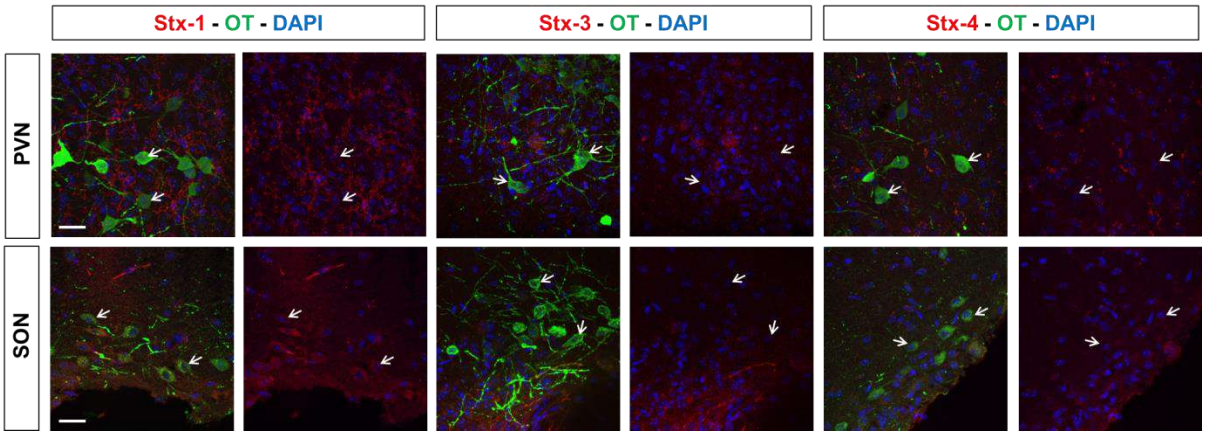

Figure 51.- Expression of Stx proteins in OT hypothalamic neurons in the adult brain. Stx-1 did not colocalize with OT hypothalamic neurons in the PVN; meanwhile it exhibited colocalization with a subpopulation of OT neurons in the SON. Stx-3 was not expressed in OT hypothalamic neurons. Stx-4 was not expressed in the PVN, although it could be found in non-OT neurons in the SON. OT staining is stained in green; Stxs are stained in red; white arrows point oxytocinergic neurons coexpressed or not with Stx proteins. Scale bar indicates 30 µm.

6.3.- Expression of synaptotagmin proteins in the adult PVN and SON

We first analyzed the expression in the PVN and SON of Syt-1, a canonical presynaptic calcium sensor. Our findings indicated no detectable expression of Syt-1 in oxytocinergic hypothalamic neurons. Similarly, Syt-7 was not detected in these cells. As expected from previous studies (G. Zhang et al., 2011), Syt-4 was found in the PVN and SON, colocalizing with oxytocinergic neurons in both regions (Fig. 52).

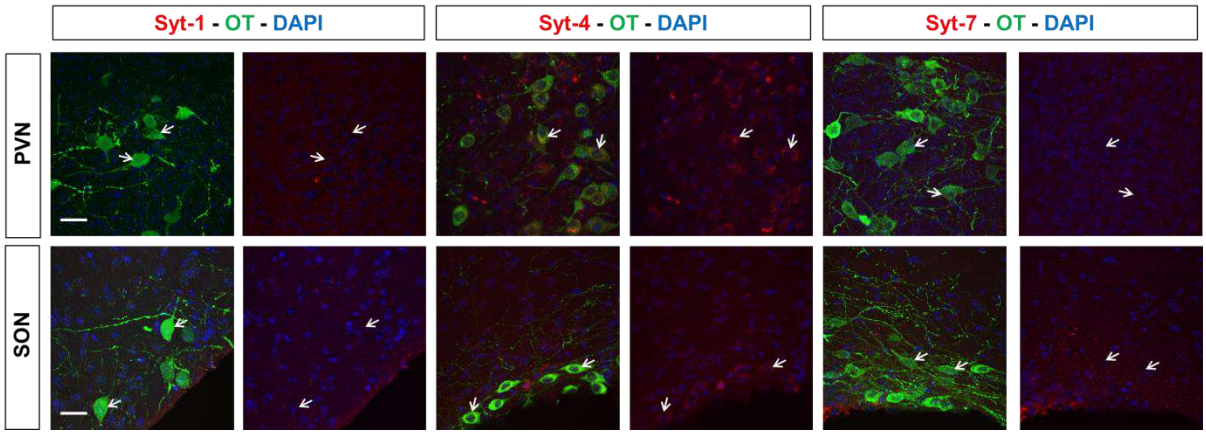

Figure 52.- Expression of Syt proteins in OT hypothalamic neurons in the adult brain. Whereas expression of either Syt-1 or Syt-7 isoforms was not detected in hypothalamic OT neurons, Syt-4 isoform showed a clear overlap with OT neurons. OT is stained in green; Syts are stained in red; white arrows point oxytocinergic neurons coexpressed or not with Syt proteins. Scale bar indicates 30 µm.

6.4.- Expression of synaptobrevin proteins in the adult PVN and SON

Finally, we analyzed the expression of Syb proteins in the PVN and SON, as the third mandatory component required to form a functional SNARE complex. Our immunohistochemistry experiments were unable to identify Syb-1, 2, 3, the most common brain Syb isoforms, in the PVN. Nonetheless, these proteins seemed to be expressed in the SON, although excluded from oxytocinergic neurons (Fig. 53).

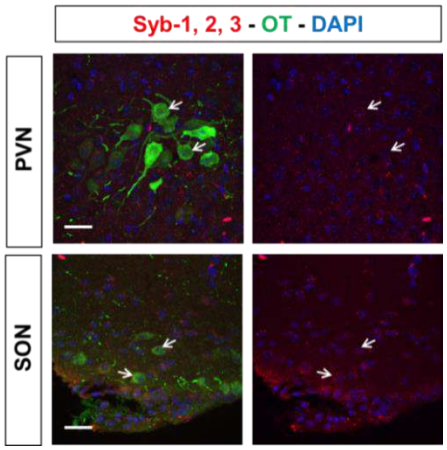

Figure 53.- Expression of Syb proteins in OT hypothalamic neurons in the adult brain. Common Syb isoforms (Syb-1, 2, 3) were not detected in PVN neurons. Although these isoforms were found in the SON, they did not colocalize with OT neurons. OT is stained in green; Sybs are stained in red; white arrows point oxytocinergic neurons coexpressed or not with Syb proteins. Scale bar indicates 30 µm.

6.5.- Developmental expression of somatodendritic SNARE isoforms in OT neurons

Our results identified Syt-4, SNAP-23, and SNAP-47 as potential candidates to mediate somatodendritic OT-compartment's dynamics in oxytocinergic neurons. Thus, we decided to explore the expression of these proteins during early postnatal development in order to better characterize their expression patterns.

Immunohistochemistry analyses revealed that SNAP-23 and Syt-4, which were found to colocalize with OT neurons in the adult brain, were not expressed in PVN and SON neurons of P0 mice (Fig. 54). In contrast, clear SNAP-47 signal was detected in oxytocinergic neurons from newborn mice (Fig. 54).

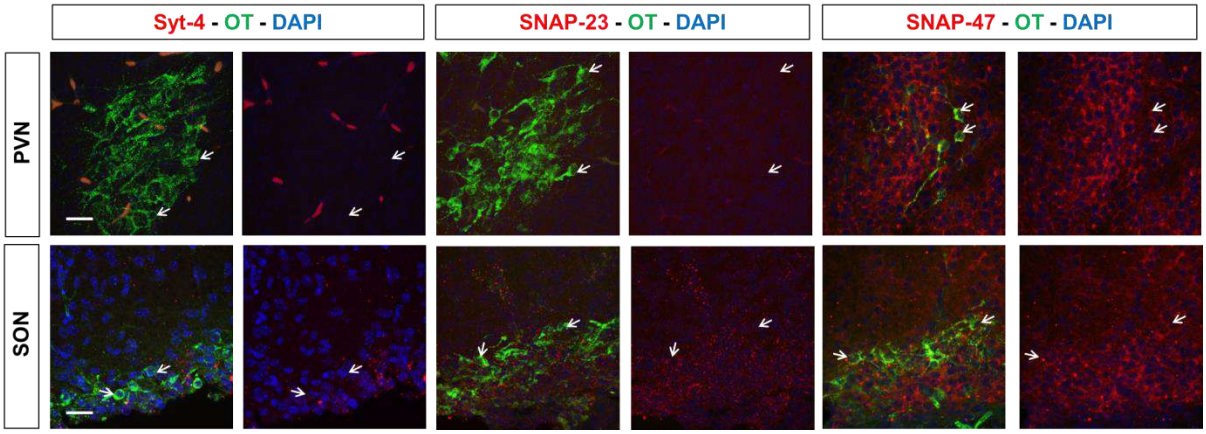

Figure 54.- Expression of SNARE proteins in OT hypothalamic neurons at P0. Syt-4 and SNAP-23 proteins were not found in OT neurons at P0 in contrast to SNAP-47, which colocalized with OT neurons within the PVN and SON at this developmental stage. OT is stained in green; Syt-4, SNAP-23 and SNAP-47 are stained in red; white arrows point oxytocinergic neurons coexpressed or not with Syt-4, SNAP-23 or SNAP-47 proteins. Scale bar indicates 30 µm.

These results indicated that non-classical SNARE proteins could be found in the somatodendritic compartment of oxytocinergic neurons, and that the expression of these proteins appeared to be developmentally regulated, with SNAP-47 being the most stably expressed throughout development.

6.6.- SNAREs' expression in hypothalamic primary cultures

In view of the results described above, we decided to focus on SNAP-47 as a potential candidate to regulate OT dynamics and exocytosis at the somatodendritic compartment of oxytocinergic neurons. Thus, to complete the characterization of SNAP-47 in oxytocinergic neurons, we performed immunocytochemistry experiments in primary hypothalamic cultures (Fig. 55A), since this was a central model for many of the assays performed in the present study. For these experiments, we employed OT^{EYFP} P0 mice, and stained OT and SNAP-47 with specific primary antibodies (Table 5. Primary antibodies: anti-GFP: chicken, and anti-SNAP-47 rabbit).

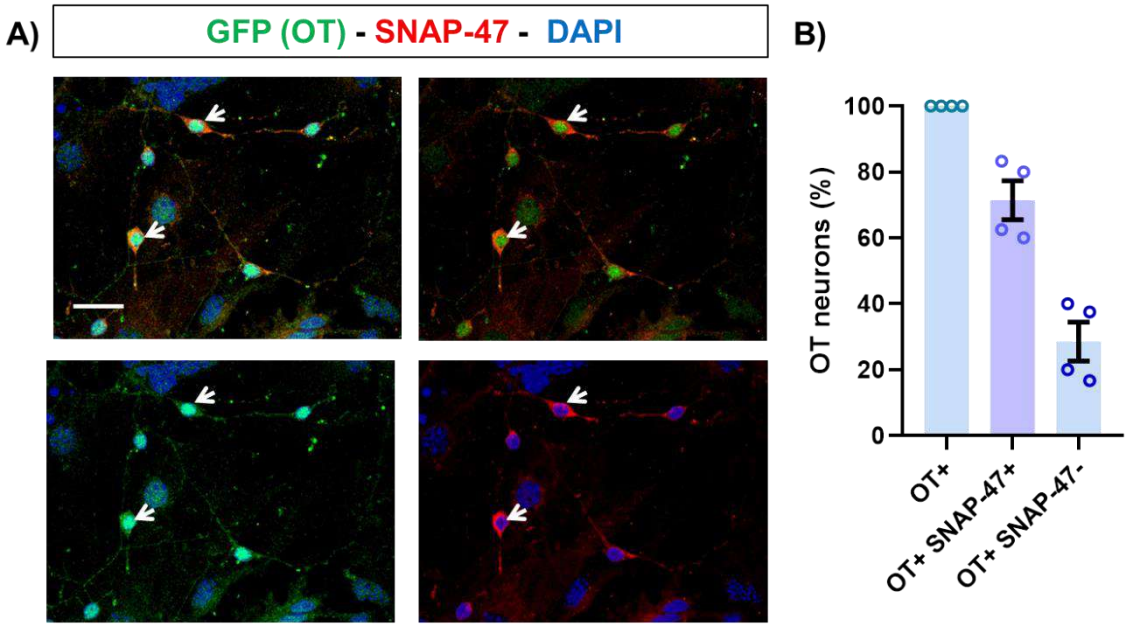

Figure 55.- Expression of SNAP-47 protein in hypohalamic primary cultures. **A)** Oxytocinergic primary cultured neurons (green) expressed SNAP-47 (red). White arrows point oxytocinergic neurons which also expressed SNAP-47 protein. Scale bar indicates 50 µm. **B)** Approximately 70 % of cultured oxytocinergic neurons also expressed SNAP-47. Appendix, table 98.

Our results indicated that 70.83 % of cultured oxytocinergic neurons also expressed SNAP-47 (Fig. 55B). This result suggested that SNAP-47 is abundant in the soma of oxytocinergic primary hypothalamic neurons, making this system suitable for studying a potential role of SNAP-47 in OT dynamics and exocytosis.

6.7.- SNAP-47 is primarily expressed in the somatodendritic compartment

Immunochemistry experiments indicated that SNAP-47 is primarily expressed in the somatodendritic compartment of oxytocinergic neurons (Fig. 50, 54, and 55). Nonetheless, we also explored a potential axonal localization by co-staining SNAP-47 and α-tubulin, a common microtubule marker enriched in axonal compartments. For these experiments, we employed hypothalamic PVN slices from adult OT^{tdTom} mice (3-4 months old).

Our findings indicated no clear colocalization between SNAP-47 and α-tubulin (Fig. 56). SNAP-47 staining was restricted to the somatodendritic compartment of oxytocinergic neurons, whereas α-tubulin staining was limited to fibers. These results indicated that SNAP-47 is primarily enriched in the postsynaptic compartment of oxytocinergic neurons.

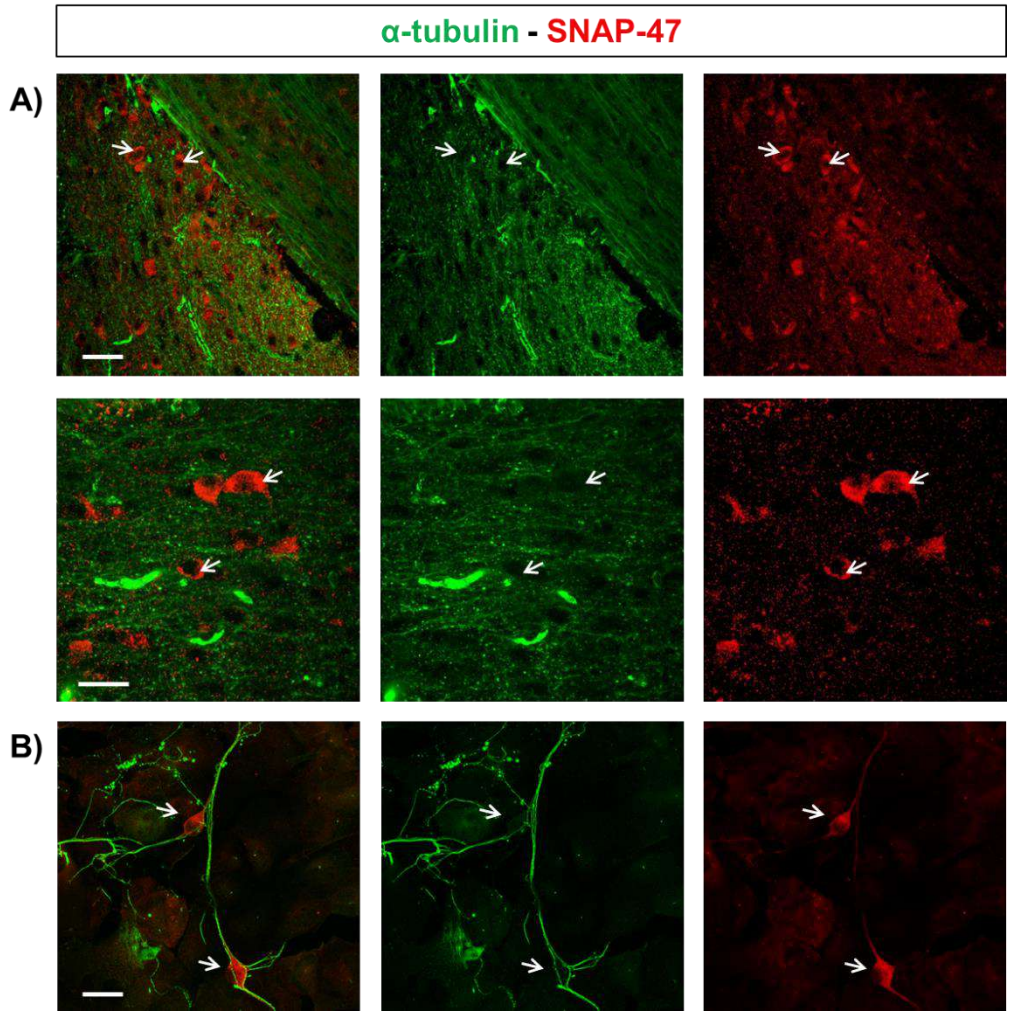

Figure 56.- Expression of SNAP-47 and α-tubulin in OT neurons. SNAP-47 (red) did not colocalize with the axonal marker α-tubulin (green) in oxytocinergic PVN neurons **(A)** or with primary cultured oxytocinergic neurons **(B)**. White arrows indicate OT neurons expressing SNAP-47, and no α-tubulin signal. Scale bars indicate 50 μm (upper panel), and 30 μm (middle and lower panel).

7.- OT and SNAP-47 interaction in the plasma membrane of hypothalamic oxytocinergic neurons

Once SNAP-47 was identified as a somatodendritic SNARE in OT neurons (Fig. 50, 54, and 55), we proceeded to investigate its interaction with OT-containing compartments. To this aim, we performed chasing experiments in primary hypothalamic cultured neurons between 10-13 DIV from OT^{EYFP} P0 mice (see "*Chasing experiments*" section from materials and methods), employing a specific anti-SNAP-47 antibody (Table 5. Primary antibody: anti-SNAP-47 rabbit) to identify SNAP-47-membrane patches (Fig. 57).

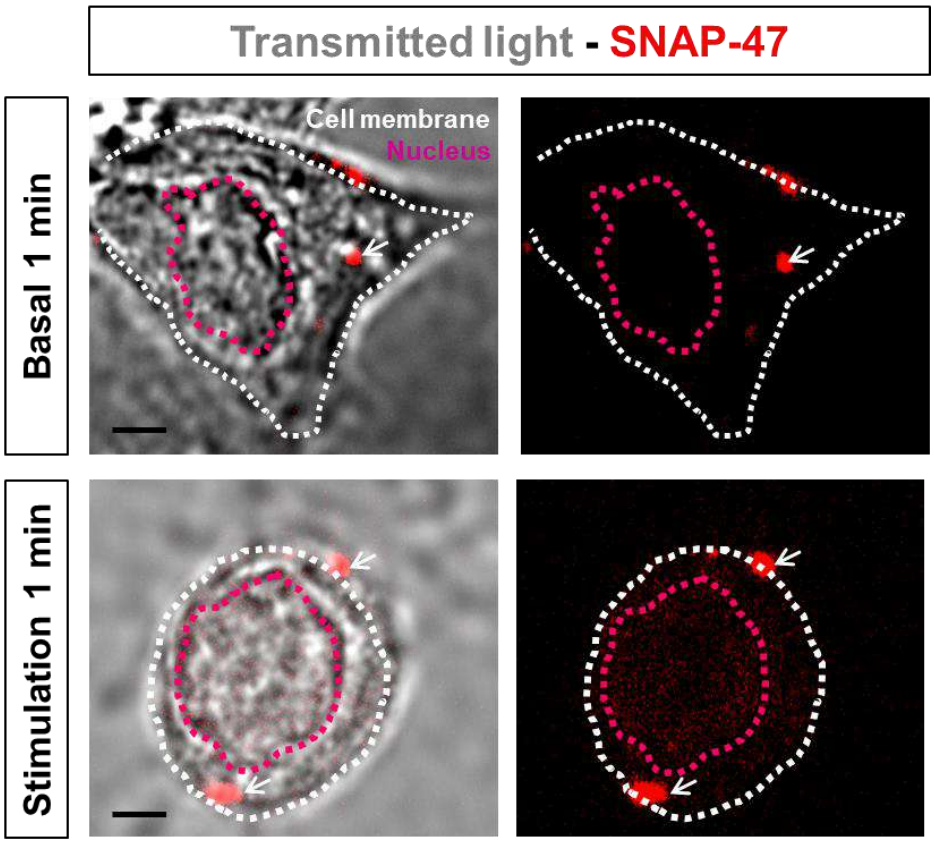

Figure 57.- SNAP-47-membrane patches in hypothalamic cultured OT neurons under basal and stimulated conditions. SNAP-47 was stained in red (white arrows). Dotted white line indicates cell membrane, and dotted pink line indicates cell nucleus. Scale bar indicates 3 µm.

7.1.- Properties of SNAP-47-membrane patches

7.1.1.- The number of SNAP-47-membrane patches is not affected by neuronal stimulation

Results from these experiments indicated that the number of SNAP-47-membrane patches was independent of the treatment (Fig. 58A. Number of SNAP-47-patches. Basal_1 min: 3.50 ± 0.40 vs. Stimulation_1 min: 3.44 ± 0.33, p-value= 0.6445; Basal_10 min: 2.50 ± 0.54 vs. Stimulation_10 min: 1.56 ± 0.24, p-value= 0.2488). Treatment duration slightly affected the number of SNAP-47-membrane patches, despite not significant results (Fig. 58A. Number of SNAP-47-patches. Basal_1 min: 3.50 ± 0.40 vs. Basal_10 min: 2.50 ± 0.54, p-value= 0.9670; Stimulation_1 min: 3.44 ± 0.33 vs. Stimulation_10 min: 1.56 ± 0.24, p-value= 0.1939). These data indicates that SNAP-47-membrane patches are quite stable across different conditions.

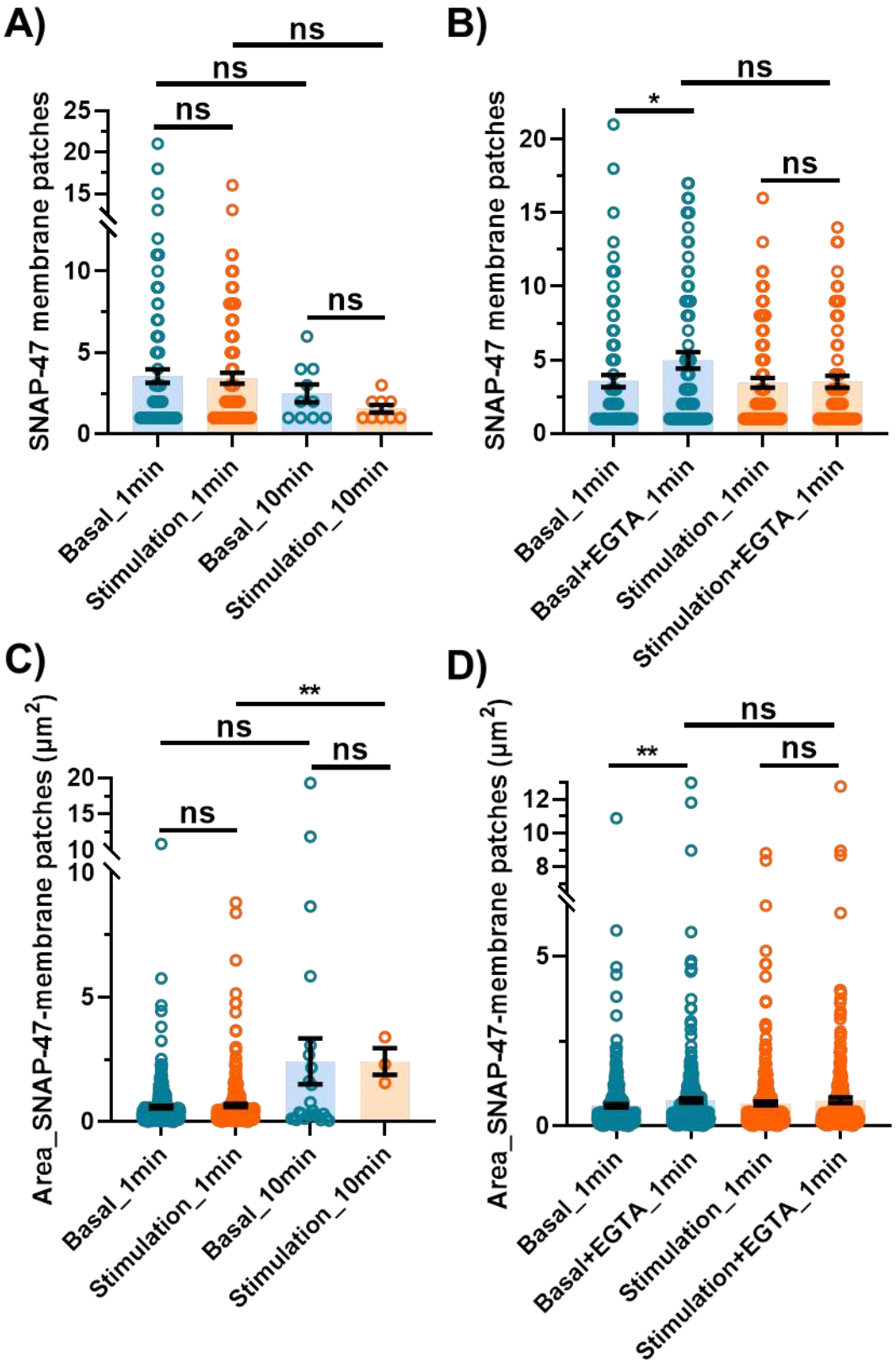

Figure 58.- SNAP47-membrane patches' number and area in hypothalamic primary cultured neurons. **A)** The number of SNAP-47-membrane patches was independent of the treatment applied and the incubation time (Number of SNAP-47-patches. Basal_1 min: 3.50 ± 0.40 vs. Stimulation_1 min: 3.44 ± 0.33, p-value= 0.6445; Basal_10 min: 2.50 ± 0.54 vs.

Stimulation_10 min: 1.56 ± 0.24, p-value= 0.2488; Basal_1 min: 3.50 ± 0.40 vs. Basal_10 min: 2.50 ± 0.54, p-value= 0.9670; Stimulation_1 min: 3.44 ± 0.33 vs. Stimulation_10 min: 1.56 ± 0.24, p-value= 0.1939)**. B)** The number of SNAP-47-membrane patches increased in the absence of extracellular calcium under basal conditions (Number of SNAP-47-patches. Basal_1 min: 3.56 ± 0.41 vs. Basal+EGTA_1 min: 4.96 ± 0.56, p-value= 0.0457). Under stimulus conditions, SNAP-47-membrane patches remained similar (Number of SNAP-47-patches. Stimulation_1 min: 3.44 ± 0.33 vs. Stimulation+EGTA_1 min: 3.51 ± 0.40, p-value= 0.8052; Basal+EGTA_1 min: 4.96 ± 0.56 vs. Stimulation+EGTA_1 min: 3.51 ± 0.40, p-value= 0.1534). **C)** SNAP-47 patches' area was not affected by the type of treatment (Area in μm^2. Basal_1 min: 0.59 ± 0.05 vs. Stimulation_1 min: 0.66 ± 0.06, p-value= 0.8451; Basal_10 min: 2.43 ± 0.92 vs. Stimulation_10 min: 2.43 ± 0.53, p-value= 0.1651). Incubation time increased the area in response to 10 min incubation Area in μm^2. Basal_1 min: 0.59 ± 0.05 vs. Basal_10 min: 2.43 ± 0.92, p-value= 0.3038; Stimulation_1 min: 0.66 ± 0.06 vs. Stimulation_10 min: 2.43 ± 0.53, p-value= 0.0014). **D)** In the absence of extracellular calcium, the area of SNAP-47-membrane patches was larger under basal conditions, and remained similar under stimulated conditions (Area in μm^2. Basal_1 min: 0.59 ± 0.05 vs. Basal + EGTA_1 min: 0.75 ± 0.06, p-value= 0.0074; Stimulation_1 min: 0.66 ± 0.06 vs. Stimulation+EGTA_1 min: 0.76 ± 0.08, p-value= 0.3154; Basal+EGTA_1 min: 0.75 ± 0.06 vs. Stimulation+EGTA_1 min: 0.76 ± 0.08, p-value= 0.1289). Statistical analysis: Mann-Whitney non-parametric test; p-value> 0.05 (ns), ≤ 0.05 (*), ≤ 0.01 (**), ≤ 0.001 (***), ≤ 0.0001 (****). Appendix, tables 99-102.

7.1.2.- Analysis of SNAP-47-membrane patches' recruitment to the plasma membrane in the absence of extracellular calcium

We then explored the role of extracellular calcium in the recruitment of SNAP-47 to the plasma membrane. To this aim, we eliminated extracellular calcium by adding EGTA (0.5 mM) as a chelating agent to Tyrode's incubation medium.

EGTA had a slightly effect on the number of SNAP-47-membrane patches under stimulated conditions compared with basal conditions (Fig. 58B. Number of SNAP-47-patches. Basal+EGTA_1 min: 4.96 ± 0.56 vs. Stimulation+EGTA_1 min: 3.51 ± 0.40, p-value= 0.1534).

Surprisingly, in basal conditions, the absence of extracellular calcium increased the number of SNAP-47-membrane patches (Fig. 58B. Number of SNAP-47-patches. Basal_1 min: 3.56 ± 0.41 vs. Basal+EGTA_1 min: 4.96 ± 0.56, p-value= 0.0457), suggesting a negative effect of extracellular calcium influx on SNAP-47 recruitment in basal conditions, in a similar fashion to what we observed with OT (Fig. 40C. Basal_1 min: 1.95 ± 0.12 vs. Basal+EGTA_1 min: 2.82 ± 0.21, p-value= 0.0011). This effect was not observed under stimulus conditions with and without extracellular calcium, as the number of SNAP-47-membrane patches remained similar in both scenarios (Fig. 58B. Number of SNAP-47-patches. Stimulation_1 min: 3.44 ± 0.33 vs. Stimulation+EGTA_1 min: 3.51 ± 0.40, p-value= 0.8052).

7.2.- Area of SNAP-47-membrane patches

7.2.1.- SNAP-47-membrane patches' area is not affected by neuronal stimulation

Similar to the number, the area of SNAP-47-membrane patches was not affected by the stimulation protocol (Fig. 58C. Area in μm^2. Basal_1 min: 0.59 ± 0.05 vs. Stimulation_1 min: 0.66 ± 0.06, p-value= 0.8451; Basal_10 min: 2.43 ± 0.92 vs. Stimulation_10 min: 2.43 ± 0.53, p-value= 0.1651). Nevertheless, incubation time affected the area of SNAP-47-membrane patches increasing it in response to 10 min incubation, despite not significant results were obtained under basal conditions (Fig. 58C. Area in μm^2. Basal_1 min: 0.59 ± 0.05 vs. Basal_10 min: 2.43 ± 0.92, p-value= 0.3038; Stimulation_1 min: 0.66 ± 0.06 vs. Stimulation_10 min: 2.43 ± 0.53, p-value= 0.0014).

7.2.2.- SNAP-47-membrane patches' area is increased in the absence of extracellular calcium under basal conditions

Comparing the same treatments with and without EGTA in basal conditions indicated that the area of SNAP-47-patches was larger in the absence of extracellular calcium (Fig. 58D. Area in μm^2. Basal_1 min: 0.59 ± 0.05 vs. Basal + EGTA_1 min: 0.75 ± 0.06, p-value= 0.0074), likely reflecting the increase in the number of SNAP-47-membrane patches (Fig. 58B). Under stimulus conditions, the absence of extracellular calcium seemed not to affect the area of SNAP-47-membrane patches (Fig. 58D. Area in μm^2. Stimulation_1 min: 0.66 ± 0.06 vs. Stimulation+EGTA_1 min: 0.76 ± 0.08, p-value= 0.3154).

7.3.- Interaction between OT- and SNAP-47-membrane patches

We then explored the relationship between the membrane microdomains enriched with OT and SNAP-47 under basal and stimulus conditions (Fig. 59A), staining SNAP-47 with an anti-SNAP-47 antibody and OT with an anti-GFP antibody (Table 5. Primary antibodies: anti-SNAP-47 rabbit, and anti-GFP chicken). First, we measured the distance, from centroid to centroid, between OT- and SNAP-47-membrane patches employing the image analysis software Imaris. These calculations provided an estimation of the distances between these two compartments.

Results indicated that the average distance between OT- and SNAP-47-membrane patches was approximately 0.10 µm, under both basal and stimulated conditions (Fig. 59B. Distance in µm. Experimental_Basal_1 min: 0.1 ± 0.00 vs. Experimental_Stimulation_1 min: 0.09 ± 0.00, p-value= 0.2735). Despite not significant differences were observed, in basal conditions 38.16 % of the analyzed patches were found at distances ≤ 0.05 µm, meanwhile under stimulated conditions, this percentage was 45.39 % (Fig. 59C). This result indicated that stimulation, even slightly, decreases the distance between OT- and SNAP-47-membrane patches.

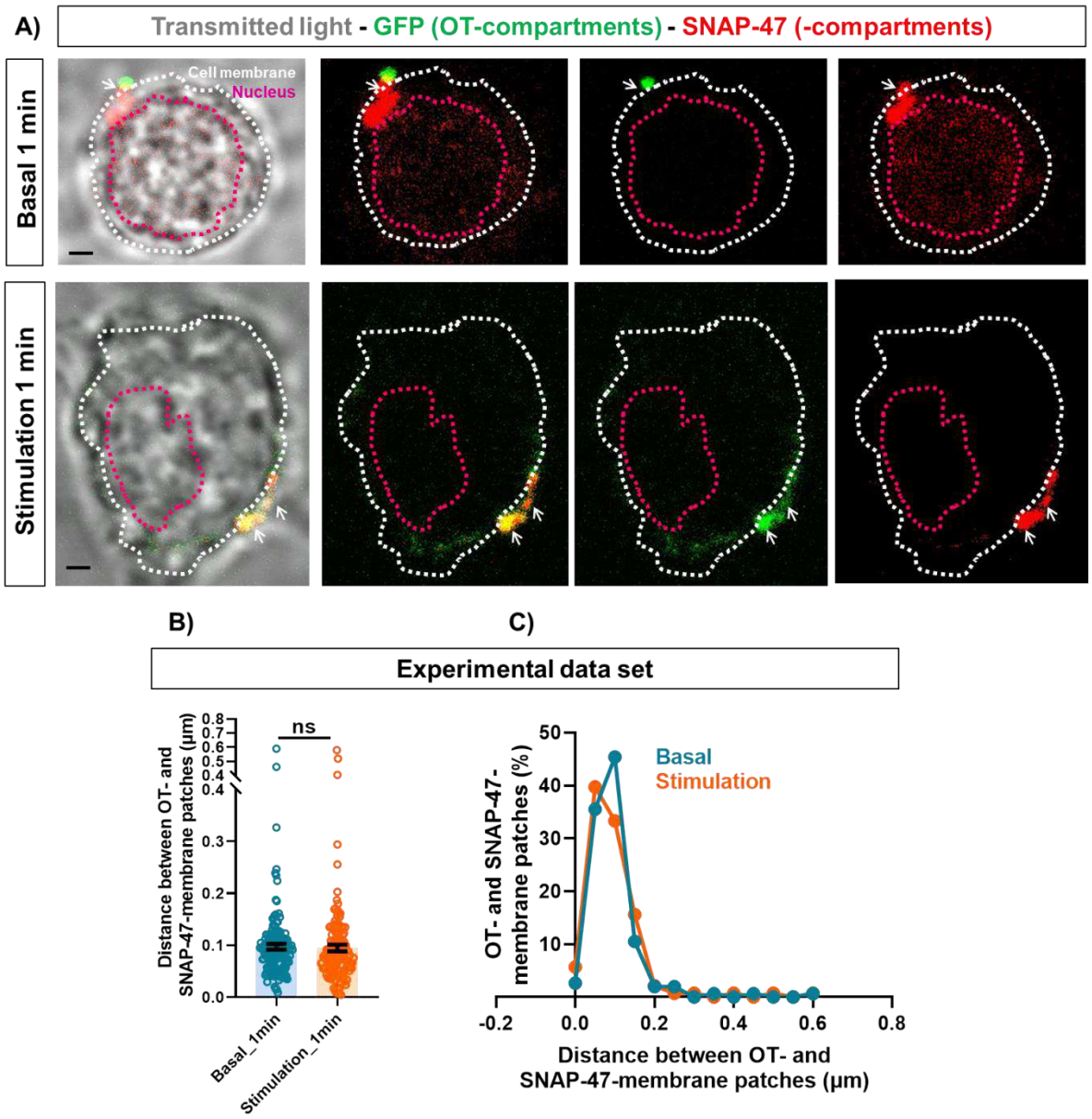

Figure 59.- Distance between OT- and SNAP-47-membrane patches from the experimental data set. **A)** OT- and SNAP-47-membrane patches in hypothalamic cultured OT neurons under basal and stimulated conditions are identified by green and red fluorescence, respectively. OT- and SNAP-47-membrane patches in close contact are indicated by white arrows. Dotted white line indicates cell membrane, dotted pink line indicates cell nucleus. Scale bars indicate 3 µm. **B-C)** Distance between OT- and SNAP-47-membrane patches in the experimental data set. Distance between OT- and SNAP-47-patches was similar between basal and stimulated conditions (B. Distance in µm. Experimental_Basal_1 min: 0.10 ± 0.00 vs. Experimental_Stimularion_1 min: 0.10 ± 0.00, p-value= 0.2735). In basal conditions, 38.16 % of the analyzed patches were found at distances ≤ 0.05 µm, meanwhile under stimulated conditions, this percentage was 45.39 % (C. Frequency distribution. Appendix, table 105). Statistical analysis: Mann-Whitney non-parametric test; p-value> 0.05 (ns), ≤ 0.05 (*), ≤ 0.01 (**), ≤ 0.001 (***), ≤ 0.0001 (****). Appendix, tables 103-105.

In parallel, we generated a random data set as an unbiased control to measure the distance between OT- and SNAP-47-membrane patches (Fig. 60A. Generation of the random data set

explained in "*Immunochemistry. Golgin GM-130 immunocytochemistry: image acquisition and analysis. Colocalization analysis between OT-compartments and Golgi*" section from materials and methods).

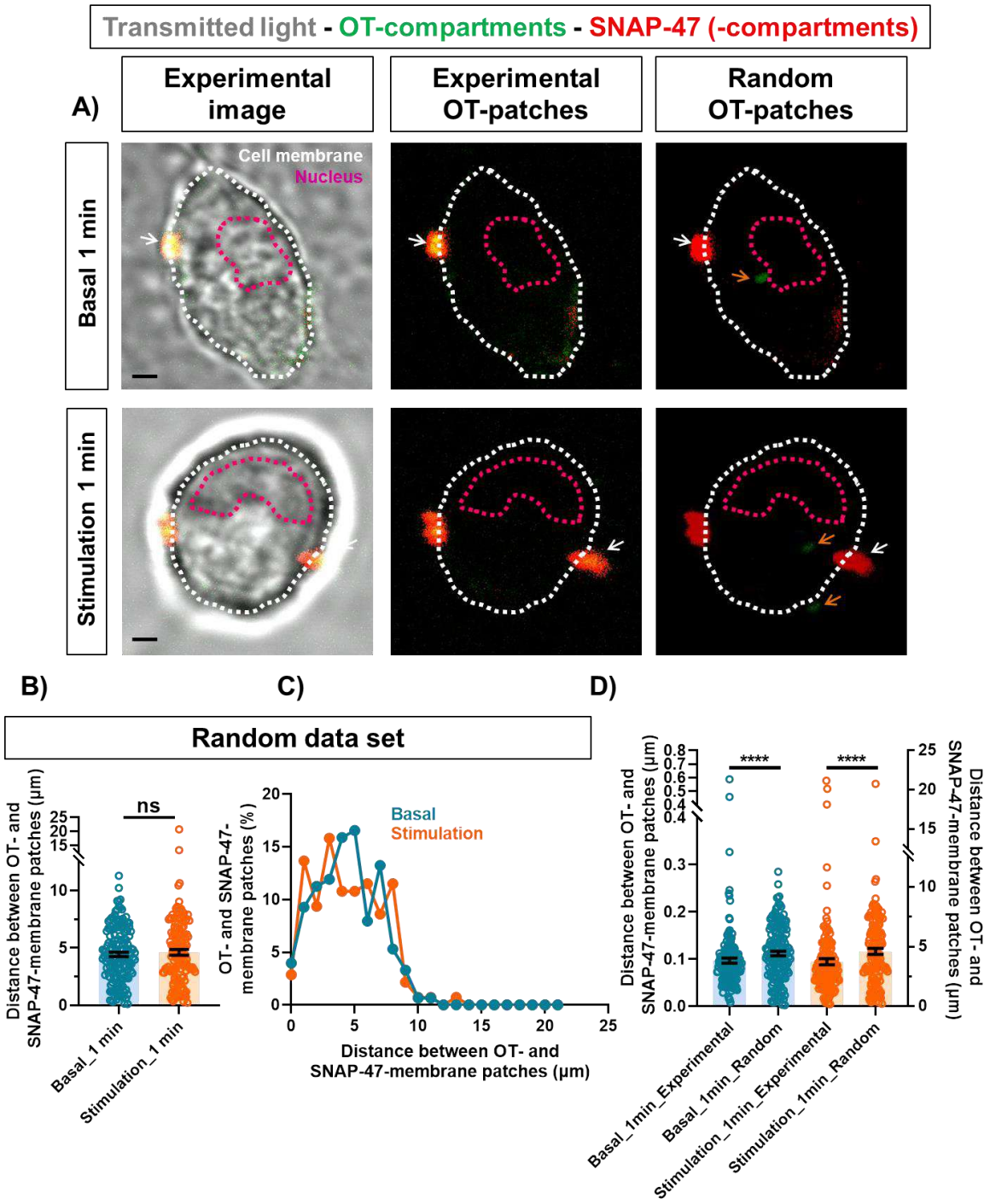

Figure 60.- Distance between OT- and SNAP-47-membrane patches from the experimental and random data sets. **A)** OT- and SNAP-47-membrane patches under basal (top) and stimulus (bottom) conditions. Random images were generated with experimental SNAP-47-membrane patches (red fluorescence, white arrows), and randomly-generated OT-membrane patches (green fluorescence, orange arrows). Dotted white line indicates cell membrane, and dotted pink line indicates cell nucleus. Scale bar indicates 3 µm. **B-C)**

Distance between OT- and SNAP-47-membrane patches in the random data set. Distance between OT- and SNAP-47 patches was similar between basal and stimulated conditions (B. Distance in µm. Random_Basal_1 min: 4.43 ± 0.19 vs. Random_Stimulation_1 min: 4.61 ± 0.25, p-value= 0.8565). Distances between OT- and SNAP-47-membrane patches were equally distributed under basal and stimulated conditions (C. Frequency distribution. Appendix, table 106). **D)** Comparison between experimental and random data set distance between OT- and SNAP-47-membrane patches under basal and stimulated conditions indicated that the distance between random patches highly differed from experimental data set (Distance in µm Experimental_Basal_1 min: 0.10 ± 0.00 vs. Random_Basal_1 min: 4.43 ± 0.19, p-value< 0.0001; Experimental_Stimulation_1 min: 0.10 ± 0.00 vs. Random_Stimulation_1 min: 4.61 ± 0.25, p-value< 0.0001). Statistical analysis: Mann-Whitney non-parametric test; p-value> 0.05 (ns), ≤ 0.05 (*), ≤ 0.01 (**), ≤ 0.001 (***), ≤ 0.0001 (****). Appendix, tables 103, 104, and 106.

Results indicated no differences between the distance of random patches neither in basal nor under stimulation (Fig. 60B. Distance in µm. Random_Basal_1 min: 4.43 ± 0.19 vs. Random_Stimulation_1 min: 4.61 ± 0.25, p-value= 0.8565).

Distances between OT- and SNAP-47-membrane patches were equally distributed in both conditions. In the random data set, approximately 5 % of the data presented a distance ranging from 0 to 1 µm, 90 % of the data ranged from 1 to 8 µm, and the 5 % of the data ranged from 9 to 21 µm (Fig. 60C). On the contrary, in the experimental data set we could observe small differences in the distance between basal and stimulated conditions (Fig. 59B). An especially interesting result from the random data set is that the distances between OT- and SNAP-47-membrane patches were larger than 1 µm, indicating a scenario far from the experimental data (Fig. 60D. Distance in µm. Experimental_Basal_1 min vs. Random_Basal_1 min, p-value< 0.0001; Experimental_Stimulation_1 min vs. Random_Stimulation_1 min, p-value< 0.0001), with only 3-4 % of the randomly-generated OT-patches exhibiting distances from SNAP-47-patches less than 1 µm (Fig. 60C).

From the randomly-generated data set, only 9 % of patches presented a distance similar to the experimental data (ranging from 0.01 to 0.6 µm) (Fig. 61A) which provided further confidence to perform the final colocalization analysis on the experimental data.

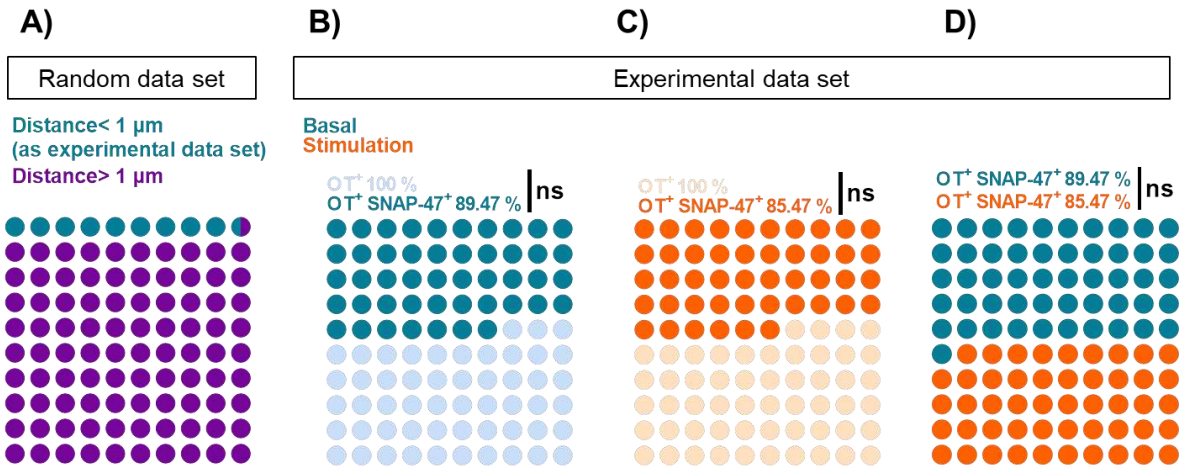

Figure 61.- Interaction between OT- and SNAP-47-membrane patches in the random and experimental data sets. **A)** Only 9.31 % of random data presented distances between OT- and SNAP-47 patches similar to the ones obtained for experimental data set. **B)** 89.47 % of experimental OT-membrane patches interacted with SNAP-47 under basal conditions (Number of experimental OT-patches. OT^+_Basal_1 min: 133 vs. OT^+ $SNAP\text{-}47^+$_Basal_1 min: 119, p-value= 0.3435). **C)** 85.47 % of experimental OT-membrane patches interacted with SNAP-47 under stimulated conditions (Number of experimental OT-patches. OT^+_Stimulation_1 min: 142 vs. OT^+ $SNAP\text{-}47^+$_Stimulation_1 min: 122, p-value= 0. 3323). **D)** The interaction of OT- and SNAP-47 patches was similar under basal and stimulated conditions in the experimental data set (Number of OT- and SNAP-47-experimental patches interacting. OT^+ $SNAP\text{-}47^+$_Basal_1 min: 133 vs. OT^+ $SNAP\text{-}47^+$_Stimulation_1 min: 142, p-value> 0.9999). Statistical analysis: Mann-Whitney non-parametric test; p-value> 0.05 (ns), ≤ 0.05 (*), ≤ 0.01 (**), ≤ 0.001 (***), ≤ 0.0001 (****). Appendix, tables 107-109.

Our results indicated that the majority of OT-membrane patches were found in close proximity with a SNAP-47-membrane patch, under both basal and stimulated conditions (Fig. 61B-D. Number of OT-patches. Basal_OT+SNAP-47_1 min: 1.83 ± 0.153 vs. Stimulation_OT-SNAP-47_1 min: 1.88 ± 0.16, p-value> 0.9999).

7.4.- OT- and SNAP-47-membrane patches present high degree of overlapping

Colocalization analysis between OT- and SNAP-47-membrane patches was performed with image analysis software Imaris (see "*Immunochemistry. Golgin GM-130 immunocytochemistry: image acquisition and analysis. Colocalization analysis between OT-compartments and Golgi*" section from materials and methods). Colocalization analysis rendered Manders' and Pearson's coefficients (Manders' and Pearson's coefficients are described in "*Immunochemistry. Golgin GM-130 immunocytochemistry: image acquisition and analysis. Colocalization analysis between OT-compartments and Golgi*" section from materials and methods).

Results indicated that the mean overlapping degree (Manders' coefficient) between OT- and SNAP-47-membrane patches under basal conditions was 76 % (Fig. 62A, blue. Manders_Basal_1min: 0.76 ± 0.01 vs. Manders_Stimulation_1 min: 0.80 ± 0.01, p-value=

0.0914). The overlapping degree ranged from 30 to 100 %, and the majority of the patches analyzed (60 %) presented an overlapping between 75 and 95 % (Fig. 62B, blue). Under stimulus conditions, the mean overlapping degree was 80 %, ranging from 35 to 100 % (Fig. 62A, B, orange). The majority of the patches analyzed under stimulus conditions (60 %) presented an overlapping between 80 and 95 % (Fig. 62B, orange). Results obtained from basal and stimulated conditions indicated that OT and SNAP-47 are found in close contact. This could mean that SNAP-47 participates in OT dynamics and release during spontaneous exocytosis (that is, under basal conditions), and under stimulated exocytosis (high KCl incubation).

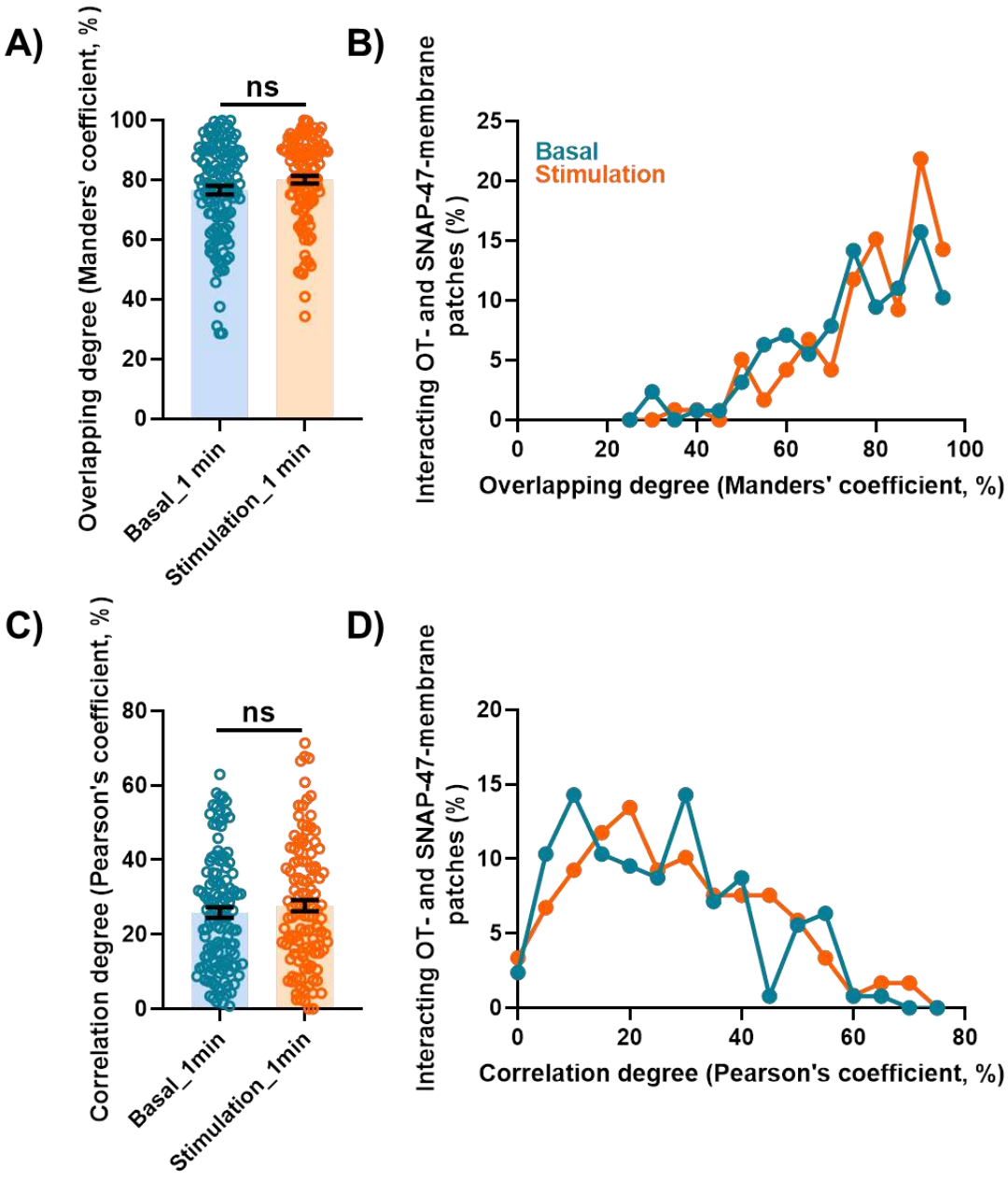

Figure 62.- Colocalization analysis of OT- and SNAP-47-membrane patches in oxytocinergic cultured neurons. **A-B)** Manders' overlapping coefficient between OT- and SNAP-47-membrane patches was similar under basal and stimulus conditions (A. Manders_Basal_1 min: 0.76 ± 0.01 vs. Manders_Stimulation_1 min: 0.80 ± 0.01, p-value= 0.0914). The overlapping degree ranged from 30 to 100 % under basal conditions and from 35 to 100 %

under stimulus conditions (B. Frequency distribution. Appendix, table 112). **C-D)** Pearson's correlation coefficient between OT- and SNAP-47-membrane patches was similar under basal and stimulus conditions (C. Pearson_Basal_1 min: 0.26 ± 0.01 vs. Pearson_Stimulation_1 min: 0.28 ± 0.01, p-value= 0.4134). The correlation degree ranged from 0 to 65 % under basal conditions and from 0 to 70 % under stimulus conditions (D. Frequency distribution. Appendix, table 113). Statistical analysis: Mann-Whitney non-parametric test; p-value> 0.05 (ns), ≤ 0.05 (*), ≤ 0.01 (**), ≤ 0.001 (***), ≤ 0.0001 (****). Appendix, tables 110-113.

Furthermore, analysis of Pearson's coefficient indicated a similar degree of correlation under both basal and stimulated conditions (Fig. 62C, D. Pearson_Basal_1 min: 0.26 ± 0.01 vs. Pearson_Stimulation_1 min: 0.28 ± 0.01, p-value= 0.4134). Nevertheless, mean Pearson's coefficient was approximately 30 % (Fig. 62C) in both basal and stimulated conditions; meanwhile mean Manders' coefficient was approximately 80 % (Fig. 62A) in both basal and stimulated conditions. This result is probably due to the different size of OT- and SNAP-47-membrane microdomains, being Mander's coefficient a more reliable parameter than Pearson's coefficient, as explained in the materials and methods section (see "*Chasing experiments. Colocalization analysis between OT- and SNAP-47-membrane patches*" section).

8.- SNAP-47-KD impairs OT recruitment to the plasma membrane under basal and stimulated conditions

Given that the colocalization analysis indicated a high degree of overlapping between SNAP-47- and OT-membrane microdomains, we ought to explore a potential role of SNAP-47 in OT exocytosis. To this aim, we infected 7 DIV hypothalamic primary cultures from P0 OT^{tdTom} mice with SNAP-47-KD virus (see "*Primary culture infection*" section from materials and methods) in order to reduce endogenous SNAP-47 protein and to study the impact on OT-containing compartments release employing a similar strategy to the aforementioned chasing protocols.

Results indicated that neurons infected with SNAP-47-KD exhibited a significant reduction in OT-membrane patches compared to uninfected neurons (Fig. 63A). This reduction was observed under both basal and stimulated conditions (Fig. 63B. Number of OT-patches. Uninfected_Basal: 1.72 ± 0.12 vs. Infected_Basal: 0.94 ± 0.23, p-value< 0.0001; Uninfected_Stimulation: 2.34 ± 0.20 vs. Infected_Stimulation: 0.46 ± 0.12, p-value< 0.0001), indicating that SNAP-47 plays a role in OT exocytosis or at least in OT recruitment to the membrane.

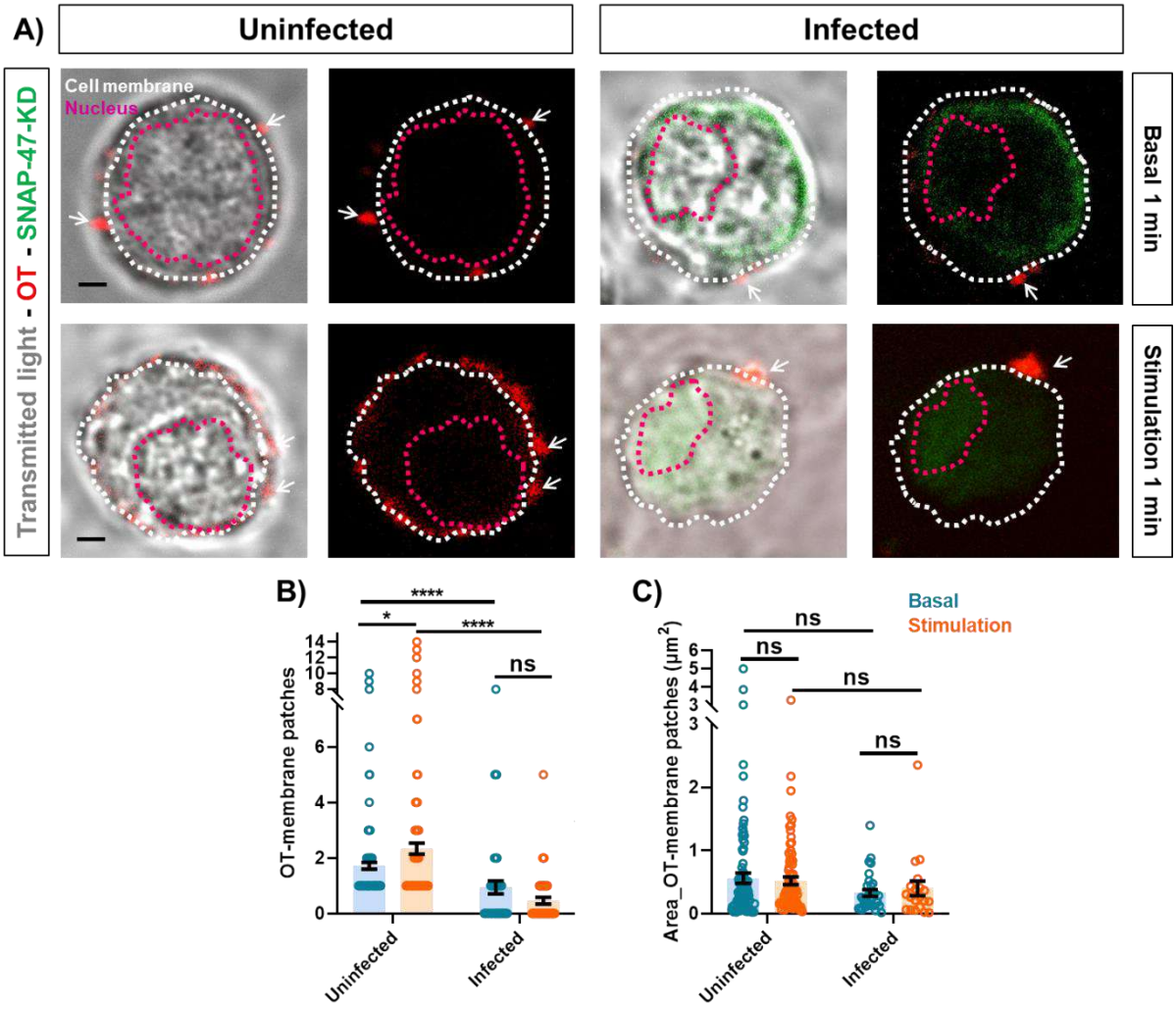

Figure 63.- OT-membrane patches in uninfected and SNAP-47-KD-infected primary cultured hypothalamic neurons. **A)** Infected and uninfected OT hypothalamic neurons under basal and stimulus conditions. Uninfected neurons presented more OT-membrane patches (red fluorescence, white arrows) than infected neurons. Dotted white line indicates cell membrane, and dotted pink line indicates cell nucleus. Scale bar indicates 3 µm. **B)** Infected neurons presented less OT-membrane patches than uninfected neurons under basal and stimulated conditions (Number of OT-patches. Uninfected_Basal: 1.72 ± 0.12 vs. Infected_Basal: 0.94 ± 0.23, p-value< 0.0001; Uninfected_Stimulation: 2.34 ± 0.20 vs. Infected_Stimulation: 0.46 ± 0.12, p-value< 0.0001). Uninfected neurons presented more OT-membrane patches under stimulus than under basal conditions (Number of OT-patches. Uninfected_Basal: 1.72 ± 0.12 vs. Uninfected_Stimulation: 2.34 ± 0.20, p-value= 0.0369; Infected_Basal: 0.94 ± 0.24 vs. Infected_Stimulation: 0.46 ± 0.12, p-value= 0.1290). **C)** The area of OT-membrane patches did not differ between infected and uninfected neurons, neither under basal or stimulated conditions (Area in μm^2. Uninfected_Basal: 0.56 ± 0.08 vs. Infected_Basal: 0.32 ± 0.05, p-value= 0.4250; Uninfected_Stimulation: 0.52 ± 0.06 vs. Infected_Stimulation: 0.40 ± 0.12, p-value= 0.2530; Uninfected_Basal: 0.56 ± 0.08 vs. Uninfected_Stimulation: 0.52 ± 0.06, p-value= 0.3595; Infected_Basal: 0.32 ± 0.05 vs. Infected_Stimulation: 0.40 ± 0.12, p-value= 0.9813). Statistical analysis: Mann-Whitney non-parametric test; p-value> 0.05 (ns), ≤ 0.05 (*), ≤ 0.01 (**), ≤ 0.001 (***), ≤ 0.0001 (****). Appendix, tables 114-117.

Comparisons between OT-membrane patches in basal and stimulus conditions from infected neurons indicated that, under stimulus conditions, neurons presented less OT-membrane patches than under basal conditions (Fig. 63B. Number of OT-patches. Infected_Basal: 0.94 ± 0.24 vs. Infected_Stimulation: 0.46 ± 0.12, p-value= 0.1290). This result could indicate that SNAP-47 plays an active role in OT membrane recruitment in response to stimulation, in agreement with results from our chasing experiments *("Chasing of OT-containing compartments"* section). Interestingly, results indicated that the area of OT-membrane patches did not differ between infected and uninfected neurons, both in basal and stimulus conditions (Fig. 63C. Area in μm^2. Uninfected_Basal: 0.56 ± 0.08 vs. Infected_Basal: 0.32 ± 0.05, p-value= 0.4250; Uninfected_Stimulation: 0.52 ± 0.06 vs. Infected_Stimulation: 0.40 ± 0.12, p-value= 0.2530).

9.- SNAP-47-KD *in vivo*

9.1.- SNAP-47-KD reduces SNAP-47 expression in PVN hypothalamic neurons

To analyze the efficacy of the viral vector to reduce endogenous levels of SNAP-47 in oxytocinergic neurons under physiological conditions, we conducted *in vivo* stereotaxic injections in the PVN of adult OT^{tdTom} mice (see "*Stereotaxic injections*" section from materials and methods). After an incubation period of 4-5 weeks, immunochemistry experiments were performed along with behavioral experiments.

Immunohistochemistry experiments were carried out in non-injected mice, injected mice with SNAP-47-KD virus, and injected mice with AAV-GFP virus (control) after 4-5 weeks post-injection to study SNAP-47 expression in to the PVN. We employed anti-RFP antibody to label oxytocinergic neurons, anti-GFP antibody to stain infected cells, and anti-SNAP-47 antibody to identify expression of SNAP-47 protein (Table 5. Primary antibodies: anti-RFP rat, anti-GFP chicken, and anti-SNAP-47 rabbit).

As previously presented (Fig. 50), SNAP-47 exhibited high levels of expression in the PVN majorly colocalizing with oxytocinergic neurons, but also with non-oxytocinergic neuros, as can also be seen in non-injected mice (Fig. 64).

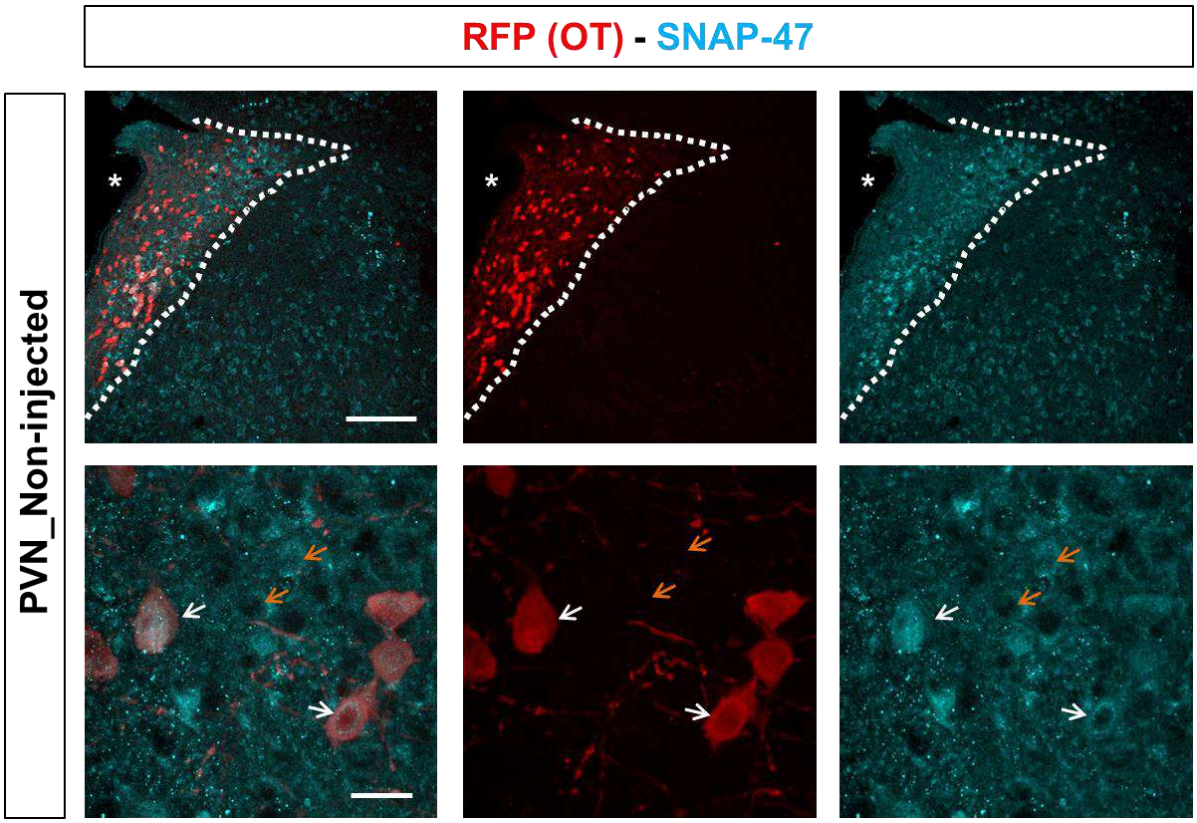

Figure 64.- SNAP-47 expression in PVN OT neurons from a non-injected mouse. SNAP-47 was expressed in the soma of OT neurons (white arrows) and non-OT neurons (orange arrows) in the non-injected mouse PVN. Dotted white line delineates PVN structure, and asterisk indicates the third ventricle. Scale bars indicate 150 µm (top panel), and 20 µm (bottom panel).

In contrast, mice injected with SNAP-47-KD virus exhibited a significant reduction of endogenous SNAP-47 expression (Fig. 65A). As such, 98 % of infected oxytocinergic neurons did not show SNAP-47 labelling (Fig. 65C. Number of neurons. SNAP-47-KD_OT^{+}: 22.86 ± 7.58 vs. SNAP-47-KD_OT^{+} SNAP47^{+}: 0.45 ± 0.30, p-value< 0.0001; SNAP-47-KD_OT^{+}: 22.86 ± 7.58 vs. SNAP-47-KD_OT^{+} SNAP47^{-}: 22.41± 7.44, p-value> 0.9999; SNAP-47-KD_OT^{+} SNAP47^{+}: 0.45 ± 0.30 vs. SNAP-47-KD_OT^{+} SNAP47^{-}: 22.41± 7.44, p-value< 0.0001).

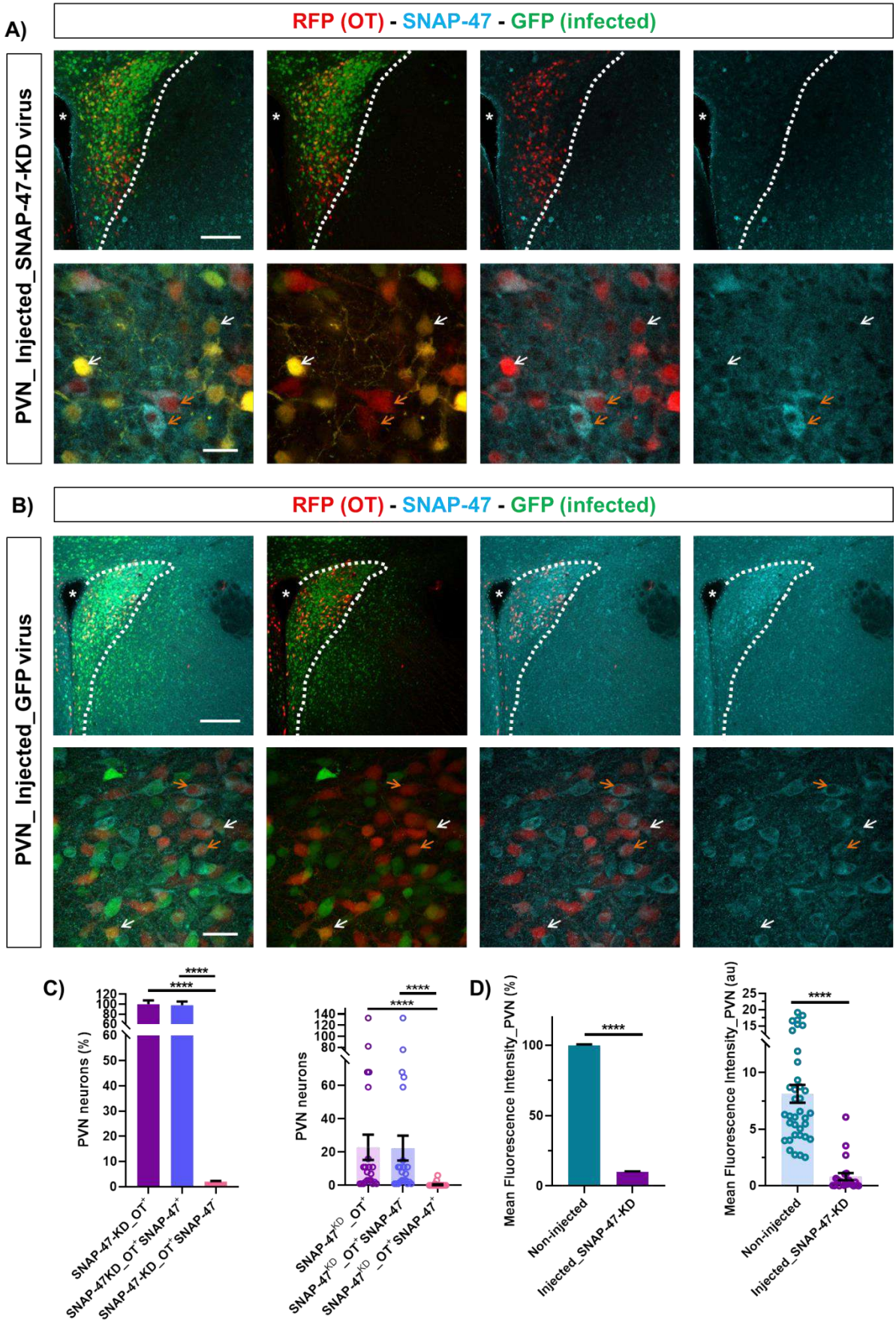
A)
RFP (OT) - SNAP-47 - GFP (infected)
PVN_ Injected_SNAP-47-KD virus
B)
RFP (OT) - SNAP-47 - GFP (infected)
PVN_ Injected_GFP virus
C)
PVN neurons (%)
SNAP-47-KD_OT+
SNAP-47KD_OT+SNAP-47+
SNAP-47-KD_OT+SNAP-47-
PVN neurons
SNAP-47KD_OT+
SNAP-47KD_OT+SNAP-47-
SNAP-47KD_OT+SNAP-47+
D)
Mean Fluorescence Intensity_PVN (%)
Non-injected
Injected_SNAP-47-KD
Mean Fluorescence Intensity_PVN (au)
Non-injected
Injected_SNAP-47-KD
****

Figure 65.- SNAP-47 expression in PVN OT neurons from injected mice. **A)** SNAP-47-KD-infected OT neurons did not express SNAP-47 in their somas (white arrows). Uninfected OT neurons clearly expressed SNAP-47 in their somas (orange arrows). **B)** AAV-GFP-infected OT neurons expressed SNAP-47 in their somas (white arrows) as well as uninfected neurons (orange arrows). (A-B) Dotted white line delineates PVN structure, and asterisk indicates the third ventricle. Scale bars indicate 150 µm (top panels), and 20 µm (bottom panels). **C)** 98 % of the PVN SNAP-47-KD-infected OT neurons did not express SNAP-47 (Number of neurons. SNAP-47-KD_OT^+: 22.86 ± 7.58 vs. SNAP-47-KD_OT^+ $SNAP47^+$: 0.45 ± 0.30, p-value< 0.0001; SNAP-47-KD_OT^+: 22.86 ± 7.58 vs. SNAP-47-KD_OT^+ $SNAP47^-$:22.41± 7.44, p-value> 0.9999; SNAP-47-KD_OT^+ $SNAP47^+$: 0.45 ± 0.30 vs. SNAP-47-KD_OT^+ $SNAP47^-$: 22.41± 7.44, p-value< 0.0001). Statistical analysis: Kruskal-Wallis non-parametric test. **D)** SNAP-47 mean fluorescence intensity of PVN SNAP-47 infected cells was significantly reduced in comparison to non-injected animals (Mean fluorescence intensity. Non-injected: 8.11 ± 0.79 vs. SNAP-47-KD_Injected: 0.81 ± 0.31, p-value< 0.0001). Statistical analysis: Mann-Whitney non-parametric test; p-value> 0.05 (ns), ≤ 0.05 (*), ≤ 0.01 (**), ≤ 0.001 (***), ≤ 0.0001 (****). Appendix, tables 118-121.

Analysis of SNAP-47 mean fluorescence intensity indicated a significant reduction in animals injected with a specific SNAP-47-KD-expressing virus in comparison to non-injected animals (Fig. 65D. Mean fluorescence intensity. Non-injected: 8.11 ± 0.79 vs. Injected: 0.81 ± 0.31, p-value< 0.0001).

In parallel, we conducted injections with a control AAV-GFP virus to test a potential effect of the injection procedure. As shown in Fig. 65B, PVN neurons infected with the control virus showed no detectable changes in the SNAP-47 expression levels.

9.2.- In vivo injection of SNAP-47-KD in the PVN impairs sociability

OT is a key neuropeptide involved in a wide range of social behaviors, including bonding, social recognition, and stress regulation. Impairments in OT signaling are linked to various neurodevelopmental and psychiatric disorders such as autism and schizophrenia. Given SNAP-47's role in OT-compartment trafficking at the somatodendritic compartment, knocking down this protein could disrupt OT release and impact social interactions.

To start addressing this hypothesis we performed behavioral assays such as sociability and social novelty as standard approaches to measure social interaction and preference for social novelty (such as recognizing new individuals) in animal models. Behavioral experiments were performed on SNAP-47-KD and AAV-GFP injected mice 4-5 weeks post-injection. Sociability and social novelty were analyzed using a three-chamber test as described in "*Social behavior: three chamber test*" section from materials and methods. Regarding the sociability test, control mice (injected with AAV-GFP virus) spent more time in the social side of the cage (Mouse 1, M1) versus the empty one (Fig. 66A. Exploration time (s). Control: Empty: 31.30 ± 6.94 vs. M1: 72.10 ± 9.48, p-value= 0.0159). Similarly, SNAP-47-KD injected mice also exhibit normal sociability (Fig. 66B. Exploration time (s). SNAP-47-KD: 40.41 ± 4.20 vs. M1: 59.70 ± 5.61, p-value= 0.0143). Nevertheless, the total interaction time of the SNAP-47-KD-injected mice was significantly reduced compared with control animals

(Fig. 66C. Sociability index. Control: 2.65 ± 0.44 vs. SNAP-47-KD: 1.57 ± 0.20, p-value= 0.0451).

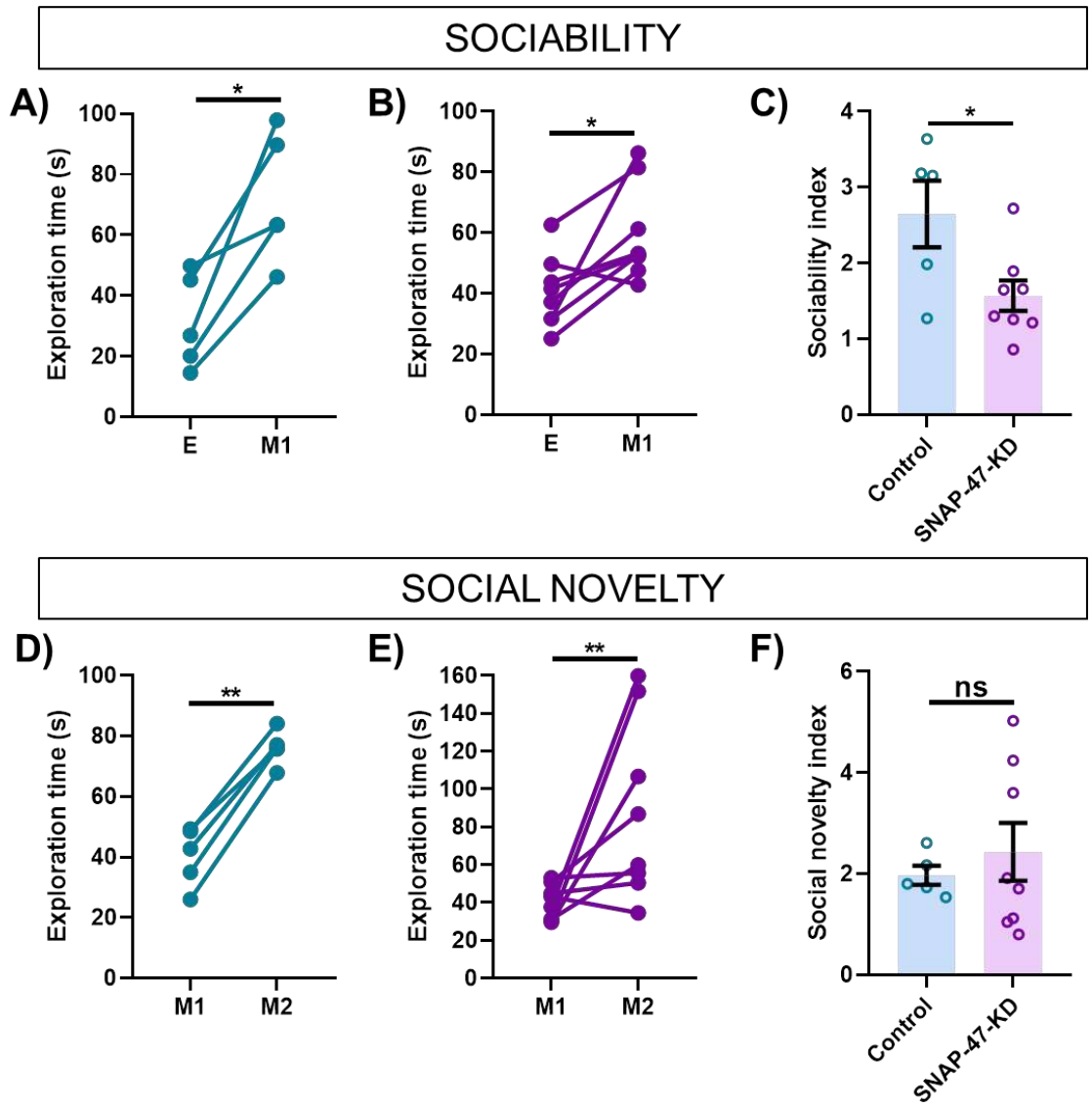

Figure 66.- Sociability and social novelty behavior in control and SNAP-47-KD mice. **A-B)** Control mice spend more time exploring M1 in comparison with the empty cage than SNAP-47-KD mice (Exploration time (s). A. Control: Empty: 31.30 ± 6.94 vs. M1: 72.10 ± 9.48, p-value= 0.0159; B. SNAP-47-KD: 40.41 ± 4.20 vs. M1: 59.70 ± 5.61, p-value= 0.0143). **C)** SNAP-47-KD mice presented reduced sociability index compared with control mice (Sociability index. Control: 2.65 ± 0.44 vs. SNAP-47-KD: 1.57 ± 0.20, p-value= 0.0451). Sociability index indicates how many time spent the test mouse exploring the empty cage vs. M1**. D-E)** The time spend by control and SNAP-47-KD mice exploring M1 compared with M2 was similar (Exploration time (s). D. Control: M1: 40.32 ± 4.40 vs. M2: 76.18 ± 2.57, p-value= 0.0079; E. SNAP-47-KD: M1: 40.08 ± 3.30 vs. M2: 88.23 ± 16.74, p-value= 0.0070). **F)** Control and SNAP-47-KD mice presented similar social novelty index (Social novelty index. Control: 1.97 ± 0.19 vs. SNAP-47-KD: 2.43 ± 0.57, p-value= 0.9433). Social novelty index indicates how many time spent the test mouse exploring M1 (already known) vs. M2. Statistical analysis: Mann-Whitney non-parametric test; p-value> 0.05 (ns), ≤ 0.05 (*), ≤ 0.01 (**), ≤ 0.001 (***), ≤ 0.0001 (****). Appendix, tables 122-125.

On the other hand, results from the social novelty test, which are related with memory, indicated that both control and SNAP-47-KD-injected mice preferred the new mouse (M2) over the previously explored one (M1) (Fig. 66D-F. Exploration time (s). D) Control: M1: 40.32 ± 4.40 vs. M2: 76.18 ± 2.57, p-value= 0.0079; E) SNAP-47-KD: M1: 40.08 ± 3.30 vs. M2: 88.23 ± 16.74, p-value= 0.0070. F) Social novelty index. Control: 1.97 ± 0.19 vs. SNAP-47-KD: 2.43 ± 0.57, p-value= 0.9433), indicating the social novelty phase was unaffected by SNAP-47-KD. To note, high variability was observed in SNAP-47-KD-injected mice, which could be due to different injection efficiency (Fig. 66F).

From these behavioral experiments, we concluded that the reduction in SNAP-47 expression in the hypothalamus affects sociability, but not social memory. These results could indicate that reducing SNAP-47 levels, and likely ambient somatic OT, may have a subtle yet specific impact on some basic aspects of social behavior.

These initial behavioral tests serve as a first attempt to understand the functional consequences of disrupting somatodendritic OT release through SNAP-47 KD, laying the groundwork for more detailed studies on OT's role in social dynamics.

DISCUSSION

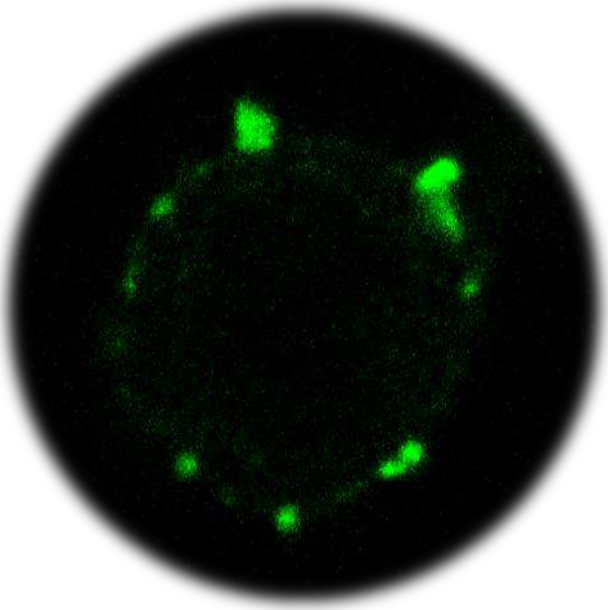

1.- Properties and localization of hypothalamic DCVs under basal and stimulated conditions: insights from electron microscopy analysis

1.1.- Analysis of DCVs' number and density at synaptic terminals

Our electron microscopy results indicated that DCVs constituted a small percentage of the total vesicles at synaptic terminals, consistent with previous electron microscopy studies performed in hippocampal neurons (Persoon et al., 2018). Under stimulation conditions, DCVs at hypothalamic synaptic terminals showed a reduction in density that, despite not statistically significant (Fig. 38K. Basal: 0.03 ± 0.01 vs. Stimulation: 0.02 ± 0.01, p = 0.3614), may suggest DCVs' activity-dependent exocytosis. However, prior studies of magnocellular neuron dendrites in the SON reported a three- to four-fold increase in neuropeptide release upon high KCl stimulation (one exocytosis event per 4620 µm), and identified a greater abundance of neuropeptide-containing DCVs than observed in our study (Pow & Morris, 1989) (Fig. 67). These discrepancies may arise from differences in the hypothalamic region studied (PVN vs. SON), cellular structure analyzed (soma vs. dendrites), osmotic stimulation concentration (100 mM KCl vs. 56 mM KCl), and/or stimulation duration (1 min vs. 10 min) (Pow & Morris, 1989).

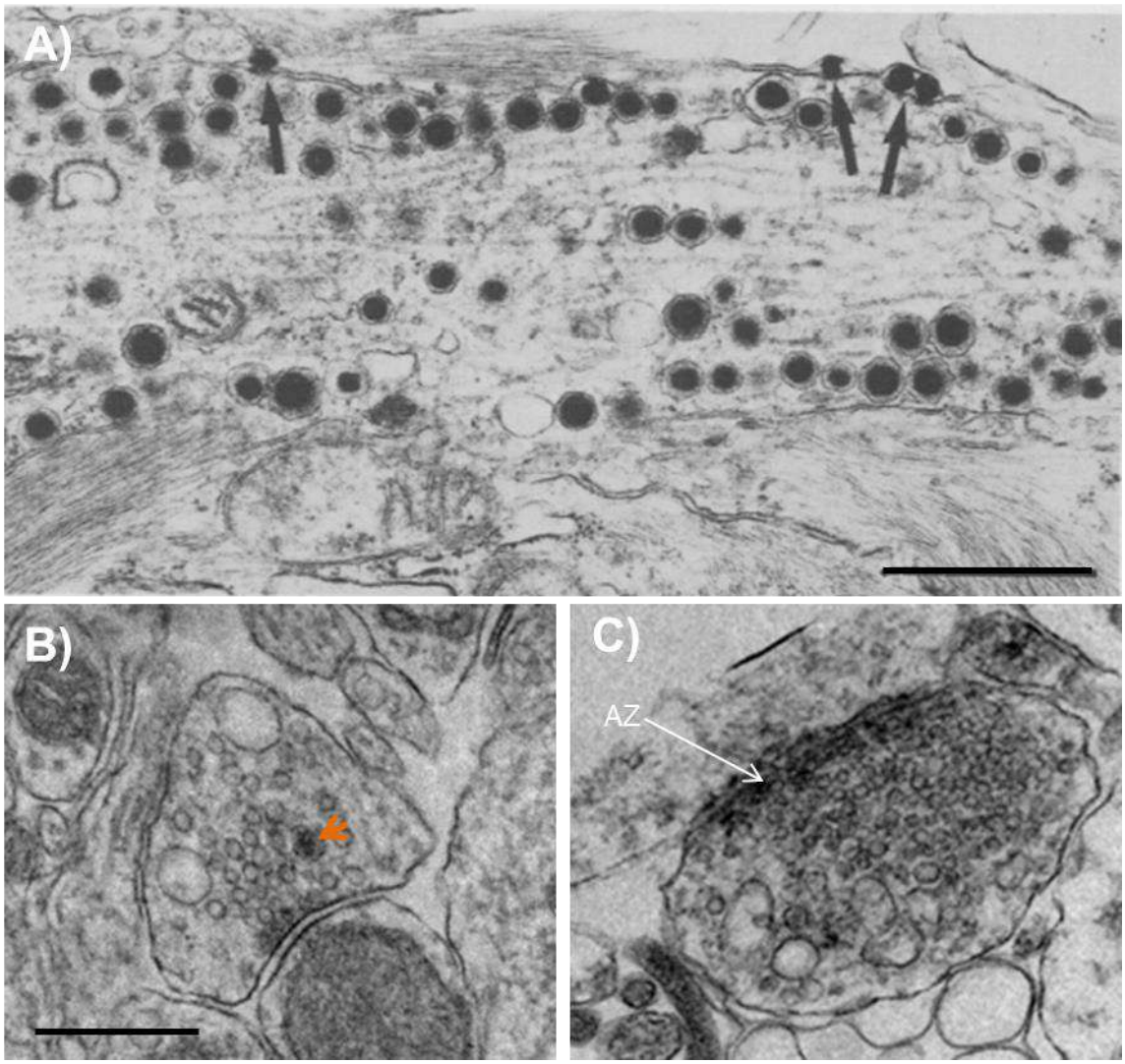

Figure 67.- Neuropeptide-containing DCVs in hypothalamic neurons under basal conditions. **A)** Longitudinal section of a SON magnocellular dendrite. Vesicles in the process of exocytosis or membrane fusion are indicated by arrows. Adapted from Pow & Morris, 1989. **B-C)** Longitudinal section of PVN's neuronal somas. DCVs are clearly identified as electron dense structures (orange arrow). AZ: active zone. Scale bars indicate 1 µm.

Although not statistically significant, our stimulation conditions (100 mM KCl during 1 min) reduced the DCVs count by 54.5 % (Fig. 38K. Density as percentage. Basal: 2.93 ± 0.72 vs. Stimulation: 2.03 ± 0.56, p-value= 0.3614), demonstrating similar efficiency than protocols utilizing high electrical stimulation, which achieved a 41 % reduction (Cifuentes et al., 2008).

Interestingly, 5-second high KCl stimulation in rat PC12 cells resulted in a 54 % reduction in DCVs (Grandolfo & Nistri, 2005), closely matching the decrease observed with our 1-minute protocol. Altogether, these results suggest that DCVs are mostly mobilized within the initial seconds of stimulation.

1.2.- Neuronal stimulation decreases hypothalamic DCVs' area and diameter

According to our electron microscopy results, two DCVs' populations can be distinguished in basal conditions according to their size: one population with a mean diameter of 70 nm (Pob1_Basal: 28.9 % of DCVs), and a more prevalent population with a mean diameter of 90 nm (Pob2_Basal: 71.1 % of DCVs; Fig. 38D. Diameter in nm. Pob1_Basal: 65.60 ± 1.30 vs. Pob2_Basal: 94.31 ± 1.60, p-value< 0.0001). We refer to the 70 nm diameter population as medium dense core vesicles and to the 90 nm diameter population as large dense core vesicles. A study by Sorra et al., (2006), also identified two DCVs' populations in the presynaptic axons of the *stratum radiatum* in the CA1 region of the adult rat hippocampus: larger DCVs with a diameter of 100 nm, and smaller DCVs with a diameter of 80 nm (Sorra et al., 2006). They hypothesized that the large DCVs likely contain neuroactive peptides and other co-transmitters, whereas medium DCVs could storage components of the presynaptic AZ (Sorra et al., 2006). Furthermore, Sorra et al., (2006), described 80 nm DCVs as "usually located near non-synaptic membranes" and less abundant than the 100 nm DCVs (Sorra et al., 2006), which coincide with the properties of our 70 nm diameter population (Pob1_Basal, a.ka. medium dense core vesicles).

Importantly, neuronal stimulation reduced the average size of DCVs (Fig. 38B. Area in nm^2. Basal: 270.1 ± 5.8 vs. Stimulation: 233.9 ± 7.3, p-value= 0.0002; Fig. 38E. Diameter in nm. Basal: 86.01 ± 1.80 vs. Stimulation: 74.4 ± 2.3, p-value= 0.0002), indicating that high KCl stimulation may affect DCVs' morphology, potentially reflecting cargo release (Vardjan et al., 2007; Xia et al., 2009; Vardjan et al., 2007).

1.3.- Analysis of DCVs' proximity to the plasma membrane

The distance of DCVs to the plasma membrane was not significantly different between basal and stimulated conditions (Fig. 38H. Distance to the plasma membrane in nm. Basal: 166.8 ± 17.0 vs. Stimulation: 127.9 ± 9.8, p-value= 0.2222).

However, there was a trend towards shorter distances in response to stimulation. Although subtle, this small difference could indicate mobilization of DCVs in response to the stimulus as a prior step to exocytosis or subsequent recycling (Cifuentes et al., 2008). Nonetheless, it is important to consider that DCVs' dynamics could be different in response to distinct stimulation patterns. For example, it has been described that high-frequency stimulation (40 Hz, 1 min) elicited to nerve terminals of the rat superior cervical ganglia did not reduce the distance between the edge of the vesicle and the plasma membrane (Cifuentes et al., 2008). In our experiments, the majority of DCVs were found ≤ 100 nm from the plasma membrane (Fig. 38I. Percentage of DCVs at ≤ 100 nm from the plasma membrane. Basal: 61.8, Stimulation: 70.21; notice that our measure begins in the centroid of the vesicle). Interestingly, 1.12 % of DCVs in basal conditions were found less than 100 nm from the plasma membrane whereas this percentage increased up to 4.25 % under stimulated conditions. We observed that during basal conditions, 37.07 % of DCVs could be found within 100-700 nm from the plasma membrane. This distance was reduced to a range of 100-300 nm under stimulated conditions for 30 % of the analyzed vesicles. This dynamic is in

agreement with previous reports (Cifuentes et al., 2008), which found a significant reduction of DCVs located at 200-300 nm from the plasma membrane after electrical stimulation.

1.4.- Analysis of DCVs' distance to the AZ

Regarding the distance to the AZ, the results obtained should be considered with caution due to the scarce number of AZs identified in our samples.

Distance from the vesicle centroid to the AZ ranged from 160 nm (stimulus conditions) to 780 nm (basal conditions) (Fig. 38J. Distance to the AZ in nm. Basal: 478.0 ± 120.3, Stimulation: 164.2 ± 0.0), which is comparable with data from hippocampal cultures (Persoon et al., 2018), suggesting that high KCl stimulation could mobilize DCVs to the AZ. On the other hand, experiments employing electrical stimulation have shown not to affect the distance of DCVs to the AZ (Cifuentes et al., 2008), indicating that different stimulation protocols may induce different trajectories of DCVs' mobilization.

Despite the few data points, we observed that, in basal conditions, DCVs locate further away from the AZ than to the membrane (Fig. 38H. Distance to the plasma membrane in nm. Basal: 166.8 ± 17.0; Fig. 38J. Distance to the AZ in nm. Basal: 478.0 ± 120.3). These results suggest that unlike SVs, DCVs are not concentrated at specialized release sites such as the AZ (Südhof, 2004; Hammarlund et al., 2008).

Interestingly, DCVs locate further away from the AZ than to the membrane under stimulus conditions (Fig. 38H. Distance to the plasma membrane in nm. Stimulation: 127.9 ± 9.8; Fig. 38J. Distance to the AZ in nm. Stimulation: 164.2 ± 0.0), which suggests that although high KCl stimulation mobilizes DCVs to the plasma membrane, the AZ is not their preferential target. This is supported by evidence indicating that DCVs do not require a specialized region for release (K. Matsui & Jahr, 2006; Tobin & Ludwig, 2007; Hammarlund et al., 2008), such as the classical experiments performed by Morris and Pow in 1989, that observed release of OT- and AVP-containing vesicles along the entire dendritic membrane (Fig. 67A).

Consistent with this, our electron microscopy experiments showed that DCVs in mouse hypothalamic slices altered their density, size, and proximity to the membrane in response to high KCl stimulation. These results indicate that this stimulation protocol is a valid strategy to mobilize and release DCVs in the hypothalamus. However, our analysis was restricted to hypothalamic terminals with recognizable AZs or nearby subcellular regions containing SVs, thus leaving open the question of how these protocols may affect DCVs dynamics and release in the somatodendritic compartment, which has been previously identified as an active region for DCVs' exocytosis (Pow and Morris, 1989).

2.- Chasing of OT-containing compartments: OT recruitment to the somatic plasma membrane

2.1.- Properties of OT-membrane patches

2.1.1.- Neuronal stimulation increases the number of OT-membrane patches

The effectiveness of our stimulation protocol (100 mM KCl, 1 min) was further supported by vesicle chasing experiments. Neuronal stimulation increased OT-membrane patches in primary cultured hypothalamic neurons (Fig. 40A. Number of OT-patches. Basal_1 min: 1.9 ± 0.1 vs. Stimulation_1 min: 2.8 ± 0.17, p-value< 0.0001). This result supports the effectiveness of protocols based on high KCl to stimulate neuropeptide release from the cell body (Troger et al., 1994; Trueta et al., 2003). Interestingly, high KCl has been shown to elicit peptides' exocytosis more effectively than electrical stimulation, unlike what happens with classical neurotransmitters (Troger et al., 1994; Trueta et al., 2003). Several lines of evidence demonstrate that electrical stimulation primarily promotes SVs' exocytosis meanwhile depolarization induced by high KCl favors DCVs' exocytosis (Troger et al., 1994; Persoon et al., 2018) without affecting cell viability (see "*Cytotoxicity*" section from materials and methods). Nevertheless, electrical stimulation at specific high frequencies has been used to effectively induce DCVs' exocytosis from neurons (Troger et al., 1994; Trueta et al., 2003; Baginska et al., 2023).

Despite its efficiency, the duration of protocols based on high KCl should be carefully considered since prolonged stimulation times may deplete the DCVs' releasable pool. As such, we observed reduced number of OT-membrane patches in response to 10 min stimulation (Fig. 40A. Number of OT-patches. Basal_10 min: 2.3 ± 0.2 vs. Stimulation_10 min: 1.6 ± 0.1, p-value= 0.0002; Stimulation_1 min: 2.85 ± 0.17 vs. Stimulation_10 min: 1.61 ± 0.13, p-value< 0.0001). This finding could indicate a depletion of DCVs during the first seconds of stimulation, and suggests a slow replenish mechanism of the DCVs' releasable pool. Similarly, prolonged electrical stimulation decreases the number of DCVs in the hippocampus, which are restored after interburst intervals of 5 s (Baginska et al., 2023). Furthermore, prolonged stimulation protocols, either electrical or osmotic, could deplete internal calcium stores, which have been identified to be required to support DCVs' exocytosis (Ludwig et al., 2002; Tobin & Ludwig, 2007; Baginska et al., 2023). In addition, prolonged stimulation may lead to desensitization of OTRs, whose activity is required for the feedback mechanism that promotes OT release (Di Scala-Guenot et al., 1994).

Moreover, DCVs' exocytosis could be influenced by their positioning. SVs are commonly concentrated near the AZ, so short electrical pulses are sufficient to increase local calcium concentration to induce SVs' release. On the other hand, DCVs are usually located scattered throughout the cell, requiring robust and prolonged stimulation protocols that result in higher intracellular calcium concentrations (Troger et al., 1994; Ludwig & Leng, 2006; Tobin & Ludwig, 2007; Persoon et al., 2018).

In the hypothalamus, L-type calcium channels, characterized by a longer duration of the open state, have been implicated in DCVs' exocytosis likely to their contribution to maintain a prolonged calcium influx (Troger et al., 1994). Intracellular calcium-dependence of somatodendritic OT-DCVs' exocytosis has been explored in experiments employing the

calcium chelator BAPTA (De Kock et al., 2003), demonstrating that the release dynamics at distinct compartments depends on different types of calcium channels (Ludwig et al., 2002; Ludwig & Leng, 2006; Qian et al., 2023). Whereas axonal release is primarily mediated by N-type calcium channels, somatodendritic release depends on L-type calcium channels' activity and requires higher increases in intracellular calcium (Ludwig & Stern, 2015; Ludwig et al., 2017; Qian et al., 2023).

In addition to calcium influx, the formation of a functional SNARE complex is critical to regulate DCVs' exocytosis (De Kock et al., 2003; Baginska et al., 2023), although its exact molecular composition remains to be elucidated, being the present study a first step towards its characterization.

2.1.2.- Membrane recruitment of OT under stimulus conditions depends on extracellular calcium

Given its crucial role in exocytosis, the sensitivity of OT release to calcium was explored using calcium-free solutions (0.5 mM EGTA). Our results indicated no increase of OT-membrane patches in response to a calcium-free stimulation solution, either 1 or 10 min (Fig. 40B. Number of OT-patches. Basal+EGTA_1 min: 2.8 ± 0.2 vs. Stimulation+EGTA_1 min: 2.9 ± 0.2, p-value= 0.5976; Basal+EGTA_10 min: 1.2 ± 0.2 vs. Stimulation+EGTA_10 min: 1.2 ± 0.2, p-value> 0.99999). Thus, these results indicate that OT recruitment to the plasma membrane is dependent on extracellular calcium, according to previous evidence showing that somatodendritic release depends on both intracellular and extracellular calcium sources (Tobin et al., 2011).

Stimulation during 1 min under calcium-free conditions leads to an increase of OT-membrane patches compared to 10 min stimulation (Fig. 40B. Number of OT-patches. Stimulation+EGTA_1 min: 2.9 ± 0.2 vs. Stimulation+EGTA_10 min: 1.2 ± 0.2, p-value= 0.0619). Similar to stimulation protocols in calcium-containing media, extended stimulation times reduced OT-membrane patches, likely due to the depletion of the OT reserve pool (Di Scala-Guenot et al., 1994; Baginska et al., 2023).

2.1.3.- Membrane recruitment of OT under basal conditions is negatively regulated by extracellular calcium

Unexpectedly, we found that the number of OT-membrane patches was increased in calcium-free basal medium (Fig. 40C. Number of OT-patches. Basal_1 min: 1.95 ± 0.12 vs. Basal+EGTA_1 min: 2.82 ± 0.21, p-value= 0.0011). This basal effect prevents the recognition that, in reality, stimulation in the presence of EGTA induces an increase in the number of OT-patches similar to that observed in the medium with calcium (Fig. 40C. Number of OT-patches. Stimulacion_1min: 2.84 ± 0.17 vs Stimulation+EGTA_1 min: 2.94 ± 0.23, p-value= 0.90), which could indicate that extracellular calcium entry is not a crucial event for OT secretion in response to this stimulation protocol and that even calcium-dependent pathways may inhibit OT exocytosis (Sabatier et al., 2003; Stojilkovic, 2005;

Ludwig & Leng, 2006; Tobin et al., 2011). In this scenario, extracellular calcium could activate calcium-dependent signaling pathways that suppress OT release through mechanisms involving specific exocytotic machinery. The increase in OT-patches in the absence of extracellular calcium may indicate a compensatory response, where the removal of external calcium relieves the inhibition on OT release, allowing for increased accumulation of OT-membrane patches. Furthermore, in calcium-free medium, neurons could employ intracellular calcium stores as their calcium source. Intracellular calcium has been shown to reach broader parts of the cell than extracellular calcium, which is constrained to the channel pore and surrounding area. (Troger et al., 1994; Persoon et al., 2018; Baginska et al., 2023). Thus in fact, intracellular calcium pathways could be more efficient to recruit OT-containing compartments scattered across non-synaptic regions (Stuenkel, 1994; Mitchell et al., 2001; Tobin et al., 2011; Kortus et al., 2016; Baginska et al., 2024).

The increased number of OT-membrane patches under calcium-free conditions could also be explained by reduced endocytosis rates. In the case of OT vesicles, such mechanism could be supported by Syt isoforms with different calcium sensitivities such as Syt-4 (Fig. 52 shows Syt-4 expression in OT neurons) (Z. Zhang et al., 2009; Wolfes & Dean, 2020). In the absence of extracellular calcium, endocytosis may be enhanced leading to an increase in the observed number of OT-membrane patches.

However, a role for extracellular calcium, albeit indirect, cannot be completely rule out since prolonged stimulation (10 min) resulted in reduced number of OT-membrane patches (Fig. 40B. Number of OT-patches. Stimulation+EGTA_1 min: 2.9 ± 0.2 vs. Stimulation+EGTA_10 min: 1.2 ± 0.2, p-value= 0.0619). Other causes such as the desensitization of OTRs, and reduced efficiency of vesicle priming in the absence of extracellular calcium can also play a role (Di Scala-Guenot et al., 1994; Ludwig et al., 2002; Tobin et al., 2011; Kortus et al., 2016; Baginska et al., 2023).

2.1.4.- Syt isoforms and sensitivity to calcium

The stimulation type and the source of calcium are key factors in the regulation of DCVs' exocytosis. Regarding the role of calcium, Syt proteins play a critical modulatory role depending on their sensitivity and subcellular location (Z. Zhang et al., 2011; Baginska et al., 2023). Distinct Syt isoforms have been identified in various types of DCVs conferring them unique sensitivity to calcium (Z. Zhang et al., 2011; P. Zhang et al., 2023). For example, in a study by Z. Zhang et al., (2011), Syt-1 expression was found to be the predominant isoform in small DCVs, whereas Syt-7 expression was typical of large DCVs (Z. Zhang et al., 2011). There is also evidence that the same Syt isoform can be positioned in different parts of the cell depending on the maturation state of the DCV, as have been observed for Syt-4 on PC12 cells (Fukuda et al., 2003). Thus, the implication of different Syts with distinct calcium sensitivities (Z. Zhang et al., 2011), could also play a role in the various effects observed in response to our stimulation protocol with and without EGTA.

2.2.- Area of OT-membrane patches

We observed that under calcium-free medium, OT-membrane patches exhibited a larger area (Fig. 41B. Area in μm^2. Basal+EGTA_1 min: 0.33 ± 0.02 vs. Basal+EGTA_10 min: 0.73 ± 0.30, p-value= 0.0308; Fig. 41D. Basal_10 min: 0.24 ± 0.02 vs. Basal+EGTA_10 min: 0.73 ± 0.30, p-value= 0.0014; Stimulation_10 min: 0.41 ± 0.04 vs. Stimulation+EGTA_10 min: 0.55 ± 0.14, p-value= 0.0598). These results could be due to a potential impairment of the endocytic and recycling processes as aforementioned (Z. Zhang et al., 2009; Z. Zhang et al., 2011), which could occur under long incubation times (10 min).

3.- Dynamic properties of OT-containing compartments in response to neuronal stimulation

3.1.- Mobility of OT-containing compartments

As aforementioned, our stimulation protocol induced a 20 % reduction of OT-containing compartments in cultured oxytocinergic neurons (Fig. 42B. t50. Basal: 2.42 ± 0.08 vs. Stimulation: 2.56 ± 0.1, p-value= 0.0240; t60. Basal: 2.4 ± 0.08 vs. Stimulation: 2.48 ± 0.1, p-value= 0.0109; t80. Basal: 2.32 ± 0.08 vs. Stimulation: 2.43 ± 0.09, p-value= 0.0281). These results are in line with similar experiments performed in chromaffin and PC12 cells, two cell models widely used to study exocytosis (Lochner et al., 2006; Ewing et al., 2020). For example, experiments in chromaffin cells have shown a 30-50 % reduction of DCVs in response to 2 min stimulation with 60 mM KCl, (Steyer et al., 1997), suggesting that DCVs' release requires robust osmotic stimulation protocols across different cell types, although with some specific properties. As such, PC12 cells might be more sensitive to osmotic than to electrical stimulation protocols, since DCVs' reduction in response to electrical stimulation was reported to be scarce in this cell type (10-20 %) (Barg et al., 2002). Furthermore, high KCl stimulation protocols might be more efficient to mobilize DCVs in cultured oxytocinergic cells than in other neuronal types such as hippocampal or striatal neurons (Silverman et al., 2005; Xia et al., 2009; Persoon et al., 2018).

In addition, the delay between the stimulation and DCVs' release is also a common feature throughout different cell preparations. A review of the current literature revealed that DCVs' kinetics range from 10 ms to 1000 s, meanwhile SVs' kinetics range between 0.1 ms to 10 s, and 1000 s in the case of spontaneous release (Kasai et al., 2012). An extreme example of prolonged and delayed release can be found in secretory β-cells and chromaffin cells, which can take 2 and 1 min to release their content, respectively (Oheim et al., 1998; Bednarska et al., 2021).

Altogether, this evidence suggests the involvement of a distinct release machinery, likely less efficient that the canonical SNARE fusion complex implicated in presynaptic release.

A particular feature of oxytocinergic neurons is the low number of DCVs released in comparison to specialized secretory cells like chromaffin or PC12 cells (Lochner et al., 2006;

Ewing et al., 2020), that led us to hypothesize that cultured oxytocinergic neurons present an intermediate scenario, or dual nature, between the fast kinetics and high number of vesicles released at their presynaptic terminals, and the slow somatic kinetics of secretory cells, suggesting a functional adaptation likely critical to their role in secreting neuropeptides into both the bloodstream and the CNS.

3.2.- Heterogeneity of OT-containing compartments

Classically, vesicles have been classified in three pools: the readily releasable pool (RRP), the slow releasable pool (SRP), and the reserve pool (RP) (Neeliyath et al., 2012; Qin et al., 2022). This classification typically associated with SVs has recently been applied to neuroendocrine and secretory cells (Neeliyath et al., 2012; Qin et al., 2022).

However, the particular properties of secretory cells have prompted new classifications to better characterize the dynamics of DCVs. So, readily releasable DCVs in PC12 cells under high KCl stimulation have been proposed to belong to two additional subpopulations depending on their priming and fusion kinetics (SP1: fast priming and slow fusion pore dilation; SP2: slowly primed and fast fusion pore expansion) (Qin et al., 2022). Also in PC12 cells, neuropeptide Y (NPY)-containing DCVs have been classified depending on their dwell time in sedentary (dwell time ≥ 102 s), mobile (disappear during the 120 s recording), and visiting (enter and left the field of view ≤ 120 s) vesicles (Xue et al., 2024). Vesicles' heterogeneity has also been found in chromaffin and human pancreatic islet cells (Xue et al., 2024).

To date, these types of classifications have not yet been performed in neuronal cells and specifically, in oxytocinergic hypothalamic neurons. Our vesicle dynamics' data have allowed us to initiate a detailed characterization of the somatic OT-containing compartments depending on their displacement, speed, and diffusion, which provides novel insights into the potential subtypes and dynamics of DCVs in these neurons.

3.3.- Displacement of OT-containing compartments

Our first attempt at DCVs' classification in oxytocinergic neurons was based on identifying the time point at which OT-containing compartments exhibited changes in their displacement. This approach yielded the following classification of OT-containing compartments: dynamic (7.32 %), delayed (56.30 %), uncoupled (23.53 %), and stable (12.60 %) (Fig. 43I-J). This classification shows similarities to other types of secretory cells. For example, in PC12 cells, islet amyloid polypeptide-containing vesicles were categorized into two groups based on their proximity to the membrane (Barg et al., 2002). Similarly, in chromaffin cells, NPY-containing DCVs exhibited directed motion, caged motion, or were nearly immobile upon stimulation (Nofal et al., 2007).

Furthermore, Park et al., (2012) established a classification of SVs in hippocampal neurons based on their net displacement as intersynaptic (4 %), intraboutonic (69 %), and minimal (27 %) (Park et al., 2012). These classifications suggest that DCVs and SVs could share

similar displacement in response to stimulation, despite differences in their release kinetics. For instance, our dynamic pool might share characteristics with the hippocampal intersynaptic population of SVs, while the delayed and uncoupled OT-compartments might correspond to the intraboutonic population, and the stable OT-compartments to the minimal SVs population identified by Park et al., (2012).

In hippocampal neurons, presynaptic DCVs exhibit slow submicron-scale mobility under basal conditions (Scalettar et al., 2012). Under high KCl stimulation, DCVs can be mobile over a time scale of less than 27 seconds, mobile but overlapping after 27 seconds, or immobile (Silverman et al., 2005). This indicates that DCVs in hippocampal neurons display various kinetics and movements similar to those observed in oxytocinergic neurons.

3.4.- Speed of OT-containing compartments

Speed analysis allowed us to perform an additional classification of OT-containing compartments as responding or mobile (29.4 %) and non-responding or immobile (70.6 %) (Fig. 44D, E). The mobile OT-compartments either increased or decreased their speed in response to stimulation, while the immobile OT-compartments showed no speed changes under the same conditions (Fig. 44F).

Under basal conditions, OT-containing compartments presented mean speed values ranging from 0.04 to 0.06 µm/s, depending on the group, with top mean speeds ranging from 0.15 to 0.32 µm/s (Table 9). Comparatively, Brain Derived Neurotrophic Factor (BDNF)-DCVs in cultured hippocampal neurons exhibited mean speed of 0.25 µm/s and top speed of over 0.4 µm/s (Xu et al., 2014). In thalamocortical axons *in vivo*, the mean speed was 1 µm/s, and the top speed was 2.06 µm/s, with some DCVs reaching velocities over 5 µm/s (Knabbe et al., 2018). Additionally, 11 % of DCVs in thalamocortical axons exhibited a pausing fraction (Knabbe et al., 2018).

Tracking AVP-DCVs in dendrites and axons of acute brain slices showed similar mean speed values in both compartments, but higher mean maximum speed values in axons (dendrites: 0.37 µm/s; axons: 0.42 µm/s) (Kirchner et al., 2023). This supports the notion that vesicle kinetics vary with cellular compartment and vesicle size, with axonal transport generally being faster.

Under 100 mM KCl stimulation, OT-containing compartments classified as mobile presented mean speeds of 0.07 µm/s (for those increasing speed) and 0.05 µm/s (for those decreasing speed, Table 9). Immobile OT-containing compartments presented a mean speed of 0.05 µm/s (Table 9).

Comparing these findings with other studies, hippocampal spines showed directed transport of DCVs at approximately 0.42 µm/s under 50 mM KCl stimulation, with a small fraction (4 %) being immobile (Silverman et al., 2005; Lochner et al., 2006). In contrast, the majority of our analyzed OT-containing compartments (70.6 %) were immobile (Fig. 44D).

Under 50-60 mM KCl stimulation, granules in chromaffin cells presented a mean speed of 0.04 µm/s (Steyer et al., 1997), while α-hydroxylating monooxygenase granules in cultured trigeminal ganglion neurons had a mean speed of 0.4 µm/s or less, with half of the vesicles

moving at 0.025 µm/s or less (Sobota et al., 2010). Peptidergic granules generally exhibited mean speed values between 0.03 and 0.07 µm/s, similar to the OT-containing compartments we analyzed. However, OT-containing compartments showed higher top speed values (0.34 µm/s for mobile increasing speed OT-compartments, 0.28 µm/s for mobile decreasing speed OT-compartments, and 0.34 µm/s for immobile OT-compartments, Table 9) compared with chromaffin cell granules (0.11 µm/s) and α-hydroxylating monooxygenase granules (0.1-2 µm/s) (Barg et al., 2002). These results highlight that while mean speed values of various granules in distinct cell types are comparable, their top speed values can differ significantly.

3.5.- Mean Square Displacement of OT-containing compartments

Finally, we analyzed MSD of OT-containing compartments to determine whether their movement was due to diffusion. According to the reviewed literature, vesicles are considered nearly immobile when displaying diffusion coefficient values of $D \leq 5*10^{-4}$ µm²/s (Silverman et al., 2005; Lochner et al., 2006; Scalettar et al., 2012).

From linear fitting and subsequent D calculation over the entire 60 seconds of KCl stimulation, we identified two populations: a majority population with $D= 1.476*10^{-4}$ µm²/s (Non-diffusive, 91.1 %), and a minority population with $D= 1.24*10^{-3}$ µm²/s (Diffusive, 8.9 %) (Table 10, Fig. 45A, B). The low slope (Y= 0.0005905*X), characteristic of non-diffusive movement, suggests non-diffusive OT-compartments might be constrained by the cytoskeleton, possibly vibrating in a reduced space. Conversely, the diffusive population moved initially but then stopped, implying they were mobilized by the high KCl stimulus and then anchored shortly after. These results suggest that both populations may be regulated by distinct anchoring mechanisms (Alabi & Tsien, 2012; Chung & Raingo, 2013).

We then analyzed diffusion coefficients under basal and KCl conditions. During the first 10 seconds of basal perfusion, all OT-containing compartments, regardless of their classification during the stimulation time, exhibited non-diffusive movement (Non-diffusive: $D= 4.02*10^{-4}$ µm²/s; Diffusive: $D= 3.535*10^{-4}$ µm²/s, Table 10, and Fig. 45D). This finding aligns with previous reports indicating low diffusion coefficients for vesicles in secretory cells under basal conditions, in the range of $D= 4*10^{-5}$ µm²/s in chromaffin cells (Steyer et al., 1997), and $D \leq 10^{-5}$ µm²/s for SVs (Scalettar et al., 2012).

During the first 10 seconds of stimulation, both diffusive and non-diffusive OT-containing compartments remained nearly immobile (Non-diffusive: $D= 7.58*10^{-5}$ µm²/s; Diffusive: $D= 4.5*10^{-5}$ µm²/s, Table 10, and Fig. 45E). However, in the subsequent 10 seconds, the diffusive population became mobile ($D= 2.56*10^{-3}$ µm²/s), while the non-diffusive population remained immobile ($D= 7.58*10^{-5}$ µm²/s, Table 10, and Fig. 45F). These results indicate a delayed response to stimulation, consistent with our previous findings indicating that most OT-containing compartments could be classified as delayed, modifying their displacement after 20-40 seconds of stimulation.

Previous studies support our findings. For instance, NPY–DCVs in PC12 cells under 105 mM KCl stimulation were classified as "active" if they moved before fusion and "inert" if they moved in a confined way (Xue et al., 2024). This classification resembles our "diffusive" and "non-diffusive" populations. In hippocampal neurons under 50-58 mM KCl, 13 % of

plasminogen activator (tPA)-DCVs were immobile, 49 % exhibited fast and directed movement, and 38 % showed slow diffusive movement (Silverman et al., 2005; Lochner et al., 2006). Our results, showing 91.1 % of non-diffusive and of 8.9 % diffusive OT-containing compartments (Fig. 45B), suggest that directed and slow vesicles in hippocampal neurons could exhibit similar properties to the non-diffusive population in oxytocinergic neurons.

Lastly, OT and glutamate vesicle dynamics were studied using genetically encoded sensors in PVN acute brain slices (Qian et al., 2023). Under electrical stimulation, the diffusion coefficient estimated for OT vesicles was approximately $5*10^3$ µm²/s, and for glutamate, D= $25.1*10^3$ µm²/s. These values are higher than those obtained in our experiments, likely due to differences in the type of stimulation (high KCl vs. electrical), and the preparation (primary culture of hypothalamic neurons vs. PVN acute brain slices) (Qian et al., 2023).

3.6.- Vesicles' dynamics are affected by different factors

Our results, along with data from the literature, indicate that vesicle populations, whether DCVs or SVs, exhibit heterogeneous dynamics according to the cell type (secretory or neuronal) or the type of stimulation (basal conditions, electrical or osmotic stimulation). This heterogeneity can be attributed to various factors like second messengers, physiological, and pharmacological modulators (Borges et al., 2023), the availability and isoforms of SNARE proteins (Baginska et al., 2023), the organization of the fusion site, calcium concentrations, and the expression of specific calcium channels (Südhof, 2004).

Additionally, the time and type of stimulation (Xia et al., 2009; Persoon et al., 2018), compartment-specific regulation (Kirchner et al., 2023), and temperature (Kirchner et al., 2023) play crucial roles in determining vesicle kinetics and exocytosis. Furthermore, the regulation of each vesicle pool likely serves distinct roles, reflecting the complexity and adaptability of the exocytic processes to meet the needs of the system.

3.7.- Role of vesicle subpopulations

The co-existence of different vesicle pools is expected to play key roles in maintaining the competence of release and recovering secretion capacity upon repeated stimulation (Qin et al., 2022). The functional diversity is further influenced by varying the recycling kinetics that dictate the rate and extent of release, as well as the presence of different cargos within distinct vesicle subpopulations (Xue et al., 2024). Additionally, vesicles may have varying requirements depending on the physiological demand or the specific region where release occurs (Ludwig & Leng, 2006; Ludwig & Stern, 2015).

Understanding the diverse roles of vesicle subpopulations is crucial, as each pool likely serves distinct functions.

3.8.- Subcellular localization of OT-containing compartments

Our analyses identified a high percentage of OT-containing vesicles which exhibited slow dynamics, thus we explored the number of OT-compartments in the proximity of the Golgi apparatus, a pool expected to exhibit low mobility. We found that, in oxytocinergic cultured neurons, 21.82 % of OT-containing vesicles were found near Golgi, with an overlapping level of ~ 55 % (Fig. 48B. Manders' coefficient_Experimental: 0.55 ± 0.01). These results could partly explain some of the kinetics of OT-containing vesicles classified as immobile or with limited movement (Beuret et al., 2004). However, this percentage could not explain the whole picture since the delayed pool of OT-containing compartments surpasses that of the overlap with the Golgi apparatus (dynamic: 7.32 %; delayed: 56.30 %; uncoupled: 23.53 %; stable: 12.60 %, Fig. 43I, J), indicating that slow kinetics may be an intrinsic property of OT-vesicle dynamics, as in the case of other neuropeptide-containing DCVs.

4.- Modeling of OT compartments' dynamics

A mathematical model of OT dynamics based on experimentally determined diffusion coefficients (D) under basal and stimulated conditions was conducted for further understanding the behavior of OT under different physiological states. The model described the OT movement within three main subcellular compartments: nucleus, cytoplasm, and plasma membrane, to gain insights into how OT distribution, release, and clearance may vary in response to changes in cellular activity.

4.1.- Modeling of OT-compartments' dynamics near the nucleus

Results from OT-compartments dynamics' simulations indicated that OT-compartments located near the nucleus, either diffusive or non-diffusive, migrated toward other cell regions under basal conditions (Fig. 49B. Diffusive, ti_Basal: 12.97 ± 0.31 vs. tf_Basal: 11.76 ± 0.61, p-value= 0.3015; Non-diffusive, ti_Basal: 13.39 ± 0.11 vs. tf_Basal: 12.58 ± 0.19, p-value= 0.0435). Cell regions were indicated by the slice number. Near the nucleus: slices from 12 to 17; in the cytoplasm: slices from 6 to 11; and at the membrane: slices from 1 to 5. These findings suggest that OT-containing compartments may be undergoing maturational steps, moving from regions near the nucleus and close organelles, such as the endoplasmic reticulum or the Golgi apparatus, towards the rest of the cell (Kim et al., 2006). However, it remains unclear what percentage of these compartments corresponds to cytoplasmic compartments versus those located in the endoplasmic reticulum or Golgi. Under stimulation, OT-compartments also moved towards the cytoplasm, and even to the membrane (Fig. 49B, C. Diffusive, ti_Stimulation: 13.36 ± 0.40 vs. tf_Stimulation: 11.70 ± 0.63, p-value= 0.0827; Non-diffusive, ti_Stimulation: 13.34 ± 0.12 vs. tf_Stimulation: 11.98 ± 0.17, p-value< 0.0001), suggesting that stimulation promotes the activation of the secretory pathway in the

anterograde direction. This mobilization could be due to the need to replenish cytoplasmic pools, particularly under stimulation conditions (Stojilkovic, 2005; Kasai et al., 2012).

4.2.- Modeling of OT-compartments' dynamics in the cytoplasm

Diffusive and non-diffusive OT-containing compartments at the cytoplasm moved throughout the entire cell under basal conditions (Fig. 49F. Diffusive, ti_Basal: 2.91 ± 0.27 vs. tf_Basal: 4.03 ± 0.57, p-value= 0.3087; Fig. 49E, Non-diffusive, ti_Basal: 7.74 ± 0.11 vs. tf_Basal: 7.13 ± 0.22, p-value= 0.0270), with their distribution becoming more heterogeneous in response to stimulation (Fig. 49F, G. Diffusive, ti_Stimulation: 3.24 ± 0.21 vs. tf_Stimulation: 4.33 ± 0.38, p-value= 0.0591; Non-diffusive, ti_Stimulation: 2.91 ± 0.09 vs. tf_Stimulation: 3.39 ± 0.12, p-value= 0.0404). These results potentially reflect active endocytic and exocytic processes, indicating ongoing vesicle recycling and trafficking within the cytoplasm (Gondré-Lewis et al., 2012; Kasai et al., 2012), and even mobilization towards the plasma membrane for supporting ongoing exocytosis under stimulus conditions.

4.3.- Modeling OT-compartments' dynamics in the membrane

Finally, OT-compartments nearby the plasma membrane moved to inner cell zones under basal conditions (Fig. 49J, K. Diffusive, ti_Basal: 2.91 ± 0.27 vs. tf_Basal: 4.03 ± 0.57, p-value= 0.3087; Non-diffusive, ti_Basal: 2.76 ± 0.08 vs. tf_Basal: 3.88 ± 0.14, p-value< 0.0001), suggesting potential recycling mechanisms (Gondré-Lewis et al., 2012; Kasai et al., 2012). Under KCl incubation, OT-compartments could be found within the plasma membrane, but also in the cytoplasm (Fig. 49J, K. Diffusive, ti_Basal: 2.91 ± 0.27 vs. tf_Stimulation: 4.33 ± 0.39, p-value= 0.0079; Non-diffusive, ti_Basal: 2.76 ± 0.08 vs. tf_Stimulation: 3.39 ± 0.12, p-value= 0.0037). A plausible explanation for this result could be that the KCl-induced depolarization may lead to increased exocytosis and endocytosis activity. This heightened activity could cause OT-compartments, initially associated with the plasma membrane, to be internalized as part of the endocytic recycling processes. Simultaneously, the compartments that remain near the membrane could reflect ongoing exocytosis. The presence of these compartments in both locations suggests a dynamic equilibrium between exocytosis and endocytosis under stimulus conditions.

Conclusions from the model support our experimental observations indicating that only a small pool of OT-containing compartments exhibits free diffusion throughout the cell, while the majority of OT-containing compartments displayed contained, vibrational-like movement (Table 10, and Fig. 45). Based on these theoretical and experimental data, we hypothesize that the diffusive group may be responsible for the basal maintenance and homeostasis of OT compartments, while the non-diffusive group may represent the traditional pools: RRP, SRP, and RP (Stojilkovic, 2005; Tobin & Ludwig, 2007).

5.- SNARE proteins' expression in hypothalamic oxytocinergic neurons

As very little is currently known regarding SNARE expression in oxytocinergic cells, we conducted a detailed immunochemistry characterization to identify SNARE proteins in hypothalamic slices from WT mice, focusing on the somas of OT neurons within the PVN and SON.

The expression analysis of SNAP, Stx, Syt, and Syb isoforms in oxytocinergic neurons within the PVN and SON reveals distinct patterns that may underline the specificity and complexity of the SNARE machinery in these neurons. Our findings demonstrate that only non-canonical SNAP-23 and SNAP-47 proteins are expressed in the soma of OT neurons in the PVN and SON, without any visible signal for SNAP-25 (Fig. 50). While SNAP-23 and SNAP-47 are generally found across various brain regions and in non-neuronal tissues (Holt et al., 2006; Kádková et al., 2019), they are also involved in exocytosis, with SNAP-47 additionally playing a role in postsynaptic function (Jurado et al., 2013). Our study is the first to identify SNAP-47 in hypothalamic neurons highlighting its potential significance in somatic OT dynamics.

Although SNAP-25 is commonly associated with SVs' exocytosis in neurons and it is also present in other secretory cells such as adrenal chromaffin cells and β-pancreatic cells, it was not detected in OT neurons of the PVN and SON under our experimental conditions. This isoform plays a crucial role in SNARE-dependent exocytosis, particularly in facilitating SVs' release (Rizo & Südhof, 2002). However, our findings suggest that in hypothalamic neurons, SNAP-25 is replaced by non-canonical isoforms such as SNAP-23 and SNAP-47, potentially supporting peptide exocytosis in the somatodendritic compartment.

Examining the syntaxin family, we found a region-specific expression of Stx isoforms in the PVN and SON. Canonical Stx-1 is present in non-oxytocinergic fibers in the PVN and some oxytocinergic neurons in the SON, suggesting differential expression across hypothalamic nuclei (Fig. 51). This region-specificity could be attributed to the subcellular localization determined by syntaxin cytoplasmic domains (Teng et al., 2001). This subcellular distribution aligns with its potential role in somatodendritic release, whereas Stx-3 and Stx-4 were notably absent in PVN and SON oxytocinergic neurons (Fig. 51). Consistently, Stx-1a has been shown to facilitate exocytosis in other neuroendocrine cells through interactions with potassium channels (Singer-Lahat et al., 2007).

Regarding synaptotagmin isoforms, neither the canonical calcium sensor Syt-1 nor the non-canonical Syt-7 were detected in the PVN or SON oxytocinergic neurons (Fig. 52). In contrast, both isoforms are typically expressed in DCVs within adrenal chromaffin cells, where they support fast and slow fusion events, respectively (Brown et al., 2020). In hippocampal neurons, Syt-1 and Syt-7 colocalize with DCVs, indicating a role in their release. However, the absence of these isoforms in hypothalamic OT neurons suggests that another Syt isoform/s mediates OT exocytosis in these regions. Supporting this, our findings confirmed the expression of Syt-4 in the soma of OT neurons in both PVN and SON (Fig. 52), consistent with previous studies in PC12 cells and the neurohypophysis, where Syt-4 is implicated in peptide release dynamics and DCVs' physiology, from biogenesis to membrane fusion (Fukuda et al., 2003). The specific role of Syt-4 in somatodendritic OT exocytosis remains to be explored in detail.

Our investigation of Syb isoforms revealed that Syb-1, -2, and -3 were not expressed in the PVN and were only present in non-OT neurons in the SON (Fig. 53). This result diverges from previous studies which reported Syb-2-mediated DCVs' release in rat SON neurons, a discrepancy possibly explained by species-specific differences and the inherent limitations of immunohistochemistry methods (Bergquist & Ludwig, 2008; De Kock et al., 2003). These findings emphasize the need for further research to determine Syb expression and function across species and experimental conditions.

Overall, our findings suggest that SNARE-mediated OT release in PVN and SON neurons relies on non-canonical, distinct SNARE isoforms. SNARE proteins like Syb-2, SNAP-25, and Syt-1, traditionally involved in SVs' exocytosis, are absent in these hypothalamic nuclei, with SNAP-23, SNAP-47, and Syt-4 potentially playing prominent roles in somatodendritic exocytosis. However, the current literature presents a complex and sometimes contradictory view of SNARE involvement in OT release, with studies showing varying expression patterns for SNAP-25, Syb, and Stx-1 across different neuron types and species (Ovsepian & Dolly, 2011; Tobin et al., 2012; Qian et al., 2023). This complexity underscores the need of further research to elucidate the molecular mechanisms possibly supporting OT release in response to various physiological demands.

5.1.- Developmental expression of somatodendritic SNARE isoforms in OT neurons

Our immunohistochemistry results in adult mice revealed SNAP-23, SNAP-47, and Syt-4 in the soma of OT neurons in both the PVN and SON (Fig. 50, and Fig. 52). Interestingly, in newborn mice, we observed no signal for SNAP-23 and Syt-4, while SNAP-47 was clearly detected (Fig. 54), suggesting a potential developmental regulation of SNARE protein expression in these neurons.

Evidence from various studies underlines the dynamic nature of SNARE protein expression during neuronal development. As such, Syb-2 expression increases steadily throughout development, while SNAP-25 and SNAP-47 are particularly enriched during the prenatal stage, with Syb-2 and SNAP-25 showing higher expression levels postnatally compared to other SNARE proteins (Urbina & Gupton, 2020). As such, DCVs' release in 3 DIV hippocampal cultures is independent of SNAP-25. By 4 DIV, however, SNAP-25 dependence starts to emerge (Arora et al., 2017). These findings indicate the involvement of different SNARE proteins at distinct stages of vesicle maturation (Eaton et al., 2000). Although additional complexities arise in neuronal cultures constituted by immature neurons undergoing maturation under non-physiological conditions, the observed developmental shifts in SNARE expression strongly indicate that neurons rely on specific isoforms at different developmental stages. Beyond developmental changes, it is also plausible that SNARE protein expression is influenced by external factors, such as specific types of stimulation, functional demands (e.g., lactation), or physiological conditions (e.g., stress, deprivation, or pathology). This suggests a dual regulatory mechanism for SNARE expression: one layer governed by developmental timing and another modulated by environmental conditions.

5.2.- Roles of SNARE and Syt proteins in DCVs' exocytosis

Previous works suggest that SNARE isoforms can either substitute for one another or act selectively in specialized contexts. For example, SNAP-25 and SNAP-23 can interchangeably perform similar functions in mammalian cells, supporting the adaptability of SNARE components (Ovsepian & Dolly, 2011). In nigral dopaminergic neurons, distinct Syb isoforms are engaged depending on the specific functional requirement, demonstrating the selective use of SNAREs based on cellular demands. Additionally, Syt isoforms, such as Syt-1 and Syt-7, modulate calcium-dependent exocytosis in dendrites, underscoring their role in fine-tuning physiological responses (Ovsepian & Dolly, 2011).

In cultured hippocampal neurons, both Syt-1 and Syt-7 act as calcium sensors for DCVs, indicating that neurons can utilize different Syt isoforms depending on their needs (Baginska et al., 2023). Further evidence of functional redundancy within the SNAP-25 family comes from neurons lacking SNAP-25, where SNAP-23 and SNAP-29 compensate by supporting vesicle fusion (Arora et al., 2017). In PC12 cells, Syt isoforms vary according to vesicle size, which influences calcium sensitivity and fusion type, indicating a highly adaptable exocytic system that accommodates vesicle-specific requirements (Z. Zhang et al., 2011).

Whether this functional versatility could be extended to non-canonical SNARE complexes remains to be investigated. In this regard, our findings reveal that OT neurons in the mouse PVN and SON primarily express non-canonical SNARE proteins in the somatic compartments, providing a novel scenario to explore the properties of alternate forms of fusion. However, this pattern is not unique to OT neurons; nigral dopaminergic neurons, for instance, seem to rely on a SNARE complex constituted by Stx-3, Syb-2, and SNAP-25 to regulate somatodendritic exocytosis (Ovsepian & Dolly, 2011). Similarly, cultured trigeminal ganglion neurons contain a variety of non-canonical Syb isoforms, along with SNAP-25 and Stx-1, to regulate DCVs (Merighi, 2018). In cortical neurons, SNAP-47 coexists with SNAP-25 and Syb-2 within DCVs, further illustrating the adaptability of the SNARE complexes associated with DCVs' function (Merighi, 2018).

5.3.- SNAP-47 expression in oxytocinergic neurons

Our findings demonstrate high expression levels of SNAP-47 in the somas of hypothalamic neurons within the PVN and SON during both adulthood and early development, as well as in primary cultured oxytocinergic neurons (Fig. 50, 54, and 55). Immunohistochemical analysis using α-tubulin antibody showed no colocalization with SNAP-47, indicating that SNAP-47 is absent from the axons of these hypothalamic neurons (Fig. 56). SNAP-47's postsynaptic expression pattern in OT neurons suggests a prominent role in somatic OT dynamics and exocytosis, believed to be distinct from the machinery supporting axonal release (Gerber & Südhof, 2002; Südhof & Rothman, 2009).

Existing literature highlights the varied cellular localization and functional diversity of SNAP-47. SNAP-47 has been identified in the ER, Golgi, post-Golgi compartments, cytosol, and neurites, emphasizing its involvement in multiple cellular contexts (Kuster et al., 2015; Münster-Wandowski et al., 2017; Kádková et al., 2019; Urbina et al., 2021). Interestingly, in

cortical and hippocampal neurons, SNAP-47 is present presynaptically but it is not associated with synaptic vesicles (Shimojo et al., 2015).

SNAP-47 primarily interacts with various Syb isoforms, including Syb-4, Syb-7, and Syb-8 in the Golgi, supporting a role in regulating their trafficking through the secretory pathway (Kuster et al., 2015). Additionally, SNAP-47 associates with Stx-5 and Stx-1 in the ER and Golgi, and with Stx-3 and Syb-2 to facilitate postsynaptic AMPA receptor release in hippocampal and cortical neurons (Shimojo et al., 2015; Kádková et al., 2019). These interactions highlight SNAP-47's specialized roles in diverse cellular environments and exocytic processes.

6.- OT and SNAP-47 interaction in the plasma membrane of hypothalamic oxytocinergic neurons

Considering the prominent role of SNAP-47 as a somatic SNARE protein in OT neurons, we performed chasing experiments to study the dynamics of SNAP-47-containing compartments under basal, stimulus, and calcium chelated media.

6.1.- Properties of SNAP-47-membrane patches

6.1.1.- The number of SNAP-47-membrane patches is not affected by neuronal stimulation

The number of SNAP-47-enriched membrane patches was similar under basal and stimulated conditions at both 1 and 10 minutes of incubation, suggesting that SNAP-47 localization is not significantly affected by neuronal stimulation (Fig. 58A. Number of SNAP-47 patches. Basal_1 min: 3.50 ± 0.40 vs. Stimulation_1 min: 3.44 ± 0.33, p=0.6445; Basal_10 min: 2.50 ± 0.54 vs. Stimulation_10 min: 1.56 ± 0.24, p=0.2488). This stability suggests that SNAP-47-enriched microdomains may serve as anchor sites at the plasma membrane to coordinate the recruitment of OT-containing vesicles.

However, prolonged incubation times led to a reduction in the number of SNAP-47 microdomains, though the decrease was not statistically significant (Fig. 58A. Basal_1 min: 3.50 ± 0.40 vs. Basal_10 min: 2.50 ± 0.54, p=0.9670; Stimulation_1 min: 3.44 ± 0.33 vs. Stimulation_10 min: 1.56 ± 0.24, p=0.1939). This reduction might be explained by depletion of exocytotic activity or increased calcium-dependent endocytosis during extended incubation times. Both processes are likely influenced by specific Syts with varying calcium sensitivity (Z. Zhang et al., 2009; G. Zhang et al., 2011; Z. Zhang et al., 2011). Calcium elevation, for instance, may selectively recruit certain Syts to induce vesicle fusion, particularly those with lower affinity that respond only to high calcium levels (Baginska et al., 2023).

6.1.2.- Analysis of SNAP-47-membrane patches' recruitment to the plasma membrane in the absence of extracellular calcium

We also explored the impact of removing extracellular calcium for the SNAP-47-enriched microdomains at the plasma membrane, finding that stimulation with EGTA-containing solutions did not affect the number of SNAP-47-membrane patches, providing further support to the notion that SNAP-47 is quite stable at the plasma membrane (Fig. 58B. Number of SNAP-47-patches. Basal+EGTA_1 min: 4.96 ± 0.56 vs. Stimulation+EGTA_1 min: 3.51 ± 0.40, p-value= 0.1534).

Nevertheless, the removal of extracellular calcium under basal conditions resulted in a significant increase in the number of SNAP-47-membrane patches (Fig. 58B. Number of SNAP-47-patches. Basal_1 min: 3.56 ± 0.41 vs. Basal+EGTA_1 min: 4.96 ± 0.56, p-value= 0.0457), similar to the results observed with OT (Fig. 40C. Number of OT-patches. Basal_1 min: 1.95 ± 0.12 vs. Basal+EGTA_1 min: 2.82 ± 0.21, p-value= 0.0011). As in the case of OT, we hypothesize that SNAP-47 transport to the membrane could be slowed down by extracellular calcium (Troger et al., 1994; Sabatier et al., 2003; Stojilkovic, 2005; Tobin et al., 2011; Kortus et al., 2016; Persoon et al., 2018; Baginska et al., 2023). In contrast, under stimulated conditions, SNAP-47 recruitment to the membrane was independent of extracellular calcium (Fig. 58B. Number of SNAP-47-patches. Stimulation_1 min: 3.44 ± 0.33 vs. Stimulation+EGTA_1 min: 3.51 ± 0.40, p-value= 0.8052), also similar to OT (Fig. 40C. Number of OT-patches. Stimulation_1 min: 2.84 ± 0.17 vs. Stimulation+EGTA_1 min: 2.94 ± 0.23, p-value= 0.8934). This could be explained by the fact that under stimulus conditions, somatic exocytosis may majorly rely on intracellular calcium stores as the main calcium source (Mitchell et al., 2001; Ludwig et al., 2002; Persoon et al., 2018).

6.2.- Area of SNAP-47-membrane patches

6.2.1.- SNAP-47-membrane patches' area is not affected by neuronal stimulation

The area of SNAP-47-membrane patches was not affected by the type of treatment, similar to the number of patches (Fig. 58C. Area in μm^2. Basal_1 min: 0.59 ± 0.05 vs. Stimulation_1 min: 0.66 ± 0.06, p-value= 0.8451; Basal_10 min: 2.43 ± 0.92 vs. Stimulation_10 min: 2.43 ± 0.53, p-value= 0.1651).

Longer incubation times (10 min) increased the area of SNAP-47-membrane patches, despite not significant results were observed under basal conditions (Fig. 58C. Area in μm^2. Basal_1 min: 0.59 ± 0.05 vs. Basal_10 min: 2.43 ± 0.92, p-value= 0.3038; Stimulation_1 min: 0.66 ± 0.06 vs. Stimulation_10 min: 2.43 ± 0.53, p-value= 0.0014). These results present a paradox: after 10 min of incubation, the number of SNAP-47-patches decreases compared to 1 min, yet the patch area increases. This seems an apparent contradiction, since larger patches would typically indicate a greater number of molecules. Given that the size of a SNAP-47 molecule is constant, these findings imply a more complex mechanism affecting patch formation and distribution under prolonged incubation times, which warrants further investigation.

6.2.2.- SNAP-47-membrane patches' area is increased in the absence of extracellular calcium under basal conditions

In the absence of extracellular calcium, SNAP-47 membrane patches were larger than in regular basal medium (Fig. 58D. Area in μm²: Basal_1 min: 0.59 ± 0.05 vs. Basal + EGTA_1 min: 0.75 ± 0.06, p=0.0074). However, under stimulation, there was not significant difference in patch size between conditions with and without extracellular calcium (Fig. 58D. Area in μm²: Stimulation_1 min: 0.66 ± 0.06 vs. Stimulation + EGTA_1 min: 0.76 ± 0.08, p=0.3154).

These observations are consistent with findings on the number of SNAP-47 membrane patches (Fig. 58B. Number of SNAP-47-patches: Basal_1 min: 3.56 ± 0.41 vs. Basal + EGTA_1 min: 4.96 ± 0.56, p=0.0457; Stimulation_1 min: 3.44 ± 0.33 vs. Stimulation + EGTA_1 min: 3.51 ± 0.40, p=0.8052). Under basal conditions, the increase in both patch size and number suggests that SNAP-47 patch formation is less dependent on extracellular calcium. In contrast, during stimulation, these results may imply that SNAP-47 recruitment to the membrane is linked to extracellular calcium entry, reflecting a greater reliance on a calcium-dependent mechanism under stimulated conditions.

These data suggest that SNAP-47-membrane compartments' dynamics are influenced by extracellular calcium levels rather than by neuronal stimulation alone. This again points to a potential calcium-dependent mechanism regulating SNAP-47's mobilization and membrane association. Understanding this mechanism could provide insights into the role of SNAP-47 in synaptic function and plasticity, highlighting its potential involvement in calcium-mediated cellular processes.

6.2.3.- Role of SNAP-47 in oxytocin recruitment and exocytosis

Regarding colocalization analysis between OT- and SNAP-47-membrane patches, we found that both molecules were in close contact under basal and stimulated conditions (Fig. 59B. Distance in μm. Experimental_Basal_1 min: 0.1 ± 0.00 vs. Experimental_Stimulation_1 min: 0.09 ± 0.00, p-value= 0.2735; Fig. 62A. Overlapping coefficient. Manders_Basal_1min: 0.76 ± 0.01 vs. Manders_Stimulation_1 min: 0.80 ± 0.01, p-value= 0.0914; Fig. 62C. Correlation coefficient. Pearson_Basal_1 min: 0.26 ± 0.01 vs. Pearson_Stimulation_1 min: 0.28 ± 0.01, p-value= 0.4134).

Chasing experiments in cultured oxytocinergic neurons infected with a virus expressing a specific SNAP-47-KD showed that infected neurons exhibited significantly fewer OT-membrane patches compared to uninfected neurons, under both basal and stimulated conditions (Fig. 63B. Number of OT-patches. Uninfected_Basal: 1.72 ± 0.12 vs. Infected_Basal: 0.94 ± 0.23, p-value< 0.0001; Uninfected_Stimulation: 2.34 ± 0.20 vs. Infected_Stimulation: 0.46 ± 0.12, p-value< 0.0001).

Together, these experiments suggest that the interaction between OT and SNAP-47 likely has a functional role, implicating SNAP-47 in OT exocytosis or, at least, in the recruitment of OT to the somatic plasma membrane.

7.- SNAP-47 *in vivo* knock down: implications in social behavior

In vivo stereotaxic injections into the PVN of adult OT^{tdTom} mice indicated that SNAP-47-KD reduced 98 % SNAP-47 expression in OT neurons (Fig. 65C. Number of neurons. SNAP-47-KD_OT^{+}: 22.86 ± 7.58 vs. SNAP-47-KD_OT^{+} $SNAP47^{+}$: 0.45 ± 0.30, p-value< 0.0001; SNAP-47-KD_OT^{+}: 22.86 ± 7.58 vs. SNAP-47-KD_OT^{+} $SNAP47^{-}$: 22.41± 7.44, p-value> 0.9999; SNAP-47-KD_OT^{+} $SNAP47^{+}$: 0.45 ± 0.30 vs. SNAP-47-KD_OT^{+} $SNAP47^{-}$: 22.41± 7.44, p-value< 0.0001), as well as their SNAP-47 mean fluorescence intensity (Fig. 65D. Mean fluorescence intensity. Non-injected: 8.11 ± 0.79 vs. Injected: 0.81 ± 0.31, p-value< 0.0001), indicating that the knockdown was highly effective in reducing SNAP-47 protein levels.

Regarding behavioral experiments, sociability test indicated that SNAP-47-KD injected mice exhibited reduced sociability compared with animals injected with a control GFP virus (Fig. 66C. Sociability index. Control: 2.65 ± 0.44 vs. SNAP-47-KD: 1.57 ± 0.20, p-value= 0.0451); whereas social novelty remained unaffected (Fig. 66F. Social novelty index. Control: 1.97 ± 0.19 vs. SNAP-47-KD: 2.43 ± 0.57, p-value= 0.9433). These results suggest that SNAP-47 levels, and likely ambient somatic OT, may have a subtle yet specific impact on some basic aspects of social behavior. Nevertheless, sociability was not entirely abolished in the SNAP-47-KD animals (Fig. 66A. Exploration time (s). Control: Empty: 31.30 ± 6.94 vs. M1: 72.10 ± 9.48, p-value= 0.0159; Fig. 66B. Exploration time (s). SNAP-47-KD: 40.41 ± 4.20 vs. M1: 59.70 ± 5.61, p-value= 0.0143), indicating that other factors may contribute to sociability and partially compensate for the disruption of basal OT. Besides, lack of effect on the social novelty phase in the three-chamber test (Fig. 66D-F. Exploration time (s). D) Control: M1: 40.32 ± 4.40 vs. M2: 76.18 ± 2.57, p-value= 0.0079; E) SNAP-47-KD: M1: 40.08 ± 3.30 vs. M2: 88.23 ± 16.74, p-value= 0.0070. F) Social novelty index. Control: 1.97 ± 0.19 vs. SNAP-47-KD: 2.43 ± 0.57, p-value= 0.9433) suggests that reducing SNAP-47, and thereby disrupting somatic OT dynamics, may impact specific aspects of social behavior. Specifically, OT somatic release might affect more sustained and context-dependent behaviors, such as sociability, while OT axonal release could be more crucial for behaviors involving rapid communication and signaling, such as aggression.

Previous studies linked reduced OT plasma membrane with social impairments, such as impaired social memory and social interaction, as a result of the abolishment of release proteins such as Stx-1a and CAPS2 (Fujiwara et al., 2016; Fujima et al., 2021; Fujiwara et al., 2021).

Thus, from our experiments we can conclude that SNAP-47 reduces the number of OT-containing compartments in the plasma membrane, likely reducing the level of ambient OT with behavioral consequences.

Although the literature on SNAP-47 is scarce, a study by Bereczki et al., (2018) correlated cognitive impairment before death with loss of SNAP-47 in Alzheimer´s disease patients, suggesting a potential role as a predictive molecular fingerprint in neurodegenerative diseases (Bereczki et al., 2018). However, the understanding of SNAP-47's function in the brain is just beginning to arise through the application of knockout and knockdown strategies. Nevertheless, several studies indicate the functional impact of SNAP protein alterations in

both mice and humans (Müller et al., 2011; Huang et al., 2023; Ali et al., 2023; Ansari et al., 2024; Ma et al., 2024).

This thesis project covers from molecular to behavioral approaches to study the postsynaptic exocytosis machinery, focusing on the little studied protein SNAP-47 expression in neurons. Our work represents the first advance in the knowledge of the involvement of a non-canonical SNAP in the somatodendritic OT exocytosis, being the first step for future studies.

SUMMARY

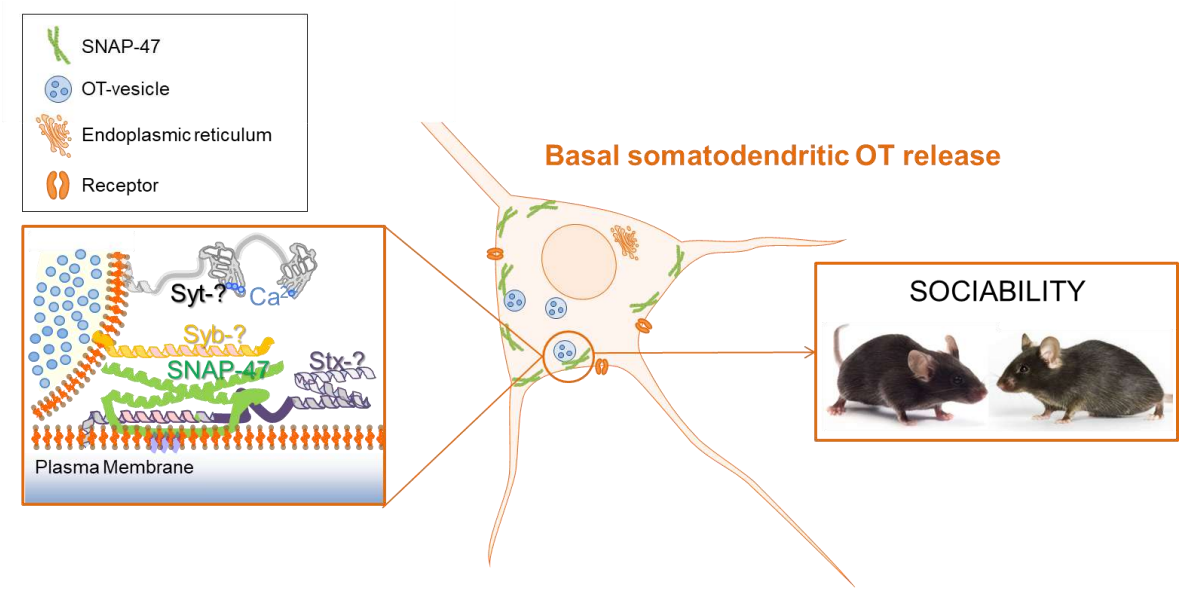
SNAP-47
OT-vesicle
Endoplasmic reticulum
Receptor
Syt-?
Ca2+
Syb-?
SNAP-47
Stx-?
Plasma Membrane
Basal somatodendritic OT release
SOCIABILITY

CONCLUSIONS/CONCLUSIONES

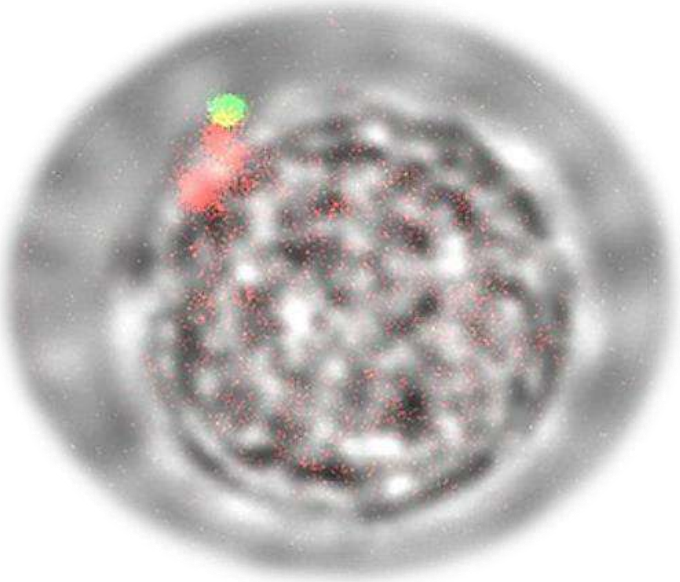

CONCLUSIONS

1.- Neuronal stimulation mobilizes OT to the plasma membrane of the soma, promoting its release through an extracellular calcium-dependent mechanism, which in turn limits its recruitment under basal conditions.

2.- OT compartments in the soma of cultured hypothalamic neurons exhibit high heterogeneity in displacement, velocity, and diffusion, suggesting distinct functions among subpopulations.

3.- Syt-4, SNAP-23, and SNAP-47 are expressed in the soma of OT neurons with distinct developmental regulation, suggesting specific SNARE machinery for somatic OT exocytosis, different from the canonical presynaptic SNARE complex.

4.- SNAP-47 microdomains in the somatic membrane of oxytocinergic neurons are stable under basal and stimulation conditions, showing high colocalization with OT. SNAP-47 deletion suggests a role in OT recruitment to the membrane and in the regulation of sociability.

CONCLUSIONES

1.- La estimulación neuronal (100 mM KCl) moviliza la OT hacia la membrana plasmática del soma, favoreciendo su liberación mediante un mecanismo dependiente de calcio extracelular, que a su vez limita su reclutamiento en condiciones basales.

2.- Los compartimentos de OT en el soma de neuronas hipotalámicas en cultivo presentan una alta heterogeneidad en desplazamiento, velocidad y difusión, sugiriendo funciones distintas entre subpoblaciones.

3.- Syt-4, SNAP-23, y SNAP-47 se expresan en el soma de las neuronas de OT, con distinta regulación durante el desarrollo, sugiriendo una maquinaria SNARE específica para la exocitosis somática de OT, distinta del complejo SNARE presináptico canónico.

4.- Los microdominios de SNAP-47 en la membrana somática de neuronas oxitocinérgicas son estables en condiciones basales y durante la estimulación neuronal, mostrando alta colocalización con OT. Su eliminación sugiere un papel en el reclutamiento de OT a la membrana y en la regulación de la sociabilidad.

BIBLIOGRAPHY

Abramova, O., Zorkina, Y., Ushakova, V., Zubkov, E., Morozova, A., & Chekhonin, V. (2020). The role of oxytocin and vasopressin dysfunction in cognitive impairment and mental disorders. *Neuropeptides, 83*(May), 102079. https://doi.org/10.1016/j.npep.2020.102079

Alabi, A. R. A., & Tsien, R. W. (2012). Synaptic vesicle pools and dynamics. *Cold Spring Harbor Perspectives in Biology, 4*(8), 1–18. https://doi.org/10.1101/cshperspect.a013680

Alarcón, M., Abrahams, B. S., Stone, J. L., Duvall, J. A., Perederiy, J. V., Bomar, J. M., Sebat, J., Wigler, M., Martin, C. L., Ledbetter, D. H., Nelson, S. F., Cantor, R. M., & Geschwind, D. H. (2008). Linkage, Association, and Gene-Expression Analyses Identify CNTNAP2 as an Autism-Susceptibility Gene. *American Journal of Human Genetics, 82*(1), 150–159. https://doi.org/10.1016/j.ajhg.2007.09.005

Ali, J., Khan, A., Park, J.S., Tahir, M., Ahmad, W., Choe, K., & Kim, M.O. (2023). Neuroprotective Effects of N-methyl-(2S, 4R)-trans-4-hydroxy-L-proline (NMP) against Amyloid-β-Induced Alzheimer's Disease Mouse Model. *Nutrients, 15*(23), 4986. https://doi: 10.3390/nu15234986.

Althammer, F., & Grinevich, V. (2018). Diversity of oxytocin neurones: Beyond magno- and parvocellular cell types? *Journal of Neuroendocrinology* (Vol. 30, Issue 8). https://doi.org/10.1111/jne.12549

Ansari, M.A., Rao, M.S., & Al-Jarallah, A. (2024). Insights into early pathogenesis of sporadic Alzheimer's disease: role of oxidative stress and loss of synaptic proteins. *Frontiers in Neuroscience, 17*, 1273626. https://doi: 10.3389/fnins.2023.1273626.

Aoyagi, K., Itakura, M., Fukutomi, T., Nishiwaki, C., Nakamichi, Y., Torii, S., Makiyama, T., Harada, A., & Ohara-Imaizumi, M. (2018). VAMP7 regulates autophagosome formation by supporting Atg9a functions in pancreatic β-cells from Male mice. *Endocrinology, 159*(11), 3674–3688. https://doi.org/10.1210/en.2018-00447

Arendt, K.L., Zhang, Y., Jurado, S., Malenka, R.C., Südhof, T.C., & Chen. L. (2015). Retinoic Acid and LTP Recruit Postsynaptic AMPA Receptors Using Distinct SNARE-Dependent Mechanisms. *Neuron, 86*(2), 442-56. https://doi: 10.1016/j.neuron.2015.03.009.

Arora, S., Saarloos, I., Kooistra, R., van de Bospoort, R., Verhage, M., & Toonen, R. F. (2017). SNAP-25 gene family members differentially support secretory vesicle fusion. *Journal of Cell Science, 130*(11), 1877–1889. https://doi.org/10.1242/jcs.201889

Aspesi, D., & Choleris, E. (2022). Neuroendocrine underpinning of social recognition in males and females. *Journal of Neuroendocrinology, 34*(2), 1–14. https://doi.org/10.1111/jne.13070

Baginska, U., Balagura, G., Toonen, R. F., & Verhage, M. (2024). High-throughput assay for regulated secretion of neuropeptides in mouse and human neurons. *Journal of Biological Chemistry, 300*(6), 107321. https://doi.org/10.1016/j.jbc.2024.107321

Baginska, U., Moro, A., Toonen, R. F., & Verhage, M. (2023). Maximal Fusion Capacity and Efficient Replenishment of the Dense Core Vesicle Pool in Hippocampal Neurons. *The Journal of Neuroscience : The Official Journal of the Society for Neuroscience, 43*(45), 7616–7625. https://doi.org/10.1523/JNEUROSCI.2251-22.2023

Barg, S., Olofsson, C. S., Schriever-Abeln, J., Wendt, A., Gebre-Medhin, S., Renström, E., & Rorsman, P. (2002). Delay between fusion pore opening and peptide release from large dense-core vesicles in neuroendocrine cells. *Neuron, 33*(2), 287–299. https://doi.org/10.1016/S0896-6273(02)00563-9

Bednarska, J., Novak, P., Korchev, Y., Rorsman, P., Tarasov, A. I., & Shevchuk, A. (2021). Release of insulin granules by simultaneous, high-speed correlative SICM-FCM. *Journal of Microscopy, 282*(1), 21–29. https://doi.org/10.1111/jmi.12972

Benarroch, E. E. (2013). Oxytocin and vasopressin: Social neuropeptides with complex neuromodulatory functions. *Neurology, 80*(16), 1521–1528. https://doi.org/10.1212/WNL.0b013e31828cfb15

Bereczki, E., Branca, R. M., Francis, P. T., Pereira, J. B., Baek, J. H., Hortobágyi, T., Winblad, B., Ballard, C., Lehtiö, J., & Aarsland, D. (2018). Synaptic markers of cognitive decline in neurodegenerative diseases: A proteomic approach. *Brain, 141*(2), 582–595. https://doi.org/10.1093/brain/awx352

Berendzen, K.M., Sharma, R., Mandujano, M.A., Wei, Y., Rogers, F.D., Simmons, T.C., Seelke, A.M.H., Bond, J.M., Larios, R., Goodwin, N.L., Sherman, M., Parthasarthy, S., Espineda, I., Knoedler, J.R., Beery, A., Bales, K.L., Shah, N.M., & Manoli, D.S. (2023). Oxytocin receptor is not required for social attachment in prairie voles. *Neuron, 111*(6), 787-796. https://doi: 10.1016/j.neuron.2022.12.011.

Bergquist, F., & Ludwig, M. (2008). Dendritic transmitter release: A comparison of two model systems. *Journal of Neuroendocrinology, 20*(6), 677–686. https://doi.org/10.1111/j.1365-2826.2008.01714.x

Beuret, N., Stettler, H., Renold, A., Rutishauser, J., & Spiess, M. (2004). Expression of Regulated Secretory Proteins Is Sufficient to Generate Granule-like Structures in Constitutively Secreting Cells. *Journal of Biological Chemistry, 279*(19), 20242–20249. https://doi.org/10.1074/jbc.M310613200

Bolte, S., & Cordelières, F. P. (2006). A guided tour into subcellular colocalization analysis in light microscopy. *Journal of Microscopy, 224*(3), 213–232. https://doi.org/10.1111/j.1365-2818.2006.01706.x

Borges, R., Gu, C., Machado, J. D., & Ewing, A. G. (2023). The dynamic nature of exocytosis from large secretory vesicles. A view from electrochemistry and imaging. *Cell Calcium, 110,* 102699*.* https://doi.org/10.1016/j.ceca.2023.102699

Borie, A.M., Theofanopoulou, C., & Andari, E. (2021) The promiscuity of the oxytocin-vasopressin systems and their involvement in autism spectrum disorder. *Handbook of clinical neurology, 182,* 121-140. https://doi: 10.1016/B978-0-12-819973-2.00009-5.

Brown, C.H., Ludwig, M., Tasker, J.G., & Stern, J.E. (2020). Somato-dendritic vasopressin and oxytocin secretion in endocrine and autonomic regulation. *Journal of Neuroendocrinology, 32*(6), e12856. https://doi: 10.1111/jne.12856.

Camerino, C. (2023). The long way of oxytocin. *International Journal of Molecular Sciences, 24*(3), 2556. https://doi: 10.3390/ijms24032556.

Caro, P. (2020). Analysis of the release machinery of oxytocin. Master thesis project. IN-UMH.

Castel, M., Morris, J., & Belenky, M. (1996). Non-synaptic and dendritic exocytosis from dense-cored vesicles in the suprachiasmatic nucleus. *Neuroreport, 7*(2), 543-7. https://doi: 10.1097/00001756-199601310-00040.

Chung, C., & Raingo, J. (2013). Vesicle dynamics: How synaptic proteins regulate different modes of neurotransmission. *Journal of Neurochemistry, 126*(2), 146–154. https://doi.org/10.1111/jnc.12245

Cifuentes, F., Montoya, M., & Morales, M. A. (2008). High-frequency stimuli preferentially release large dense-core vesicles located in the proximity of nonspecialized zones of the presynaptic membrane in sympathetic ganglia. *Developmental Neurobiology, 68*(4), 446–456. https://doi.org/10.1002/dneu.20604

Corona, A. K., Saulsbery, H. M., Corona Velazquez, A. F., & Jackson, W. T. (2018). Enteroviruses Remodel Autophagic Trafficking through Regulation of Host SNARE Proteins to Promote Virus Replication and Cell Exit. *Cell Reports, 22*(12), 3304–3314. https://doi.org/10.1016/j.celrep.2018.03.003

Dale, H. H., (1906). On some physiological actions of ergot. *Journal of Physiology, 34*(3), 163-206. https://10.1113/jphysiol.1906.sp001148

Danoff, J.S., Whelan, E.A., & Connelly, J.J. (2023) Is oxytocin receptor signaling really dispensable for social attachment? *Comprehensive Psychoneuroendocrinoly, 14,* 100178. https://doi: 10.1016/j.cpnec.2023.100178. PMID: 36872951; PMCID: PMC9981807.

De Kock, C. P. J., Wierda, K. D. B., Bosman, L. W. J., Min, R., Koksma, J. J., Mansvelder, H. D., Verhage, M., & Brussaard, A. B. (2003). Somatodendritic secretion in oxytocin neurons is upregulated during the female reproductive cycle. *Journal of Neuroscience, 23*(7), 2726–2734. https://doi.org/10.1523/jneurosci.23-07-02726.2003

Dean, C., Dunning, F.M., Liu, H., Bomba-Warczak, E., Martens, H., Bharat, V., Ahmed, S., & Chapman, E.R. (2012). Axonal and dendritic synaptotagmin isoforms revealed by a pHluorin-syt functional screen. *Molecular Biology of the Cell, 23*(9), 1715-27. https://doi: 10.1091/mbc.E11-08-0707.

Del Prete, D., Lombino, F., Liu, X., & D'Adamio, L. (2014). APP is cleaved by bace1 in pre-synaptic vesicles and establishes a pre-synaptic interactome, viaIts intracellular domain, with molecular complexes that regulate pre-synaptic vesicles functions. *PLoS ONE,* 9(9). https://doi.org/10.1371/journal.pone.0108576

De-Miguel, F. F., & Trueta, C. (2005). Synaptic and extrasynaptic secretion of serotonin. *Cellular and Molecular Neurobiology, 25*(2), 297–312. https://doi.org/10.1007/s10571-005-3061-z

Di Scala-Guenot, D., Mouginot, D., & Strosser, M.T. (1994). Increase of intracellular calcium induced by oxytocin in hypothalamic cultured astrocytes. *Glia, 11*(3), 269-76. https://doi: 10.1002/glia.440110308.

Dölen, G. (2015a). Autism: Oxytocin, serotonin, and social reward. *Social Neuroscience, 10*(5), 450–465. https://doi.org/10.1080/17470919.2015.1087875

Dölen, G. (2015b). Oxytocin: Parallel Processing in the Social Brain? *Journal of Neuroendocrinology, 27*(6), 516–535. https://doi.org/10.1111/jne.12284

Dölen, G., & Sahin, M. (2016). Essential pathways and circuits of autism pathogenesis. *Frontiers in Neuroscience, 10*(APR), 1–2. https://doi.org/10.3389/fnins.2016.00182

Dumais, K. M., & Veenema, A. H. (2016). Vasopressin and oxytocin receptor systems in the brain: Sex differences and sex-specific regulation of social behavior. *Frontiers in Neuroendocrinology, 40,* 1–23. https://doi.org/10.1016/j.yfrne.2015.04.003

Duque-Wilckens, N., Steinman, M. Q., Busnelli, M., Chini, B., Yokoyama, S., Pham, M., Laredo, S. A., Hao, R., Perkeybile, A. M., Minie, V. A., Tan, P. B., Bales, K. L., & Trainor, B. C. (2018). Oxytocin Receptors in the Anteromedial Bed Nucleus of the Stria Terminalis Promote Stress-Induced Social Avoidance in Female California Mice. *Biological Psychiatry, 83*(3), 203–213. https://doi.org/10.1016/j.biopsych.2017.08.024

Eaton, B. A., Haugwitz, M., Lau, D., & Moore, H. P. H. (2000). Biogenesis of regulated exocytotic carriers in neuroendocrine cells. *Journal of Neuroscience, 20*(19), 7334–7344. https://doi.org/10.1523/jneurosci.20-19-07334.2000

Ebstein, R. P., Israel, S., Lerer, E., Uzefovsky, F., Shalev, I., Gritsenko, I., Riebold, M., Salomon, S., & Yirmiya, N. (2009). Arginine vasopressin and oxytocin modulate human social behavior. *Annals of the New York Academy of Sciences, 1167,* 87–102. https://doi.org/10.1111/j.1749-6632.2009.04541.x

Eliava, M., Melchior, M., Knobloch-Bollmann, H. S., Wahis, J., da Silva Gouveia, M., Tang, Y., Ciobanu, A. C., Triana del Rio, R., Roth, L. C., Althammer, F., Chavant, V., Goumon, Y., Gruber, T., Petit-Demoulière, N., Busnelli, M., Chini, B., Tan, L. L., Mitre, M., Froemke, R. C., … Grinevich, V. (2016). A New Population of Parvocellular Oxytocin Neurons Controlling Magnocellular Neuron Activity and Inflammatory Pain Processing. *Neuron, 89*(6), 1291–1304. https://doi.org/10.1016/j.neuron.2016.01.041

Erdozain, A. M., & Peñagarikano, O. (2020). Oxytocin as Treatment for Social Cognition, Not There Yet. *Frontiers in Psychiatry, 10*(January), 1–8. https://doi.org/10.3389/fpsyt.2019.00930

Ewing, A. G., Hu, K., Jia, R., Hatamie, A., Le Vo, K. L., & Mirkin, M. V. (2020). Correlating molecule count and release kinetics with vesicular size using open carbon nanopipettes. *Journal of the American Chemical Society, 142*(40), 16910–16914. https://doi.org/10.1021/jacs.0c07169

Eyigor, O., Centers, A., & Jennes, L. (2001). Distribution of ionotropic glutamate receptor subunit mRNAs in the rat hypothalamus. *Jornal of Comparative Neurology, 434,* 101–124. https://doi: 10.1002/cne.1167

Ferguson, J. N., Young, L. J., Hearn, E. F., Matzuk, M. M., Insel, T. R., & Winslow, J. T. (2000). Social amnesia in mice lacking the oxytocin gene. *Nature Genetics, 25*(3), 284–288. https://doi.org/10.1038/77040

Fossati, G., Morini, R., Corradini, I., Antonucci, F., Trepte, P., Edry, E., Sharma, V., Papale, A., Pozzi, D., Defilippi, P., Meier, J. C., Brambilla, R., Turco, E., Rosenblum, K., Wanker, E. E., Ziv, N. E., Menna, E., & Matteoli, M. (2015). Reduced SNAP-25 increases PSD-95 mobility and impairs spine morphogenesis. *Cell Death and Differentiation, 22*(9), 1425–1436. https://doi.org/10.1038/cdd.2014.227

Fries, A. B. W., Ziegler, T. E., Kurian, J. R., Jacoris, S., & Pollak, S. D. (2005). Early experience in humans is associated with changes in neuropeptides critical for regulating social behavior. *Proceedings of the National Academy of Sciences of the United States of America, 102*(47), 17237–17240. https://doi.org/10.1073/pnas.0504767102

Fujima, S., Yamaga, R., Minami, H., Mizuno, S., Shinoda, Y., Sadakata, T., Abe, M., Sakimura, K., Sano, Y., & Furuichi, T. (2021). CAPS2 deficiency impairs the release of the social peptide oxytocin, as well as oxytocin-associated social behavior. *Journal of Neuroscience, 41*(20), 4524–4535. https://doi.org/10.1523/JNEUROSCI.3240-20.2021

Fujiwara, T., Kofuji, T., & Akagawa, K. (2021). Disturbance of the reciprocal-interaction between the OXTergic and DAergic systems in the CNS causes atypical social behavior in syntaxin 1A knockout mice. *Behavioural Brain Research, 413*(July), 113447. https://doi.org/10.1016/j.bbr.2021.113447

Fujiwara, T., Sanada, M., Kofuji, T., Akagawa, K. (2016). Unusual social behavior in HPC-1/syntaxin1A knockout mice is caused by disruption of the oxytocinergic neural system. *Journal of Neurochemistry, 138*(1), 117-23. https://doi: 10.1111/jnc.13634.

Fukuda, M., & Mikoshiba, K. (2001). Characterization of KIAA1427 protein as an atypical synaptotagmin (Syt XIII). *Biochemical Journal, 354*(2), 249–257. https://doi.org/10.1042/0264-6021:3540249

Fukuda, M., Kanno, E., Ogata, Y., Saegusa, C., Kim, T., Loh, Y. P., & Yamamoto, A. (2003). Nerve growth factor-dependent sorting of synaptotagmin IV protein to mature dense-core vesicles that undergo calcium-dependent exocytosis in PC12 cells. *Journal of Biological Chemistry, 278*(5), 3220–3226. https://doi.org/10.1074/jbc.M208323200

Gerber, S. H., & Südhof, T. C. (2002). Molecular determinants of regulated exocytosis. *Diabetes, 51*(SUPPL.), 3–11. https://doi.org/10.2337/diabetes.51.2007.s3

Gimpl, G., & Fahrenholz, F. (2001). The oxytocin receptor system: Structure, function, and regulation. *Physiological Reviews, 81*(2), 629–683. https://doi.org/10.1152/physrev.2001.81.2.629

Gondré-Lewis, M. C., Park, J. J., & Loh, Y. P. (2012). Cellular Mechanisms for the Biogenesis and Transport of Synaptic and Dense-Core Vesicles. *International Review of Cell and Molecular Biology, 299*, 27-115. https://doi.org/10.1016/B978-0-12-394310-1.00002-3

Gonzalo, S., & Linder, M. E. (1998). SNAP-25 palmitoylation and plasma membrane targeting require a functional secretory pathway. *Molecular Biology of the Cell, 9*(3), 585–597. https://doi.org/10.1091/mbc.9.3.585

Grandolfo, M., & Nistri, A. (2005). An electron microscopy study of changes in dense core vesicles of PC12 cells following pulse depolarization. *NeuroReport, 16*(4), 381–385. https://doi.org/10.1097/00001756-200503150-00015

Grinevich, V., Desarménien, M. G., Chini, B., Tauber, M., & Muscatelli, F. (2015). Ontogenesis of oxytocin pathways in the mammalian brain: Late maturation and psychosocial disorders. *Frontiers in Neuroanatomy, 8*(JAN), 1–17. https://doi.org/10.3389/fnana.2014.00164

Guillemyn, B., De Saffel, H., Bek, J. W., Tapaneeyaphan, P., De Clercq, A., Jarayseh, T., Debaenst, S., Willaert, A., De Rycke, R., Byers, P. H., Rosseel, T., Coucke, P., Blaumeiser, B., Syx, D., Malfait, F., & Symoens, S. (2023). Syntaxin 18 Defects in Human and Zebrafish Unravel Key Roles in Early Cartilage and Bone Development. *Journal of Bone and Mineral Research, 38*(11), 1718–1730. https://doi.org/10.1002/jbmr.4914

Hammarlund, M., Watanabe, S., Schuske, K., & Jorgensen, E.M. (2008). CAPS and syntaxin dock dense core vesicles to the plasma membrane in neurons. *The Journal of Cell Biology, 180*(3), 483-91. https://doi: 10.1083/jcb.200708018.

Hashimoto, H., Matsuura, T., & Ueta, Y. (2014). Fluorescent visualization of oxytocin in the hypothalamo-neurohypophysial system. *Frontiers in Neuroscience, 8*(8 JUL), 1–7. https://doi.org/10.3389/fnins.2014.00213

Herman, J. P., Eyigor, O., Ziegler, D. R., & Jennes, L. (2000). Expression of ionotropic glutamate receptor subunit mRNAs in the hypothalamic paraventricular nucleus of the rat. *Jornal of Comparative Neurology, 422,* 352–362. https://doi: 10.1002/1096-9861

Holt, M., Varoqueaux, F., Wiederhold, K., Takamori, S., Urlaub, H., Fasshauer, D., & Jahn, R. (2006). Identification of SNAP-47, a novel Qbc-SNARE with ubiquitous expression. *Journal of Biological Chemistry, 281*(25), 17076–17083. https://doi.org/10.1074/jbc.M513838200

Huang, M., Bin, N.R., Rai, J., Ma, K., Chow, C.H., Eide, S., Harada, H., Xiao, J., Feng, D., Sun, H.S., Feng, Z.P., Gaisano, H.Y., Pessin, J.E., Monnier, P.P., Okamoto, K., Zhang, L., & Sugita, S. (2023). Neuronal SNAP-23 is critical for synaptic plasticity and spatial memory independently of NMDA receptor regulation. *iScience, 26*(5), 106664. https://doi: 10.1016/j.isci.2023.106664.

Insel, T. R., Winslow, J. T., Wang, Z., & Young, L. J. (1998). Neuroendocrine basis of pair bond formation. *Advances in Experimental Medicine and Biology, 449*, 215–224. https://doi: 10.1007/978-1-4615-4871-3_28.

Insel, T.R. (2010). The Challenge of Translation in Social Neuroscience: A Review of Oxytocin, Vasopressin, and Affiliative Behavior. *Neuron, 65*(6), 768–799. https://doi.org/10.1016/j.neuron.2010.03.005.

Insel, T.R., & Young, L.J. (2001). The neurobiology of attachment. *Nature Reviews Neuroscience, 2,* 129–136. https://doi.org/10.4324/9780203703878-3

Irfan, M., Gopaul, K.R., Miry, O., Hökfelt, T., Stanton, P.K., & Bark, C. (2019). SNAP-25 isoforms differentially regulate synaptic transmission and long-term synaptic plasticity at central synapses. *Scientific Reports, 9*(1), 6403. https://doi: 10.1038/s41598-019-42833-3.

Jian, F., Wang, S., Tian, R., Wang, Y., Li, C., Li, Y., Wang, S., Fang, C., Ma, C., Rong, Y. (2024). The STX17-SNAP47-VAMP7/VAMP8 complex is the default SNARE complex mediating autophagosome–lysosome fusion. *Cell Reports, 34*(2), 151-168. https://doi.org/10.1038/s41422-023-00916-x

Jurado, S. (2014). The dendritic SNARE fusion machinery involved in AMPARs insertion during long-term potentiation. *Frontiers in Cellular Neuroscience, 8,* 407. https://doi: 10.3389/fncel.2014.00407.

Jurado, S., Goswami, D., Zhang, Y., Molina, A. J. M., Südhof, T. C., & Malenka, R. C. (2013). LTP Requires a Unique Postsynaptic SNARE Fusion Machinery. *Neuron, 77*(3), 542–558. https://doi.org/10.1016/j.neuron.2012.11.029

Jurek, B., & Neumann, I. D. (2018). The oxytocin receptor: From intracellular signaling to behavior. *Physiological Reviews, 98*(3), 1805–1908. https://doi.org/10.1152/physrev.00031.2017

Kádková, A., Radecke, J., & Sørensen, J. B. (2019). The SNAP-25 Protein Family. *Neuroscience, 420,* 50–71. https://doi.org/10.1016/j.neuroscience.2018.09.020

Kasai, H., Takahashi, N., & Tokumaru, H. (2012). Distinct initial SNARE configurations underlying the diversity of exocytosis. *Physiological Reviews, 92*(4), 1915–1964. https://doi.org/10.1152/physrev.00007.2012

Kelly & Karten. (2000). UCSD Confocal Microscopy Plugins. Available from: https://imagej.net/ij/plugins/ucsd.html [2020]

Kennedy, M. J., & Ehlers, M. D. (2011). Mechanisms and Function of Dendritic Exocytosis. *Neuron, 69*(5), 856–875. https://doi.org/10.1016/j.neuron.2011.02.032

Kennedy, M.J., Davison, I.G., Robinson, C.G., & Ehlers, M.D. (2010). Syntaxin-4 defines a domain for activity-dependent exocytosis in dendritic spines. *Cell, 141*(3), 524-35. https://doi: 10.1016/j.cell.2010.02.042.

Kim, T., Gondré-Lewis, M. C., Arnaoutova, I., & Loh, Y. P. (2006). Dense-core secretory granule biogenesis. *Physiology, 21*(2), 124–133. https://doi.org/10.1152/physiol.00043.2005

Kirchner, M. K., Althammer, F., Donaldson, K. J., Cox, D. N., & Stern, J. E. (2023). Changes in neuropeptide large dense core vesicle trafficking dynamics contribute to adaptive responses to a systemic homeostatic challenge. *IScience, 26*(11), 108243. https://doi.org/10.1016/j.isci.2023.108243

Knabbe, J., Nassal, J. P., Verhage, M., & Kuner, T. (2018). Secretory vesicle trafficking in awake and anaesthetized mice: differential speeds in axons versus synapses. *Journal of Physiology, 596*(16), 3759–3773. https://doi.org/10.1113/JP276022

Kortus, S., Srinivasan, C., Forostyak, O., Zapotocky, M., Ueta, Y., Sykova, E., Chvatal, A., Verkhratsky, A., & Dayanithi, G. (2016). Sodium-calcium exchanger and R-type Ca2+ channels mediate spontaneous [Ca2+]i oscillations in magnocellular neurones of the rat supraoptic nucleus. *Cell Calcium, 59*(6), 289–298. https://doi.org/10.1016/j.ceca.2016.03.010

Kosfeld, M., Heinrichs, M., Zak, P. J., Fischbacher, U., & Fehr, E. (2005). Oxytocin increases trust in humans. *Nature, 435*(7042), 673–676. https://doi.org/10.1038/nature03701

Kuster, A., Nola, S., Dingli, F., Vacca, B., Gauchy, C., Beaujouan, J. C., Nunez, M., Moncion, T., Loew, D., Formstecher, E., Galli, T., & Proux-Gillardeaux, V. (2015). The Q-soluble N-ethylmaleimide-sensitive factor attachment protein receptor (Q-SNARE) SNAP-47 regulates trafficking of selected vesicle-associated membrane proteins (VAMPs). *Journal of Biological Chemistry, 290*(47), 28056–28069. https://doi.org/10.1074/jbc.M115.666362

Labrador (2014). Introducción a Colocalización cuantitativa ImageJ/Fiji [PowerPoint]. Available from: https://www.cbm.uam.es/images/servicios/microscopia-optica-confocal/documentos/seminarios/SMOC_VLabrador-ColocalizacionCuantitativa.pdf [2023]

Lazaro, M. T., Taxidis, J., Shuman, T., Bachmutsky, I., Ikrar, T., Santos, R., Marcello, G. M., Mylavarapu, A., Chandra, S., Foreman, A., Goli, R., Tran, D., Sharma, N., Azhdam, M., Dong, H., Choe, K. Y., Peñagarikano, O., Masmanidis, S. C., Rácz, B., … Golshani, P. (2019). Reduced Prefrontal Synaptic Connectivity and Disturbed Oscillatory Population Dynamics in the CNTNAP2 Model of Autism. *Cell Reports, 27*(9), 2567–2578.e6. https://doi.org/10.1016/j.celrep.2019.05.006

Lee, H. J., Macbeth, A. H., Pagani, J. H., & Scott Young, W. (2009). Oxytocin: The great facilitator of life. *Progress in Neurobiology, 88*(2), 127–151. https://doi.org/10.1016/j.pneurobio.2009.04.001

Leng, G., & Ludwig, M. (2016). Intranasal Oxytocin: Myths and Delusions. *Biological Psychiatry, 79*(3), 243–250. https://doi.org/10.1016/j.biopsych.2015.05.003

Lewis, E. M., Stein-O'Brien, G. L., Patino, A. V., Nardou, R., Grossman, C. D., Brown, M., Bangamwabo, B., Ndiaye, N., Giovinazzo, D., Dardani, I., Jiang, C., Goff, L. A., & Dölen, G. (2020). Parallel Social Information Processing Circuits Are Differentially Impacted in Autism. *Neuron, 108*(4), 659–675.e6. https://doi.org/10.1016/j.neuron.2020.10.002

Lochner, J. E., Honigman, L. S., Grant, W. F., Gessford, S. K., Hansen, A. B., Silverman, M. A., & Scalettar, B. A. (2006). Activity-dependent release of tissue plasminogen activator from the dendritic spines of hippocampal neurons revealed by live-cell imaging. *Journal of Neurobiology, 66*(6), 564–577. https://doi.org/10.1002/neu.20250

Ludwig, M., & Leng, G. (2006). Dendritic peptide release and peptide-dependent behaviours. *Nature Reviews Neuroscience, 7*(2), 126–136. https://doi.org/10.1038/nrn1845

Ludwig, M., & Stern, J. (2015). Multiple signalling modalities mediated by dendritic exocytosis of oxytocin and vasopressin. *Philosophical Transactions of the Royal Society B: Biological Sciences, 370*(1672), 1–9. https://doi.org/10.1098/rstb.2014.0182

Ludwig, M., Apps, D., Menzies, J., Patel, J. C., & Rice, M. E. (2017). Dendritic release of neurotransmitters. *Comprehensive Physiology, 7*(1), 235–252. https://doi.org/10.1002/cphy.c160007

Ludwig, M., Sabatier, N., Bull, P. M., Landgraf, R., Dayanithi, G., & Leng, G. (2002). Intracellular calcium stores regulate activity-dependent neuropeptide release from dendrites. *Nature, 418*(6893), 85–89. https://doi.org/10.1038/nature00822

Ma, Z., Yu, Y., Gao, M., Chen, P., Hong, H., Yu, D., Liang, Z., Bai, Y., Ye, Q., Wang, Y., Huang, G., & Tan, H. (2024). Protective Effect of Hop Ethyl Acetate Extract on Corticosterone-Induced PC12 and Improvement of Depression-like Behavior in Mice. *ACS Chemical Neuroscience, 15*(9), 1893-1903. https://doi: 10.1021/acschemneuro.4c00081.

Madisen, L., Zwingman, T.A., Sunkin, S.M., Oh, S.W., Zariwala, H.A., Gu, H., Ng, L.L., Palmiter, R.D., Hawrylycz, M.J., Jones, A.R., Lein, E.S., & Zeng, H. (2009) A robust and high-throughput Cre reporting and characterization system for the whole mouse brain. *Nature Neuroscience, 13*(1), 133-40. https://doi: 10.1038/nn.2467.

Madrigal, M. P., & Jurado, S. (2021). Specification of oxytocinergic and vasopressinergic circuits in the developing mouse brain. *Communications Biology, 4*(1), 1–16. https://doi.org/10.1038/s42003-021-02110-4

Madrigal, M. P., Portalés, A., SanJuan, M. P., & Jurado, S. (2019). Postsynaptic SNARE Proteins: Role in Synaptic Transmission and Plasticity. *Neuroscience, 420,* 12–21. https://doi.org/10.1016/j.neuroscience.2018.11.012

Mascalchi, P., & Cordelières, F.P. (2019). Which Elements to Build Co-localization Workflows? From Metrology to Analysis. *Methods in Molecular Biology, 2040*, 177-213. https://doi: 10.1007/978-1-4939-9686-5_10.

Matsui, K., & Jahr, C. E. (2006). Exocytosis unbound. *Current Opinion in Neurobiology, 16*(3), 305-11. https://doi: 10.1016/j.conb.2006.04.001.

Matsui, T., Sakamaki, Y., Hiragi, S., & Fukuda, M. (2023). VAMP5 and distinct sets of cognate Q-SNAREs mediate exosome release. *Cell Structure and Function, 48*(2), 187–198. https://doi.org/10.1247/csf.23067

Meas-Yedid (2017). Colocalisation. Available from https://research.pasteur.fr/wp-content/uploads/2015/05/research_pasteur-vannary-meas-yedid-hardy-courscoloc2017.pdf [18-06-2024]

Merighi, A. (2018). Costorage of high molecular weight neurotransmitters in large dense core vesicles of mammalian neurons. *Frontiers in Cellular Neuroscience, 12*, 1–7. https://doi.org/10.3389/fncel.2018.00272

Meyer-Lindenberg, A., Domes, G., Kirsch, P., & Heinrichs, M. (2011). Oxytocin and vasopressin in the human brain: Social neuropeptides for translational medicine. *Nature Reviews Neuroscience, 12*(9), 524–538. https://doi.org/10.1038/nrn3044

Mitchell, K. J., Pinton, P., Varadi, A., Tacchetti, C., Ainscow, E. K., Pozzan, T., Rizzuto, R., & Rutter, G. A. (2001). Dense core secretory vesicles revealed as a dynamic Ca2+ store in neuroendocrine cells with a vesicle-associated membrane protein aequorin chimaera. *Journal of Cell Biology, 155*(1), 41–51. https://doi.org/10.1083/jcb.200103145

Miyata, S., Takamatsu, H., Maekawa, S., Matsumoto, N., Watanabe, K., Kiyohara, T., & Hatton, G. I. (2001). Plasticity of neurohypophysial terminals with increased hormonal release during dehydration: Ultrastructural and biochemical analyses. *Journal of Comparative Neurology, 434*(4), 413–427. https://doi.org/10.1002/cne.1184

Modi, M.E., & Young, L.J. (2012). The oxytocin system in drug discovery for autism: Animal models and novel therapeutic strategies. *Hormones and Behavior, 61*(3), 340-350. https://doi.org/10.1016/j.yhbeh.2011.12.010.

Müller, H.K., Wegener, G., Popoli, M., & Elfving, B. (2011). Differential expression of synaptic proteins after chronic restraint stress in rat prefrontal cortex and hippocampus. *Brain Research, 1385*, 26-37. https://doi: 10.1016/j.brainres.2011.02.048.

Münster-Wandowski, A., Heilmann, H., Bolduan, F., Trimbuch, T., Yanagawa, Y., & Vida, I. (2017). Distinct localization of SNAP47 protein in GABAergic and glutamatergic neurons in the mouse and the rat hippocampus. *Frontiers in Neuroanatomy, 11*(July), 1–18. https://doi.org/10.3389/fnana.2017.00056

Nadler, J. J., Moy, S. S., Dold, G., Trang, D., Simmons, N., Perez, A., Young, N. B., Barbaro, R. P., Piven, J., Magnuson, T. R., & Crawley, J. N. (2004). Automated apparatus for quantitation of social approach behaviors in mice. *Genes, Brain and Behavior, 3*(5), 303–314. https://doi.org/10.1111/j.1601-183X.2004.00071.x

Ramakrishnan, N.A., Drescher, M.J., & Drescher, D.G. (2012). The SNARE complex in neuronal and sensory cells. *Molecular and Cellular Neurosciences, 50*(1), 58-69. https://doi: 10.1016/j.mcn.2012.03.009.

Neumann, I. D. (2008). Brain oxytocin: A key regulator of emotional and social behaviours in both females and males. *Journal of Neuroendocrinology, 20*(6), 858–865. https://doi.org/10.1111/j.1365-2826.2008.01726.x

Nofal, S., Becherer, U., Hof, D., Matti, U., & Rettig, J. (2007). Primed vesicles can be distinguished from docked vesicles by analyzing their mobility. *Journal of Neuroscience, 27*(6), 1386–1395. https://doi.org/10.1523/JNEUROSCI.4714-06.2007

Oheim, M., Loerke, D., Stühmer, W., & Chow, R. H. (1998). The last few milliseconds in the life of a secretory granule. *European Biophysics Journal, 27*(2), 83–98. https://doi.org/10.1007/s002490050114

Osakada, T., Yan, R., Jiang, Y., Wei, D., Tabuchi, R., Dai, B., Wang, X., Zhao, G., Wang, C.X., Liu, J.J., Tsien, R.W., Mar, A.C., & Lin, D. (2024). A dedicated hypothalamic oxytocin circuit controls aversive social learning. *Nature, 626*(7998), 347-356. https://doi: 10.1038/s41586-023-06958-w.

Otero-García, M., Agustín-Pavón, C., Lanuza, E., & Martínez-García, F. (2016). Distribution of oxytocin and co-localization with arginine vasopressin in the brain of mice. *Brain Structure and Function, 221*(7), 3445–3473. https://doi.org/10.1007/s00429-015-1111-y

Ott, I., & Scott, J.C. (1910). The action of infundibulin upon the mammary secretion. *Proceedings of the Society for Experimental Biology and Medicine, 27*(552). https://doi.org/:10.3181/00379727-8-27

Ovsepian, S. V., & Dolly, J. O. (2011). Dendritic SNAREs add a new twist to the old neuron theory. *Proceedings of the National Academy of Sciences of the United States of America, 108*(48), 19113–19120. https://doi.org/10.1073/pnas.1017235108

Park, H., Li, Y., & Tsien, R. W. (2012). Influence of synaptic vesicle position on release probability and exocytotic fusion mode. *Science, 335*(6074), 1362–1366. https://doi.org/10.1126/science.1216937

Peñagarikano, O., Abrahams, B.S., Herman, E.I., Winden, K.D., Gdalyahu, A., Dong, H., Sonnenblick, L.I., Gruver, R., Almajano, J., Bragin, A., Golshani, P., Trachtenberg, J.T., Peles, E., & Geschwind, D.H. (2011) Absence of CNTNAP2 leads to epilepsy, neuronal migration abnormalities and core autism-related deficits. *Cell, 147*(1), 235-46. https://doi.org/10.1016/j.cell.2011.08.040.

Peñagarikano, O., Lázaro, M.T., Lu, X.H., Gordon, A., Dong, H., Lam, H.A., Peles, E., Maidment, N.T., Murphy, N.P., Yang, X.W., Golshani, P., & Geschwind, D.H. (2015). Exogenous and evoked OXT restores social behavior in the Cntnap2 mouse model of autism. *Science Translational Medicine, 271*(1), 139–148. https://doi.org/10.1126/scitranslmed.3010257

Perez-Hurtado, M., Dao, C., Saenz, A.E., & Heidelberger, R. (2023). Syntaxin 3 is haplosufficient for long-term photoreceptor survival in the mouse retina. *Frontiers in Ophthalmoly (Lausanne), 3,* 1208805. https://doi: 10.3389/fopht.2023.1208805.

Persoon, C. M., Moro, A., Nassal, J. P., Farina, M., Broeke, J. H., Arora, S., Dominguez, N., van Weering, J. R., Toonen, R. F., & Verhage, M. (2018). Pool size estimations for dense-core vesicles in mammalian CNS neurons. *The EMBO Journal, 37*(20), 1–18. https://doi.org/10.15252/embj.201899672

Portalés, A., Chamero, P., & Jurado, S. (2023). Natural and Pathological Aging Distinctively Impacts the Pheromone Detection System and Social Behavior. *Molecular Neurobiology, 60*(8), 4641–4658. https://doi.org/10.1007/s12035-023-03362-3

Pow, D. V., & Morris, J. F. (1989). Dendrites of hypothalamic magnocellular neurons release neurohypophysial peptides by exocytosis. *Neuroscience, 32*(2), 435–439. https://doi.org/10.1016/0306-4522(89)90091-2

Praschberger, R., Jacquemyn, J., & Verstreken, P. (2021). Molecule-to-Circuit Disease Mechanisms of a Synaptic SNAREopathy. *Neuron, 109*(1), 1–3. https://doi.org/10.1016/j.neuron.2020.12.009

Qian, T., Wang, H., Wang, P., Geng, L., Mei, L., Osakada, T., Wang, L., Tang, Y., Kania, A., Grinevich, V., Stoop, R., Lin, D., Luo, M., & Li, Y. (2023). A genetically encoded sensor

measures temporal oxytocin release from different neuronal compartments. *Nature Biotechnology, 41*(7), 944–957. https://doi.org/10.1038/s41587-022-01561-2

Qin, N., Chen, Z., & Xue, R. (2022). A two-subpopulation model that reflects heterogeneity of large dense core vesicles in exocytosis. *Cell Cycle, 21*(5), 531–546. https://doi.org/10.1080/15384101.2022.2026576

Rajamani, K. T., Wagner, S., Grinevich, V., & Harony-Nicolas, H. (2018). Oxytocin as a Modulator of Synaptic Plasticity: Implications for Neurodevelopmental Disorders. *Frontiers in Synaptic Neuroscience, 10*(June), 1–8. https://doi.org/10.3389/fnsyn.2018.00017

Ramakrishnan, N.A., Dreschera, M.J., & Drescher, D.G. (2012). The SNARE complex in neuronal and sensory cells. *Molecular Cell Neuroscience, 50*(1), 58–69. https://doi.org/10.1016/j.mcn.2012.03.009.

Rizo, J., & Rosenmund, C. (2008). Synaptic vesicle fusion. *Nature Structural Molecular Biology, 15*(7), 665–674. https://doi: 10.1038/nsmb.1450

Rizo, J., & Südhof, T. C. (2002). Snares and munc18 in synaptic vesicle fusion. *Nature Reviews Neuroscience, 3*(8), 641–653. https://doi.org/10.1038/nrn898

Rizo, J., & Südhof, T. C. (2012). The membrane fusion enigma: SNAREs, Sec1/Munc18 proteins, and their accomplices guilty as charged? *Annual Review of Cell and Developmental Biology, 28,* 279-308. https://doi.org/10.1146/annurev-cellbio-101011-155818

Royo, M., Escolano, B. A., Madrigal, M. P., & Jurado, S. (2022). AMPA Receptor Function in Hypothalamic Synapses. *Frontiers in Synaptic Neuroscience, 14*(January), 1–16. https://doi.org/10.3389/fnsyn.2022.833449

Sabatier, N., Caquineau, C., Dayanithi, G., Bull, P., Douglas, A. J., Guan, X. M. M., Jiang, M., Van Der Ploeg, L., & Leng, G. (2003). α-Melanocyte-Stimulating Hormone Stimulates Oxytocin Release from the Dendrites of Hypothalamic Neurons while Inhibiting Oxytocin Release from Their Terminals in the Neurohypophysis. *Journal of Neuroscience, 23*(32), 10351–10358. https://doi.org/10.1523/jneurosci.23-32-10351.2003

Sap, K. A., Guler, A. T., Bury, A., Dekkers, D., Demmers, J. A. A., & Reits, E. A. (2021). Identification of Full-Length Wild-Type and Mutant Huntingtin Interacting Proteins by Crosslinking Immunoprecipitation in Mice Brain Cortex. *Journal of Huntington's Disease, 10*(3), 335–347. https://doi.org/10.3233/JHD-210476

Scalettar, B.A., Jacobs, C., Fulwiler, A., Prahl, L., Simon, A., Hilken, L., & Lochner, J.E. (2012). Hindered submicron mobility and long-term storage of presynaptic dense-core granules revealed by single-particle tracking. *Developmental Neurobiology, 72*(9), 1181-95. https://doi: 10.1002/dneu.20984.

Sharma, K., LeBlanc, R., Haque, M., Nishimori, K., Reid, M. M., & Teruyama, R. (2019). Sexually dimorphic oxytocin receptorexpressing neurons in the preoptic area of the mouse brain. *PLoS ONE, 14*(7), 1–19. https://doi.org/10.1371/journal.pone.0219784

Shen, H. (2015). The hard science of oxytocin. *Nature, 25,* 410-2. https://doi: 10.1038/522410a.

Shimojo, M., Courchet, J., Pieraut, S., Torabi-Rander, N., Sando, R. 3rd, Polleux, F., & Maximov, A. (2015). SNAREs Controlling Vesicular Release of BDNF and Development of Callosal Axons. *Cell Reports, 11*(7), 1054-66. https://doi: 10.1016/j.celrep.2015.04.032.

Silverman, M. A., Johnson, S., Gurkins, D., Farmer, M., Lochner, J. E., Rosa, P., & Scalettar, B. A. (2005). Mechanisms of transport and exocytosis of dense-core granules containing tissue plasminogen activator in developing hippocampal neurons. *Journal of Neuroscience, 25*(12), 3095–3106. https://doi.org/10.1523/JNEUROSCI.4694-04.2005

Singer-Lahat, D., Sheinin, A., Chikvashvili, D., Tsuk, S., Greitzer, D., Friedrich, R., Feinshreiber, L., Ashery, U., Benveniste, M., Levitan, E. S., & Lotan, I. (2007). K+ channel facilitation of exocytosis by dynamic interaction with syntaxin. *Journal of Neuroscience, 27*(7), 1651–1658. https://doi.org/10.1523/JNEUROSCI.4006-06.2007

Sobota, J. A., Mohler, W. A., Cowan, A. E., Eipper, B. A., & Mains, R. E. (2010). Dynamics of peptidergic secretory granule transport are regulated by neuronal stimulation. *BMC Neuroscience, 11,* 32. https://doi.org/10.1186/1471-2202-11-32

Son, S., Manjila, S. B., Newmaster, K. T., Wu, Y. T., Vanselow, D. J., Ciarletta, M., Anthony, T. E., Cheng, K. C., & Kim, Y. (2022). Whole-Brain Wiring Diagram of Oxytocin System in Adult Mice. *Journal of Neuroscience, 42*(25), 5021–5033. https://doi.org/10.1523/JNEUROSCI.0307-22.2022

Sorra, K. E., Mishra, A., Kirov, S. A., & Harris, K. M. (2006). Dense core vesicles resemble active-zone transport vesicles and are diminished following synaptogenesis in mature hippocampal slices. *Neuroscience, 141*(4), 2097–2106. https://doi.org/10.1016/j.neuroscience.2006.05.033

Steyer, J.A., Horstmann, H., & Almers, W. (1997). Transport, docking and exocytosis of single secretory granules in live chromaffin cells. *Nature, 388*(6641), 474-8. https://doi: 10.1038/41329.

Stojilkovic, S. S. (2005). Ca2+-regulated exocytosis and SNARE function. Trends in *Endocrinology and Metabolism, 16*(3), 81–83. https://doi.org/10.1016/j.tem.2005.02.002

Stoop, R. (2012). Neuromodulation by Oxytocin and Vasopressin. *Neuron, 76*(1), 142–159. https://doi.org/10.1016/j.neuron.2012.09.025

Stringer, C., Wang, T., Michaelos, M., & Pachitariu, M. (2021). Cellpose: a generalist algorithm for cellular segmentation. *Nature Methods, 18*(1), 100–106. https://doi.org/10.1038/s41592-020-01018-x

Stuenkel, E. L. (1994). Regulation of intracellular calcium and calcium buffering properties of rat isolated neurohypophysial nerve endings. *The Journal of Physiology, 481*(2), 251–271. https://doi.org/10.1113/jphysiol.1994.sp020436

Südhof, T. C. (2004). The synaptic vesicle cycle. *Annual Review of Neuroscience, 27,* 509–547. https://doi.org/10.1146/annurev.neuro.26.041002.131412

Südhof, T. C. (2012). Calcium control of neurotransmitter release. Cold Spring Harbor Perspectives in Biology, 4(1). https://doi.org/10.1101/cshperspect.a011353

Südhof, T. C., & Rizo, J. (2011). Synaptic vesicle exocytosis. *Perspectives in Biology, 3*(12), 1–14. https://doi.org/10.1101/cshperspect.a005637

Südhof, T.C. (2013). Neurotransmitter release: the last millisecond in the life of a synaptic vesicle. *Neuron, 80*(3), 675-90. https://doi: 10.1016/j.neuron.2013.10.022.

Südhof, T.C., & Rothman, J.E. (2009). Membrane Fusion: Grappling with SNARE and SM Proteins. *Science. 323*(5913), 474–477. https://doi.org/10.1126/science.1161748.

Swanson, L.W., & Sawchenko, P.E. (1983). Hypothalamic integration: organization of the paraventricular and supraoptic nuclei. *Annual Review of Neuroscience, 6,* 6:269-324. https://doi: 10.1146/annurev.ne.06.030183.001413.

Takayanagi, Y., Yoshida, M., Bielsky, I.F., Ross, H.E., Kawamata, M., Onaka, T., Yanagisawa, T., Kimura, T., Matzuk, M.M., Young, L.J., & Nishimori, K. (2005). Pervasive social deficits, but normal parturition, in oxytocin receptor-deficient mice. *Proceedings of the National Academy of Sciences of the United States of America, 102*(44), 16096-101. https://doi: 10.1073/pnas.0505312102.

Tang, B. L. (2019). Syntaxin 16's newly deciphered roles in autophagy. *Cells, 8*(12), 25–29. https://doi.org/10.3390/cells8121655

Teng, H., Wang, Y., & Tang, B. L. (2001). The syntaxins. *Genome Biology, 2*(11), 1–7. https://doi: 10.1186/gb-2001-2-11-reviews3012

Tobin, V. A., & Ludwig, M. (2007). The actin filament and dendritic peptide release. *Biochemical Society Transactions, 35*(5), 1243–1246. https://doi.org/10.1042/BST0351243

Tobin, V. A., Douglas, A. J., Leng, G., & Ludwig, M. (2011). The involvement of voltage-operated calcium channels in somato-dendritic oxytocin release. *PLoS ONE, 6*(10). https://doi.org/10.1371/journal.pone.0025366

Tobin, V., Leng, G., & Ludwig, M. (2012). The involvement of actin, calcium channels and exocytosis proteins in somato-dendritic oxytocin and vasopressin release. *Frontiers in Physiology, 3*(July), 1–7. https://doi.org/10.3389/fphys.2012.00261

Tobin, V., Schwab, Y., Lelos, N., Onaka, T., Pittman, Q. J., & Ludwig, M. (2012). Expression of Exocytosis Proteins in Rat Supraoptic Nucleus Neurones. *Journal of Neuroendocrinology, 24*(4), 629–641. https://doi.org/10.1111/j.1365-2826.2011.02237.x

Tom, N., & Assinder, S. J. (2010). Oxytocin in health and disease. *International Journal of Biochemistry and Cell Biology, 42*(2), 202–205. https://doi.org/10.1016/j.biocel.2009.10.008

Troger, J., Kirchmair, R., Marksteiner, J., Seidl, C.V., Fischer-Colbrie, R., Saria, A., & Winkler, H. (1994). Release of secretoneurin and noradrenaline from hypothalamic slices and its differential inhibition by calcium channel blockers. *Naunyn-Schmiedebergs' Archives of Pharmacology, 349*(6), 565-9. https://doi: 10.1007/BF01258460.

Trueta, C., Méndez, B., & De-Miguel, F. F. (2003). Somatic exocytosis of serotonin mediated by L-type calcium channels in cultured leech neurones. *Journal of Physiology, 547*(2), 405–416. https://doi.org/10.1113/jphysiol.2002.030684

Ubero (2008). Fundamentos de microscopía electrónica. Available from: https://www.um.es/innova/OCW/Microscop%C3%ADa-aplicada-a-las-ciencias-forenses/microscopia/material_clase/Sesion_Teorico-04.pdf [14-06-2022]

Universidad politécnica de Valencia (2020). Microscopía electrónica de transmisión. Available from: https://www.upv.es/entidades/SME/info/753329normalc.html [14-06-22]

Urbina, F. L., & Gupton, S. L. (2020). SNARE-Mediated Exocytosis in Neuronal Development. *Frontiers in Molecular Neuroscience, 13*(August), 1–17. https://doi.org/10.3389/fnmol.2020.00133

Urbina, F. L., Menon, S., Goldfarb, D., Edwards, R., Ben Major, M., Brennwald, P., & Gupton, S. L. (2021). TRIM67 regulates exocytic mode and neuronal morphogenesis via SNAP47. *Cell Reports, 34*(6). https://doi.org/10.1016/j.celrep.2021.108743

Uzay, B., & Kavalali, E. T. (2023). Genetic disorders of neurotransmitter release machinery. *Frontiers in Synaptic Neuroscience, 15*(March), 1–16. https://doi.org/10.3389/fnsyn.2023.1148957

Van Den Pol, A. N. (1982). The magnocellular and parvocellular paraventricular nucleus of rat: Intrinsic organization. *Journal of Comparative Neurology, 206*(4), 317–345. https://doi.org/10.1002/cne.902060402

Van Den Pol, A. N. (1994). Metabotropic glutamate receptor mGluR1 distribution and ultrastructural localization in hypothalamus. *Journal of Comparative Neurology, 349,* 615–632. https://doi: 10.1002/cne.903490409

Van Den Pol, A. N. (2012). Neuropeptide Transmission in Brain Circuits. *Neuron, 76*(1), 98–115. https://doi.org/10.1016/j.neuron.2012.09.014

Vardjan, N., Stenovec, M., Jorgačevski, J., Kreft, M., & Zorec, R. (2007). Subnanometer fusion pores in spontaneous exocytosis of peptidergic vesicles. *Journal of Neuroscience, 27*(17), 4737–4746. https://doi.org/10.1523/JNEUROSCI.0351-07.2007

Verhage, M., & Sørensen, J. B. (2020). SNAREopathies: Diversity in Mechanisms and Symptoms. *Neuron, 107*(1), 22–37. https://doi.org/10.1016/j.neuron.2020.05.036

Viero, C., Shibuya, I., Kitamura, N., Verkhratsky, A., Fujihara, H., Katoh, A., Ueta, Y., Zingg, H. H., Chvatal, A., Sykova, E., & Dayanithi, G. (2010). Oxytocin: Crossing the bridge between basic science and pharmacotherapy. *CNS Neuroscience and Therapeutics, 16*(5), 138–156. https://doi.org/10.1111/j.1755-5949.2010.00185.x

Viudes, N. (2021). Analysis of the SNARE fusion machinery in oxytocin magnocellular and parvocellular neurons in the mouse hypothalamus. Master thesis project. IN-UMH.

Wolfes, A. C., & Dean, C. (2020). The diversity of synaptotagmin isoforms. *Current Opinion in Neurobiology, 63,* 198–209. https://doi.org/10.1016/j.conb.2020.04.006

Wu, Z., Xu, Y., Zhu, Y., Sutton, A.K., Zhao, R., Lowell, B.B., Olson, D.P., & Tong, Q. (2012). An obligate role of oxytocin neurons in diet induced energy expenditure. *PLoS One, 7*(9), e45167. https://doi: 10.1371/journal.pone.0045167.

Xia, X., Lessmann, V., & Martin, T. F. J. (2009). Imaging of evoked dense-core-vesicle exocytosis in hippocampal neurons reveals long latencies and kiss-and-run fusion events. *Journal of Cell Science, 122*(1), 75–82. https://doi.org/10.1242/jcs.034603

Xu, X., Kozikowski, A. P., & Pozzo-Miller, L. (2014). A selective histone deacetylase-6 inhibitor improves BDNF trafficking in hippocampal neurons from Mecp2 knockout mice: Implications for Rett syndrome. *Frontiers in Cellular Neuroscience, 8*(MAR), 1–9. https://doi.org/10.3389/fncel.2014.00068

Xue, R., Zhang, E., & Wang, Y. (2024). Pre-fusion motion state determines the heterogeneity of membrane fusion dynamics for large dense-core vesicles. *Acta Physiologica, 240*(4), 1–12. https://doi.org/10.1111/apha.14115

Young, L. J., & Barrett, C. E. (2015). Can oxytocin treat autism? *Science, 347*(6224), 825–826. https://doi.org/10.1126/science.aaa8120

Young, L. J., & Wang, Z. (2004). The neurobiology of pair bonding. *Nature Neuroscience, 7*(10), 1048–1054. https://doi.org/10.1038/nn1327

Zhang, G., Bai, H., Zhang, H., Dean, C., Wu, Q., Li, J., Guariglia, S., Meng, Q., & Cai, D. (2011). Neuropeptide Exocytosis Involving Synaptotagmin-4 and Oxytocin in Hypothalamic Programming of Body Weight and Energy Balance. *Neuron, 69*(3), 523–535. https://doi.org/10.1016/j.neuron.2010.12.036

Zhang, P., Rumschitzki, D., & Edwards, R.H. (2023). High-speed imaging reveals the bimodal nature of dense core vesicle exocytosis. *Proceeding of the National Academy of Sciences of the United States of America, 120*(1). https://doi: 10.1073/pnas.2214897120.

Zhang, Z., Bhalla, A., Dean, C., Chapman, E.R., & Jackson, M.B. (2009). Synaptotagmin IV: a multifunctional regulator of peptidergic nerve terminals. *Nature Neuroscience, 12*(2), 163-71. https://doi: 10.1038/nn.2252.

Zhang, Z., Wu, Y., Wang, Z., Dunning, F. M., Rehfuss, J., Ramanan, D., Chapman, E. R., & Jackson, M. B. (2011). Release mode of large and small dense-core vesicles specified by different synaptotagmin isoforms in PC12 cells. *Molecular Biology of the Cell, 22*(13), 2324–2336. https://doi.org/10.1091/mbc.E11-02-0159

APPENDIX.- Statistical data

MATERIALS AND METHODS

3.-Primary culture of hypothalamic neurons.

Table 1.- OT neurons identified in OT^{tdTom} and OT^{EYFP} hypothalamic cultures with anti-RFP and anti-GFP antibodies, respectively. n= 3 hypothalamic primary cultures.

	OT neurons (% ± SEM)
anti-RFP (OT^{tdTom})	20.6 ± 1.6
anti-GFP (OT^{EYFP})	24.39 ± 2.5

Table 2.- OT neurons identified with anti-OT and anti-RFP antibodies in OT^{tdTom} hypothalamic cultures, and anti-OT and anti-GFP antibodies in OT^{EYFP} hypothalamic cultures. n= 3 hypothalamic primary cultures.

	OT neurons (% ± SEM)
anti-OT+anti-RFP (OT^{tdTom})	97.7 ± 1.2
anti-OT+anti-GFP (OT^{EYFP})	96.6 ± 1.5

6.-Cytotoxicity.

Table 3.- Descriptive statistics of cytotoxicity experiments. n= 2 hypothalamic primary cultures (5 images/condition).

Treatment	**DAPI (Mean ± SEM)**	**DAPI (%)**	**Live (Mean ± SEM)**	**Live (%)**	**Dead (Mean ± SEM)**	**Dead (%)**
Basal_1 min	2255 ± 46.96	100	1971 ± 43.99	87.40	284 ± 3.72	12.59
Basal_10 min	2152 ± 26.4	100	1859 ± 23.58	86.38	296 ± 4.44	86.38
EtOH 70 %_1 min	2508 ± 29.83	100	0 ± 0	0	2508 ± 29.83	100
EtOH 70 %_10 min	2419 ± 28.60	100	0 ± 0	0	2419 ± 28.6	100
50 mM KCl_1 min	2086 ± 17.35	100	1743 ± 18.67	83.56	342 ± 3.49	16.39
50 mM KCl_10 min	1631 ± 16.35	100	1282 ± 19.19	78.60	349 ± 7.06	21.40

100 mM_KCl 1 min	2150 ± 32.33	100	1846 ± 31.29	85.86	304 ± 2.78	14.14
100 mM_KCl 10 min	2119 ± 23.99	100	1822 ± 20.74	85.98	297 ± 3.77	14.01

Table 4.- Statistical analysis of cytotoxicity experiments.

Treatment	Comparison	Statistical test	p-value	p-value summary
Basal_1 min	Live vs. Dead	Mann-Whitney	0.0001	***
Basal_10 min	Live vs. Dead	Mann-Whitney	<0.0001	****
50 mM KCl_10 min	Live vs. Dead	Mann-Whitney	0.0007	***
50 mM KCl_1 min	Live vs. Dead	Mann-Whitney	<0.0001	****
100 mM KCl_10 min	Live vs. Dead	Mann-Whitney	<0.0001	****
100 mM KCl_1 min	Live vs. Dead	Mann-Whitney	<0.0001	****
EtOH 70 %_10 min	Live vs. Dead	Mann-Whitney	<0.0001	****
EtOH 70 %_1 min	Live vs. Dead	Mann-Whitney	<0.0001	****

Table 5.- Statistical analysis of “Live” data from cytotoxicity experiments.

Comparison	Statistical test	p-value	p-value summary
Basal_1 min vs. Basal_10 min	Kruskal-Wallis	>0.9999	ns
Basal_1 min vs. EtOH_1 min	Kruskal-Wallis	0.0015	**
Basal_1 min vs. EtoH_10 min	Kruskal-Wallis	0.0015	**
Basal_1 min vs. 50 mM KCl_1 min	Kruskal-Wallis	>0.9999	ns
Basal_1 min vs. 50 mM KCl_10 min	Kruskal-Wallis	>0.9999	ns
Basal_1 min vs. 100 mM KCl_1 min	Kruskal-Wallis	>0.9999	ns
Basal_1 min vs. 100 mM KCl_10 min	Kruskal-Wallis	>0.9999	ns
Basal_10 min vs. EtOH 70 %_1 min	Kruskal-Wallis	0.0016	**
Basal_10 min vs. EtOH 70 %_10 min	Kruskal-Wallis	0.0016	**
Basal_10 min vs. 50 mM KCl_1min	Kruskal-Wallis	>0.9999	ns
Basal_10 min vs. 50 mM KCl_10 min	Kruskal-Wallis	>0.9999	ns
Basal_10 min vs. 100 mM KCl_1 min	Kruskal-Wallis	>0.9999	ns
Basal_10 min vs. 100 mM KCl_10 min	Kruskal-Wallis	>0.9999	ns
EtOH 70 %_1 min vs. EtOH 70 %_10	Kruskal-Wallis	>0.9999	ns

min			
EtOH 70 %_1 min vs. 50 mM KCl_1min	Kruskal-Wallis	0.0017	**
EtOH 70 %_1 min vs. 50 mM KCl_10 min	Kruskal-Wallis	0.0683	ns
EtOH 70 %_1 min vs. 100 mM KCl_1 min	Kruskal-Wallis	0.0023	**
EtOH 70 %_1 min vs. 100 mM KCl_10 min.	Kruskal-Wallis	0.0007	***
EtOH 70 %_10 min vs. 50 mM KCl_1 min	Kruskal-Wallis	0.0017	**
EtOH 70 %_10 min vs. 50 mM KCl_10 min	Kruskal-Wallis	0.0683	ns
EtOH 70 %_1 min vs. 100 mM KCl_1 min	Kruskal-Wallis	0.0023	**
EtOH 70 %_10 min vs. 100 mM KCl_10 min	Kruskal-Wallis	0.0007	***
50 mM KCl_1 min vs. 50 mM KCl-10 min	Kruskal-Wallis	>0.9999	ns
50 mM KCl_1 min vs. 100 mM KCl_1 min	Kruskal-Wallis	>0.9999	ns
50 mM KCl_1 min vs. 100 mM KCl_10 min	Kruskal-Wallis	>0.9999	ns
50 mM KCl_10 min vs. 100 mM KCl_1 min	Kruskal-Wallis	>0.9999	ns
50 mM KCl_10 min vs. 100 mM KCl_10 min	Kruskal-Wallis	>0.9999	ns
100 mM KCl_1 min vs. 100 mM KCl_10 min	Kruskal-Wallis	>0.9999	ns

Table 6.- Statistical analysis of “Dead” data from cytotoxicity experiments.

Comparison	Statistical test	p-value	p-value summary
Basal_1 min vs. Basal_10 min	Kruskal-Wallis	>0.9999	ns
Basal_1 min vs. EtOH_1 min	Kruskal-Wallis	>0.9999	***
Basal_1 min vs. EtoH_10 min	Kruskal-Wallis	>0.9999	***

Basal_1 min vs. 50 mM KCl_1 min	Kruskal-Wallis	0.0009	ns
Basal_1 min vs. 50 mM KCl_10 min	Kruskal-Wallis	0.0012	ns
Basal_1 min vs. 100 mM KCl_1 min	Kruskal-Wallis	>0.9999	ns
Basal_1 min vs. 100 mM KCl_10 min	Kruskal-Wallis	>0.9999	ns
Basal_10 min vs. EtOH 70 %_1 min	Kruskal-Wallis	>0.9999	***
Basal_10 min vs. EtOH 70 %_10 min	Kruskal-Wallis	>0.9999	**
Basal_10 min vs. 50 mM KCl_1 min	Kruskal-Wallis	>0.9999	ns
Basal_10 min vs. 50 mM KCl_10 min	Kruskal-Wallis	0.0226	ns
Basal_10 min vs. 100 mM KCl_1 min	Kruskal-Wallis	0.0019	ns
Basal_10 min vs. 100 mM KCl_10 min	Kruskal-Wallis	0.0057	ns
EtOH 70 %_1 min vs. EtOH 70 %_10 min	Kruskal-Wallis	0.0040	ns
EtOH 70 %_1 min vs. 50 mM KCl_1 min	Kruskal-Wallis	0.0288	*
EtOH 70 %_1 min vs. 50 mM KCl_10 min	Kruskal-Wallis	0.0025	**
EtOH 70 %_1 min vs. 100 mM KCl_1 min	Kruskal-Wallis	0.0074	**
EtOH 70 %_1 min vs. 100 mM KCl_10 min	Kruskal-Wallis	0.0053	**
EtOH 70 %_10 min vs. 50 mM KCl_1min	Kruskal-Wallis	>0.9999	*
EtOH 70 %_10 min vs. 50 mM KCl_10 min	Kruskal-Wallis	>0.9999	**
EtOH 70 %_1 min vs. 100 mM KCl_1 min	Kruskal-Wallis	>0.9999	**
EtOH 70 %_10 min vs. 100 mM KCl_10 min	Kruskal-Wallis	>0.9999	**
50 mM KCl_1 min vs. 50 mM KCl_10 min	Kruskal-Wallis	>0.9999	ns
50 mM KCl_1 min vs. 100 mM KCl_1	Kruskal-Wallis	>0.9999	ns

min			
50 mM KCl_1 min vs. 100 mM KCl_10 min	Kruskal-Wallis	>0.9999	ns
50 mM KCl_10 min vs. 100 mM KCl_1 min	Kruskal-Wallis	>0.9999	ns
50 mM KCl_10 min vs. 100 mM KCl_10 min	Kruskal-Wallis	>0.9999	ns
100 mM KCl_1 min vs. 100 mM KCl_10 min	Kruskal-Wallis	>0.9999	ns

8.-Chasing experiments.

Table 7.- Descriptive statistics of OT- and SNAP-47-membrane patches.

Condition	Membrane patches' type	Cells (n)	Number of patches (Mean ± SEM)
Basal_1 min	OT	71	1.96 ± 0.16
	SNAP-47	98	3.56 ± 0.41
Stimulation_ 1 min	OT	82	2.15 ± 0.18
	SNAP-47	103	3.44 ± 0.33
Basal_10 min	OT	9	1.33 ± 0.24
	SNAP-47	10	2.50 ± 0.54
Stimulation_10 min	OT	7	1.71 ± 0.36
	SNAP-47	9	1.56 ± 0.24
Basal+EGTA_1 min	OT	71	3.21 ± 0.36
	SNAP-47	79	4.96 ± 0.56
Stimulation+EGTA_ 1 min	OT	68	1.76 ± 0.16
	SNAP-47	76	3.51 ± 0.40

Table 8.- Statistical analysis of OT- and SNAP-47-membrane patches.

Condition	Comparison	Statistical test	p-value	p-value summary
Basal_1 min	OT vs. SNAP-47	Mann-Whitney	0.1001	ns
Stimulation_1 min	OT vs. SNAP-47	Mann-Whitney	0.0558	ns
Basal_10 min	OT vs. SNAP-47	Mann-Whitney	0.0859	ns
Stimulation_10 min	OT vs. SNAP-47	Mann-Whitney	0.7944	ns
Basal+EGTA_ 1 min	OT vs. SNAP-47	Mann-Whitney	0.1426	ns
Stimulation+ EGTA_1 min	OT vs. SNAP-47	Mann-Whitney	0.0032	**

Table 9.- Descriptive statistics of OT- and SNAP-47-membrane patches' area.

Condition	Membrane patches' type	Membrane patches (n)	Area (Mean ± SEM), μm^2
Basal_1 min	OT	139	0.35 ± 0.03
	SNAP-47	330	0.59 ± 0.05
Stimulation_ 1 min	OT	174	0.37 ± 0.03
	SNAP-47	318	0.66 ± 0.06
Basal_10 min	OT	12	0.50 ± 0.16
	SNAP-47	25	2.43 ± 0.92
Stimulation_10 min	OT	3	2.43 ± 0.53
	SNAP-47	12	0.28 ± 0.07
Basal+EGTA_1 min	OT	227	0.39 ± 0.02
	SNAP-47	374	0.75 ± 0.06
Stimulation+EGTA _1 min	OT	120	0.42 ± 0.04
	SNAP-47	260	0.76 ± 0.08

Table 10.- Statistical analysis of OT- and SNAP-47-membrane patches' area.

Condition	Comparison	Statistical test	p-value	p-value summary
Basal_1 min	OT vs. SNAP-47	Mann-Whitney	0.0004	***
Stimulation_1 min	OT vs. SNAP-47	Mann-Whitney	0.0024	**
Basal_10 min	OT vs. SNAP-47	Mann-Whitney	0.6255	ns
Stimulation_10 min	OT vs. SNAP-47	Mann-Whitney	0.0044	**
Basal+EGTA_1 min	OT vs. SNAP-47	Mann-Whitney	<0.0001	****
Stimulation+EGTA_1 min	OT vs. SNAP-47	Mann-Whitney	0.0163	*

Table 11.- Descriptive statistics of OT-membrane patches in OT^{tdTom} and OT^{EYFP} mice.

Parameter	Cells (n)	OT-membrane patches (Mean ± SEM)
OT^{tdTom}_anti-OT_Basal	38	1.71 ± 0.15
OT^{tdTom}_anti-OT_Stimulation	33	2.76 ± 0.24
OT^{EYFP}_anti-GFP_Basal	30	2.4 ± 0.33
OT^{EYFP}_anti-GFP_Stimulation	34	3.06 ± 0.32

Table 12.- Statistical analysis of OT-membrane patches in OT^{tdTom} and OT^{EYFP} mice.

Comparison	Statistical test	p-value	p-value summary
OT^{tdTom}_Basal vs. OT^{EYFP}_Basal	Mann-Whitney	0.1218	ns
OT^{tdTom}_Stimulation vs. OT^{EYFP}_Stimulation	Mann-Whitney	0.7098	ns

Table 13.- Descriptive statistics of OT-membrane patches identified with anti-OT and anti-GFP antibodies (OT^{EYFP} mice).

Parameter	Cells (n)	OT-membrane patches (Mean ± SEM)
anti-OT_Basal	36	2.5 ± 0.27
anti-OT_Stimulation	11	1.54 ± 0.21
anti-GFP_Basal	36	2.44 ± 0.24
anti-GFP_Stimulation	11	1.27 ± 0.14

Table 14.- Statistical analysis of OT-membrane patches in OT^{tdTom} and OT^{EYFP} mice.

Comparison	Statistical test	p-value	p-value summary
anti-OT_Basal vs. anti-GFP_Basal	Mann-Whitney	0.9936	ns
anti-OT_Stimulation vs. anti-GFP_Stimulation	Mann-Whitney	0.4807	ns

Table 15.- Descriptive statistics of colocalization (overlapping) analysis.

Condition	OT-membrane patches (n)	Coefficient value (Mean ± SEM)	Coefficient value (% ± SEM)
Manders' 1_Basal	46	0.87 ± 0.02	87 ± 2
Manders' 2_Basal	46	0.82 ± 0.02	82 ± 2
Manders' 1_Stimulation	11	0.68 ± 0.07	68 ± 7
Manders' 2_Stimulation	11	0.89 ± 0.04	89 ± 4

Table 16.- Statistical analysis of colocalization (overlapping) analysis.

Comparison	Statistical test	p-value	p-value summary
Manders' 1 vs. Manders' 2_Basal	Mann-Whitney	0.0270	*
Manders' 1 vs. Manders' 2_Stimulation	Mann-Whitney	0.0232	*

RESULTS

1.-Electron microscopy.

Table 17.- Descriptive statistics of DCVs' area.

Parameter	DCVs (n)	Area (Mean ± SEM), nm^2
Area_Basal	89	270.1 ± 5.78
Area_Stimulation	47	233.9 ± 7.29
Area_Pob1_Basal	23	202.6 ± 4.07
Area_Pob2_Basal	66	293.7 ± 5.11

Table 18.- Statistical analysis of DCVs' area.

Comparison	Statistical test	p-value	p-value summary
Basal vs. Stimulation	Mann-Whitney	0.0002	***
Pob1_Basal vs. Pob2_Basal	Mann-Whitney	<0.0001	****

Table 19.- Frequency distribution of DCVs' area.

Area (nm^2)	Basal (raw data)	Basal (%)	Stimulation (raw data)	Stimulation (%)
120	0	0	1	2.13
140	0	0	1	2.13
160	1	1.12	2	4.26
180	4	4.49	5	10.64
200	6	6.74	6	12.77
220	12	13.48	7	14.89
240	8	8.99	9	19.15
260	10	11.24	6	12.77
280	17	19.10	3	6.38
300	14	15.73	3	6.38
320	5	5.62	2	4.26
340	4	4.49	1	2.13
360	4	4.49	1	2.13
380	3	3.37	0	0
400	0	0	0	0
420	0	0	0	0
440	1	1.12	0	0
DCVs	89	100	47	100

Table 20.- Descriptive statistics of DCVs' diameter.

Parameter	DCVs (n)	Diameter (Mean ± SEM), nm
Diameter_Basal	90	86.01 ± 1.82
Diameter_Stimulation	47	74.44 ± 2.32
Diameter_Pob1_Basal	26	65.60 ± 1.29
Diameter_Pob2_Basal	64	94.31 ± 1.59

Table 21.- Statistical analysis of DCVs' diameter.

Comparison	Statistical test	p-value	p-value summary
Basal vs. Stimulation	Mann-Whitney	0.0002	***
Pob1_Basal vs. Pob2_Basal	Mann-Whitney	<0.0001	****

Table 22.- Frequency distribution of DCVs' diameter.

Diameter (nm)	Basal (raw data)	Basal (%)	Stimulation (raw data)	Stimulation (%)
30	0	0	0	0
40	0	0	1	2.13
50	3	3.33	3	6.38
60	7	7.78	10	21.28
70	16	17.78	12	25.53
80	15	16.67	10	21.28
90	25	27.78	6	12.77
100	12	13.33	3	6.38
110	8	8.89	1	2.13
120	3	3.33	1	2.13
130	0	0	0	0
140	1	1.11	0	0
DCVs	90	100	47	100

Table 23.- Descriptive statistics of DCVs' distance to the membrane.

Parameter	DCVs (n)	Distance to the membrane (Mean ± SEM), nm
Dist_Mb_Basal	89	166.8 ± 17.01
Dist_Mb_Stimulation	47	127.9 ± 9.79
Dist_Mb_Pob1_Basal	85	139.2 ± 7.71
Dist_Mb_Pob2_Basal	4	753.3 ± 182.50

Table 24.- Statistical analysis of DCVs' distance to the membrane.

Comparison	Statistical test	p-value	p-value summary
Basal vs. Stimulation	Mann-Whitney	0.2222	ns
Pob1_Basal vs. Pob2_Basal	Mann-Whitney	<0.0001	****

Table 25.- Frequency distribution of DCVs' distance to the membrane.

Distance to the membrane (nm)	Basal (raw data)	Basal (%)	Stimulation (raw data)	Stimulation (%)
0	1	1.12	2	4.26
100	54	60.67	31	65.96
200	23	25.84	12	25.53
300	7	7.87	2	4.26
400	1	1.12	0	0
500	0	0	0	0
600	0	0	0	0
700	2	2.25	0	0
800	0	0	0	0
900	0	0	0	0
1000	0	0	0	0
1100	0	0	0	0
1200	0	0	0	0
1300	1	1.12	0	0
DCVs	89	100	47	100

Table 26.- Descriptive statistics of DCVs' distance to the AZ.

Parameter	Synaptic terminals (n)	Distance to the AZ (Mean ± SEM), nm
Dist_AZ_Basal	4	478.0 ± 120.3
Dist_AZ_Stimulation	1	164.2 ± 0.00

Table 27.- Descriptive statistics of DCVs' density in synaptic terminals.

Parameter	Synaptic terminals (n)	Density (Mean ± SEM)	Density (Mean ± SEM), %
Density_Basal	35	0.03 ± 0.01	2.93 ± 0.72
Density_ Stimulation	24	0.02 ± 0.01	2.03 ± 0.56

Table 28.- Statistical analysis of DCVs' density.

Comparison	Statistical test	p-value	p-value summary
Basal vs. Stimulation	Mann-Whitney	0.3614	ns

Table 29.- Frequency distribution of DCVs' density/terminal.

Density/ terminal (%)	Basal (raw data)	Basal (%)	Stimulation (raw data)	Stimulation (%)
0	2	5.88	2	8.33
0.5	8	23.53	6	25
1.0	8	23.53	4	16.67
1.5	2	5.88	7	29.17

2.0	3	8.82	0	0
2.5	1	2.94	0	0
3.0	1	2.94	2	8.33
3.5	0	0	0	0
4.0	2	5.88	1	4.17
4.5	0	0	0	0
5.0	0	0	0	0
5.5	2	5.88	0	0
6.0	2	5.88	0	0
6.5	1	2.94	0	0
7.0	1	2.94	0	0
7.5	1	0	0	0
8.0	0	0	0	0
8.5	0	0	0	0
9.0	0	0	0	0
9.5	0	0	0	0
10.0	0	0	1	4.17
10.5	0	0	1	4.17
11.0	0	0	0	0
11.5	0	0	0	0
12.0	0	0	0	0
DCVs	34	100	24	100

2.-Chasing of OT-containing compartments: OT recruitment to the somatic plasma membrane.

Table 30.- Descriptive statistics of OT-membrane patches.

Condition	Cells (n)	OT-membrane patches (Mean ± SEM)
Basal_1 min	194	1.95 ± 0.11
Stimulation_1 min	206	2.84 ± 0.17
Basal_10 min	117	2.32 ± 0.18
Stimulation_10 min	102	1.61 ± 0.13
Basal+EGTA_1 min	142	2.82 ± 0.21
Stimulation+EGTA_1 min	136	2.94 ± 0.23
Basal+EGTA_10 min	5	1.20 ± 0.20
Stimulation+EGTA_10 min	5	1.20 ± 0.20

Table 31.- Statistical analysis of OT-membrane patches.

Comparison	Statistical test	p-value	p-value summary
Basal_1 min vs. Stimulation_1 min	Mann-Whitney	<0.0001	****
Basal_10 min vs. Stimulation_10 min	Mann-Whitney	0.0002	***
Basal_1 min vs. Basal_10 min	Mann-Whitney	0.1023	ns
Stimulation_1 min vs. Stimulation_10	Mann-Whitney	<0.0001	****

min			
Basal+EGTA_1 min vs. Stimulation+EGTA_1 min	Mann-Whitney	0.5976	ns
Basal+EGTA_10 min vs. Stimulation+EGTA_10 min	Mann-Whitney	>0.9999	ns
Basal+EGTA_1 min vs. Basal+EGTA_10 min	Mann-Whitney	0.0833	ns
Stimulation+EGTA_1 min vs. Stimulation+EGTA_10 min	Mann-Whitney	0.0619	ns
Basal_1 min vs. Basal+EGTA_1 min	Mann-Whitney	0.0011	**
Stimulation_1 min vs. Stimulation+EGTA_1 min	Mann-Whitney	0.8934	ns
Basal_10 min vs. Basal+EGTA_10 min	Mann-Whitney	0.1524	ns
Stimulation_10 min vs. Stimulation+EGTA_10 min	Mann-Whitney	0.6824	ns

Table 32.- Descriptive statistics of OT-membrane patches' area.

Condition	OT-membrane patches (n)	Area (Mean ± SEM), μm^2
Basal_1 min	378	0.36 ± 0.03
Stimulation_1 min	583	0.34 ± 0.02
Basal_10 min	272	0.24 ± 0.02
Stimulation_10 min	169	0.41 ± 0.04
Basal+EGTA_1 min	336	0.33 ± 0.02
Stimulation+EGTA_1 min	400	0.31 ± 0.02
Basal+EGTA_10 min	6	0.73 ± 0.29
Stimulation+EGTA_10 min	5	0.55 ± 0.14

Table 33.- Statistical analysis of OT-membrane patches' area.

Comparison	Statistical test	p-value	p-value summary
Basal_1 min vs. Stimulation_1 min	Mann-Whitney	0.4634	ns
Basal_10 min vs. Stimulation_10 min	Mann-Whitney	<0.0001	****

Basal_1 min vs. Basal_10 min	Mann-Whitney	<0.0001	****
Stimulation_1 min vs. Stimulation_10 min	Mann-Whitney	0.6985	ns
Basal+EGTA_1 min vs. Stimulation+EGTA_1 min	Mann-Whitney	0.1217	ns
Basal+EGTA_10 min vs. Stimulation+EGTA_10 min	Mann-Whitney	>0.9999	ns
Basal+EGTA_1 min vs. Basal+EGTA_10 min	Mann-Whitney	0.0308	*
Stimulation+EGTA_1 min vs. Stimulation+EGTA_10 min	Mann-Whitney	0.0271	*
Basal_1 min vs. Basal+EGTA_1 min	Mann-Whitney	0.1592	ns
Stimulation_1 min vs. Stimulation+EGTA_1 min	Mann-Whitney	0.3376	ns
Basal_10 min vs. Basal+EGTA_10 min	Mann-Whitney	0.0014	**
Stimulation_10 min vs. Stimulation+EGTA_10 min	Mann-Whitney	0.0598	ns

3.-Dynamic properties of OT-containing compartments in response to neuronal stimulation.

Table 34.- Number of cells and OT-containing compartments analyzed in the dynamics experiment.

Condition	Cells (n)	OT-containing compartments (n)
Basal	31	80
Stimulation	54	180

Table 35.- Descriptive statistics of OT-containing compartments analyzed in the dynamics experiment.

Time (s)	Control condition	OT-comprt_ Basal (Mean ± SEM)	OT-comprt_ Basal (%)	Experimt. condition	OT-comprt_ Stim (Mean ± SEM)	OT-comprt_ Stim (%)
0-10 (t10)	Basal	2.56 ± 0.1	100	Basal	2.96 ± 0.11	100
10-20 (t20)	Basal	2.48 ± 0.09	96.85	Stim.	2.91 ± 0.11	98.13
20-30 (t30)	Basal	2.45 ± 0.08	95.84	Stim.	2.85 ± 0.11	96.25
30-40 (t40)	Basal	2.42 ± 0.08	94.70	Stim.	2.68 ± 0.11	90.63
40-50 (t50)	Basal	2.42 ± 0.08	94.58	Stim.	2.56 ± 0.10	86.25
50-60 (t60)	Basal	2.40 ± 0.08	93.82	Stim.	2.48 ± 0.10	83.75
60-70 (t70)	Basal	2.33 ± 0.08	91.30	Stim.	2.46 ± 0.09	83.13
70-80 (t80)	Basal	2.32 ± 0.08	90.79	Basal	2.43 ± 0.09	81.88

Table 36.- Statistical analysis of OT-containing compartments' mobility under basal conditions.

Comparison	Statistical test	p-value	p-value summary
t10 vs. t20	Kruskal-Wallis	>0.9999	ns
t10 vs. t30	Kruskal-Wallis	>0.9999	ns
t10 vs. t40	Kruskal-Wallis	>0.9999	ns
t10 vs. t50	Kruskal-Wallis	>0.9999	ns
t10 vs. t60	Kruskal-Wallis	>0.9999	ns
t10 vs. t70	Kruskal-Wallis	>0.9999	ns
t10 vs. t80	Kruskal-Wallis	>0.9999	ns

Table 37.- Statistical analysis of OT-containing compartments' mobility under stimulus conditions.

Comparison	Statistical test	p-value	p-value summary
t10 vs. t20	Kruskal-Wallis	>0.9999	ns
t10 vs. t30	Kruskal-Wallis	0.6443	ns
t10 vs. t40	Kruskal-Wallis	0.0242	*
t10 vs. t50	Kruskal-Wallis	0.0041	**
t10 vs. t60	Kruskal-Wallis	0.0007	***
t10 vs. t70	Kruskal-Wallis	0.0006	***
t10 vs. t80	Kruskal-Wallis	<0.0001	****

Table 38.- Statistical analysis of OT-containing compartments' mobility between basal and stimulus conditions.

Comparison	Statistical test	p-value	p-value summary
Basal vs. Basal-t10	Mann-Whitney	0.7204	ns
Basal vs. Stimulation-t20	Mann-Whitney	0.8758	ns
Basal vs. Stimulation-t30	Mann-Whitney	0.2847	ns
Basal vs. Stimulation-t40	Mann-Whitney	0.0620	ns
Basal vs. Stimulation-t50	Mann-Whitney	0.0240	*
Basal vs. Stimulation-t60	Mann-Whitney	0.0109	*
Basal vs. Stimulation-t70	Mann-Whitney	0.0630	ns
Basal vs. Basal-t80	Mann-Whitney	0.0281	*

Table 39.- Descriptive statistics of the displacement length of an OT-containing compartment from the Dynamic group, modifying its displacement during the first 10 s of stimulation (Fig. 43A).

Time (s)	Experimental condition	Displacement length (Mean ± SEM), µm	Displacement length (norm)
0-10 (t10)	Basal	0.09 ± 0.01	1.00 ± 0.14
10-20 (t20)	Stimulation	0.20 ± 0.01	2.23 ± 0.14
20-30 (t30)	Stimulation	0.27 ± 0.02	3.05 ± 0.17
30-40 (t40)	Stimulation	0.22 ± 0.01	2.51 ± 0.14
40-50 (t50)	Stimulation	0.19 ± 0.02	2.12 ± 0.21
50-60 (t60)	Stimulation	0.22 ± 0.01	2.46 ± 0.14
60-70 (t70)	Stimulation	0.21 ± 0.01	2.31 ± 0.13
70-80 (t80)	Basal	0.23 ± 0.01	2.56 ± 0.14

Table 40.- Statistical analysis of the displacement length of an OT-containing compartment from the Dynamic group, modifying its displacement during the first 10 s of stimulation (Fig. 43A).

Comparison	Statistical test	p-value	p-value summary
t10 vs. t20	Friedman	0.0244	*
t10 vs. t30	Friedman	<0.0001	****
t10 vs. t40	Friedman	0.0006	***
t10 vs. t50	Friedman	0.0741	ns
t10 vs. t60	Friedman	0.0009	***
t10 vs. t70	Friedman	0.0071	**
t10 vs. t80	Friedman	0.0009	***

Table 41.- Descriptive statistics of the displacement length of an OT-containing compartment from the Delayed group, modifying its displacement after 20 s of stimulation (Fig. 43B).

Time (s)	Experimental condition	Displacement length (Mean ± SEM), µm	Displacement length (norm)
0-10 (t10)	Basal	0.07 ± 0.02	1.00 ± 0.22
10-20 (t20)	Stimulation	0.27 ± 0.02	3.58 ± 0.29
20-30 (t30)	Stimulation	0.53 ± 0.05	7.19 ± 0.61
30-40 (t40)	Stimulation	0.68 ± 0.02	9.15 ± 0.31
40-50 (t50)	Stimulation	0.65 ± 0.03	8.75 ± 0.34
50-60 (t60)	Stimulation	0.71 ± 0.01	9.53 ± 0.09
60-70 (t70)	Stimulation	0.71 ± 0.01	9.54 ± 0.11
70-80 (t80)	Basal	0.73 ± 0.02	9.88 ± 0.31

Table 42.- Statistical analysis of the displacement length of an OT-containing compartment from the Delayed group, modifying its displacement after 20 s of stimulation (Fig. 43B).

Comparison	Statistical test	p-value	p-value summary
t10 vs. t20	Friedman	>0.9999	ns
t10 vs. t30	Friedman	0.0432	*
t10 vs. t40	Friedman	<0.0001	****
t10 vs. t50	Friedman	0.0098	**
t10 vs. t60	Friedman	<0.0001	****
t10 vs. t70	Friedman	<0.0001	****
t10 vs. t80	Friedman	<0.0001	****

Table 43.- Descriptive statistics of the displacement length of an OT-containing compartment from the Delayed group, modifying its displacement after 30 s of stimulation (Fig. 43C).

Time (s)	Experimental condition	Displacement length (Mean ± SEM), µm	Displacement length (norm)
0-10 (t10)	Basal	0.09 ± 0.01	1.00 ± 0.16
10-20 (t20)	Stimulation	0.08 ± 0.01	0.91 ± 0.16
20-30 (t30)	Stimulation	0.19 ± 0.02	2.16 ± 0.19
30-40 (t40)	Stimulation	0.30 ± 0.04	3.43 ± 0.42
40-50 (t50)	Stimulation	0.42 ± 0.05	4.78 ± 0.60
50-60 (t60)	Stimulation	0.42 ± 0.03	4.77 ± 0.36
60-70 (t70)	Stimulation	0.46 ± 0.04	5.22 ± 0.46
70-80 (t80)	Basal	0.53 ± 0.02	5.96 ± 0.23

Table 44.- Statistical analysis of the displacement length of an OT-containing compartment from the Delayed group, modifying its displacement after 30 s of stimulation (Fig. 43C).

Comparison	Statistical test	p-value	p-value summary
t10 vs. t20	Friedman	>0.9999	ns
t10 vs. t30	Friedman	>0.9999	ns
t10 vs. t40	Friedman	0.0326	*
t10 vs. t50	Friedman	0.0013	**
t10 vs. t60	Friedman	0.0013	**
t10 vs. t70	Friedman	0.0003	***
t10 vs. t80	Friedman	<0.0001	****

Table 45.- Descriptive statistics of the displacement length of an OT-containing compartment from the Delayed group, modifying its displacement after 40 s of stimulation (Fig. 43D).

Time (s)	Experimental condition	Displacement length (Mean ± SEM), µm	Displacement length (norm)
0-10 (t10)	Basal	0.07 ± 0.01	1.00 ± 0.16
10-20 (t20)	Stimulation	0.12 ± 0.01	1.90 ± 0.10
20-30 (t30)	Stimulation	0.11 ± 0.01	1.70 ± 0.13
30-40 (t40)	Stimulation	0.14 ± 0.01	2.10 ± 0.19
40-50 (t50)	Stimulation	0.27 ± 0.02	4.18 ± 0.38
50-60 (t60)	Stimulation	0.33 ± 0.02	4.99 ± 0.26
60-70 (t70)	Stimulation	0.33 ± 0.02	5.08 ± 0.29
70-80 (t80)	Basal	0.32 ± 0.02	4.84 ± 0.31

Table 46.- Statistical analysis of the displacement length of an OT-containing compartment from the Delayed group, modifying its displacement after 40 s of stimulation (Fig. 43D).

Comparison	Statistical test	p-value	p-value summary
t10 vs. t20	Friedman	0.5799	ns
t10 vs. t30	Friedman	>0.9999	ns
t10 vs. t40	Friedman	0.3866	ns
t10 vs. t50	Friedman	0.0001	***
t10 vs. t60	Friedman	<0.0001	****
t10 vs. t70	Friedman	<0.0001	****
t10 vs. t80	Friedman	<0.0001	****

Table 47.- Descriptive statistics of the displacement length of an OT-containing compartment from the Uncoupled group, modifying its displacement after 50 s of stimulation (Fig. 43E).

Time (s)	Experimental condition	Displacement length (Mean ± SEM), µm	Displacement length (norm)
0-10 (t10)	Basal	0.12 ± 0.02	1.00 ± 0.19
10-20 (t20)	Stimulation	0.17 ± 0.01	1.42 ± 0.07
20-30 (t30)	Stimulation	0.17 ± 0.02	1.37 ± 0.18
30-40 (t40)	Stimulation	0.20 ± 0.03	1.63 ± 0.23
40-50 (t50)	Stimulation	0.23 ± 0.01	1.90 ± 0.11
50-60 (t60)	Stimulation	0.28 ± 0.03	2.29 ± 0.24
60-70 (t70)	Stimulation	0.34 ± 0.02	2.73 ± 0.16
70-80 (t80)	Basal	0.36 ± 0.03	2.92 ± 0.24

Table 48.- Statistical analysis of the displacement length of an OT-containing compartment from the Uncoupled group, modifying its displacement after 50 s of stimulation (Fig. 43E).

Comparison	Statistical test	p-value	p-value summary
t10 vs. t20	Friedman	>0.9999	ns
t10 vs. t30	Friedman	>0.9999	ns
t10 vs. t40	Friedman	0.3866	ns
t10 vs. t50	Friedman	0.0741	ns
t10 vs. t60	Friedman	0.0009	***
t10 vs. t70	Friedman	<0.0001	****
t10 vs. t80	Friedman	<0.0001	****

Table 49.- Descriptive statistics of the displacement length of an OT-containing compartment from the Uncoupled group, modifying its displacement after 60 s of stimulation (Fig. 43F).

Time (s)	Experimental condition	Displacement length (Mean ± SEM), µm	Displacement length (norm)
0-10 (t10)	Basal	0.10 ± 0.02	1.00 ± 0.02
10-20 (t20)	Stimulation	0.14 ± 0.02	1.40 ± 0.02
20-30 (t30)	Stimulation	0.21 ± 0.02	2.17 ± 0.02
30-40 (t40)	Stimulation	0.18 ± 0.02	1.80 ± 0.02
40-50 (t50)	Stimulation	0.24 ± 0.04	2.43 ± 0.04
50-60 (t60)	Stimulation	0.21 ± 0.03	2.17 ± 0.03
60-70 (t70)	Stimulation	0.25 ± 0.03	2.58 ± 0.03
70-80 (t80)	Basal	0.30 ± 0.04	3.06 ± 0.04

Table 50.- Statistical analysis of the displacement length of an OT-containing compartment from the Uncoupled group, modifying its displacement after 60 s of stimulation (Fig. 43F).

Comparison	Statistical test	p-value	p-value summary
t10 vs. t20	Friedman	>0.9999	ns
t10 vs. t30	Friedman	0.1234	ns
t10 vs. t40	Friedman	>0.9999	ns
t10 vs. t50	Friedman	0.0960	ns
t10 vs. t60	Friedman	0.1992	ns
t10 vs. t70	Friedman	0.0326	*
t10 vs. t80	Friedman	0.0051	**

Table 51.- Descriptive statistics of the displacement length of an OT-containing compartment from the Uncoupled group, modifying its displacement in the last seconds of basal medium application (Fig. 43G).

Time (s)	Experimental condition	Displacement length (Mean ± SEM), µm	Displacement length (norm)
0-10 (t10)	Basal	0.09 ± 0.02	1.00 ± 0.17
10-20 (t20)	Stimulation	0.10 ± 0.01	1.10 ± 0.16
20-30 (t30)	Stimulation	0.11 ± 0.02	1.25 ± 0.18
30-40 (t40)	Stimulation	0.09 ± 0.01	0.98 ± 0.10
40-50 (t50)	Stimulation	0.10 ± 0.02	1.18 ± 0.19
50-60 (t60)	Stimulation	0.16 ± 0.02	1.81 ± 0.25
60-70 (t70)	Stimulation	0.18 ± 0.02	2.06 ± 0.28
70-80 (t80)	Basal	0.26 ± 0.02	2.95 ± 0.28

Table 52.- Statistical analysis of the displacement length of an OT-containing compartment from the Uncoupled group, modifying its displacement in the last seconds of basal medium application. Fig. 43G).

Comparison	Statistical test	p-value	p-value summary
t10 vs. t20	Friedman	>0.9999	ns
t10 vs. t30	Friedman	>0.9999	ns
t10 vs. t40	Friedman	>0.9999	ns
t10 vs. t50	Friedman	>0.9999	ns
t10 vs. t60	Friedman	0.1992	ns
t10 vs. t70	Friedman	0.0960	ns
t10 vs. t80	Friedman	0.0004	***

Table 53.- Descriptive statistics of the displacement length of an OT-containing compartment from the Stable group, not modifying its displacement in response to stimulus (Fig. 43H).

Time (s)	Experimental condition	Displacement length (Mean ± SEM), µm	Displacement length (norm)
0-10 (t10)	Basal	0.08 ± 0.01	1.00 ± 0.14
10-20 (t20)	Stimulation	0.07 ± 0.01	0.87 ± 0.14
20-30 (t30)	Stimulation	0.06 ± 0.02	0.84 ± 0.23
30-40 (t40)	Stimulation	0.07 ± 0.01	0.87 ± 0.17
40-50 (t50)	Stimulation	0.08 ± 0.02	1.08 ± 0.24
50-60 (t60)	Stimulation	0.08 ± 0.02	1.07 ± 0.20
60-70 (t70)	Stimulation	0.10 ± 0.02	1.30 ± 0.26
70-80 (t80)	Basal	0.09 ± 0.01	1.14 ± 0.12

Table 54.- Statistical analysis of the displacement length of an OT-containing compartment from the Stable group, not modifying its displacement in response to stimulus (Fig. 43H).

Comparison	Statistical test	p-value	p-value summary
t10 vs. t20	Friedman	>0.9999	ns
t10 vs. t30	Friedman	>0.9999	ns
t10 vs. t40	Friedman	>0.9999	ns
t10 vs. t50	Friedman	>0.9999	ns
t10 vs. t60	Friedman	>0.9999	ns
t10 vs. t70	Friedman	>0.9999	ns
t10 vs. t80	Friedman	>0.9999	ns

Table 55.- Number of OT-containing compartments considered for the displacement analysis.

Population	OT-containing compartments (Mean)	OT-containing compartments (%)
Total	119	100
Dynamic	9	7.32
Delayed	67	56.30
Delayed (20 s post-KCl)	20	16.81
Delayed (30 s post-KCl)	27	22.69
Delayed (40 s post-KCl)	20	16.81
Uncoupled	28	23.53
Uncoupled (50 s post-KCl)	11	9.24
Uncoupled (60 s post-KCl)	7	5.88
Uncoupled (last 10 s basal)	10	8.40
Stable	15	12.60

Table 56.- Descriptive statistics of the speed of an OT-containing compartment from the increasing speed group. This OT-compartment increased its speed after 10 s of stimulation (Fig. 44A, v1).

Time (s)	Experimental condition	Speed (Mean ± SEM), µm/s	Speed (norm)
0-10 (t10)	Basal	2.80 ± 0.39	1.00 ± 0.39
10-20 (t20)	Stimulation	3.63 ± 0.39	1.29 ± 0.39
20-30 (t30)	Stimulation	3.31 ± 0.49	1.18 ± 0.49
30-40 (t40)	Stimulation	3.70 ± 0.51	1.32 ± 0.51
40-50 (t50)	Stimulation	3.71 ± 0.53	1.32 ± 0.53
50-60 (t60)	Stimulation	3.47 ± 0.79	1.24 ± 0.79
60-70 (t70)	Stimulation	5.96 ± 0.84	2.13 ± 0.84
70-80 (t80)	Basal	3.60 ± 0.83	1.28 ± 0.83

Table 57.- Statistical analysis of the speed of an OT-containing compartment from the increasing speed group. This OT-compartment increased its speed after 10 s of stimulation (Fig. 44A, v1).

OT-containing compartment	Statistical test	p-value	p-value summary
t10 vs. t20	Friedman	>0.9999	ns
t10 vs. t30	Friedman	>0.9999	ns
t10 vs. t40	Friedman	>0.9999	ns
t10 vs. t50	Friedman	0.4752	ns
t10 vs. t60	Friedman	>0.9999	ns
t10 vs. t70	Friedman	00432	*
t10 vs. t80	Friedman	>0.9999	ns

Table 58.- Descriptive statistics of the speed of an OT-containing compartment from the increasing speed group. This OT-compartment increased its speed after 20 s of stimulation (Fig. 44A, v2).

Time (s)	Experimental condition	Speed (Mean ± SEM), µm/s	Speed (norm)
0-10 (t10)	Basal	2.32 ± 0.32	1.00 ± 0.14
10-20 (t20)	Stimulation	3.02 ± 0.38	1.30 ± 0.16
20-30 (t30)	Stimulation	6.94 ± 1.08	2.99 ± 0.46
30-40 (t40)	Stimulation	9.09 ± 2.09	3.92 ± 0.90
40-50 (t50)	Stimulation	6.61 ± 1.55	2.85 ± 0.67
50-60 (t60)	Stimulation	6.16 ± 0.83	2.66 ± 0.36
60-70 (t70)	Stimulation	6.19 ± 0.99	2.67 ± 0.43
70-80 (t80)	Basal	7.22 ± 1.64	3.12 ± 0.71

Table 59.- Statistical analysis of the speed of an OT-containing compartment from the increasing speed group. This OT-compartment increased its speed after 20 s of stimulation (Fig. 44A, v2).

OT-containing compartment	Statistical test	p-value	p-value summary
t10 vs. t20	Friedman	>0.9999	ns
t10 vs. t30	Friedman	0.0326	*
t10 vs. t40	Friedman	0.0741	ns
t10 vs. t50	Friedman	0.4752	ns
t10 vs. t60	Friedman	0.1234	ns
t10 vs. t70	Friedman	0.0326	*
t10 vs. t80	Friedman	0.1234	ns

Table 60.- Descriptive statistics of the speed of an OT-containing compartment from the increasing speed group. This OT-compartment increased its speed after 40 s of stimulation (Fig. 44A, v3).

Time (s)	Experimental condition	Speed (Mean ± SEM), µm/s	Speed (norm)
0-10 (t10)	Basal	1.52 ± 0.37	1.00 ± 0.24
10-20 (t20)	Stimulation	2.14 ± 0.74	1.41 ± 0.49
20-30 (t30)	Stimulation	3.54 ± 0.62	2.34 ± 0.41
30-40 (t40)	Stimulation	3.67 ± 0.65	2.42 ± 0.43
40-50 (t50)	Stimulation	4.47 ± 0.69	2.95 ± 0.46
50-60 (t60)	Stimulation	3.06 ± 0.93	2.02 ± 0.62
60-70 (t70)	Stimulation	3.47 ± 0.45	2.29 ± 0.30
70-80 (t80)	Basal	2.68 ± 0.53	1.77 ± 0.35

Table 61.- Statistical analysis of the speed of an OT-containing compartment from the increasing speed group. This OT-compartment increased its speed after 40 s of stimulation (Fig. 44A, v3).

OT-containing compartment	Statistical test	p-value	p-value summary
t10 vs. t20	Friedman	>0.9999	ns
t10 vs. t30	Friedman	0.3123	ns
t10 vs. t40	Friedman	0.1992	ns
t10 vs. t50	Friedman	0.0134	*
t10 vs. t60	Friedman	>0.9999	ns
t10 vs. t70	Friedman	0.0741	ns
t10 vs. t80	Friedman	>0.9999	ns

Table 62.- Descriptive statistics of the speed of an OT-containing compartment from the increasing speed group. This OT-compartment increased its speed after 60 s of stimulation (Fig. 44A, v4).

Time (s)	Experimental condition	Speed (Mean ± SEM), µm/s	Speed (norm)
0-10 (t10)	Basal	1.64 ± 0.24	1.00 ± 0.15
10-20 (t20)	Stimulation	1.90 ± 0.25	1.15 ± 0.15
20-30 (t30)	Stimulation	1.73 ± 0.39	1.05 ± 0.24
30-40 (t40)	Stimulation	2.49 ± 0.32	1.51 ± 0.20
40-50(t50)	Stimulation	2.67 ± 0.45	1.62 ± 0.27
50-60 (t60)	Stimulation	2.39 ± 0.32	1.45 ± 0.20
60-70 (t70)	Stimulation	3.43 ± 0.30	2.09 ± 0.18
70-80 (t80)	Basal	2.63 ± 0.39	1.60 ± 0.24

Table 63.- Statistical analysis of the speed of an OT-containing compartment from the increasing speed group. This OT-compartment increased its speed after 60 s of stimulation (Fig. 44A, v4).

OT-containing compartment	Statistical test	p-value	p-value summary
t10 vs. t20	Friedman	>0.9999	ns
t10 vs. t30	Friedman	>0.9999	ns
t10 vs. t40	Friedman	0.2503	ns
t10 vs. t50	Friedman	0.1992	ns
t10 vs. t60	Friedman	0.4752	ns
t10 vs. t70	Friedman	0.0026	**
t10 vs. t80	Friedman	0.3866	ns

Table 64.- Descriptive statistics of the speed of an OT-containing compartment from the increasing speed group. This OT-compartment increased its speed in the last seconds of basal medium application (Fig. 44A, v5).

Time (s)	Experimental condition	Speed (Mean ± SEM), µm/s	Speed (norm)
0-10 (t10)	Basal	1.94 ± 0.36	1.00 ± 0.18
10-20 (t20)	Stimulation	1.03 ± 0.12	0.53 ± 0.06
20-30 (t30)	Stimulation	2.03 ± 0.35	1.04 ± 0.18
30-40 (t40)	Stimulation	1.50 ± 0.18	0.77 ± 0.09
40-50 (t50)	Stimulation	3.05 ± 0.56	1.57 ± 0.29
50-60 (t60)	Stimulation	2.58 ± 0.39	1.33 ± 0.20
60-70 (t70)	Stimulation	2.75 ± 0.44	1.42 ± 0.23
70-80 (t80)	Basal	5.46 ± 0.57	2.81 ± 0.29

Table 65.- Statistical analysis of the speed of an OT-containing compartment from the increasing speed group. This OT-compartment increased its speed in the last seconds of basal medium application (Fig. 44A, v5).

OT-containing compartment	Statistical test	p-value	p-value summary
t10 vs. t20	Friedman	0.5799	ns
t10 vs. t30	Friedman	>0.9999	ns
t10 vs. t40	Friedman	>0.9999	ns
t10 vs. t50	Friedman	>0.9999	ns
t10 vs. t60	Friedman	>0.9999	ns
t10 vs. t70	Friedman	>0.9999	ns
t10 vs. t80	Friedman	0.0098	**

Table 66.- Descriptive statistics of the speed of an OT-containing compartment from the decreasing speed group. This OT-compartment decreased its speed after 20 s of stimulation (Fig. 44B, v1).

Time (s)	Experimental condition	Speed (Mean ± SEM), µm/s	Speed (norm)
0-10 (t10)	Basal	2.43 ± 0.46	1.00 ± 0.19
10-20 (t20)	Stimulation	1.76 ± 0.36	0.72 ± 0.15
20-30 (t30)	Stimulation	1.55 ± 0.28	0.64 ± 0.11
30-40 (t40)	Stimulation	1.33 ± 0.17	0.55 ± 0.07
40-50 (t50)	Stimulation	1.47 ± 0.19	0.61 ± 0.08
50-60 (t60)	Stimulation	1.19 ± 0.20	0.49 ± 0.08
60-70 (t70)	Stimulation	1.47 ± 0.17	0.60 ± 0.07
70-80 (t80)	Basal	1.06 ± 0.22	0.44 ± 0.99

Table 67.- Statistical analysis of the speed of an OT-containing compartment from the decreasing speed group. This OT-compartment decreased its speed after 20 s of stimulation (Fig. 44B, v1).

OT-containing compartment	Statistical test	p-value	p-value summary
t10 vs. t20	Friedman	0.8448	ns
t10 vs. t30	Friedman	0.5799	ns
t10 vs. t40	Friedman	>0.9999	ns
t10 vs. t50	Friedman	0.8448	ns
t10 vs. t60	Friedman	0.4752	ns
t10 vs. t70	Friedman	>0.9999	ns
t10 vs. t80	Friedman	0.0244	*

Table 68.- Descriptive statistics of the speed of an OT-containing compartment from the decreasing speed group. This OT-compartment decreased its speed after 40 s of stimulation (Fig. 44B, v2).

Time (s)	Experimental condition	Speed (Mean ± SEM), µm/s	Speed (norm)
0-10 (t10)	Basal	2.95 ± 0.56	1.00 ± 0.19
10-20 (t20)	Stimulation	2.21 ± 0.23	0.75 ± 0.08
20-30 (t30)	Stimulation	2.10 ± 0.32	0.71 ± 0.11
30-40 (t40)	Stimulation	2.16 ± 0.40	0.73 ± 0.14
40-50 (t50)	Stimulation	1.74 ± 0.29	0.59 ± 0.10
50-60 (t60)	Stimulation	2.41 ± 0.38	0.82 ± 0.13
60-70 (t70)	Stimulation	1.43 ± 0.26	0.49 ± 0.09
70-80 (t80)	Basal	2.19 ± 0.33	0.79 ± 0.11

Table 69.- Statistical analysis of the speed of an OT-containing compartment from the decreasing speed group. This OT-compartment decreased its speed after 40 s of stimulation (Fig. 44B, v2).

OT-containing compartment	Statistical test	p-value	p-value summary
t10 vs. t20	Friedman	>0.9999	ns
t10 vs. t30	Friedman	>0.9999	ns
t10 vs. t40	Friedman	>0.9999	ns
t10 vs. t50	Friedman	0.1992	ns
t10 vs. t60	Friedman	>0.9999	ns
t10 vs. t70	Friedman	0.0432	*
t10 vs. t80	Friedman	>0.9999	ns

Table 70.- Descriptive statistics of the speed of an OT-containing compartment from the decreasing speed group. This OT-compartment decreased its speed after 50 s of stimulation (Fig. 44B, v3).

Time (s)	Experimental condition	Speed (Mean ± SEM), µm/s	Speed (norm)
0-10 (t10)	Basal	2.49 ± 0.44	1.00 ± 0.18
10-20 (t20)	Stimulation	4.56 ± 0.78	1.83 ± 0.31
20-30 (t30)	Stimulation	1.99 ± 0.40	0.80 ± 0.16
30-40 (t40)	Stimulation	2.56 ± 0.52	1.03 ± 0.21
40-50 (t50)	Stimulation	2.11 ± 0.81	0.85 ± 0.33
50-60 (t60)	Stimulation	0.00 ± 0.00	0.00 ± 0.00
60-70 (t70)	Stimulation	0.33 ± 0.22	0.13 ± 0.09
70-80 (t80)	Basal	0.80 ± 0.57	0.32 ± 0.23

Table 71.- Statistical analysis of the speed of an OT-containing compartment from the decreasing speed group. This OT-compartment decreased its speed after 50 s of stimulation (Fig. 44B, v3).

OT-containing compartment	Statistical test	p-value	p-value summary
t10 vs. t20	Friedman	>0.9999	ns
t10 vs. t30	Friedman	>0.9999	ns
t10 vs. t40	Friedman	>0.9999	ns
t10 vs. t50	Friedman	>0.9999	ns
t10 vs. t60	Friedman	0.0037	**
t10 vs. t70	Friedman	0.0432	*
t10 vs. t80	Friedman	0.0432	*

Table 72.- Descriptive statistics of the speed of an OT-containing compartment from the decreasing speed group. This OT-compartment decreased its speed after 60 s of stimulation (Fig. 44B, v4).

Time (s)	Experimental condition	Speed (Mean ± SEM), µm/s	Speed (norm)
0-10 (t10)	Basal	2.57 ± 0.44	1.00 ± 0.17
10-20 (t20)	Stimulation	3.70 ± 0.65	1.44 ± 0.25
20-30 (t30)	Stimulation	5.56 ± 1.32	2.17 ± 0.52
30-40 (t40)	Stimulation	3.11 ± 0.82	1.21 ± 0.32
40-50 (t50)	Stimulation	1.90 ± 0.66	0.74 ± 0.26
50-60 (t60)	Stimulation	1.26 ± 0.65	0.49 ± 0.25
60-70 (t70)	Stimulation	0.82 ± 0.58	0.32 ± 0.23
70-80 (t80)	Basal	2.27 ± 1.18	0.88 ± 0.46

Table 73.- Statistical analysis of the speed of an OT-containing compartment from the decreasing speed group. This OT-compartment decreased its speed after 60 s of stimulation (Fig. 44B, v4).

OT-containing compartment	Statistical test	p-value	p-value summary
t10 vs. t20	Friedman	>0.9999	ns
t10 vs. t30	Friedman	>0.9999	ns
t10 vs. t40	Friedman	>0.9999	ns
t10 vs. t50	Friedman	>0.9999	ns
t10 vs. t60	Friedman	0.3123	ns
t10 vs. t70	Friedman	0.0432	*
t10 vs. t80	Friedman	0.5799	ns

Table 74.- Descriptive statistics of the speed of an OT-containing compartment from the immobile group. This OT-compartment did not modify its speed during the stimulation protocol (Fig. 44C, v1).

Time (s)	Experimental condition	Speed (Mean ± SEM), µm/s	Speed (norm)
0-10 (t10)	Basal	1.21 ± 0.33	1.00 ± 0.27
10-20 (t20)	Stimulation	1.07 ± 0.13	0.88 ± 0.11
20-30 (t30)	Stimulation	1.09 ± 0.18	0.90 ± 0.15
30-40 (t40)	Stimulation	1.05 ± 0.20	0.86 ± 0.17
40-50 (t50)	Stimulation	0.99 ± 0.14	0.82 ± 0.11
50-60 (t60)	Stimulation	1.29 ± 0.27	1.07 ± 0.22
60-70 (t70)	Stimulation	1.21 ± 0.15	1.00 ± 0.12
70-80 (t80)	Basal	1.00 ± 0.16	0.82 ± 0.14

Table 75.- Statistical analysis of the speed of an OT-containing compartment from the immobile group. This OT-compartment did not modify its speed during the stimulation protocol (Fig. 44C, v1).

OT-containing compartment	Statistical test	p-value	p-value summary
t10 vs. t20	Friedman	>0.9999	ns
t10 vs. t30	Friedman	>0.9999	ns
t10 vs. t40	Friedman	>0.9999	ns
t10 vs. t50	Friedman	>0.9999	ns
t10 vs.t60	Friedman	>0.9999	ns
t10 vs. t70	Friedman	>0.9999	ns
t10 vs. t80	Friedman	>0.9999	ns

Table 76.- Descriptive statistics of the speed of an OT-containing compartment from the immobile group. This OT-compartment did not modify its speed during the stimulation protocol (Fig. 44C, v2).

Time (s)	Experimental condition	Speed (Mean ± SEM), µm/s	Speed (norm)
0-10 (t10)	Basal	1.59 ± 0.30	1.00 ± 0.19
10-20 (t20)	Stimulation	2.17 ± 0.38	1.36 ± 0.24
20-30 (t30)	Stimulation	1.25 ± 0.19	0.78 ± 0.12
30-40 (t40)	Stimulation	1.74 ± 0.25	1.10 ± 0.16
40-50 (t50)	Stimulation	1.79 ± 0.40	1.12 ± 0.25
50-60 (t60)	Stimulation	1.48 ± 0.27	0.93 ± 0.17
60-70 (t70)	Stimulation	1.09 ± 0.26	0.68 ± 0.16
70-80 (t80)	Basal	1.94 ± 0.57	1.22 ± 0.36

Table 77.- Statistical analysis of the speed of an OT-containing compartment from the immobile group. This OT-compartment did not modify its speed during the stimulation protocol (Fig. 44C, v2).

OT-containing compartment	Statistical test	p-value	p-value summary
t10 vs. t20	Friedman	0.5799	ns
t10 vs. t30	Friedman	>0.9999	ns
t10 vs. t40	Friedman	>0.9999	ns
t10 vs. t50	Friedman	>0.9999	ns
t10 vs. t60	Friedman	>0.9999	ns
t10 vs. t70	Friedman	>0.9999	ns
t10 vs. t80	Friedman	>0.9999	ns

Table 78.- Descriptive statistics of the speed of an OT-containing compartment from the immobile group. This OT-compartment did not modify its speed during the stimulation protocol (Fig. 44C, v3).

Time (s)	Experimental condition	Speed (Mean ± SEM), µm/s	Speed (norm)
0-10 (t10)	Basal	3.23 ± 0.57	1.00 ± 0.18
10-20 (t20)	Stimulation	2.52 ± 0.49	0.78 ± 0.15
20-30 (t30)	Stimulation	3.98 ± 1.01	1.23 ± 0.31
30-40 (t40)	Stimulation	1.88 ± 0.38	0.58 ± 0.12
40-50 (t50)	Stimulation	3.00 ± 0.60	0.93 ± 0.19
50-60 (t60)	Stimulation	2.72 ± 0.51	0.84 ± 0.16
60-70 (t70)	Stimulation	1.94 ± 0.48	0.60 ± 0.15
70-80 (t80)	Basal	3.21 ± 0.46	0.99 ± 0.14

Table 79.- Statistical analysis of the speed of an OT-containing compartment from the immobile group. This OT-compartment did not modify its speed during the stimulation protocol (Fig. 44C, v3).

OT-containing compartment	Statistical test	p-value	p-value summary
t10 vs. t20	Friedman	>0.9999	ns
t10 vs. t30	Friedman	>0.9999	ns
t10 vs. t40	Friedman	0.0568	ns
t10 vs. t50	Friedman	>0.9999	ns
t10 vs. t60	Friedman	>0.9999	ns
t10 vs. t70	Friedman	0.0960	ns
t10 vs. t80	Friedman	>0.9999	ns

Table 80.- Descriptive statistics of the speed of an OT-containing compartment from the immobile group. This OT-compartment did not modify its speed during the stimulation protocol (Fig. 44C, v4).

Time (s)	Experimental condition	Speed (Mean ± SEM), µm/s	Speed (norm)
0-10 (t10)	Basal	2.31 ± 0.37	1.00 ± 0.16
10-20 (t20)	Stimulation	3.61 ± 0.83	1.57 ± 0.36
20-30 (t30)	Stimulation	4.00 ± 0.58	1.74 ± 0.25
30-40 (t40)	Stimulation	3.35 ± 0.56	1.45 ± 0.24
40-50 (t50)	Stimulation	3.13 ± 0.54	1.36 ± 0.23
50-60 (t60)	Stimulation	3.79 ± 0.71	1.64 ± 0.31
60-70 (t70)	Stimulation	3.72 ± 0.72	1.62 ± 0.31
70-80 (t80)	Basal	4.23 ± 0.70	1.83 ± 0.30

Table 81.- Statistical analysis of the speed of an OT-containing compartment from the immobile group. This OT-compartment did not modify its speed during the stimulation protocol (Fig. 44C, v4).

OT-containing compartment	Statistical test	p-value	p-value summary
t10 vs. t20	Friedman	>0.9999	ns
t10 vs. t30	Friedman	>0.9999	ns
t10 vs. t40	Friedman	>0.9999	ns
t10 vs. t50	Friedman	>0.9999	ns
t10 vs. t60	Friedman	>0.9999	ns
t10 vs. t70	Friedman	>0.9999	ns
t10 vs. t80	Friedman	0.8448	ns

Table 82.- Number of OT-containing vesicles examined in the speed analysis.

Population	OT-containing compartments (Mean)	OT-containing compartments (%)
Total	119	100
Mobile (increase and decrease)	35	29.41
Increase speed (mobile)	24	20.17
Decrease speed (mobile)	11	9.24
Immobile	84	70.59

Table 83.- Number of OT-containing vesicles analyzed for MSD.

Population	OT-containing compartments	OT-containing compartments (%)
Total	124	100
Diffusive	11	8.87
Non-diffusive	113	91.13

4.-Subcellular localization of OT-containing compartments.

Table 84.- Descriptive statistics of OT-containing compartments analyzed in Golgi experiments. n= 18 cells.

	OT-containing compartments (n)	OT-containing compartments/cell (Mean ± SEM)	OT-containing compartments (% ± SEM)
Cell	446	21.39 ± 2.55	100
Cytoplasm	301	16.72 ± 2.35	67.49
Golgi	84	4.68 ± 0.45	18.83
Membrane	61	3.39 ± 0.47	13.68

Table 85.- Statistical analysis of OT-containing compartments analyzed in Golgi experiments.

Comparison	Statistical test	p-value	p-value summary
Cell vs. Cytoplasm	Kruskal-Wallis	>0.9999	ns
Cell vs. Golgi	Kruskal-Wallis	<0.0001	****
Cell vs. Membrane	Kruskal-Wallis	<0.0001	****
Cytoplasm vs. Golgi	Kruskal-Wallis	0.0004	***
Cytoplasm vs. Membrane	Kruskal-Wallis	<0.0001	****
Golgi vs. Membrane	Kruskal-Wallis	>0.9999	ns

Table 86.- Descriptive statistics of Golgi and OT-containing compartments' area.

	Area (Mean ± SEM), μm^2
Golgi	6.23 ± 0.69
OT-containing compartment	0.07 ± 0.01

Table 87.- Statistical analysis of Golgi and OT-containing compartments' area.

Comparison	Statistical test	p-value	p-value summary
OT-compartments vs. Golgi	Mann-Whitney	<0.0001	****

Table 88.- Descriptive statistics of colocalization analysis between Golgi and OT-containing compartments.

Condition	OT-containing compartments (n)	Coefficient value (Mean ± SEM)	Coefficient value (% ± SEM)
Manders'_Experimental data set	85	0.55 ± 0.01	55 ± 1
Manders'_Random data set	61	0.38 ± 0.03	38 ± 3
Pearson_Experimental data set	84	0.55 ± 0.01	55 ± 1
Pearson_Random data set	61	0.42 ± 0.01	42 ± 1

Table 89.- Frequency distribution of Manders' coefficient.

Manders' coefficient (%)	OT-containing compartments_Experimental data set (raw data)	OT-containing compartments_Experimental data set (%)	OT-containing compartments_Random data set (raw data)	OT-containing compartments_Random data set (%)
0	0	0	2	3.28
10	0	0	5	8.20
20	1	1.18	7	11.47
30	4	4.70	23	37.70
40	14	16.47	9	14.75
50	26	30.59	6	9.84
60	20	23.53	2	3.28
70	14	16.47	1	1.64
80	4	4.70	0	0
90	2	2.35	2	3.28
100	0	0	4	6.56
OT-containing compartments	85	100	61	100

Table 90.- Frequency distribution of Pearson's coefficient.

Pearson's coefficient (%)	OT-compartments_Experimental data set (raw data)	OT-compartments_Experimental data set (%)	OT-compartments_Random data set (raw data)	OT-compartments_Random data set (%)
15	0	0	0	0
20	1	1.19	4	6.56
25	1	1.19	2	3.28
30	0	0	6	9.84
35	7	8.33	7	11.47
40	5	5.95	15	24.59

45	7	8.33	9	14.75
50	16	19.05	10	16.39
55	13	15.48	2	3.28
60	11	13.09	3	4.92
65	9	10.71	2	3.28
70	8	9.52	0	0
75	3	3.57	1	1.64
80	0	0	0	0
85	3	3.57	0	0
90	0	0	0	0
OT-containing compartments	84	100	61	100

Table 91.- Statistical analysis of colocalization analysis.

Comparison	Statistical test	p-value	p-value summary
Manders_ Experimental data set vs. Manders_Random data set	Mann-Whitney	<0.0001	****
Pearson_ Experimental data set vs. Pearson_Random data set	Mann-Whitney	<0.0001	****

5.-Modeling of OT-compartments' dynamics.

Table 92.- Descriptive statistics of OT-containing compartments' simulation starting near the nucleus (slices from 12 to 17).

Condition	Simulated OT-compartments (n)	Position (Mean ± SEM)
Diffusive_ti_Basal	11	12.97 ± 0.31
Diffusive_tf_Basal	11	11.76 ± 0.61
Diffusive_ti_Stimulation	11	13.36 ± 0.40
Diffusive_tf_Stimulation	11	11.70 ± 0.63
Non-diffusive_ti_Basal	93	13.39 ± 0.11
Non-diffusive_tf_Basal	93	12.58 ± 0.19
Non-diffusive_ti_Stimulation	93	13.34 ± 0.12
Non-diffusive_tf_Stimulation	93	11.98 ± 0.17

Table 93.- Statistical analysis of OT-containing compartments' simulation starting near the nucleus.

Comparison	Statistical test	p-value	p-value summary
Dif, ti_Basal vs. tf_Basal	Mann-Whitney	0.3015	ns
Dif, ti_Stimulation vs. tf_Stimulation	Mann-Whitney	0.0827	ns
Dif, ti_Basal vs. tf_Stimulation	Mann-Whitney	0.2577	ns
Non-dif, ti_Basal vs. tf_Basal	Mann-Whitney	0.0435	*
Non-dif, ti_Stimulation vs. tf_Stimulation	Mann-Whitney	<0.0001	****
Non-dif, ti_Basal vs. tf_Stimulation	Mann-Whitney	<0.0001	****

Table 94.- Descriptive statistics of OT-containing compartments' simulation starting from the cytoplasm (slices from 6 to 11).

Condition	Simulated OT-compartments (n)	Position (Mean ± SEM)
Diffusive_ti_Basal	11	7.58 ± 0.37
Diffusive_tf_Basal	11	8.06 ± 0.60
Diffusive_ti_Stimulation	11	7.58 ± 0.43
Diffusive_tf_Stimulation	11	7.94 ± 0.64
Non-diffusive_ti_Basal	93	7.74 ± 0.11
Non-diffusive_tf_Basal	93	7.13 ± 0.22
Non-diffusive_ti_Stimulation	93	7.54 ± 0.12
Non-diffusive_tf_Stimulation	93	6.80 ± 0.20

Table 95.- Statistical analysis of OT-containing compartments' simulation starting from the cytoplasm.

Comparison	Statistical test	p-value	p-value summary
Dif, ti_Basal vs. tf_Basal	Mann-Whitney	0.5833	ns
Dif, ti_Stimulation vs. tf_Stimulation	Mann-Whitney	0.9821	ns
Dif, ti_Basal vs. tf_Stimulation	Mann-Whitney	0.9310	ns
Non-dif, ti_Basal vs. tf_Basal	Mann-Whitney	0.0270	*
Non-dif, ti_Stimulation vs. tf_Stimulation	Mann-Whitney	0.0022	**
Non-dif, ti_Basal vs. tf_Stimulation	Mann-Whitney	0.0001	***

Table 96.- Descriptive statistics of OT-containing compartments' simulation at the membrane (slices from 1 to 5).

Condition	Simulated OT-compartments (n)	Position (Mean ± SEM)
Diffusive_ti_Basal	11	2.91 ± 0.27
Diffusive_tf_Basal	11	4.03 ± 0.57
Diffusive_ti_Stimulation	11	3.24 ± 0.21
Diffusive_tf_Stimulation	11	4.33 ± 0.38
Non-diffusive_ti_Basal	93	2.76 ± 0.08
Non-diffusive_tf_Basal	93	3.88 ± 0.14
Non-diffusive_ti_Stimulation	93	2.91 ± 0.09
Non-diffusive_tf_Stimulation	93	3.39 ± 0.12

Table 97.- Statistical analysis of OT-containing compartments' simulation at the membrane.

Comparison	Statistical test	p-value	p-value summary
Dif, ti_Basal vs. tf_Basal	Mann-Whitney	0.3087	ns
Dif, ti_Stimulation vs. tf_Stimulation	Mann-Whitney	0.0591	ns
Dif, ti_Basal vs. tf_Stimulation	Mann-Whitney	0.0079	**
Non-dif, ti_Basal vs. tf_Basal	Mann-Whitney	<0.0001	****
Non-dif, ti_Stimulation vs. tf_Stimulation	Mann-Whitney	0.0404	*
Non-dif, ti_Basal vs. tf_Stimulation	Mann-Whitney	0.0037	**

6.-SNARE proteins expression in hypothalamic oxytocinergic neurons.

Table 98.- Descriptive statistics of SNAP-47 expression in primary cultured hypothalamic neurons. n= 4 cells.

	OT^+	OT^+ $SNAP\text{-}47^+$	OT^+ $SNAP\text{-}47^-$	OT^+ (%)	OT^+ $SNAP\text{-}47^+$ (%)	OT^+ $SNAP\text{-}47^-$ (%)
Total	8	5	3	100	62.5	37.5
	5	4	1	100	80	20
	5	3	2	100	60	40
	6	5	1	100	83.33	16.67
	24	17	7	100	70.83	29.17

7.-OT and SNAP-47 interaction in the plasma membrane of hypothalamic oxytocinergic neurons.

Table 99.- Descriptive statistics of SNAP-47-membrane patches.

Condition	Cells (n)	SNAP-47-membrane patches (Mean ± SEM)
Basal_1 min	98	3.56 ± 0.41
Stimulation_1 min	103	3.44 ± 0.33
Basal_10 min	10	2.50 ± 0.54
Stimulation_10 min	9	1.56 ± 0.24
Basal+EGTA_1 min	79	4.96 ± 0.56
Stimulation+EGTA_1 min	76	3.51 ± 0.40

Table 100.- Statistical analysis of SNAP-47-membrane patches.

Comparison	Statistical test	p-value	p-value summary
Basal_1 min vs. Stimulation_1 min	Mann-Whitney	0.6445	ns
Basal_10 min vs. Stimulation_10 min	Mann-Whitney	0.2488	ns
Basal_1 min vs. Basal_10 min	Mann-Whitney	0.9670	ns
Stimulation_1 min vs. Stimulation_10 min	Mann-Whitney	0.1939	ns
Basal+EGTA_1 min vs. Stimulation+EGTA_1 min	Mann-Whitney	0.1534	ns
Basal_1 min vs. Basal+EGTA_1 min	Mann-Whitney	0.0457	*
Stimulation_1 min vs. Stimulation+EGTA_1 min	Mann-Whitney	0.8052	ns

Table 101.- Descriptive statistics of SNAP-47-membrane patches' area.

Condition	SNAP-47-membrane patches (n)	Area (Mean ± SEM), μm^2
Basal_1 min	330	0.59 ± 0.05
Stimulation_1 min	318	0.66 ± 0.06
Basal_10 min	25	2.43 ± 0.91
Stimulation_10 min	3	2.43 ± 0.53
Basal+EGTA_1 min	374	0.75 ± 0.06
Stimulation+EGTA_1 min	260	0.76 ± 0.08

Table 102.- Statistical analysis of SNAP-47-membrane patches' area.

Comparison	Statistical test	p-value	p-value summary
Basal_1 min vs. Stimulation_1 min	Mann-Whitney	0.8451	ns
Basal_10 min vs. Stimulation_10 min	Mann-Whitney	0.1651	ns
Basal_1 min vs. Basal_10 min	Mann-Whitney	0.3038	ns
Stimulation_1 min vs. Stimulation_10 min	Mann-Whitney	0.0014	**
Basal+EGTA_1 min vs. Stimulation+EGTA_1 min	Mann-Whitney	0.1289	ns
Basal_1 min vs. Basal+EGTA_1 min	Mann-Whitney	0.0074	**
Stimulation_1 min vs. Stimulation+EGTA_1 min	Mann-Whitney	0.3154	ns

Table 103.- Descriptive statistics of OT- and SNAP-47-membrane patches' distance from experimental and randomly-generated data set.

Condition	Measurements between OT- and SNAP-47-membrane patches	OT- and SNAP-47-membrane patches' distance (Mean ± SEM), µm
Experimental_Basal_1 min	152	0.10 ± 0.00
Experimental_Stimulation_1 min	141	0.10 ± 0.00
Random_Basal_1 min	151	4.43 ± 0.19
Random_Stimulation_1 min	139	4.61 ± 0.25

Table 104.- Statistical analysis of OT- and SNAP-47-membrane patches' distance.

Comparison	Statistical test	p-value	p-value summary
Experimental_Basal_1 min vs. Experimental_Stimulation_1 min	Mann-Whitney	0.2735	ns
Random_Basal_1 min vs. Random_Stimulation_1 min	Mann-Whitney	0.8565	ns
Experimental_Basal_1 min vs. Random_Basal_1 min	Mann-Whitney	<0.0001	****

Experimental_ Stimulation_1 min vs. Random_ Stimulation_1 min	Mann-Whitney	<0.0001	****

Table 105.- Frequency distribution of OT- and SNAP-47-membrane patches' distance in experimental data set.

Distance (µm)	Basal (raw data)	Basal (%)	Stimulation (raw data)	Stimulation (%)
0.0	4	2.63	8	5.67
0.05	54	35.53	56	39.72
0.10	69	45.39	47	33.33
0.15	16	10.53	22	15.60
0.20	3	1.97	3	2.13
0.25	3	1.97	1	0.71
0.30	0	0	1	0.71
0.35	1	0.66	0	0
0.40	0	0	1	0.71
0.45	1	0.66	0	0
0.50	0	0	1	0.71
0.55	0	0	0	0
0.60	1	0.66	1	0.71
Total	152	100	141	100

Table 106.- Frequency distribution of OT- and SNAP-47-membrane patches' distance in randomly-generated data set.

Distance (μm)	Basal (raw data)	Basal (%)	Stimulus (raw data)	Stimulus (%)
0	6	3.97	4	2.88
1	14	9.27	19	13.67
2	17	11.26	13	9.35
3	18	11.92	22	15.83
4	24	15.89	15	10.79
5	25	16.56	15	10.79
6	12	7.95	16	11.51
7	20	13.24	12	8.63
8	8	5.30	16	11.51
9	5	3.31	3	2.16
10	1	0.66	1	0.72
11	1	0.66	1	0.72
12	0	0	0	0
13	0	0	1	0.72
14	0	0	0	0
15	0	0	0	0
16	0	0	0	0
17	0	0	0	0
18	0	0	0	0
19	0	0	0	0
20	0	0	0	0
21	0	0	1	0
Total	151	100	139	100

Table 107.- Descriptive statistics of distance between randomly-generated OT- and SNAP-47-membrane patches.

	Random patches (n)	Random patches (%)
Random patches_distance_0-1 μm	27	9.31
Random patches_distance_>1 μm	263	90.69

Table 108.- Descriptive statistics of interaction between experimental OT- and SNAP-47-membrane patches.

Condition	OT-membrane patches (n)	OT-membrane patches colocalizing with SNAP-47 (n)	OT-membrane patches (%)	OT-membrane patches colocalizing with SNAP-47 (%)
Basal_1 min	133	119	100	89.47
Stimulation_1 min	142	122	100	85.91

Table 109.- Statistical analysis of interaction between experimental OT- and SNAP-47-membrane patches.

Comparison	Statistical test	p-value	p-value summary
OT^+_Basal_1 min vs. OT^+ $SNAP\text{-}47^+$_Basal_1 min	Mann-Whitney	0.3435	ns
OT^+_Stim_1 min vs. OT^+ $SNAP\text{-}47^+$_Stim_1 min	Mann-Whitney	0.3323	ns
OT^+ $SNAP\text{-}47^+$_Basal_1 min vs. OT^+ $SNAP\text{-}47^+$_Stim_1 min	Mann-Whitney	>0,9999	ns

Table 110.- Descriptive statistics of Manders' and Pearson´s coefficients from experimental data set. n= 132 cells.

Condition	OT-membrane patches colocalizing with SNAP-47 (n)	Colocalization coefficient (Mean ± SEM)	Colocalization coefficient (% ± SEM)
Manders_Basal	127	0.76 ± 0.01	76 ± 1
Manders_Stimulation	119	0.80 ± 0.01	80 ± 1
Pearson_Basal	126	0.26 ± 0.01	26 ± 1
Pearson_Stimulation	119	0.28 ± 0.01	28 ± 1

Table 111.- Statistical analysis of Mander's and Pearson's coefficients for OT- and SNAP-47-membrane patches in experimental data set.

Comparison	Statistical test	p-value	p-value summary
Manders_Basal_1 min vs. Manders_Stimulation_1 min	Mann-Whitney	0.0914	ns
Pearson_Basal_1 min vs. Pearson_Stimulation_1 min	Mann-Whitney	0.4134	ns

Table 112.- Frequency distribution of Manders' coefficient for OT- and SNAP-47-membrane patches in experimental data set.

Manders' coefficient	Basal (raw data)	Basal (%)	Stimulation (raw data)	Stimulation (%)
0.25	0	0	0	0
0.3	3	2.36	0	0
0.35	0	0	1	0.84
0.4	1	0.79	1	0.84
0.45	1	0.79	0	0
0.5	4	3.15	6	5.04
0.55	8	6.30	2	1.68

0.6	9	7.09	5	4.20
0.65	7	5.51	8	6.72
0.7	10	7.87	5	4.20
0.75	18	14.17	14	11.76
0.8	12	9.45	18	15.13
0.85	14	11.02	11	9.24
0.9	20	15.75	26	21.85
0.95	13	10.24	17	14.28
1	7	5.51	5	4.20
Total	127	100	119	100

Table 113.- Frequency distribution of Pearson's coefficient for OT- and SNAP-47-membrane patches in experimental data set.

Pearsons' coefficient	Basal (raw data)	Basal (%)	Stimulation (raw data)	Stimulation (%)
0	3	2.38	4	3.36
0.05	13	10.32	8	6.72
0.1	18	14.28	11	9.24
0.15	13	10.32	14	11.76
0.2	12	9.52	16	13.44
0.25	11	8.73	11	9.24
0.3	18	14.28	12	10.08
0.35	9	7.14	9	7.56
0.4	11	8.73	9	7.56
0.45	1	0.79	9	7.56
0.5	7	5.55	7	5.88
0.55	8	6.35	4	3.36
0.6	1	0.79	1	0.84
0.65	1	0.79	2	1.68
0.7	0	0	2	1.68
0.75	0	0	0	0
Total	126	100	119	100

8.-SNAP-47-KD impairs OT recruitment to the plasma membrane under basal and stimulated conditions.

Table 114.- Descriptive statistics of OT-membrane patches in uninfected and SNAP-47-KD-expressing neurons.

Condition	Cells (n)	OT-membrane patches (Mean ± SEM)
Uninfected_Basal_1 min	147	1.72 ± 0.12
Uninfected_Stimulation_1 min	145	2.34 ± 0.20
Infected_Basal_1 min	48	0.94 ± 0.24
Infected_Stimulation_1 min	52	0.46 ± 0.12

Table 115.- Statistical analysis of OT-membrane patches in uninfected and SNAP-47-KD-expressing neurons.

Comparison	Statistical test	p-value	p-value summary
Uninfected_Basal_1 min vs. Infected_Basal_1 min	Mann-Whitney	<0.0001	****
Uninfected_Stimulation_1 min vs. Infected_Stimulation_1 min	Mann-Whitney	<0.0001	****
Uninfected_Basal_1 min vs. Uninfected_Stimulation_1 min	Mann-Whitney	0.0369	*
Infected_Basal_1 min vs. Infected_Stimulation_1 min	Mann-Whitney	0.1290	ns

Table 116.- Descriptive statistics of OT-membrane patches' area in uninfected and SNAP-47-KD-expressing neurons.

Condition	Cells (n)	OT-membrane patches (Mean ± SEM)
Uninfected_Basal_1 min	95	0.56 ± 0.08
Uninfected_Stimulation_1 min	81	0.52 ± 0.06
Infected_Basal_1 min	32	0.32 ± 0.05
Infected_Stimulation_1 min	20	0.40 ± 0.12

Table 117.- Statistical analysis of OT-membrane patches' area in uninfected and SNAP-47-KD-expressing neurons.

Comparison	Statistical test	p-value	p-value summary
Uninfected_Basal_1 min vs. Infected_Basal_1 min	Mann-Whitney	0.4250	ns
Uninfected_ Stimulation_1 min vs. Infected_Stimulation_1 min	Mann-Whitney	0.2530	ns
Uninfected_Basal_1 min vs. Uninfected_ Stimulation_1 min	Mann-Whitney	0.3595	ns
Infected_Basal_1 min vs. Infected_ Stimulation_1 min	Mann-Whitney	0.9813	ns

9.-SNAP-47-KD *in vivo*

Table 118.- Descriptive statistics of oxytocinergic neurons infected with AAV-SNAP-47-KD-GFP virus.

	Slices (n)	Infected OT neurons (n)	Infected OT neurons (Mean ± SEM)	Infected OT neurons (% ± SEM)
OT^+	22	503	22.86 ± 7.58	100
OT^+ $SNAP47^+$	22	10	0.45 ± 0.30	1.99
OT^+ $SNAP47^-$	22	493	22.41± 7.44	98.01

Table 119.- Statistical analysis of oxytocinergic neurons infected with AAV-SNAP-47-KD-GFP virus.

Comparison (Infected)	Statistical test	p-value	p-value summary
OT^+ vs. OT^+ $SNAP47^+$	Kruskal-Wallis	<0.0001	****
OT^+ vs. OT^+ $SNAP47^-$	Kruskal-Wallis	>0.9999	ns
OT^+ $SNAP47^+$ vs. OT^+ $SNAP47^-$	Kruskal-Wallis	<0.0001	****

Table 120.- Descriptive statistics of SNAP-47 mean fluorescence intensity in the PVN.

	Slices (n)	Mean fluorescence intensity (Mean ± SEM)	Mean fluorescence intensity (% ± SEM)
Injected_ SNAP-47-KD virus	22	0.81 ± 0.31	10
Non-injected	36	8.11 ± 0.79	100

Table 121.- Statistical analysis of SNAP-47 mean fluorescence intensity in the PVN.

Comparison	Statistical test	p-value	p-value summary
SNAP-47 fluo intensity_Injected vs. Non-injected	Mann-Whitney	<0.0001	****

Table 122.- Descriptive statistics of sociability test in control and SNAP-47-KD mice.

Condition	Tested mice (n)	Exploration time_Empty (Mean ±SEM), s	Exploration time_M1 (Mean ± SEM), s	Sociability index
Control	5	31.30 ± 6.94	72.10 ± 9.48	2.65 ± 0.44
SNAP-47-KD	8	40.41 ± 4.20	59.70 ± 5.61	1.57 ± 0.20

Table 123.- Statistical analysis of sociability in control and SNAP-47-KD-mice

Comparison	Statistical test	p-value	p-value summary
Control: E vs. M1	Mann-Whitney	0.0159	*
SNAP-47-KD: E vs. M1	Mann-Whitney	0.0143	*
Control vs. SNAP-47-KD	Mann-Whitney	0.0451	*

Table 124.- Descriptive statistics of social novelty test in control and SNAP-47-KD mice.

Condition	Tested mice (n)	Exploration time_M1 (Mean ±SEM), s	Exploration time_M2 (Mean ± SEM), s	Social novelty index
Control	5	40.32 ± 4.40	76.18 ± 2.57	1.97 ± 0.19
SNAP-47-KD	8	40.08 ± 3.3	88.23 ± 16.74	2.43 ± 0.57

Table 125.- Statistical analysis of social novelty in control and SNAP-47-KD-mice

Comparison	Statistical test	p-value	p-value summary
Control: E vs. M1	Mann-Whitney	0.0079	**
SNAP-47-KD: E vs. M1	Mann-Whitney	0.0070	**
Control vs. SNAP-47-KD	Mann-Whitney	0.9433	ns